Inorganic and Hybrid Analogues of Kagomé and Triangular Magnets

Thesis submitted in accordance with the requirements of the University of Liverpool for the degree of Doctor in Philosophy by

Katherine Rose Tustain

July 2021

Abstract

Geometric magnetic frustration is a phenomenon that arises through the competing exchange interactions that occur due to the arrangement of magnetic ions within the crystal structure of a material. In this work, the structural and magnetic behaviour of inorganic and hybrid systems that contain a triangular or kagomé arrangement of ions is explored through the complementary use of powder diffraction, magnetometry, heat capacity and muon spectroscopy measurements.

The first series of materials reported are the mineral barlowite, $Cu_4(OH)_6FBr$, and its halide analogues, $Cu_4(OH)_6FCl$ and $Cu_4(OH)_6FI$. Each of these systems contain a kagomé network of Cu^{2+} ions which are separated by an additional Cu^{2+} site. At room temperature, the crystal structures belong to the $P6_3/mmc$ hexagonal space group, where the interlayer Cu^{2+} is disordered. Upon cooling, a structural transition takes place to varying extents across the series, in which the average structure can be described by the orthorhombic $Pnma$ space group. However, some remaining disorder on the interlayer site is unearthed, which can be correlated to features observed in the magnetic behaviour across this series.

Next, the magnetic behaviour of the Zn-barlowite series, $Zn_xCu_{4-x}(OH)_6FBr$, is investigated using neutron powder diffraction, magnetometry and muon spectroscopy techniques. There is evidence to suggest that Zn^{2+} preferentially occupies the interlayer Cu^{2+} site, which magnetically decouples the kagomé layers from each other. This is shown via muon spin relaxation measurements, alongside supporting DFT muon-site calculations, that provide evidence for fluctuating magnetic moments in highly-substituted samples at sub-kelvin temperatures. This behaviour is indicative of the presence of a dynamic magnetic ground state such as that associated with the elusive quantum spin liquid.

The family of metal-organic frameworks with the formula $Cu_3(CO_3)_2(X)_3{\cdot}2ClO_4$ are formed from kagomé layers that are separated by an organic linker, X = 1,2-bis(4-pyridyl)ethane, 1,2-bis(4-pyridyl)ethylene or 4,4'-azopyridine. A new crystal structure with the space group $P3$ is proposed for these systems, which adequately describes the disorder present in the organic linkers. Through characterisation via magnetic susceptibility, heat capacity and powder diffraction measurements, the magnetic structures of these systems suggest that antiferromagnetic exchange occurs through these linkers. Meanwhile, the nature of the exchange within the kagomé layers is predicted to be ferromagnetic rather than antiferromagnetic.

$KFe(C_2O_4)F$ is a hybrid coordination framework containing a distorted triangular arrangement of Fe^{2+} ions that are bound through oxalate linkers. A comprehensive neutron powder diffraction and muon spectroscopy study reveals that the magnetic structure of this material contains quasi-one-dimensional Fe–F–Fe chains that are antiferromagnetically coupled, suggesting that a combination of low-dimensionality and magnetic frustration characterises the magnetic ground state of this system.

Declaration

The work presented in this thesis was carried out by the author and using the references contained herein, unless explicitly stated otherwise in the text or acknowledgements. This thesis has not been submitted to any other institution for the award of a degree.

K. Tustain
July 2021

Acknowledgements

First and foremost, I would like to thank my supervisor, Dr Lucy Clark, for her constant support, guidance and encouragement over the past few years. I am incredibly grateful to have had such a well-rounded and fun PhD experience and for all of the opportunities that have been made available to me. At this point I should additionally acknowledge the University of Liverpool for providing funding for my PhD studentship. I'd also like to thank my MChem supervisor in Durham, Dr Karen Johnston, without whose encouragement I would never have had the confidence to pursue a PhD.

This thesis would not exist without the expertise of many talented people. In particular, Dr Gøran Nilsen's (ISIS) assistance was crucial for the magnetic structure work presented in Chapter 3, as well as many instructive discussions otherwise; Dr Emma McCabe (Durham) was incredibly helpful with understanding our diffraction data in Chapter 3, and performing preliminary refinements; Prof Tom Lancaster's and Dr Ben Huddart's (Durham) DFT calculations in Chapter 4 were pivotal to our understanding of our muon data, along with the supporting data collected and analysed by Prof Fabrice Bert and his students Quentin Barthélemy and Brendan Le Pennec (Paris-Saclay); Tristan Dolling's crystal growth and Dr Sam Ivko's (Birmingham) structure solution advanced our understanding of the materials discussed in Chapter 5; and the work by Dr Wenjiao Yao (St Andrews) and Lewis Farrar (Liverpool) laid the groundwork for the findings in Chapter 6. Thank you to the Science and Technology Facilities Council for funding the numerous central facilities experiments that form the bulk of this thesis, and to the many instrument scientists who I've worked with over the years: Dr Peter Baker, Dr Ivan da Silva, Dr Mark Telling, Dr Pascal Manuel, Dr Alex Gibbs, Dr Claire Murray, Dr Stephen Thompson, Dr Clemens Ritter, Dr Hubertus Luetkens, Dr Chennan Wang, and Dr Ross Stewart.

Further recognition goes to the Rosseinsky group, particularly Dr Luke Daniels, Dr Hongjun Niu and Richard Feetham, for regular access to powder diffraction and MPMS facilities, as well as Prof Rick Cosstick and Dr Neil Kershaw for offering their lab space upon my arrival in Liverpool. I'm also grateful for the

additional MPMS measurements conducted by Dr Gavin Stenning at the ISIS Materials Characterisation Laboratory, for the help of Dr Sarah Youngs and the ISIS Deuteration Facility, and for Stephen Moss and the Analytical Services in Liverpool for conducting countless ICP measurements for me. A huge thank you also to Dr Angel Arévalo-López for collecting all of the PPMS data presented within this thesis, and for hosting my visit to Lille.

Many thanks must go to the present Clark group members: Aly Abdeldaim, Jen Graham, Sam Ivko, Tristan Dolling – thank you for sitting through endless barlowite talks, for keeping me sane through beamtime with exploding kittens, and for regular Fika! I'm also grateful to the past group members—Brendan Ward-O'Brien, Lewis Farrar, Adam Hayward, Rich Lyons and Rory Powell—for useful discussions as well as assistance in the lab. To all of the friends who have come and gone from the MIF and Liverpool over the years, thank you for popping by the office and for many trips to the AJ. Particular thanks go to Olly Rogan (or maybe not), without whom I would have finished this thesis much sooner. I must also thank Amy Robinson for keeping me company during lockdown and for taking me on regular walks. Finally, I have met many inspiring people over the years at conferences and on courses, but particular appreciation goes to Dan Martin (and the shrunken heads).

Last but not least, I am grateful for my parents, Rose and Steve, who have always gone out of their way for me and encouraged me despite not having a clue what I do, and for my big brothers, Joe and Sam, who I've always looked up to. Consider this thesis revision material for the next Christmas quiz.

Contents

Chapter 1

Introduction

Solid state materials are the foundation of many areas of modern science and technology as a result of the structure-property relationships that arise within them [1]. Our fundamental understanding of these properties has led to ground-breaking developments in applications including, but certainly not limited to, solid state batteries [2], light-emitting diodes [3], and sensors [4]. The theme of this thesis, however, surrounds the property of magnetism that arises in solid state materials that typically contain metal ions hosting unpaired electrons. Magnetism has been harnessed for centuries in applications that are integral to our everyday lives, such as in compasses [5], for memory storage [6], magnetic imaging for medical purposes [7], and in cooling devices [8]. Of course, whilst the components that make up these materials, on the whole, can be understood using quantum mechanical concepts, the macroscopic behaviour of a typical magnet can be described in a classical manner [9]. Even so, there was once a time where magnetism was largely misunderstood, but in the past century our developed understanding of the quantum world has brought with it a new, more elusive class of materials named quantum materials, in which classical concepts are unable to describe the unusual electronic and magnetic properties which emerge from them [10]. This interdisciplinary topic spans the fields of materials chemistry and condensed matter physics, and examples of such exotic states include superconductors, skyrmions, topological insulators and quantum spin liquids [11]. It is the latter class of materials which are of interest in this thesis.

A quantum spin liquid, first and foremost, is a crystalline *solid*, and at least one of the atoms that form its periodic structure must contain unpaired electrons, which have a corresponding *spin*. In typical magnetic materials, the direction of the magnetic moment associated with this spin may order in a particular pattern. For example, in a ferromagnet the magnetic moments on each atom will point in one direction, either when magnetised by an external field or when cooled below a critical magnetic ordering temperature. On the contrary, in an antiferromagnet

the magnetic moments will point antiparallel to each other. In between these two extremes there are many different ways in which magnetic moments can order themselves into a regular pattern, which depends on the identity and placement of atoms in a particular material and the various interactions between them. In a quantum spin liquid, however, these unpaired electrons will never order into such a pattern. Instead they remain dynamically fluctuating, analogous to the molecules in a liquid, in a manner that can only be described using quantum mechanics [12]. One consequence of this is that exotic quasiparticles are expected to emerge from such materials. It is hoped that our understanding of these phenomena will allow us to grasp some of the outstanding challenges that exist in quantum physics, and ultimately contribute to the development of the quantum devices which are expected to transform next-generation technology [13].

In this regard, one of the many challenges presented to materials scientists is the discovery and characterisation of new solid state materials that realise such intriguing magnetic behaviour, and it is this aim which this thesis strives to achieve. All of the materials studied within this work give rise to such behaviour because the geometry of the magnetic ions with respect to one another prevents their spins from ordering in a conventional way. This chapter aims to provide an introduction to this concept, termed magnetic frustration, alongside some of the fundamentals of the study of magnetism and quantum materials. In Chapter 2, an overview of the synthetic and characterisation routes relevant to the study of frustrated magnets is given, with a focus on the advantages and limitations of these techniques in this particular field. Chapters 3 – 6 form the bulk of the research carried out for this thesis, which has involved the characterisation of four inorganic or hybrid systems that contain a triangular arrangement of magnetic ions expected to display magnetic frustration. A thorough investigation into these systems' structural and magnetic properties has been undertaken via a combination of powder X-ray and neutron diffraction, magnetometry and heat capacity measurements, as well as muon spectroscopy. Finally, Chapter 7 aims to summarise the results presented in this thesis, and to provide an outlook for future work in this field.

1.1 The Fundamentals of Magnetism

Magnetism is brought about through the motion of electrical charges. In electromagnetism, for example, magnetism is created by running a current through a coil of wire. On the microscopic level, the smallest charge is the electron, which

is often visualised as a tiny bar magnet because it has an associated "spin" that generates a magnetic field. However, the electron is a point charge and thus cannot really spin and generate a magnetic field in the way that a charged wire does, and for this reason the electron spin is often termed the *intrinsic* spin angular momentum. Electrons also orbit the nucleus, which gives rise to what is termed the orbital angular momentum. In 1922, the Stern-Gerlach experiment elegantly demonstrated that both of these phenomena take values which are quantised in discrete values when placed in an inhomogeneous magnetic field [14]. In this section, a brief overview of the concepts that describe electrons in transition metal elements is given.

1.1.1 The Magnetic Moment

Classically, the angular momentum that arises through the motion of electrical charge has a magnetic moment associated with it, which is proportional to the area loop created about the axis of rotation [15]. In the case of atoms or ions where electrons orbit a nucleus, there are a set of quantum numbers which describe their behaviour, and therefore their magnetic moments, as outlined below:

- The motion of electrons about a nucleus results in a total orbital angular momentum, $\mathbf{L}$, which is proportional to the magnetic moment via a constant termed the gyromagnetic ratio, γ, via,

$$\boldsymbol{\mu} = \gamma \mathbf{L}. \tag{1.1}$$

- The intrinsic spin angular momentum of a single electron about a nucleus (*i.e.* the electron in a hydrogen atom) has a magnetic moment defined as

$$\mu = -\frac{e\hbar}{2m_{\mathrm{e}}} = -\mu_{\mathrm{B}}, \tag{1.2}$$

  where e is the charge of an electron, m_{e} is the mass of an electron, and $\hbar$ is the reduced Planck's constant. μ_{B} is the Bohr magneton, which has a value of 9.274×10^{-24} J T^{-1}. Magnetic moments are commonly expressed in terms of this unit.

- When an external field, $\mathbf{B}$, is applied to a magnetic moment, its potential energy is given by,

$$E = \boldsymbol{\mu} \cdot \mathbf{B} = -\mu B \cos\theta, \tag{1.3}$$

so that the energy is minimized when the magnetic moment lies parallel to the magnetic field. Because the magnetic moment is associated with an angular momentum, the change in μ is perpendicular to both μ and B, and thus the magnetic field causes the direction of μ to precess about B. Crucially, the components of the magnetic moments projected along the field direction due to the intrinsic spin and orbital angular momenta are quantised, so that only certain values of the angle θ are allowed [16].

- The magnitudes of the spin angular momentum, $\mathbf{S}$, and the orbital angular momentum, $\mathbf{L}$, of an electron orbiting a nucleus are quantised as follows,

$$S = \sqrt{s(s+1)}\hbar \quad \text{and} \quad L = \sqrt{l(l+1)}\hbar \tag{1.4}$$

  where s and l are the spin and orbital angular momentum quantum numbers, respectively. For an electron, s is always equal to $\frac{1}{2}$, whereas l depends on the electronic state of the system, with $l = 0, 1, 2...n-1$. n is the principal quantum number, which always has an integer value. Here, a larger n describes a larger probable electron distance from the nucleus, or an electron "shell".

- The directions of $\mathbf{L}$ and $\mathbf{S}$ are also quantised in terms of the magnetic quantum number, m_l, and the spin quantum number, m_s, which take $2l+1$ and $2s+1$ values between $-l$ and $+l$, and $-s$ and $+s$, respectively.

- Because $s = \frac{1}{2}$ for an electron, it follows that $m_s = \pm\frac{1}{2}$. This means that the electron spin points in one of two directions, termed spin-up and spin-down.

- The total angular momentum, $\mathbf{J}$, is the sum of the orbital angular momentum, $\mathbf{L}$, and the spin angular momentum, $\mathbf{S}$. The total magnetic moment in an atom or ion, therefore, depends on the relative contributions of the orbital and spin angular momenta.

- The magnitude of the total effective magnetic moment in an atom or ion is given by,

$$\mu_{\text{eff}} = g_{\text{J}}\sqrt{J(J+1)}\mu_{\text{B}} \tag{1.5}$$

  where g_{J} is a special case of a dimensionless proportionality constant g-factor, named the Lande g-factor, for an electron with both spin and orbital angular momenta. The spin and orbital angular momenta can interact via the spin-orbit coupling interaction, $\lambda\mathbf{L}\cdot\mathbf{S}$, where λ is the spin-orbit coupling constant.

- However, in the majority of the transition metal ions the orbital angular momentum is said to be quenched, so that $L = 0$ and by approximation $J = S$. As a result, the spin-only estimate for the magnetic moment can be used,

$$\mu_{\text{so}} = g\sqrt{S(S+1)}\mu_B, \tag{1.6}$$

where $g = 2$ for the intrinsic spin angular momentum [15].

The Pauli exclusion principle states that no two electrons in an atom or ion can have the same set of quantum numbers. In practice this means that in a many-electron system, no two electron spins can be parallel with respect to one another ($m_s = \pm\frac{1}{2}$) if they have the same value of m_l. In fact, the structure of the periodic table in which elements are separated into s, p, d and f blocks arises due to the Pauli exclusion principle. The combination of quantum numbers which minimise the overall energy can be further estimated using Hund's rules, which state that the lowest energy electron configuration is one where the total number of unpaired electrons, S, and the orbital angular momentum, L, are maximised [17].

1.1.2 Crystal Fields

An orbital approximation is used to visualise the wavefunctions which describe the $2l+1$ degenerate states of an ion. In the transition metals, it is the d-orbitals which are most important in terms of the magnetic and electronic properties because they are spatially expanded and interact strongly with their surroundings, and this is the reason that the orbital angular momentum is typically "quenched" in systems which contain transition metal ions. The $3d$ orbitals have orbital angular momentum represented by $l = 2$, and so there are $2l + 1$ different d orbitals whose shapes, depicted in Figure 1.1, have a pronounced angular dependence which describes the electron density for a given orbital. In the case of a free ion, the $3d$ orbitals are degenerate in energy. However, in a real material a metal ion experiences what is known as the crystal field, which arises due to the repulsion between the electrons in the d-orbitals and the coordinated ligands, which are modelled as point charges. Depending on the symmetry of the resulting environment, a perturbation to the energy levels which represent these orbitals occurs which can then be used to rationalise the magnetic properties of a given system [18]. When placed in an octahedral crystal field, for example, the d_{z^2} and $d_{x^2-y^2}$ orbitals have components which point directly into the path of the ligands, whilst the d_{xy}, d_{yz} and d_{xz} orbitals are directed between the ligands. This means that the former set of orbitals, termed the e_g orbitals, are doubly degenerate and are higher in energy

than the latter set, termed t_{2g} orbitals, which are triply degenerate, because there is an energetic cost associated with the electrostatic repulsion between the metal and the ligands. This is demonstrated via a crystal field splitting energy diagram in Figure 1.1. In contrast, in the case of a tetrahedral crystal environment the opposite is true and the two sets of orbitals switch around in energy. There is a third crystal field that is relevant to the work within this thesis, which is the trigonal prismatic coordination, shown in Figure 1.2. In this case, the orientation of the ligands with respect to the d-orbitals of the metal centre leads to three different sets of energy levels [19].

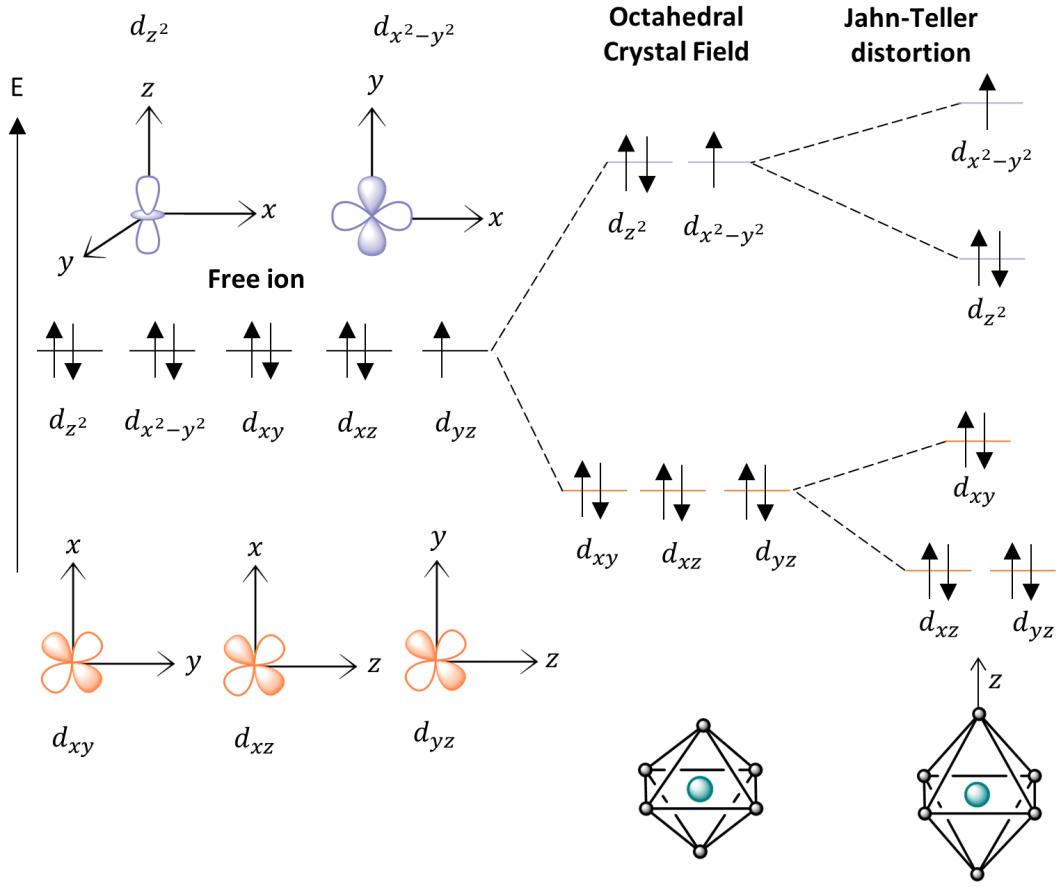

Figure 1.1: The d-orbitals which are occupied by the outermost electrons in a typical transition metal are split in energy in the presence of a crystal field. In an octahedral crystal field, as shown, orbitals which point towards the ligands are raised in energy, and vice versa. These energy levels are further split in the case of a d^9 electron configuration due to the Jahn-Teller effect, where the system spontaneously distorts, here shown via an elongation along z. This effect acts to remove the degeneracy associated with the unpaired electron.

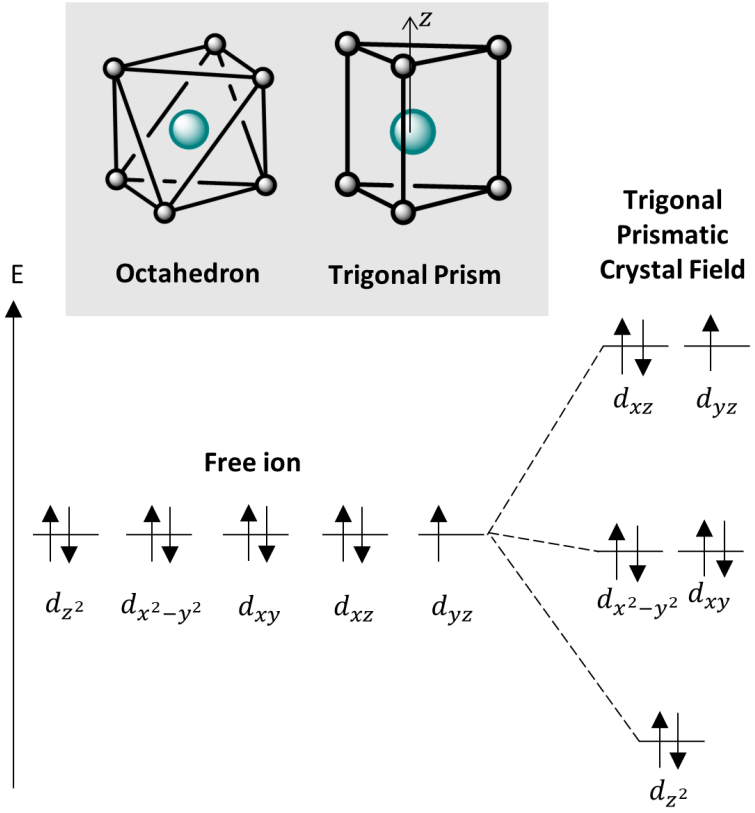

Figure 1.2: In a trigonal prismatic coordination environment, the d-orbitals are split into three energy levels. This coordination environment is typically observed in metals with d^0, d^1 and d^2 electron configurations [19]. Trigonal prismatic coordination is particularly rare for a d^9 metal such as Cu^{2+}, because the system must further distort via a Jahn-Teller mechanism to remove the degeneracy associated with the unpaired electron, which can occupy one of two degenerate orbitals in the crystal field splitting energy diagram depicted here.

1.1.3 The Jahn-Teller Effect

A large part of this thesis surrounds the study of Cu^{2+}-based materials. Cu^{2+} is an interesting case because it has a d^9 electron configuration and therefore a total spin of $S = \frac{1}{2}$. In an octahedral crystal field, the unpaired electron in the Cu^{2+} electron configuration has a choice about which of the doubly degenerate e_g orbitals discussed above that it occupies. To circumvent this choice, the octahedral crystal field around the Cu^{2+} ion typically spontaneously distorts in one of two ways to remove the degeneracy associated with these orbitals. The bonds connecting the ligands along the axial directions, shown in Figure 1.1, can elongate, which causes the orbitals with components along this z axis to lower in energy. Conversely, these

same bonds can compress, resulting in an increase in the energy levels of the same orbitals. Both of these instances break the degeneracy of the e_g orbitals, so that there is now a single high-energy orbital that the unpaired electron of the Cu^{2+} ion can occupy, which is energetically favourable. This phenomenon is termed a Jahn-Teller distortion, and this concept often governs the crystal field environment assumed by transition metal ions whose electron configuration means there is some orbital degeneracy. The former example, where two axial bonds elongate, is termed a [4+2] Jahn-Teller distortion, and is typically observed amongst the mineral systems relevant to Chapters 3 and 4 of this thesis. In an extended solid, if the directions of this elongation are ordered—*i.e.* there is no directional disorder associated with the distortion—then the effect is termed cooperative Jahn-Teller distortion. An extreme example of [4+2] Jahn-Teller distortion is where the ligands along the z-axis are completely removed, resulting in a square planar crystal field environment which is common amongst metals with a d^8 electron configuration, such as Ni^{2+}. The Jahn-Teller effect can be temperature-dependent, so that there is a dynamic switching of the orientation along which the elongated bonds occur which slows down with decreasing temperature. In an extended solid, this dynamic effect can present itself as a [2+4] Jahn-Teller distortion when using methods which probe average order over a long range [20].

1.2 Materials and Magnetism in the Solid State

The collective interactions between many atoms in a solid gives rise to a long-range periodic arrangement of these atoms, and their orientation with respect to one another is what typically gives rise to the functional properties relevant to modern day technology. In this section, the concepts required to aid in the understanding of the collective magnetic response in materials are outlined.

1.2.1 Crystallography

In order to optimise the functional properties of interest, a thorough understanding of the crystal structure of a given solid state material is required. A description of the regular arrangement of ions in three dimensions is given by a set of crystallographic rules which describe the symmetry operations that they obey in space. Each system is described by a unit cell which can be repeated to construct the entire crystal, with dimensions a, b and c, and angles α, β and γ. There are 7 crystal systems which are categorised depending on these unit cell lengths and angles, which are further divided into 14 Bravais lattices depending on their translational

symmetry. By considering the further symmetry operations of screw axes, mirror planes, glide planes and inversions, a total of 230 unique combinations exist which describe three dimensional symmetry, and are termed the crystallographic space groups. The symbols within a space group describe the symmetry operations which can be applied to the asymmetric unit—a fraction of the repeating unit—to generate the entire unit cell [1].

Further to this, there are a set of 1651 magnetic space groups which describe the arrangement of magnetic moments in space, and which are deduced by combining the 230 crystallographic space groups with an additional symmetry operation known as the time reversal operator. Magnetic moments are represented as axial vectors, which behave differently under symmetry operations than polar vectors, which can be used to represent the positions of atoms. As a result, the effect of the time reversal operator is to essentially flip the direction of a magnetic spin, and this is demonstrated in Figure 1.3 [21]. The relationship between the crystal unit cell and the magnetic unit cell is given by a propagation vector, **k**. The ability to represent the crystal and magnetic structures of materials in this way is vital to understanding the phenomena observed in functional materials. A clear understanding of both of these structures is important because, as will be demonstrated, the crystal structure of a material is one factor which governs the strength and

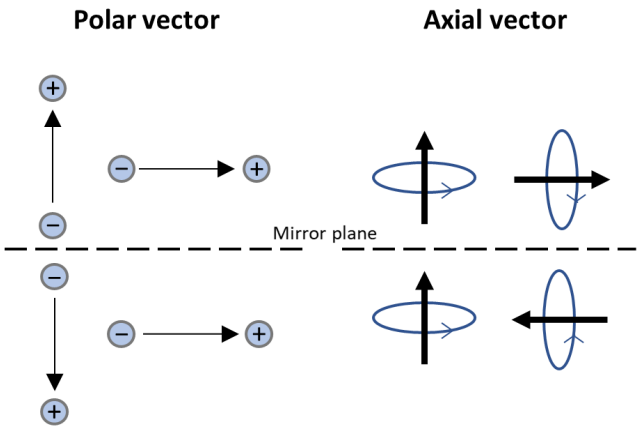

Figure 1.3: The time reversal operator is best understood by considering a mirror plane symmetry operation on polar and axial vectors that represent an atom and a magnetic moment, respectively. The polar vector is analogous to a dipole moment, whilst the axial vector is like an electric current loop, and these both transform differently in a mirror plane. To account for this, the time reversal operator is used to invert the magnetic moments without moving the atoms. The combination of a symmetry operation with time-reversal is called a primed operation [21].

nature of the interactions which arise in a magnetic solid.

1.2.2 Magnetisation and Susceptibility

In a solid state magnetic material there are a large number of atoms or ions which each possess their own magnetic moment. When a magnetic field, $\mathbf{H}$, is applied the material produces a macroscopic magnetic field in response called the magnetisation, $\mathbf{M}$. The relation between these two parameters is given by,

$$\mathbf{M} = \chi \mathbf{H}, \tag{1.7}$$

where χ is the magnetic susceptibility of the material, and represents the magnetic moment induced in a magnetic solid per unit volume. In other words, χ is a measure of the response of a magnetic material in an applied magnetic field. The total magnetic field, the flux density $\mathbf{B}$, is then the sum of the applied field and the magnetisation related via the permeability of free space,

$$\mathbf{B} = \mu_0(\mathbf{H} + \mathbf{M}). \tag{1.8}$$

The flux density can either decrease or increase in the presence of an applied field. The former occurs in diamagnetic materials due to the paired spins within their electron configurations, and whilst this is present in all materials, the resulting diamagnetic susceptibility is temperature independent and relatively small. However, this contribution becomes more significant in materials containing organic components with delocalised electrons. On the other hand, materials with unpaired electrons are termed paramagnetic and act to produce an increase in the magnetic flux density. This contribution is large relative to the diamagnetic susceptibility and is temperature dependent [15].

At high temperatures the spins of the unpaired electrons on paramagnetic ions are only weakly interacting and point in random directions, but still produce a positive magnetic susceptibility whose temperature dependence is described by,

$$\chi = \frac{C}{T}, \tag{1.9}$$

where C is the Curie constant. This is the Curie law, and is only valid at high temperatures or in the presence of weak magnetic fields. Importantly, the parameter

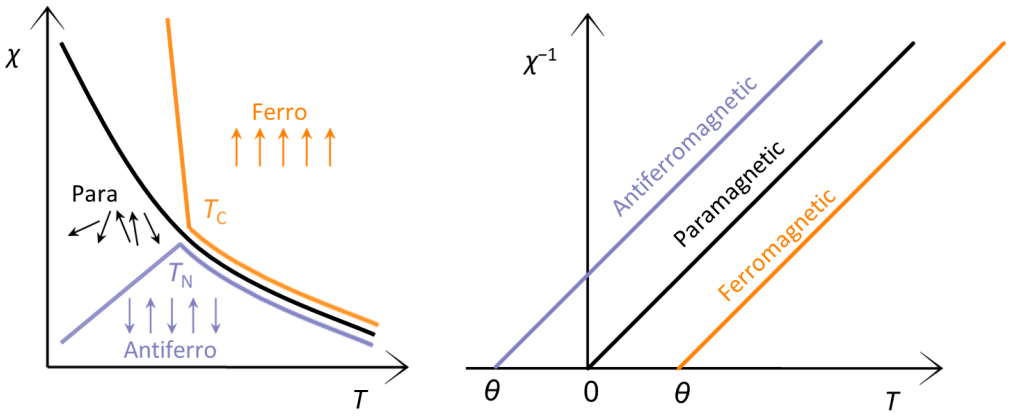

Figure 1.4: The temperature dependence of the magnetic susceptibility for a typical paramagnet, ferromagnet and antiferromagnet (left). By fitting the inverse susceptibility (right) to the Curie-Weiss law (Equation 1.11), the sign of the resulting Weiss temperature, θ, indicates whether the dominant magnetic interactions are ferromagnetic or antiferromagnetic for the measured material.

χ can be related to the magnetic moment via,

$$\mu_{\text{eff}} = \sqrt{\frac{3k_{\text{B}}\chi_{\text{M}}T}{N_{\text{A}}\mu_0}}, \tag{1.10}$$

where k_{B} is the Boltzmann constant, χ_{M} is the molar magnetic susceptibility and N_{A} is Avogadro's number. Substituting Equation 1.9, this simplifies to approximately $\mu_{\text{eff}} = \sqrt{8C}\ \mu_{\text{B}}$.

In most instances, however, the magnetic interactions between the magnetic atoms or ions mean that Curie's law is not obeyed, and these materials instead follow the Curie-Weiss law,

$$\chi = \frac{C}{T - \theta} \tag{1.11}$$

where θ is the Weiss constant, and represents the sum of all of the interactions between magnetic ions. In a typical magnetic material, a sharp transition in the temperature-dependent magnetic susceptibility is observed as the temperature approaches the energy scale of the interactions between the magnetic ions. The consequence of this is that the magnetic moments arrange themselves into an ordered array, such as shown in Figure 1.4. In ferromagnetic materials, the individual magnetic moments align parallel to each other below a transition temperature known as the Curie temperature, T_{C}. Conversely, in an antiferromagnet, nearest neighbour magnetic moments align antiparallel with respect to each other

below a transition temperature known as the Néel temperature, T_{N}. This instance can be considered to be two interpenetrating sublattices, on one of which the magnetic moments point up and the other they point down, such that there is no net magnetisation. The Weiss constant θ takes positive and negative values for ferromagnets and antiferromagnets, respectively, and is zero for paramagnets. θ also provides an estimate for the energy scale of the interactions in a magnetic material, and can therefore be used to predict when T_{C} or T_{N} might arise [15, 16].

The concept of spontaneous symmetry breaking—where a high-symmetry state ends up in an lower symmetry state—is a useful concept to consider at this point [22]. In a paramagnet, all magnetic moment directions are equivalent and each spin has rotational symmetry because the magnetic moments are randomly oriented, *i.e.* the system is invariant under a symmetry transformation. As the paramagnet is cooled, the magnetic moments align and rotational symmetry is broken, and so the system is said to have undergone a phase transition which is characterised by an order parameter, which in this example is the magnetisation. This concept is important because the quantum states of matter which will be discussed in Section 1.3 are particularly intriguing owing to the fact that they do not undergo spontaneous symmetry breaking.

1.2.3 Magnetic Exchange

The interactions described above that occur between magnetic ions is called magnetic exchange, and an important concept in this regard is the Heisenberg model which is represented by the Hamiltonian [15],

$$\hat{H} = -\sum_{ij} J_{\mathrm{ex}} \mathbf{S}_i . \mathbf{S}_j, \tag{1.12}$$

which represents the sum of all of the interactions between neighbouring magnetic moments in a system containing many spins, $\mathbf{S}_i$ and $\mathbf{S}_j$. J is the exchange integral, and determines whether the exchange between neighbouring spins is antisymmetric (antiferromagnetic) or symmetric (ferromagnetic), and takes positive or negative values for each, respectively. Note that in Equation 1.12, the vectors $\mathbf{S}_i$ and $\mathbf{S}_j$ imply that the magnetic moments can point in any direction in space. There are analogous Hamiltonians which describe XY and Ising models in which the moments are confined to a plane and along one axis, respectively. Several mechanisms exist through which magnetic exchange can occur, which are summarised below:

- **Direct exchange:** Here, the interaction is directly through neighbouring magnetic ions. However, in most systems there is insufficient overlap between the orbitals containing unpaired electrons for this type of exchange to arise [15].

- **Superexchange:** This mechanism depends on the overlap of partially occupied d-orbitals of the transition metal magnetic ion (M) with the occupied orbitals of a non-magnetic mediator, for example the $2p$ orbitals of the oxide ions (O) in a transition metal oxide. There are a set of rules devised by Goodenough [23, 24] and Kanamori [25] that describe the angular dependency on the nature and strength of magnetic superexchange in oxides. The theory predicts that the exchange is antiferromagnetic if the M–O–M bond angles are close to 180° so that the e_{g} or $t_{2\mathrm{g}}$ orbitals of both metal ions sufficiently overlap. Conversely, when the M–O–M bond angles are close to 90° then ferromagnetic exchange is predicted to take place. Of course, in real materials the situation is often complicated by the presence of many exchange pathways, and so the Goodenough-Kanamori rules are merely guidelines. Superexchange is the mechanism through which magnetic exchange typically occurs in the materials relevant to the work in this thesis.

- **Dzyaloshinskii–Moriya (DM) interaction:** This is an antisymmetric exchange which arises through the interplay between the spin-orbit interaction and superexchange. The DM interaction essentially results in a canting of two antiferromagnetically coupled spins which leads to a weak ferromagnetism in the material. There are several symmetry rules required for the DM interaction to persist and, importantly, if there is a centre of inversion at the point between the two magnetic ions, the DM interaction is equal to zero. The DM interaction plays an important role in materials containing large spin-orbit coupling and, in fact, this interaction is fundamental to the stabilisation of spin textures in topological materials such as skyrmions [26]. Furthermore, the DM interaction is allowed by the symmetry of the materials studied within this thesis.

- **RKKY interaction:** Discovered by Ruderman, Kittel, Kasuya and Yosida, this type of exchange is mediated by conduction electrons in metallic materials, which become polarised by a nearby magnetic moment and then couple to other nearby moments [27]. This is a much longer range interaction than those described above, and is common in rare earth metals [16].

- **Double exchange:** In materials which contain magnetic ions that can exist in more than one oxidation state, there is a hopping process where the e_g electrons transfer to a neighbouring ion. The process favours ferromagnetic alignment of spins in neighbouring ions, because it is energetically unfavourable for the hopping e_g electron to move to a neighbouring ion where the t_g spins are antiparallel to it [28, 29].

- **Dipolar exchange**: This exchange involves the interaction between two magnetic dipoles, the extent of which depends on their separation [15]. Dipolar exchange is typically too weak to explain spontaneous magnetisation, although it can become significant in rare-earth systems at very low temperatures [30].

1.3 Magnetic Frustration

When there are competing exchange interactions in a magnetic material, a form of frustration arises because the interactions cannot be simultaneously satisfied [31, 32]. This results in many states with equal energy which the system fluctuates between, and the material is said to be magnetically frustrated. As a consequence of this large ground state degeneracy, the magnetic ordering temperature is reduced in comparison to the energy scale of the exchange interactions, and this often leads to unconventional magnetic ground states. A measure of this phenomenon is therefore given by the ratio between the energy scale of the magnetic interactions, $|\theta|$, and the critical temperature, T_C, and the resulting number is known as the frustration index, f. The work in this thesis is concerned with geometric magnetic frustration, where the magnetic ions sit in an ordered arrangement but where the exchange interactions are frustrated via the topology of the magnetic ions.

1.3.1 Geometrically Frustrated Lattices

The standard way to understand geometric frustration is by attempting to place Ising spins in an antiferromagnetic arrangement onto an equilateral triangle; arranging the first two spins is intuitive, but there is no way to place the third spin so that it is antiparallel to both of its neighbours, as depicted in Figure 1.5, and there are six degenerate ground states which this particular system could select [33]. A similar concept can be applied to antiferromagnetically coupled Ising spins on the vertices of a tetrahedron. When this idea is extended over an

infinite array of edge-sharing triangles (or corner-sharing tetrahedra, in what is known as the pyrochlore structure), then macroscopic degeneracy emerges. For this reason, materials which bear a triangular topology of magnetic ions, such as in edge-sharing and corner-sharing triangular (kagomé) arrangements, as well as the three-dimensional pyrochlore lattice, are of great interest in the field of geometric frustrated magnetism.

An interesting case of magnetic frustration on the pyrochlore lattice is that of spin ice, where the dominant exchange is ferromagnetic rather than antiferromagnet. Magnetic frustration arises in this instance because of the existence of an easy-axis anisotropy present in materials such as $Dy_2Ti_2O_7$ [34] and $Ho_2Ti_2O_7$ [35], which means that the magnetic moments must point towards the centre of the tetrahedra. The result of this is that, if ferromagnetic exchange is dominant, the spins align so that two point inwards and two point out of the tetrahedra (see Figure 1.5), and the many ways in which this arrangement of spins can exist in an infinite lattice is what gives rise to macroscopic degeneracy. In fact, spin ice is an example of a classical spin liquid, in that the moments remain dynamically fluctuating between these different conformations (akin to the molecules in liquids) until the energy k_BT becomes too small and the spins freeze into a conformation which can be likened to the electric dipoles in water ice. In the temperature range $T_C < T < \theta$, the material behaves as a cooperative paramagnet in that the magnetic moments are dynamic like in a paramagnet, but are strongly correlated. Similarly, this idea can be applied in two dimensions to the kagomé lattice—named after a Japanese type of basket weaving—where ferromagnetically coupled Ising spins must follow similar "ice rules" with the spins in an individual triangle having a two-in-one-out or one-in-two-out configuration. Such behaviour has been reported in the aforementioned pyrochlore systems under fields along the Ising axis [36, 37], but more recently in the kagomé intermetallic HoAgGe [38].

Another ground state which is driven by classical fluctuations is one where magnetic moments freeze randomly below a critical temperature, T_F, and the resulting state is known as a spin glass [39]. A spin glass typically arises due to frustration stemming from site disorder, for example, when magnetic atoms are distributed randomly throughout a metallic matrix [40]. In this instance, frustration originates from competing ferromagnetic and antiferromagnetic RKKY interactions between randomly placed magnetic ions, rather than from the geometry of the magnetic sublattice, and the consequence of this frustration is that the magnetic

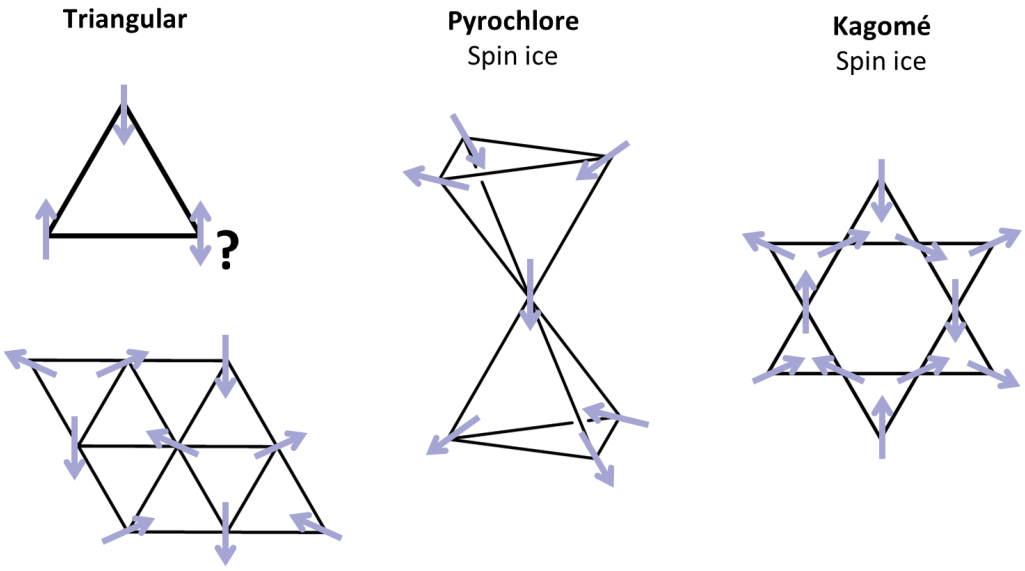

Figure 1.5: Geometric frustration can be described by arranging antiferromagnetically coupled Ising spins onto an equilateral triangle (top left). However, in a typical triangular antiferromagnet the spins will adopt a non-collinear ground state to "share" the magnetic frustration (bottom left). Other frustrated lattice types which contain triangular plaquettes are the pyrochlore (centre) and kagomé (right) lattices. However, there exist frustrated states of matter in these types of systems even in the presence of ferromagnetic nearest-neighbour exchange, such as in the spin ice phases where the magnetic ions contain an easy-axis spin anisotropy which contrains them to point in a particular direction.

moments freeze, albeit cooperatively, into a random glass-like arrangement [39]. This phenomenon, in fact, was one of the early models in which competing exchange interactions were originally discussed [41]. Spin glass behaviour is also commonly observed in geometrically frustrated magnets, although there typically appears to be some level of site or bond disorder as well as geometric frustration which drives the formation of such a system. Examples include $YbZnGaO_4$, where Zn^{2+} and Ga^{3+} cation site disorder is thought to induce a spin glass state [42], and $Y_2Mo_2O_7$, in which variations in Mo–Mo bond lengths are the source of disorder [43]. In both of these examples, however, it is unclear if the resulting ground states are comparable to those observed in conventional spin glasses.

It should be noted at this point that there are increasingly more lattice types being explored in the context of frustrated magnetism, such as the three-dimensional hyperkagomé, two-dimensional square-kagomé [44], star [45] and "stagomé" [46] lattices, as well as the square lattice [47, 48]. In the latter, frustration arises due to a competition between the edge and diagonal exchange interactions on the square

plaquette. It is also important to note that, whilst all of the solids discussed in this context are technically three-dimensional, the quasi-two-dimensional (and even one-dimensional) behaviour of many of these systems arises through dominant exchange interactions along specific directions, and in many cases this is crucial to stabilising frustration (or destabilising magnetic order).

1.3.2 Quantum Spin Liquids and the Kagomé Antiferromagnet

Whilst the dynamics in spin glasses and spin ices are driven by thermal fluctuations associated with magnetic ions which typically have large values of S, quantum fluctuations come into play when $S = \frac{1}{2}$ ions are utilised [12]. These quantum fluctuations act to destabilise conventional magnetically ordered states even further, and can theoretically persist down to absolute zero so that the magnetic moments remain dynamically fluctuating at all measurable temperatures. The resulting state of matter is termed a quantum spin liquid (QSL), and is an example of a ground state that does not break symmetry upon cooling like a ferromagnet or antiferromagnet does, and where there is no order parameter that can be tracked upon entering the correlated regime.

A key feature of the QSL that separates it from a conventional paramagnet is that of quantum entanglement which, in essence, implies that the magnetic moments must be strongly interacting rather than fluctuating randomly [33]. In 1973, Anderson proposed that the QSL state could be described using a model in which unpaired spins form short-range entangled $S = 0$ singlets [49]. If these singlets form a static, ordered arrangement onto the underlying lattice, the state is called a valence bond solid (VBS) and is not a true QSL because it breaks translational symmetry. However, it was hypothesised that the singlets could resonate from bond to bond in a manner similar to the resonating carbon double bonds in a benzene ring. The resulting state, which is essentially a quantum superposition of a large number of dimer coverings onto a frustrated lattice, was named a resonating valence bond (RVB) state, and is visualised on the kagomé lattice in Figure 1.6. A consequence of these entangled states is the possibility that they may host non-trivial excitations with fractional quantum numbers, as opposed to the magnon excitations expected for a typical magnet. A key example is that of spinons, which have zero charge but contain a spin $S = \frac{1}{2}$, and could be formed through breaking apart one of the singlet bonds depicted in Figure 1.6. Generally speaking, there are two categories of QSL ground states. In the first, there is an

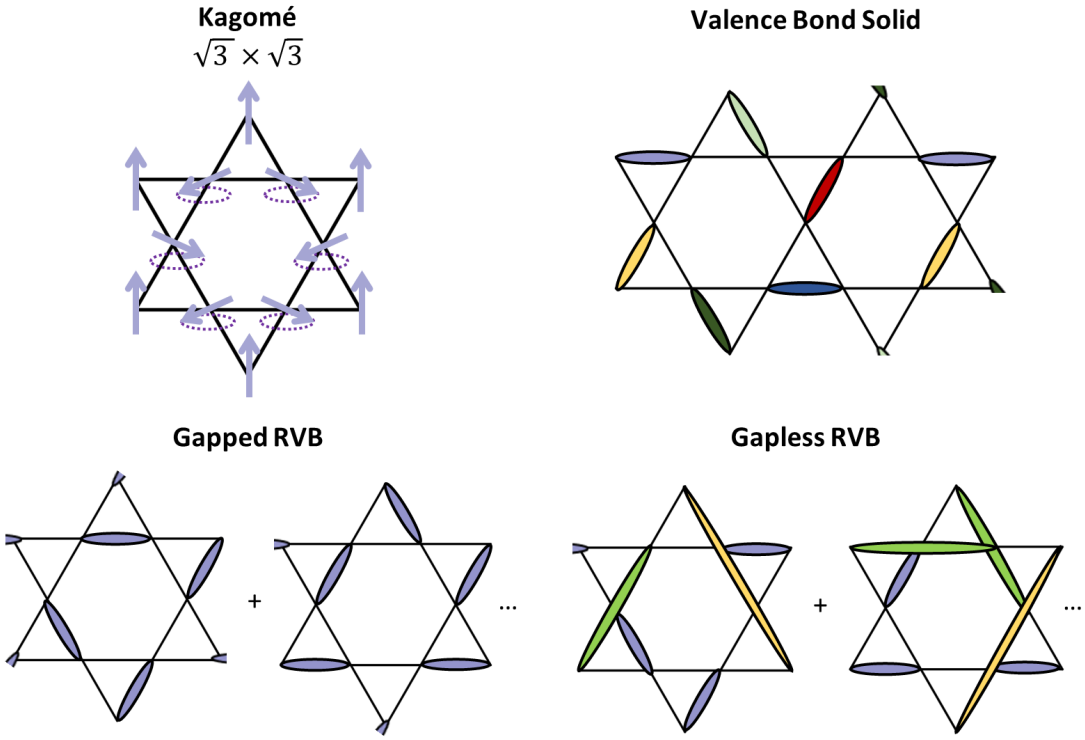

Figure 1.6: One of the predicted ground states of a classical kagomé antiferromagnet is called the $\sqrt{3} \times \sqrt{3}$ state, where the chirality of each neighbouring triangle alternates. However, there exist zero-point modes whereby certain spins can rotate in or out of the plane with no cost in energy, as depicted by the dashed lines. This means the kagomé antiferromagnet has a large ground state degeneracy. When utilising low spin magnetic ions, various models exist for the types of quantum states of matter which can arise, which involve the formation of singlets, which here are represented by ovals and can be short-range (bottom left) or long-range (bottom right).

energy cost that must be overcome to break a singlet bond and promote such an excitation, and these gapped states are typically known as Z_2 QSLs. This model has been linked to superconductivity in high-T_C cuprates [50], and for this reason there is interest in electron doping a Z_2 QSL state to realise superconductivity [51, 52]. The second, gapless QSL type possesses a continuous low energy excitation spectrum, which indicates that the singlets are comparably longer-range and therefore less tightly bound.

The QSL was initially proposed as a potential ground state for the triangular antiferromagnet [29]. Nowadays, it is widely thought that the triangular antiferromagnet does not host a spin liquid state [53], because in an extended array of edge-sharing triangles the magnetic moments are rather XY or Heisenberg, and the system alleviates any geometric frustration by adopting a compromise non-

collinear ground state where each moment points at 120° to its neighbour. The outcome is a doubly degenerate ground state that arises via the chirality of the resulting spin arrangement. Even so, there are increasingly more studies which suggest that a consideration of the next-nearest-neighbour exchange can stabilise a QSL state in triangular magnets, provided the magnetic ion of choice has a spin $S = \frac{1}{2}$ [54]. Alternatively, the kagomé lattice has garnered considerable attention in the search for material realisations of a QSL [55]. The kagomé arrangement has a larger degeneracy than the triangular alternative, because each vertex on the latter is shared by six surrounding triangles, whilst only two are shared in the former. As a result, a 120° arrangement of spins on a kagomé network still results in an infinite amount of degenerate ground states, which is illustrated by considering one of the classical ground states of the kagomé antiferromagnet, shown in Figure 1.6, in which certain spins can be rotated without any energy cost. This makes the kagomé network an ideal structure type within which to explore QSL physics. There are several proposed models which pertain to the $S = \frac{1}{2}$ kagomé antiferromagnet, in particular those that relate to the RVB state originally proposed for the triangular antiferromagnet, although theorists are limited by current computational power [56]. Whether these models effectively describe any real materials, therefore, is an open debate.

Of course, in real materials there are inevitably perturbations to the spin Hamiltonian introduced via Equation 1.12, such as the DM interaction, long-range exchange, and disorder [57]. Consequently, the challenges that the concept of a QSL presents to materials scientists are three-fold. Firstly, there is a need for the development of models that effectively describe the exotic magnetic ground states which arise in frustrated magnets. Secondly, there is a drive to produce real materialisations of such systems, and especially ones that represent the "ideal" topologies discussed above. Finally, characterising and detecting the signatures of the quantum states of matter that are expected to emerge offers its own set of challenges. Naturally, all three of these challenges are connected, given that a clear understanding of potential QSL systems is often complicated by a disconnect between theory and experiment. Indeed, for decades after the inception of the QSL there was scepticism surrounding whether such a state could exist in real materials, but in the past two decades development in theory [58] has ignited interest in QSLs from a materials science perspective [59], and the discovery of a large number of magnetic compounds as promising candidate systems has transpired [60]. This thesis aims to contribute to this work via the synthesis and characterisation of

new frustrated magnets.

1.3.3 Materials of Interest in this Thesis

A variety of classes of materials have been explored in the search for one that represents the quantum states of matter discussed above. Those previously mentioned include oxides and intermetallics, although further examples can be found in the study of, for instance, van der Waals crystals [61, 62] and organic radical systems [63, 64]. However, the following classes of materials are those that are explored within this thesis, and a more comprehensive literature review for each of these groups of materials are given within each chapter.

- **Mineral Systems:** Rather conveniently, the kagomé arrangement of ions is often found in the form of naturally-occurring mineral systems, making nature the ideal realm within which to explore frustrated magnets. The prime example is herbertsmithite [65], discovered in 1972 in Chile and named after the mineralogist Herbert Smith, although many more examples exist [66–69]. A related mineral is barlowite, which was discovered in the 1980s in Queensland, Australia [70] and named in honour of the amateur crystallographer William Barlow. It is this mineral, which contains a kagomé network of Cu^{2+} ions, that is the subject of the work within the first two results chapters in this thesis: Chapter 3 focusses on the synthesis and structural characterisation of barlowite and its halide analogues using powder diffraction techniques, and contributes to the elucidation of the role of subtle structural distortions on the magnetic behaviour in this mineral family. Following this, Chapter 4 utilises muon spectroscopy to explore the magnetic behaviour upon substituting Zn^{2+} into the crystal structure of barlowite, which has the effect of suppressing magnetic order.

- **Metal-Organic Frameworks:** A common drawback of using purely inorganic compounds is that the interpretation of the magnetic ground states in such systems is often plagued by the presence of site disorder [71, 72]. One route that aims to circumvent this issue is the use of organic components, in metal-organic frameworks, for example, to separate the magnetically frustrated layers [73]. The incorporation of organics also opens up a huge potential for new systems, offers a route to controlling the dimensionality of magnetic materials, and provides an opportunity to incorporate multifunctionality into such hybrid systems. In Chapter 5, a powder diffraction, muon spectroscopy and heat capacity study of a family of related

metal-organic frameworks that contain a kagomé network of Cu^{2+} ions separated by bipyridyl ligands is explored to exemplify the diversity afforded by MOFs. The intriguing structural and magnetic behaviour observed in this family of MOFs opens up new questions about our understanding of magnetic exchange through organic moieties.

- **Coordination Frameworks:** Coordination frameworks offer similar advantages to metal-organic frameworks, although the shorter length of the organics typically used in such materials means they can be further used to control the magnetic exchange within the frustrated geometries of interest [74]. This versatility is demonstrated in Chapter 6, where a coordination framework with the formula $KFe(C_2O_4)F$ is explored through powder diffraction and muon spectroscopy data analysis. In this case, the material is formed from distorted triangular layers of Fe^{2+} bound by oxalate linkers, although the quasi-one-dimensional chains which exist in $KFe(C_2O_4)F$ appear to play a significant role in the magnetic behaviour observed.

Chapter 2

Experimental Methods

Detecting and classifying the various states of matter which arise in magnetically frustrated systems is an ongoing challenge. This is partially due to the difficulty in defining the quantum states that can arise from this phenomenon, which is especially challenging given that there is no local order parameter which can be tracked if a non-symmetry broken state such as a QSL does prevail. For example, whilst a lack of long-range magnetic order is a prerequisite for QSL formation, this is not direct evidence for such a state because there are other explanations or "hidden" order that can be responsible for a lack of detectable long-range order [75]. A true quantum spin liquid state can only be identified through the detection of spinons, for example. For this, experimental techniques that can detect excitations are necessary, such as inelastic neutron scattering, thermal conductivity, nuclear magnetic resonance and electron spin resonance [76]. These techniques are beyond the scope of this thesis, although the work contained herein will enable and inform future studies in this direction.

Geometric frustration occurs through the particular arrangement of magnetic ions with respect to one another which induces competing interactions. As a consequence, a thorough understanding of the crystal structure of a given material following its synthesis is one of the first critical steps towards characterising frustrated magnets. Subsequently, an understanding of the bulk magnetic behaviour is necessary to confirm frustrated interactions, and even if magnetic order does prevail, an understanding of why that might be the case, based on the crystal and magnetic structures, is crucial if we are to design and discover new model systems. Finally, techniques that detect local magnetic behaviour can provide further insight into whether any disorder remains, which may not be accessible via bulk methods. The following chapter aims to summarise the techniques used within this thesis to achieve these goals.

2.1 Synthetic Methods

2.1.1 Hydrothermal Synthesis

Hydrothermal synthesis involves the chemical reaction of substances in an aqueous solution above the boiling point of water. The reactions are usually contained in a steel autoclave containing an inert lining, typically Teflon, designed to withstand corrosive reagents and high temperatures and pressures. Hydrothermal reactions proceed via reaction in solution, and thus offer the benefit of requiring relatively low reaction temperatures when compared to conventional solid state methods, as well as the ability to use sparingly soluble compounds which may not react in ambient conditions. Moreover, this technique has been shown to provide access to otherwise inaccessible oxidation states [77]. For these reasons, this type of synthetic route is commonly used to prepare a broad range of polycrystalline and single crystal samples of, for instance, oxides, fluorides, and inorganic-organic hybrid materials such as metal-organic and coordination frameworks [78]. The hydrothermal synthetic routes employed in this thesis are especially useful because they are able to emulate the high temperatures and pressures at which minerals form in nature, making this technique particularly relevant to the synthesis of barlowite and its analogues in Chapters 3 and 4. As will be demonstrated in these chapters, hydrothermal synthesis is highly sensitive to small changes in the experimental environment, such as the reactant ratio, the temperature and length of heating, the pH and the volume of solvent.

2.1.2 Solvay-Based Synthesis

The Solvay process is an industrial technique which utilises ammonia in brine to fix CO_2 as hydrogen carbonate, and is ordinarily used for the large-scale production of sodium carbonate. This idea has been extended to the use of nitrogen containing ligands under aqueous basic conditions with transition metal ions. Here, the transition metal ions rapidly uptake atmospheric CO_2, which is fixed in an ammonia solution as hydrogencarbonate, and when the ammonia is allowed to evaporate this frees up carbonate anions for the chelation of metal ions. As a result, methods based on this process offer a somewhat environmentally friendly synthetic route and there is interest in using a similar method for the sequestration of atmospheric CO_2 [79]. The diverse coordination chemistry of the CO_3^{2-} anion, which can bind in a uni-, bi-, tri- and even a tetradentate manner, makes this an appealing approach for the synthesis of new frameworks with a range of topologies

and dimensionalities [80, 81]. In Chapter 5, the fixation of CO_2 is used to generate a family of metal-organic frameworks whose quasi-two-dimensional kagomé structure forms through the tridentate coordination of CO_3^{2-} anions.

2.2 Elemental Analysis

2.2.1 ICP-OES

In many instances, the exploration of new frustrated magnets, and functional materials in general, is accomplished through doping of known materials. As a result, gaining knowledge about the chemical composition of a given material is a crucial step towards characterising it, as is demonstrated in Zn-substituted barlowite in Chapter 4 where the dopant is used to control the dimensionality of the magnetic sublattice. One analytical method commonly used for the determination of elemental composition is inductively coupled plasma optical emission spectrometry (ICP-OES). The technique requires the injection of a sample into radiofrequency-induced argon plasma, which is quickly vaporised in the high temperatures (approximately 10,000 K at the core) of the inductively coupled plasma. The resultant free atoms are promoted to their excited states, which subsequently relax to the ground state via the emission of a photon. The emitted photons have characteristic energies corresponding to the quantized energy levels for the particular atom or ion in question, and so the wavelength of the photons can be used to determine the elements from which they were produced. The total number of photons is directly proportional to the concentration of the element in the sample [82]. Ordinarily, many characteristic wavelengths for a given element are detected and an averaged concentration is deduced, and a composition can be determined either via a ratio of two elements or through knowledge of the initial sample concentration of the measured solution.

This method allows for a quick determination of composition because many elements can be detected simultaneously. However, ICP-OES is limited to materials which are readily soluble in solutions, although ICP methods do exist which allow for the analysis of solid samples, such as ICP-MS. Furthermore, even small impurities will contribute to the outcome of ICP-OES, and so confidence in the phase purity of a given sample is crucial. Another drawback of ICP-OES is that there can be interferences in the outputted signal depending on the combination of elements in a given sample. Moreover, not all elements are easily detectable via

this method and are restricted by the detection limit of the instrument. A prime example is in the identification of halides, whose associated transitions lie in the high-energy ultraviolet wavelengths and are therefore outside of the detectable range of many ICP-OES instruments [83].

2.3 Diffraction Methods

As was touched on in Chapter 1, a thorough understanding of the crystal structure of a solid state material is crucial to understanding the functional properties that it displays. The concept used to achieve this, which is ubiquitous to all branches of solid state chemistry, is diffraction. The reason this technique works is because the wavelengths of radiation employed, $\sim$ 1 Å, are of comparable length to the interatomic spacing in crystalline solids. When a beam of radiation is incident upon the atoms in a periodic crystal lattice, the waves are scattered and interfere with each other. Bragg's law, $2d_{\mathrm{hkl}} \sin\theta = n\lambda$, describes crystals as being built up of layers or planes of atoms, where d_{hkl} represents the perpendicular distance between adjacent planes (d-spacing), θ represents the incident angle (Bragg angle) and λ represents the wavelength of the radiation used. When n is an integer Bragg's law is satisfied, and it is this constructive interference that is recorded to produce the Bragg reflections that form a diffraction pattern [1].

In the absence of suitable single crystals, only powder samples have been measured within this work. A powder sample ideally contains millions of microcrystals arranged in every possible orientation. Subsequently, when a beam of radiation strikes a powdered sample it is diffracted as, what appears to be, a cone of radiation. Each different diffraction cone corresponds to a set of crystallographic planes which are labelled with Miller indices, denoted by integers hkl. In a typical powder pattern, the intensity of the diffracted beam is then recorded as a function of 2θ, which is the angle between the incident and diffracted beams, or as a function of d-spacing or momentum transfer Q. The characteristic powder pattern obtained for each crystalline phase contains Bragg peaks which are representative of Miller indices. Their positions yield information about the size and symmetry of the unit cell, whilst their intensities signify the identity and placement of atoms within the unit cell. The shape of the Bragg peaks depends on both instrumental parameters and intrinsic structural features [84].

In this thesis, the sources of radiation used are X-rays and neutrons. The scatter-

ing of these can be either elastic or inelastic, with the latter able to provide information about the excitations present in the material, such as phonons produced through lattice vibrations, magnons produced by spin waves, or spinons produced by the entangled states present in a QSL. However, it is elastic scattering which gives rise to diffraction, and this is the technique implemented throughout this thesis. Powder X-ray and neutron diffraction each offer their own advantages and limitations because the mechanisms through which they interact with matter are different. The rest of this section aims to outline why one may choose a particular method over the other, and to illustrate why diffraction methods are crucial to our understanding of frustrated systems.

2.3.1 Powder X-Ray Diffraction

In powder X-ray diffraction (PXRD), the incoming X-rays are scattered by the electron cloud surrounding the nucleus of an atom via a long-range electromagnetic interaction, and consequently, X-rays are more strongly scattered by heavier elements than lighter ones. The scattering of X-rays from the atoms of a crystal is given by the structure factor F_{hkl},

$$F_{hkl} = \sum_n f_n \exp[2\pi i(hx_n + ky_n + lz_n)], \tag{2.1}$$

where x_n, y_n and z_n are the positions of the nth atom, and f_n is the X-ray form factor, and describes the scattering power of the atom in question. With increasing scattering angle, there is increasingly more interference between X-rays diffracted by all of the electrons in an atom, and so the intensities of the Bragg peaks, which are proportional to the square of the structure factor, decrease correspondingly.

Due to the accessibility of powder X-ray diffractometers in the majority of solid-state laboratories and the speed at which PXRD data for small sample sizes can be acquired, the collection of a powder pattern for a newly synthesised material is typically the first step towards confirming its phase purity. Furthermore, the various experimental setups and radiation sources available to users mean that this method caters to the majority of materials of interest. Unless stated otherwise, the preliminary structural characterisation of the samples explored in this thesis were collected using a Bruker D8 diffractometer in Debye-Scherrer geometry and utilising monochromated Cu $K_{\alpha 1}$ radiation with a wavelength $\lambda = 1.54056$ Å. However, typically, care must be taken in the analysis of laboratory PXRD data because there are numerous sources of error related to experimental setup which can affect

the peak positions and intensities that are crucial to understanding a material's crystal structure. For this reason, it is preferable to use a high-resolution source such as those provided by synchrotron facilities, which use electrons travelling at close to the speed of light to generate an intense beam of X-rays whose wavelength can be tuned. A relevant example is discussed in Chapter 3, where the resolution afforded by synchrotron PXRD at the Diamond Light Source is required to characterise the subtle structural distortion related to Cu^{2+} ions in the mineral barlowite, which manifests itself in extremely weak Bragg peaks which would be unobservable in laboratory PXRD data.

Whilst PXRD is undoubtedly crucial to the characterisation of frustrated magnets, it is normally insufficient to fully characterise many of the materials relevant to this thesis. This is because the scattering power of an element scales with the square of the number of electrons that it possesses, meaning that lighter elements cannot be straightforwardly located using X-rays. This is problematic for several reasons. Firstly, hybrid materials that are of increasing interest in the field of frustrated magnetism contain organic components that consist of light atoms such as hydrogen. Secondly, as was outlined in Section 1.2, the magnetic exchange in many systems is via superexchange through the orbitals on oxygen ions. As a consequence, having a clear understanding of the position of these ions in relation to the magnetic ions is crucial to understanding the magnetic behaviour displayed.

2.3.2 Neutron Powder Diffraction

The neutron is an uncharged $S = \frac{1}{2}$ particle that interacts with the nucleus of an atom via the strong nuclear force. This interaction is short-range compared to the long-range electromagnetic interaction of X-rays with electrons. The scattering can thus be viewed as from a point source, the resultant scattering is isotropic, and scattering power does not depend on the number of electrons possessed by an atom. The quantity relevant to the neutron scattering power is the total scattering cross section σ_{tot}, which can be viewed as the effective area of the target that is accessible by incoming neutrons, and is related to the scattering length b of a nucleus by $\sigma_{\text{tot}} = 4\pi b^2$. b depends on the makeup of the nucleus and the orientation of its spin, and is therefore both isotope specific and does not vary with atomic number in an intuitive way as it does for X-ray scattering [85]. This makes neutron powder diffraction (NPD) ideal for distinguishing between atoms with similar atomic numbers, and this is demonstrated in Chapter 4 where the locations and occupancies of Zn^{2+} and Cu^{2+} sites, which are indistinguishable

via PXRD, are able to be determined. The total scattering cross section is the sum of coherent scattering σ_{coh} and incoherent scattering σ_{incoh} components. The former provides information about the correlations between nuclei, and therefore provides structural information about crystalline materials. The latter takes into account the deviation of the scattering length as a result of the different isotopes and spin states of the nucleus. The prime example is the proton, which typically superimposes a featureless background onto the collected NPD pattern due to its large incoherent cross section. As a result, it is preferable for samples to be deuterated to increase the signal-to-background ratio and to locate the positions of this element. A comparison of NPD data collected for protonated and deuterated samples is shown in Figure 2.1. Of course, whilst this is straightforward in many cases, the deuteration of more complex organics can be challenging [86]. Similarly, certain elements are highly absorbing, for example gadolinium [75], or are essentially invisible to the neutron, such as vanadium which has a small σ_{coh}. In fact, this is why vanadium cans are used as sample holders in neutron diffraction experiments. Another important point to note is that neutron scattering is a weak interaction compared to X-ray scattering, and requires comparably large sample sizes and long counting times to acquire sufficient data [85].

The production of neutrons is not possible in the laboratory, and instead requires either a nuclear reactor or a spallation source, such as the Institut Laue-Langevin (ILL) or the ISIS Neutron and Muon Source, respectively. As a result of the

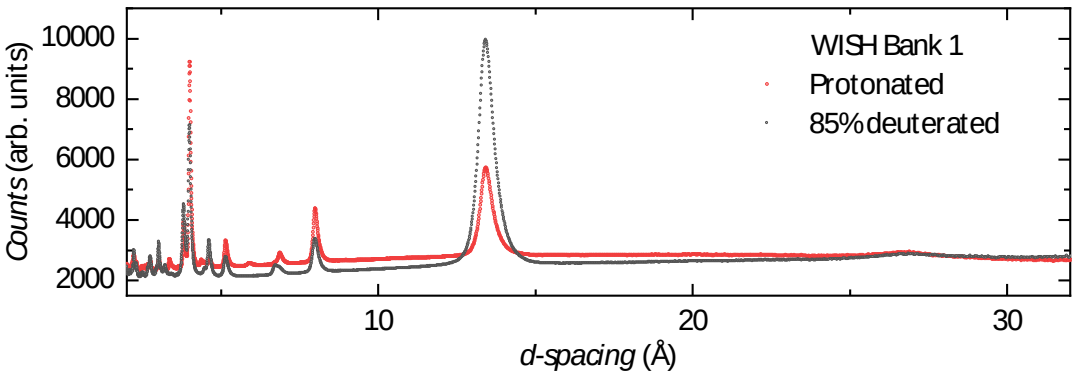

Figure 2.1: Due to the large incoherent cross section of the proton, a large background in NPD data can arise, shown here in red for a metal-organic framework measured on the WISH diffractometer. Deuteration of this sample, shown in black, reduces the background and correspondingly alters the Bragg peak intensities. These data also demonstrate the long *d*-spacing capabilities of the WISH diffractometer.

processes that these types of facilities undergo to produce neutrons, the beam of radiation can be continuous, where a single neutron wavelength is selected using a monochromator, or delivered in "pulses" which contain neutrons with a range of energies. In the latter, the wavelengths are calculated by considering the time it takes for the neutrons to get from a moderator to a detector via the sample, *i.e.* higher energy, shorter wavelength neutrons reach the detector more quickly. Typically, data are collected in multiple banks of known scattering angle, and from this and the known path length, L, the wavelength can be deduced. This can then be related to the d-spacing via Bragg's law. This approach is known as time-of-flight diffraction, and is relevant to neutrons produced from spallation sources [87]. The relative uncertainty in d-spacing, $\delta d/d$, for a given instrument is inversely proportional to the path length L [88]. The high-resolution powder diffractometer (HRPD) at ISIS, for instance, has a flight path of 100 m, and this is why it produces such high resolution data, as is demonstrated in Chapters 3 and 4. In this regard, there are many instruments across central facilities which each offer their unique advantages depending on the wavelength or flux of neutrons that they produce. For example, the use of the WISH diffractometer at ISIS in Chapter 5 was crucial because it is the only neutron diffractometer that offers access to the long d-spacing necessary to probe the large unit cells of the metal-organic frameworks of interest, as shown in Figure 2.1. Moreover, access to ever more extreme experimental setups, such as measurements under applied fields [89] and pressures [90], is making NPD increasingly relevant to exploring the effects of small perturbations to the structural and magnetic phases in frustrated magnets.

2.3.3 Magnetic Neutron Scattering

Nuclear structure determination is not the only use for neutron scattering and, in actuality, it is the fact that the neutron possesses a spin which makes it particularly crucial for the study of magnets in general. The reason for this is that the dipole moment of the neutron spin can interact with the spins associated with unpaired electrons via a magnetic dipole-dipole interaction, which gives rise to magnetic scattering and, in the elastic case and where the moments are ordered into a regular pattern, magnetic Bragg peaks in the collected powder pattern [85]. From these magnetic peaks the magnitude and direction of the magnetic moments can be determined. This is highly relevant to the study of frustrated magnets, because our understanding of the underlying magnetic structure of a material below its critical temperature is integral to understanding how it behaves. Similarly, a

lack of elastic magnetic scattering can be an indication that long-range order does not emerge at very low temperatures, which can be attributed to the presence of a quantum ground state. Of course, the use of inelastic scattering in this case becomes crucial, because the features characteristic of spinons produced by a QSL can be detected via this method [91].

In an NPD measurement, the magnetic scattering intensity falls off with increasing angle, as described by a magnetic form factor similar to X-rays, although this effect is even more pronounced because the unpaired electrons are further from the nucleus. This means that in practice magnetic Bragg peaks are mainly visible at high d-spacing or low Q. One consequence of this is that magnetic Bragg peaks may not be visible if an instrument with insufficient Q-range is selected, meaning that false conclusions regarding a lack of long-range magnetic order may be drawn [92]. Moreover, the neutron experiences only the component of magnetisation which is perpendicular to Q [93]. These restrictions are amplified when the $S = \frac{1}{2}$ ions relevant to frustrated quantum magnetism are utilised, because the lone unpaired electron results in weak scattering. In Chapter 3, this is demonstrated where the GEM diffractometer is unable to provide the necessary flux to observe magnetic scattering associated with the ordering of $S = \frac{1}{2}$ Cu^{2+} magnetic moments, and the high-flux D20 diffractometer was necessary instead. This means that even larger sample sizes, higher deuteration levels, and longer counting times are often required to resolve magnetic Bragg peaks. On the other hand, in Chapter 6 it is shown that the GEM diffractometer is sufficient to observe the magnetic Bragg peaks associated with the ordering of $S = 2$ Fe^{2+} magnetic moments.

2.3.4 Modelling Powder Diffraction Data

Structure solution from both powder X-ray and neutron diffraction is usually complicated by the overlap of Bragg peaks because many Miller planes may simultaneously satisfy Bragg's law at the same angle. Of course, this is one of the drawbacks of measuring powder samples and the synthesis of single crystals is often necessary when a new material is synthesised, although not always possible. As an alternative to structure solution, the Rietveld method, which attempts to refine a known structural model to an observed diffraction pattern, is normally implemented. This method requires that some knowledge of the crystal structure is already in place, and this is usually found in the form of a crystallographic information file (CIF) if the system of interest is related in some way to an established crystal structure. By refining a range of structural parameters within a known

space group, alongside instrumental parameters, the residual S_y between the observed and calculated (y_{oi} and y_{ci}, respectively) diffraction patterns is minimized using a least-squares fitting procedure,

$$S_y = \sum_i \frac{1}{y_{oi}}(y_{oi} - y_{ci})^2. \tag{2.2}$$

The quality of the Rietveld refinements in this thesis are assessed by the weighted R–factor,

$$R_{\mathrm{wp}} = \sqrt{\frac{\sum_i w_i(y_{oi} - yci)^2}{\sum_i w_i(y_{oi})^2}}, \tag{2.3}$$

where w_i is a weighting factor, and the chi-squared value,

$$\chi^2 = \left(\frac{R_{\mathrm{wp}}}{R_{\mathrm{e}}}\right)^2. \tag{2.4}$$

R_{e} is the expected R-factor and calculates the best possible fit depending on the total number of data points, the number of refined parameters and the constraints imposed on the model. The development of refinement softwares, such as the GSAS [94, 95] and FullProf [96] programmes utilised in this thesis, means that increasingly more complex data can be modelled relatively quickly using the Rietveld approach, providing important structural information for a given material in the absence of single crystals.

However, care must be taken to use the minimum number of parameters in a Rietveld refinement to avoid overfitting [99]. For example, theoretically, Bragg diffraction should yield infinitely sharp reflections, but in practice neither experimental setup nor sample are ideal, which leads to peak position shifts and broadening which can be difficult to model due to a convolution of these contributions. For example, the layered systems often of interest in the field of frustrated magnetism can lead to preferred orientation or stacking faults [97], whilst local defects can result in strain effects [100], all of which influence the peak profile. An example of the influence of stacking faults on a diffraction pattern is shown in Figure 2.2(a). Added to this is the complexity of modelling the instrumental factors which affect not only peak shapes but peak positions. In many cases, it is necessary to collect high-resolution diffraction data to distinguish between resolution-limited peak widths due to instrumental factors and broadness due to, for instance, short-range structural or magnetic order, which can manifest in the form of diffuse scattering, as depicted in Figure 2.2(b). In fact, one of the draw-

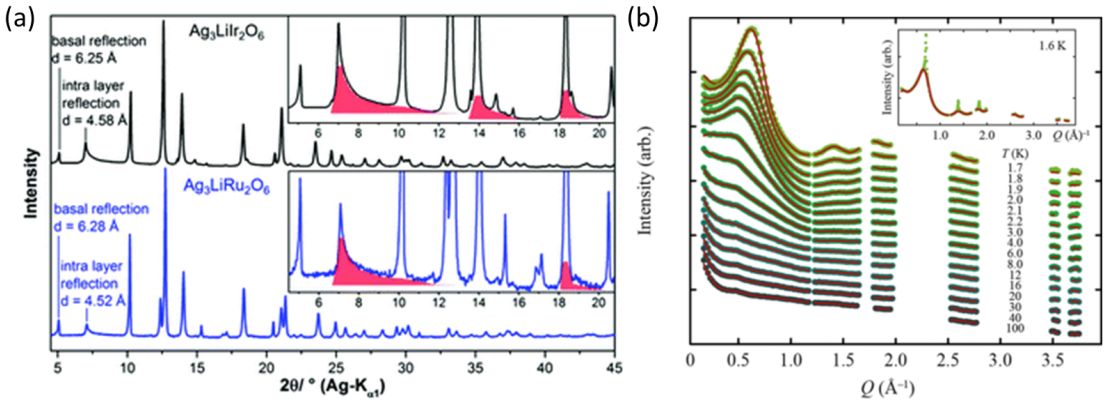

Figure 2.2: Care must be taken when modelling both powder X-ray and neutron diffraction data due to effects such as (a) stacking faults, which yield asymmetric peaks, here shown for two honeycomb iridates [97], and (b) magnetic diffuse scattering due to short-range correlations, which can broaden peaks beyond the instrumental resolution. This is shown here for $Tb(COO)_3$, where the inset reveals modelling of diffuse scattering using reverse Monte-Carlo methods on top of a Bragg peak [98].

backs of diffraction and Rietveld techniques which is highlighted by this thesis is that they are predisposed to look at long-range structural and magnetic order, rather than local effects. This means that small defects or disorder can be difficult to model using the Rietveld method, and to do so introduces many more parameters into the model. A careful inspection of the refined parameters is thus needed to ensure that they remain uncorrelated with one another and physically plausible.

2.3.5 Representation Analysis

Whilst determining the crystal and magnetic structures of a given material is achieved through Rietveld refinement, in order to attain the possible magnetic structures to begin with, a knowledge of both the underlying crystal structure and the way it relates to the magnetic structure, via the propagation vector **k**, must be known. Representation analysis is then used to determine how many different ways the symmetry restrictions of the crystal structure can be satisfied by the magnetic structure. The underlying principle of representation analysis requires a consideration of the little group, G_k, which contains the symmetry operations of the space group that involve a translation of the unit cell but do not change **k**. All of the plausible magnetic structures must then with compatible with all of the symmetry operations of G_k. The calculated irreducible representations, Γ_n, of G_k then describe the symmetry behaviour of a magnetic moment under all

the symmetry operations of G_k [101, 102]. Each of the resultant magnetic space group models are then incorporated into a Rietveld refinement and the magnetic moments are refined, with the correct magnetic structure deduced from trial-and-error as well as a knowledge of the magnetic properties from methods such as the magnetic susceptibility, discussed in Section 2.4.1.

Th development of tools such as BasIreps [96], SARAh [103, 104] and ISODISTORT [105] have made the application of representation analysis to real data extremely accessible, alongside the tool MAXMAGN [106–108] which uses an alternative approach to calculate the maximal magnetic space groups. Despite this, the analysis of magnetic diffraction data becomes increasingly challenging with incommensurate structures—where the magnetic structure has a periodicity unrelated to that of the crystal—that are common amongst the quantum materials of interest [109, 110]. Furthermore, due to the restrictions imposed by magnetic scattering of powder samples, there is always the possibility that several magnetic structures describe the data if an insufficient number of Bragg peaks are resolved, and in this case, either better quality data or single crystal neutron diffraction is required. An example is in the metal-organic frameworks discussed in Chapter 5, whose magnetic scattering is only able to uncover information about the magnetic moments in certain directions. Indeed, magnetic structure solution only provides us with the size and direction of the magnetic moments. In order to acquire information about the interactions between the magnetic moments, inelastic scattering is required which yields information on the underlying spin Hamiltonian responsible for magnetic ordering [85].

2.4 Bulk Magnetic Characterisation

2.4.1 DC Magnetic Susceptibility

Superconducting Quantum Interference Device (SQUID) magnetometry is a technique used to measure extremely small changes in magnetic flux. A direct current (DC) SQUID magnetometer consists of a superconducting ring intersected by two insulating layers known as Josephson junctions. In a typical measurement the sample is cooled to 2 K in zero field, then magnetized by an applied field and moved through a superconducting pick-up coil. The magnetic moment of the sample induces a current in the coil which is then detected via the production of a current in the SQUID ring. The induced current is proportional to the magnetisation

present in the sample, so by measuring the current as a function of displacement of the sample through the pick-up coil upon warming or under varying fields, the temperature- or field-dependent magnetic susceptibility of the sample can be determined [111].

The magnetisation as a function of temperature is one of the first measurements which must be undertaken on a magnetic system, and can be readily converted to the magnetic susceptibility using Equation 1.7. To begin with, any evidence for magnetic ordering is searched for, such as an upturn in the data, and often a plot of the differential of the measured data aids in the recognition of any gradient change in the magnetic susceptibility. Examples are shown in Figure 2.3. Next, Curie-Weiss modelling of the high-temperature inverse susceptibility provides an approximation for the nature and strength of the exchange couplings in a given material, and if this value indicates dominant antiferromagnetically interacting magnetic moments then a comparison to the scale of T_C, if observed, can provide an estimate for the frustration index, as introduced in Section 1.3. In a system which does not display any evidence for long-range magnetic ordering, then it is necessary to measure down to temperatures well below the scale of the exchange

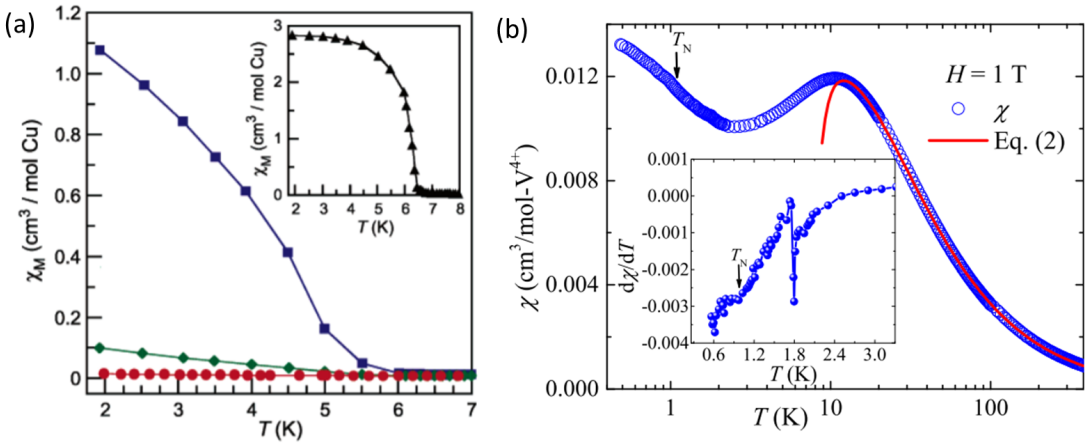

Figure 2.3: An upturn in the magnetic susceptibility is indicative of a transition to long-range magnetic order. In (a), the black data points in the inset indicate ordering at T_N = 6.5 K in the kagomé material clinoatacamite, $Cu_4(OH)_6Cl_2$, but as Zn^{2+} is doped into the structure (blue, green and red data) this effect is suppressed [112]. In (b), the square lattice bilayer material $VO(HCOO)_2{\cdot}H_2O$ requires measurements to subkelvin temperatures to observe a weak cusp in the differential at T_N = 1.1 K, shown in the inset. A broad feature at 10 K is also observed here which is characteristic of the two-dimensional nature of the magnetic sublattice. The red line is a high-temperature series expansion for an $S = \frac{1}{2}$ frustrated square lattice from which estimates for J_{ex} are extracted [113].

interactions, where the magnetic behaviour may be considered to be representative of absolute zero. Indeed, in many cases it is required to use a dilution refrigerator to measure the magnetic susceptibility in the millikelvin regime in order to rule out magnetic ordering at extremely low temperatures, as shown in Figure 2.3(b) [113]. This method offers further benefits because it is relatively straightforward to align single crystal samples, which allows access to information about the nature of exchange along particular crystallographic axes (for example, in [114]). The temperature-dependent magnetic susceptibility is also extremely useful for the detection of spin glass states via the observation of a divergence in the data below T_{F} when the sample is cooled in an applied field versus in zero field [15]. Moreover, the application of a large range of magnetic fields can be used to uncover, for example, the presence of magnetic hysteresis in the field-dependent magnetic susceptibility, which is evidence for ferromagnetism.

Despite all this, limitations in this method lie in the variation of the measured data which can arise through different experimental setups. Following on from this, the Curie-Weiss analysis of data is highly dependent on factors such as the temperature range of fitting and whether the diamagnetism of a given sample is accounted for [115], meaning that great care must be taken if comparing researchers' results and, for this reason, a clear reporting of experimental setup and analytical approach is crucial. Particularly in the area of frustrated magnetism, applying the Curie-Weiss law at temperatures outside of the paramagnetic regime can lead to large variations in the determined value of θ because terms which are not represented by this model become important. In systems where there is no ordering transition it is particularly difficult to determine where this region lies, and so θ in this case should be treated with caution [116]. Of course, SQUID magnetometry methods provide only the average information about the magnetic behaviour of a given material and so, naturally, techniques which probe the local behaviour are beneficial, such as muon spectroscopy which will be discussed in Section 2.5.

2.4.2 Heat Capacity

The heat capacity, C, of a material is defined as the amount of applied heat, Q, necessary to produce a unit change in temperature, T, which depends on the mass, identity and phase of a given sample. Measurements are usually performed in a

vacuum, so that there is constant pressure and the heat capacity is given by,

$$C_p = \left(\frac{dQ}{dT}\right)_p. \tag{2.5}$$

The specific heat is then the heat capacity per unit mass of a material. Access to the excited states in a given system is evaluated by the entropy, which the second law of thermodynamics states is equal to,

$$dS = \frac{dQ}{T}, \tag{2.6}$$

and therefore,

$$C_p = T\frac{dS}{dT}. \tag{2.7}$$

As a result, a measurement of the specific heat of a system directly gives information about the entropy evolution of that system. This technique is useful because at the point of a magnetic phase transition, when a small amount of heat is applied to an ensemble of spins the moments reorient and absorb this energy, which alters the entropy. In practice, this means that the temperature-dependent specific heat displays a discontinuity or anomaly at the point of a magnetic phase transition [117]. The change in entropy per mole for this process is predicted to be equal to $\Delta S = R\ln(2S+1)$, where S is the total electron spin of the system [118].

However, the total specific heat, and therefore the entropy, is a combination of the nuclear, electronic, lattice and magnetic contributions, each of which have characteristic excitations which are dominant at certain temperature scales. To isolate the magnetic part, the other contributions must be effectively modelled. The nuclear and electronic contributions are typically relevant at temperatures below approximately 5 K and can largely be ignored if the magnetic transitions also dominate in this temperature region. More challenging is modelling the lattice contribution to the specific heat, which arises due to phonon excitations of the vibrating lattice within a given material. This contribution dominates at much higher temperatures. A rigorous approach to this is to use a combination of the Debye model, given by,

$$C^{\mathrm{D}} = 9NR\left(\frac{\theta_{\mathrm{D}}}{T}\right)^3 \int_0^{\frac{\theta_{\mathrm{D}}}{T}} \frac{x^4 e^x}{(e^x-1)^2} dx, \tag{2.8}$$

and the Einstein model,

$$C^{\mathrm{E}} = 3NR\left(\frac{\theta_{\mathrm{E}}}{T}\right)^2 \frac{e^{\frac{\theta_{\mathrm{E}}}{T}}}{(e^{\frac{\theta_{\mathrm{E}}}{T}}-1)^2}, \tag{2.9}$$

which represent the acoustic and optical lattice vibrations, respectively. Here, N is the number of atoms in the formula unit and $\theta_{\mathrm{D(E)}}$ is the Debye or Einstein temperature, which measures the rigidity of the lattice [118, 120]. At high temperatures, both of these functions approach the classical value of $3NR$, which is the Dulong-Petit law. However, this rule makes many assumptions regarding the equivalent mechanical roles of atoms in a given solid, which means that the rule is regularly disobeyed and undergoing fits using these models is deemed unreliable

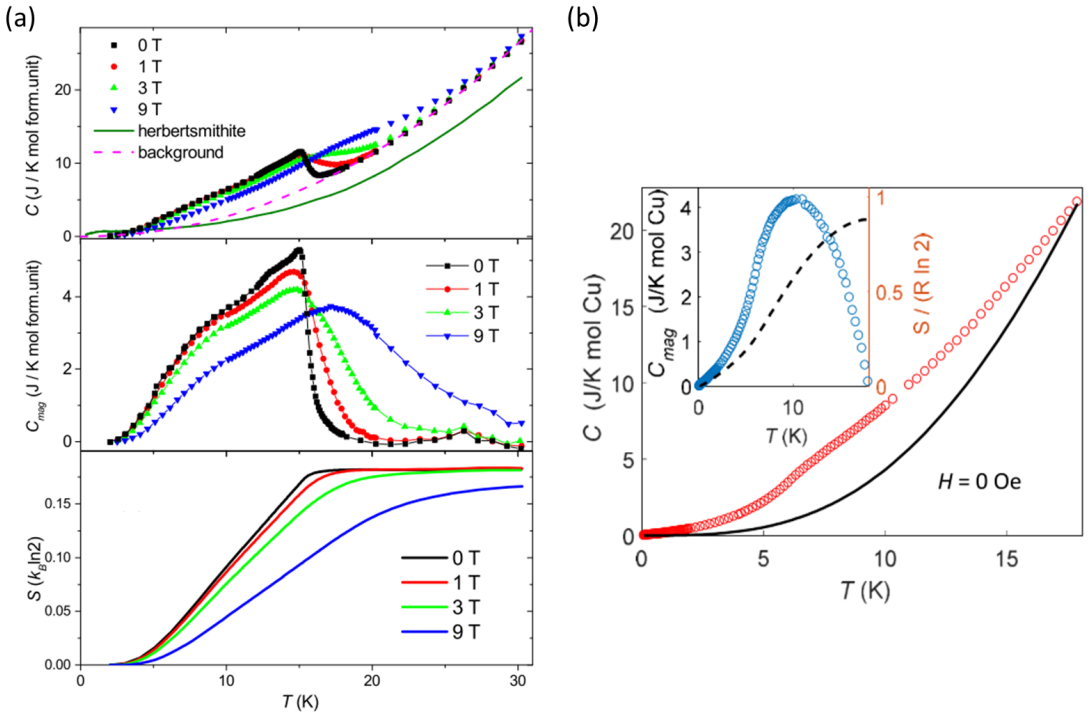

Figure 2.4: A magnetic ordering transition manifests itself in the specific heat via a cusp in the measured data, as demonstrated here for (a) the mineral barlowite under various fields [119] and (b) the metal-organic framework $Cu_3(CO_3)_2(bpe)_3{\cdot}2ClO_4$, where bpe = 1,2-bis(4-pyridyl)ethane [92]. In (a), the lattice contribution is estimated using $C_{\mathrm{latt}} = at^2 + bt^3$, where the t^2 term arises due to the two-dimensional nature of this kagomé material. In (b), a non-magnetic cadmium analogue is used to predict the lattice specific heat. Upon subtraction of this contribution in these materials, integration of C_{mag} yields the change in entropy S. In both of these systems, a partially ordered ground state is therefore predicted.

in many cases [121]. Instead, it is common to model only the low-temperature specific heat using the Debye T^3 approximation, although this is often insufficient in polyatomic solids, as is demonstrated in Chapter 3. Another approach is to measure a non-magnetic analogue which should, in theory, represent the lattice vibrations of the magnetic material which can then be subtracted from the heat capacity for the system of interest. However, this assumption depends on how different the chemical formula of the analogue is, and is limited by the existence of such an analogue. Examples of both of these approaches for modelling the lattice specific heat are shown in Figure 2.4. Of course, even if this contribution cannot be precisely modelled, the heat capacity is still useful in a qualitative sense via the observation of a magnetic anomaly in the data, but the calculated entropy change—and the extent of missing entropy which can persist in frustrated systems—should be treated with caution.

Measuring the heat capacity as a function of temperature offers a complementary technique to the magnetic susceptibility, because models such as the high-temperature series expansion can be developed to model both datasets simultaneously, from which the exchange couplings J_{ex} can be approximated [122]. Furthermore, the observation of broad features in the specific heat above a critical temperature can indicate short-range correlations which are characteristic of low-dimensionality [123], although, as is demonstrated in Chapter 5, it is possible for low-dimensional systems to disguise the characteristic features of long-range order in the measured data [124]. This is because correlated regions above the ordering temperature effectively use up the magnetic entropy, so that when the system undergoes long-range order there is a smaller entropy change than predicted and thus a smaller response in the specific heat. Another important application for this method, in cases where a dilution refrigerator is implemented, is in the analysis of the temperature-dependence of the heat capacity on the millikelvin scale, which can distinguish those excitations arising from systems which do not develop long-range order. For example, a triangular QSL is expected to show linear dependence, whilst in kagomé systems a T^2 dependence is more common [125]. Again, the heat capacity is a property which probes the bulk magnetic behaviour, and complementary techniques are always necessary to support claims for QSL behaviour.

2.5 Muon Spectroscopy

There are several complementary techniques to those already discussed which are able to probe the magnetic behaviour of a material locally, such as muon spectroscopy. For instance, the muon is capable of distinguishing between a uniformly magnetic material and a non-magnetic material with strongly interacting magnetic impurities, which the bulk methods discussed above would not be capable of. The positive muon (or antimuon) typically used to investigate magnetic properties is a lepton which has $S = \frac{1}{2}$, and so it also possesses a magnetic moment that makes it highly sensitive to very small magnetic fields ($\sim 10^{-5}$ T). As a result, the muon is an ideal probe for frustrated magnets, whose competing exchange interactions can in many cases prevent the development of long-range magnetic order, and any remaining spin dynamics can be investigated on the MHz scale [126].

The underlying principle of muon spin relaxation/rotation (μSR) is that in the presence of a magnetic field—whether applied or inherent to the sample—the muon will precess at a frequency proportional to that field. In practice, a muon is implanted into a sample where it comes to rest, typically in regions of high electron density. The muon then precesses in a field, and subsequently decays into a positron. Fortunately, the process through which this happens has a property which means that the positron which is emitted from the sample does so predominantly in the direction of the spin of the muon from which it originated. This means that the direction from which the positron is detected tells us about the polarisation of the implanted muon at the time of its decay. Because it is relatively straightforward to produce a 100% spin-polarised beam of muons, the evolution of the muon spin polarisation can be tracked as a function of time, and this directly offers information about the static or dynamic magnetic fields which the muon experienced in its average lifetime of 2.2 μs [127].

The quantity which is measured in a μSR experiment is the asymmetry,

$$A(t) = \frac{N_{\mathrm{B}}(t) - \alpha N_{\mathrm{F}}(t)}{N_{\mathrm{B}}(t) + \alpha N_{\mathrm{F}}(t)}, \tag{2.10}$$

where α is a calibration constant and N_{B} and N_{F} are the number of positron counts in detectors placed backwards and forwards, respectively, relative to the direction of the incoming muons. To understand the corresponding signal, it is helpful to visualise the muon spin precession in the presence of an applied field

perpendicular (or transverse) to the initial muon spin (which has its spin pointing antiparallel to its momentum). At time zero, a muon might decay instantly, and the resulting positron would be detected in the backwards detector. Some time later, another muon may have time to precess in the applied transverse field so that that the resultant decay-positron would be detected in the forwards detector. Upon counting millions of muon decay events, a constant oscillation with a frequency proportional to the applied transverse field as a function of time would be recorded, as depicted in Figure 2.5(a).

The production of muons requires a synchrotron or cyclotron, and so it is common for muon instruments to reside alongside neutron instruments at spallation sources. Experiments utilising the muon do not require deuteration or single crystals, and relatively small sample sizes can be measured compared with neutron experiments which makes this technique particularly useful for hybrid systems that may be challenging to characterise using neutron scattering. Muons can be produced

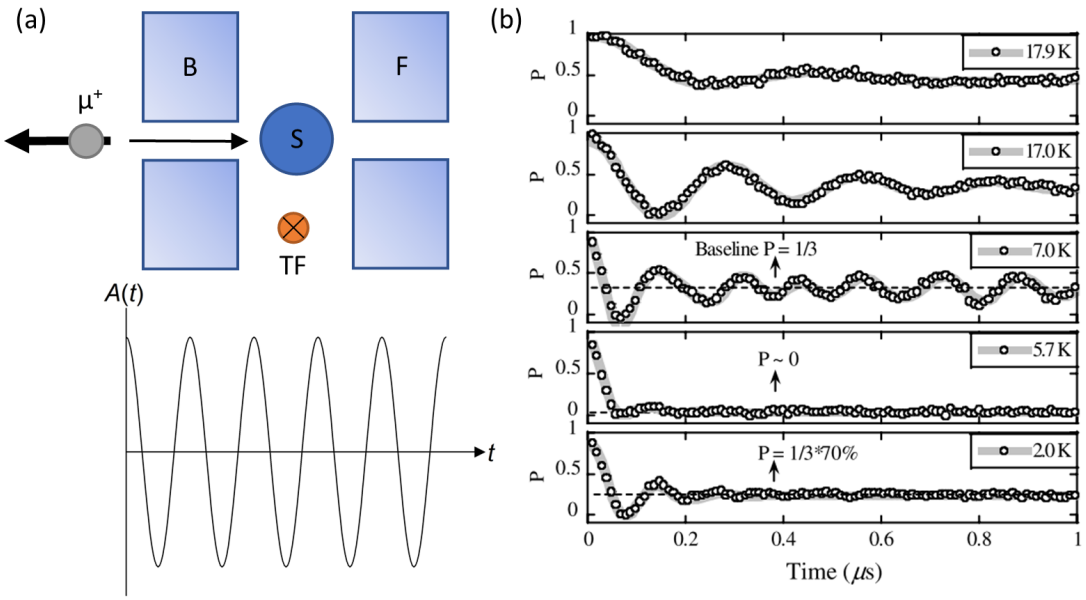

Figure 2.5: (a) In a typical muon experiment spin-polarised muons are implanted into a sample, where they precess (in this case, in an applied transverse field) and decay into positrons. The positrons are detected in forwards and backwards detectors, and the resulting oscillating signal has a frequency proportional to the applied field [126]. (b) Similarly, oscillations in the data arise when there is an internal magnetic field due to the ordered magnetic moments in a system. The example shown here is for the mineral clinoatacamite, which demonstrates a one-third tail at 7 K characteristic of long-range order. However, at 2 K this one-third tail is lost, indicating the coexistence of static and dynamic moments [128].

continuously or in pulses, depending on the method of muon production. For example, the Paul Scherrer Institute produces a continuous source of muons that arrive at the sample individually. Alternatively, the ISIS Neutron and Muon Source produces muons in pulses that arrive at the sample as a packet. The outcome of the latter is that many muons can be implanted and their decay-positrons detected simultaneously, meaning data collection is relatively quick in comparison to when one muon is implanted at a time. However, uncertainty in the timing of the muon pulses means that processes occurring on a fast time-scale cannot be resolved, and continuous sources thus offer better time resolution. The selection of a particular instrument or muon source depends on the properties and features which are expected to be observed in the time-dependent asymmetry for a given sample [129]. This is demonstrated in Chapter 4, where the use of a continuous source is necessary to resolve the spontaneous oscillations associated with the ordering of Cu^{2+} magnetic moments in barlowite.

2.5.1 Electronic Magnetic Moments and Long-Range Magnetic Order

A similar muon precession process to that in an applied transverse field occurs when a magnetic field is present due to ordered magnetic moments within a sample. In this case, muons may stop at slightly different sites within the crystal structure and experience a distribution of magnetic fields which manifests in a damping of the oscillations observed. Upon warming through the critical temperature, the oscillation frequency can be related to the internal field to determine the point at which magnetic ordering prevails. An example of the spontaneous oscillations indicative of magnetic ordering is shown in Figure 2.5(b) [128].

Also relevant to the study of ordered magnetism is the presence of a "one-third tail" in the observed time-dependent asymmetry. This phenomenon arises because if the initial muon spin is already parallel to the magnetic field, then its polarisation is preserved. In a polycrystalline sample made from grains with moments pointing in every direction, powder averaging means that statistically one-third of these grains will have their magnetic moments already pointing along the direction of the muon spin, and the resulting signal can be modelled using,

$$P(t) = \frac{1}{3} + \frac{2}{3}\cos(\gamma_\mu B_{\mathrm{loc}} t). \tag{2.11}$$

Here, γ_μ is the gyromagnetic ratio of the muon and relates the oscillation frequency to the local field, B_{loc} [130]. The one-third term gives rise to a characteristic tail at long times which is typically present in muon data collected for long-range ordered magnets, as discussed in the muon study for the Zn-barlowite series in Chapter 4. The absence of this feature can be interpreted as evidence for remaining disorder in a system, which is also depicted in Figure 2.5. However, modelling the often complex oscillatory spectra, which may contain frequencies corresponding to many different stopping sites or an inhomogeneous internal field, can be extremely challenging. Alongside this, other contributions to the data such as background signal or nuclear magnetic moments within the sample can further complicate the interpretation of data. Furthermore, the fast oscillations associated with relatively large internal magnetic fields in an ordered material in many cases require the use of a continuous-wave muon source. Otherwise, a loss of the initial asymmetry—which occurs due to the fast depolarisation of the muon spin as internal fields develop—is cited as evidence for long-range order, alongside a one-third tail [131].

2.5.2 Nuclear Magnetic Moments

The idea of a one-third tail can also be extended to nuclear magnetic moments, which are an additional source of magnetic field in a sample alongside electronic moments. The magnetic moments associated with nuclei are fluctuating very slowly and only weakly interacting, meaning that they can be considered as static on the time-scale of the muon experiment and pointing in random directions. This kind of random static field distribution—which can also describe the frozen moments in a spin glass—yields a change in polarisation described by the Kubo-Toyabe function [132], given by,

$$P_{\text{KT}}(t) = \frac{1}{3} + \frac{2}{3}(1 - \Delta^2 t^2)e^{-\Delta^2 t^2/2}, \tag{2.12}$$

where Δ is the gaussian field distribution. In practice the nuclear magnetic moments typically yield a slow muon spin depolarisation evidenced in the collected data by a relatively gradual relaxation of the time-dependent asymmetry. This contribution dominates at high temperatures, where electronic moments are normally fluctuating very quickly. The nuclear moment can be taken advantage of to probe Li-ion diffusion in battery materials, for example, and this technique offers the further advantage of being able to be performed in zero applied field, in contrast to nuclear magnetic resonance (NMR) [135]. The nuclear moment contribution is additionally useful in cases where highly electronegative ions form a

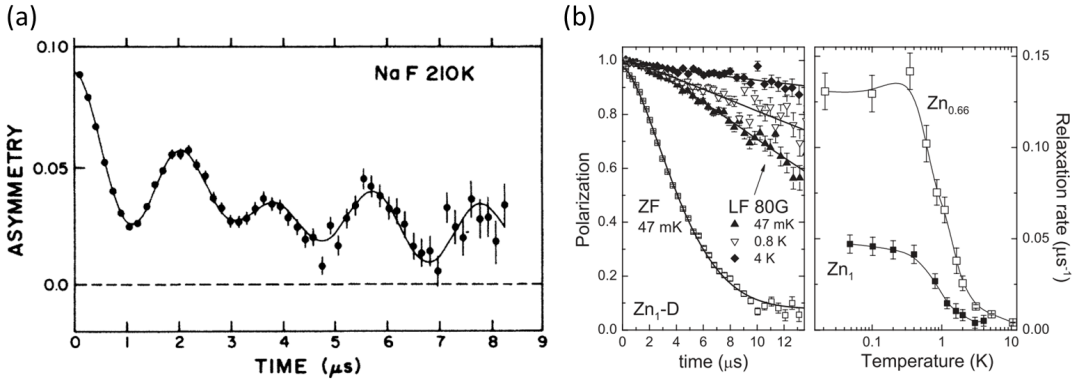

Figure 2.6: Additional contributions to the muon spin depolarisation include (a) the formation of entangled states between the muon and nuclear magnetic moments, for example the F–μ–F state observed in NaF [133], and (b) effects from dynamically fluctuating electrons which can be isolated by applying a longitudinal field. The example shown is data collected for the mineral herbertsmithite, where a plateau in the relaxation rate indicates persistent spin dynamics at 47 mK [134].

dipole-dipole interaction with the muon spin, which gives rise to entangled states that can present characteristic oscillations in the collected data, which arise at longer times than those associated with ordered electron magnetic moments. This is useful because a widely discussed limitation of the μSR technique is that there is some ambiguity in the precise location that the muons stop in a given sample. A prime example of muon entanglement is in the formation of an F–μ–F entangled state, which arises due to the high electronegativity and large nuclear moment of the fluoride anion. The oscillations in the asymmetry due to this dipolar interaction, for which an example is shown in Figure 2.6(a), can be modelled using,

$$P_{\mathrm{F}\mu\mathrm{F}} = \frac{1}{6}\Bigg[3 + \cos(\sqrt{3}\omega_{\mathrm{d}}t) + \left(1 - \frac{1}{3}\right)\cos\left(\frac{3-\sqrt{3}}{2}\omega_{\mathrm{d}}t\right) + \left(1 + \frac{1}{3}\right)\cos\left(\frac{3+\sqrt{3}}{2}\omega_{\mathrm{d}}t\right)\Bigg], \tag{2.13}$$

where the angular frequency ω_{d} can be related to the distance between the muon and the fluoride site. A similar procedure is demonstrated in Chapter 4, where instead the formation of μ–F and μ–OH entangled states indicates the presence of two muon stopping sites. In this case, the experimental data is corroborated by DFT muon-site calculations, which are becoming increasingly accessible to researchers due to the development of theory and user interfaces such as MuFinder [136]. This approach offers the further benefit of predicting whether the incoming muon distorts the local crystal structure. This potential distortion is another

criticism of muon spectroscopy, because in turn this may distort the local magnetic fields and deem the muon signal unrepresentative of the unperturbed magnetism in a given material [137].

2.5.3 Electronic Magnetic Moment Dynamics

In the absence of long-range magnetic order, the ability for μSR to detect magnetic moment dynamics presents a crucial application to the study of frustrated magnetism. In order to isolate the contribution to the measured signal from the dynamic electron moments, a field is applied parallel (or longitudinal) to the initial muon spin. This has the effect of decoupling the muon from any moments on the order of or lower than the applied field, such as nuclear magnetic moments. The fluctuating fields then associated with dynamic moments take an exponential form,

$$A(t) = Ae^{-\lambda t}, \tag{2.14}$$

where λ is a relaxation rate which is inversely proportional to the frequency of the fluctuating field. This means that as the fluctuations slow down—typically as the sample is cooled—then the relaxation rate increases [130]. This is perhaps unintuitive given that a quickly fluctuating field may be expected to depolarise the muon spin at a faster rate, but in reality the muon cannot "keep up" with the fast fluctuating field, in an effect that can be likened to motional narrowing in NMR [126]. In many cases a stretched exponential is used to model data measured in a longitudinal field instead, which could indicate the presence of a distribution of fluctuating fields, although this approach is deemed physically meaningless by many [138]. The method of applying a longitudinal field on cooling is typically used in samples that present no evidence for long-range order, because any remaining relaxation of the asymmetry under these conditions indicates electron spin dynamics. For this reason, a plateau in the temperature-dependent muon spin relaxation at sub-kelvin temperatures, demonstrated in Figure 2.6(b), is one of the first experimental observations towards identifying a QSL state [134, 139, 140]. In Chapter 4, this behaviour is presented in some members of the Zn-barlowite series.

Chapter 3

The Crystal and Magnetic Structures of a Mineral Family of Frustrated $S = \frac{1}{2}$ Kagomé Antiferromagnets

3.1 Introduction

The discovery of mineral systems has provided inspiration for the synthesis of a breadth of interesting crystal structures, and for their corresponding physical phenomena to be explored. The first class of minerals to gain attention in the context of frustrated magnetism are known as the jarosites, which have the general formula $AM_3(\mathrm{OH})_6(\mathrm{SO}_4)_2$ [68]. In the jarosite structure, kagomé layers are formed from $M_3(\mu\text{–}\mathrm{OH})_3$ triangles, with examples of variants on the M^{3+} site including Fe^{3+}, V^{3+} and Cr^{3+}. The kagomé layers are capped by sulphate anions and separated by the A^+ site, as depicted in Figure 3.1. The A^+ site can host ions such as K^+, Na^+, Rb^+ and $\mathrm{NH}_4{}^+$. However, the jarosites contain classical spins which do not lend themselves to supporting quantum behaviour and, as a result, display long-range magnetic order which is characterised by spin anisotropy [141].

Related minerals that can host the $S = \frac{1}{2}$ ions required to access more enigmatic quantum states of matter exist in the form of copper hydroxides. Volborthite, with the formula $\mathrm{Cu_3V_2O_7(OH)_2 \cdot 2H_2O}$, was the first mineral discovered to contain kagomé layers formed from Cu^{2+} ions, here separated by $\mathrm{V_2O_7}$ pillars, and represented a turning point in the exploration of quantum kagomé physics [145]. However, a structural transition occurs in volborthite due to a complex reordering of the *d*-orbitals within the kagomé planes, which is facilitated by $\mathrm{H_2O}$ molecules within its crystal structure [146]. This, in turn, modifies the magnetic interactions

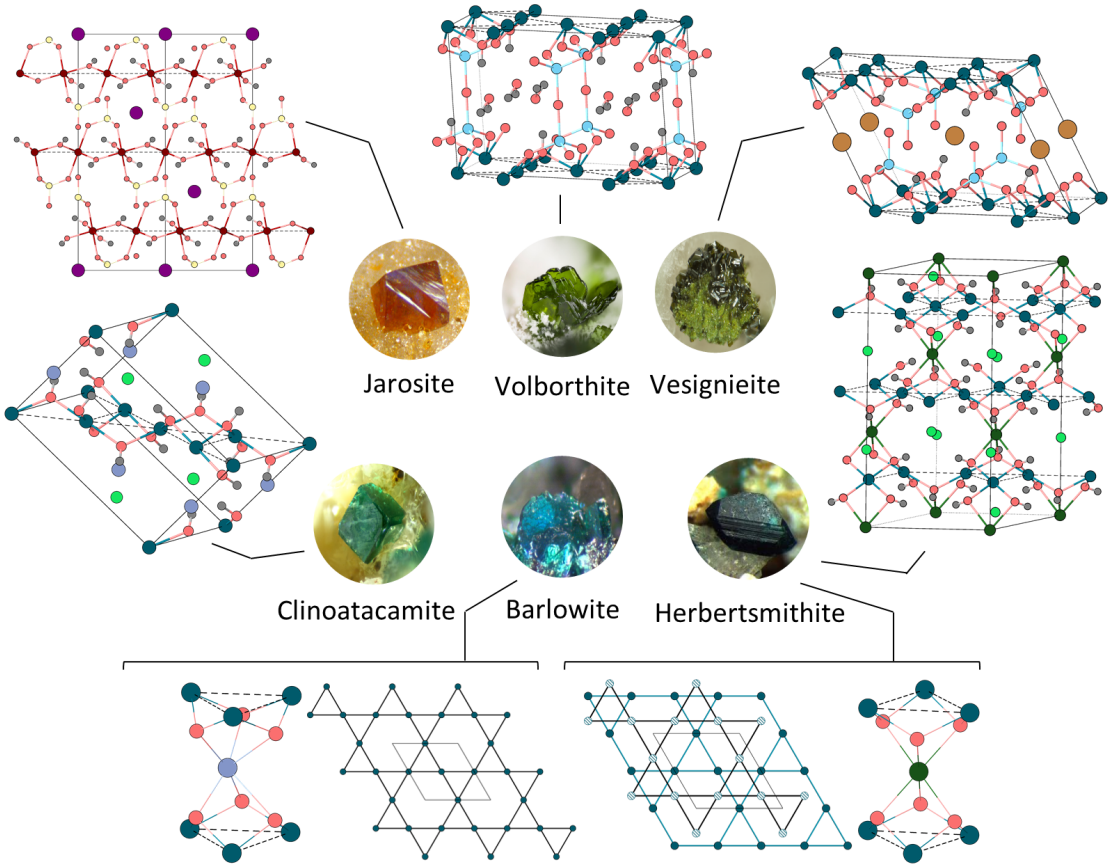

Figure 3.1: The crystal structures of mineral systems which contain kagomé networks of magnetic ions, represented by dashed lines, which are bound by hydroxide anions (red and grey spheres). In jarosite [142], the Fe^{3+} (brown spheres) form kagomé layers capped by sulphate ions (yellow) and are separated by K^{+} (purple), whilst in volborthite [66] and vesignieite [67] the Cu^{2+} (teal spheres) kagomé layers are separated by V_2O_7 (pale blue) and VO_4 (pale blue), respectively. The distorted kagomé layers in clinoatacamite [143] are separated by an additional Cu^{2+} site (lilac), whilst in the related herbertsmithite [112] these interplane sites are replaced with Zn^{2+} (dark green), which has an octahedral coordination to the layers above and below, leading to staggered kagomé layers. Finally, the interplane Cu^{2+} ion in barlowite [119] has trigonal prismatic coordination and the kagomé layers are perfectly stacked. A detailed view of the proposed crystal structures of barlowite is given in Figure 3.2. All images obtained from [144].

within volborthite, and it turns out that the magnetic ground state is actually effectively described by a square lattice model. Magnetic transitions take place at 0.8 K and 1.2 K, and Curie-Weiss analysis yields a Weiss temperature $\theta = -140$ K, demonstrating a strongly interacting system [147]. Vesignieite, $BaCu_3V_2O_8(OH)_2$, is another Cu^{2+} mineral with a kagomé structure which undergoes magnetic ordering, this time at 9 K and with $\theta = -75$ K, again indicating a highly frustrated

magnetic ground state. In this case, it is thought that orbital frustration within the kagomé network due to a dynamic Jahn-Teller effect leads to significant magnetostructural coupling [100].

The atacamite family is another class of minerals which offer a rich variety of structural and magnetic behaviour. There are three polymorphs within this family with the formula $Cu_2(OH)_3Cl$: atacamite, botallackite and clinoatacamite [148]. Botallackite is a layered structure with monoclinic symmetry, and the Cu^{2+} ions form edge-sharing triangles rather than corner-sharing. Atacamite and clinoatacamite, meanwhile, have orthorhombic and monoclinic symmetries, respectively, and both structures can be visualised as distorted kagomé layers separated by additional Cu^{2+} and Cl^- ions, with the differences in their structures stemming from the distribution of OH^- and Cl^- anions. The magnetism in both of these systems, however, is better described in terms of a distorted pyrochlore network [69, 143, 149].

In clinoatacamite, the replacement of Cu^{2+} by diamagnetic cations, such as Zn^{2+}, occurs predominantly at the interlayer site. This has the effect of removing the monoclinic distortion and results in the Zn-paratacamite series, $Zn_xCu_{4-x}(OH)_6Cl_2$, which has trigonal $R\bar{3}m$ symmetry when $x > 0.33$ [65]. Crucially, compositions with this symmetry contain perfect kagomé layers of Cu^{2+} which are separated by Cu^{2+}/Zn^{2+} cations and Cl^- anions, the latter of which are covalently bonded to Cu^{2+} in the layers above and hydrogen bonded to hydroxide anions below, leading to staggered kagomé planes. The $x = 1$ end-member, $ZnCu_3(OH)_6Cl_2$, is the mineral herbertsmithite which, in the ideal structure, should contain magnetically decoupled kagomé layers. However, even herbertsmithite, lacking long-range order down to 50 mK and widely accepted to be the first kagomé host for a quantum spin liquid (QSL) [112, 152], has been found to suffer from transition metal site disorder [71] which is thought to dominate its low-temperature magnetic behaviour [153–156].

The complexities of the systems discussed so far, whose structures are summarised in Figure 3.1, are motivation for the discovery of alternative materials which represent the kagomé antiferromagnet. In recent years, the mineral barlowite [70]—with formula $Cu_4(OH)_6FBr$—has been hailed as a promising new mineral within which to explore this topic. Formed from Cu^{2+}-based kagomé layers separated by a mixture of Cu^{2+} and halide anions, F^- and Br^-, it is well established via

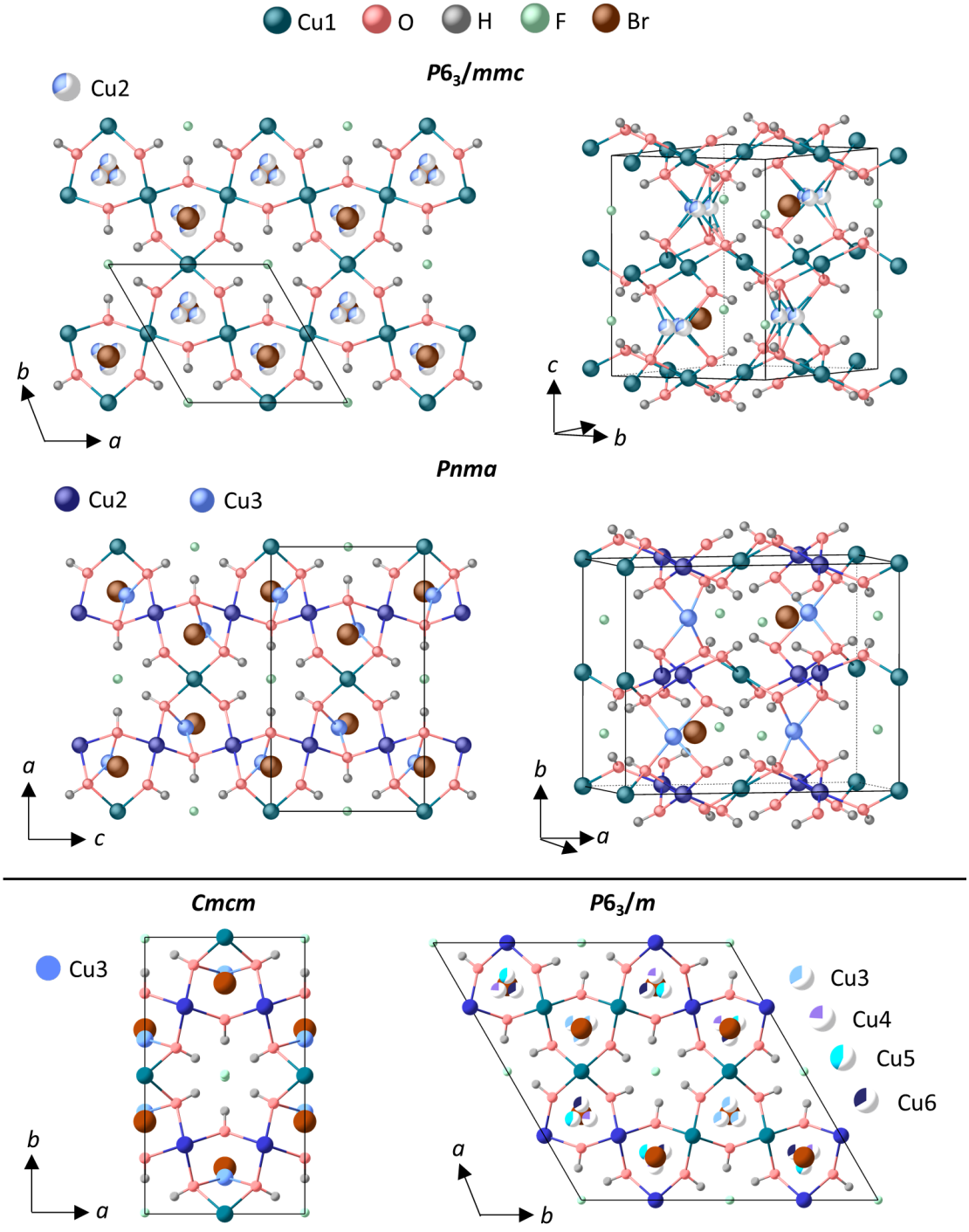

Figure 3.2: At room temperature, the hexagonal $P6_3/mmc$ structural model (top) of barlowite, $Cu(OH)_6FBr$, contains Cu^{2+} ions which form kagomé layers in the *ab*-plane, and an additional disordered copper site between the layers. A symmetry lowering to *Pnma* (middle) occurs, where the kagomé layers are formed from two Cu sites and the interlayer site is ordered. The alternative proposed models of barlowite (bottom) are *Cmcm* [150] and $P6_3/m$ [151], and both contain a level of occupational disorder on the interlayer copper sites.

bulk magnetometry measurements that barlowite orders antiferromagnetically below $T_N = 15$ K, although a detailed description of the magnetic structure of barlowite remained undetermined [114, 119, 150, 157–161]. However, DFT calculations have indicated that replacing the interlayer Cu^{2+} with Zn^{2+}—which is the topic of Chapter 4—could magnetically decouple the kagomé layers akin to herbertsmithite. The mixed halide system in barlowite leads to perfectly aligned kagomé layers, whilst the interlayer Cu^{2+} site adopts a rare trigonal prismatic coordination, depicted in Figure 3.1. Both of these features have been predicted to contribute to increased site selectivity and reduced antisite disorder in Zn-barlowite in comparison to herbertsmithite [162, 163]. Furthermore, DFT calculations point to a reduction of interplane coupling upon substitution, which is motivation to explore barlowite as a parent compound to a QSL candidate. This, in turn, may reveal insights into the role of disorder via a comparison to herbertsmithite. The evolution of the magnetic ground states in Zn-doped barlowite are explored in Chapter 4.

Despite this, barlowite itself has been the subject of intense debate in recent years, because there are several proposed room-temperature and low-temperature crystal structures which are all characterised by some degree of disorder on the interlayer Cu^{2+} site. In the widely reported hexagonal room-temperature structure, $P6_3/mmc$, the interlayer Cu^{2+} is disordered over three equivalent sites [70, 119, 151, 158, 160, 161], and the ordering of this site upon cooling leads to a symmetry lowering of the crystal structure. There are two proposed orthorhombic structures, $Pnma$ [158, 161] and $Cmcm$ [150], which are presented in Figure 3.2. In both structures, the interlayer Cu^{2+} orders onto one site, but the structures differ in the ordering scheme of this interlayer site. More recently, a third low-temperature structure of barlowite has been found with $P6_3/m$ symmetry, which appears to be favoured under certain synthetic conditions [151]. In this low-temperature hexagonal structure, the kagomé layers are formed from alternating equilateral and scalene triangles, and it follows that the interlayer Cu^{2+} sites contain a mixture of order and disorder. One study describes the interlayer ordering in barlowite, as well as in the isostructural mineral claringbullite, $Cu_4(OH)_6FCl$ [20, 164], as a dynamic to static Jahn-Teller effect which might vary between samples owing to the presence of defects which occur relating to synthetic conditions [161]. Intriguingly, the magnetic properties of barlowite appear to be highly dependent on the crystal structure which is adopted at low temperature, indicating that each proposed model is characterised by its own magnetic ground

state. For example, in samples with $P6_3/m$ symmetry a pinwheel valence bond crystal state is predicted to arise rather than a QSL state [151]. As a consequence, a definitive understanding of the factors which drive this structural distortion are necessary in order to understand the magnetism which arises within barlowite and its analogues.

To address the complexities surrounding the structure and properties of barlowite and its analogues, this chapter presents a comprehensive study of barlowite, claringbullite and a novel synthetic iodide analogue, $Cu_4(OH)_6FI$. This chapter is composed of three parts. The first section describes preliminary neutron powder diffraction (NPD) measurements, which reveal the average crystal and magnetic structures of barlowite. Following this, a combination of high-resolution NPD and synchrotron powder X-ray diffraction (PXRD) data collected for barlowite and related halide analogues elucidates the nature of the structural transition observed in these phases. Finally, the magnetic behaviour across this series is explored using magnetic susceptibility, heat capacity and NPD, and provides evidence that the complex structural behaviour in these systems is related to the selected magnetic ground state. Parts of this work have been published in Physical Review Materials [165], or are in preparation for publication in Inorganic Chemistry.

3.2 Experimental Methods

3.2.1 Synthesis

Deuterated samples of $Cu_4(OD)_6FX$ (X = Br, Cl, I) were synthesised via a hydrothermal method. Barlowite (referred to as FBr) was produced using 4 mmol $CuCO_3{\cdot}Cu(OH)_2$ (Alfa Aesar, Cu 55%), 8 mmol $CuBr_2$ (Sigma Aldrich, 99%) and 12 mmol NH_4F (Alfa Aesar, 98%), which were combined with 20 mL D_2O (Sigma Aldrich, 99.9% D) and sealed in a 50 mL Teflon-lined stainless steel autoclave. The autoclave was heated at a rate of 10 °C/min to 200 °C and held for 72 hours, after which the autoclave was allowed to cool to room temperature at 5 °C/min. Claringbullite (FCl) was synthesised by combining 2 mmol $CuCO_3{\cdot}Cu(OH)_2$, 2 mmol $CuCl_2$ (Acros Organics, 99%), 4 mmol NH_4F and 10 mL D_2O in a 23 mL autoclave. The autoclave was heated at a rate of 10 °C/min to 200 °C and held for 48 hours, and the autoclave allowed to cool to room temperature at 5 °C/min. An excess of NH_4F was required in this case to avoid the formation of polymorphs

of clinoatacamite, $Cu_4(OH)_6Cl_2$, which form when there is an excess of Cl^- ions in the reaction mixture. Finally, the iodide analogue (FI) was synthesised using 2 mmol $CuCO_3{\cdot}Cu(OH)_2$, 2 mmol NH_4F, 0.2 mL HI (Sigma Aldrich, 58%) and 10 mL D_2O in a 23 mL autoclave, which was heated at 10 °C/min to 140 °C and held for 72 hours, and then allowed to cool to room temperature at 5 °C/min. This method resulted in a small CuI impurity, which was removed by stirring the sample in a dilute aqueous solution of ammonium hydroxide. Note that using temperatures any higher than 150 °C to synthesise FI failed to produce the required product, leading to CuO and CuI phases instead. Each of these synthetic methods were repeated several times and the resulting samples for each were combined and ground thoroughly in order to produce sample sizes adequate for NPD measurements. The same deuterated samples were measured for all diffraction methods described in this chapter, although the samples were added to in subsequent experiments. Magnetometry measurements were performed on protonated samples synthesised via the same routes.

3.2.2 Powder Neutron and X-ray Diffraction

Powder diffraction data were collected for the $Cu_4(OD)_6FX$ series in four parts. Firstly, neutron powder diffraction data (NPD) for FBr were measured on the time-of-flight General Materials (GEM) diffractometer of the ISIS Neutron and Muon Source at the Rutherford Appleton Laboratory. A 1 g sample was packed into a cylindrical vanadium can and data were collected at regular intervals between $1.5 - 300$ K in a helium cryostat. Following this, additional NPD data for all members of the $Cu_4(OH)_6FX$ family were collected on the high-resolution powder diffractometer (HRPD), also at the ISIS Neutron and Muon Source, where the samples (4.2 g for FBr, 3.2 g for FCl and 2.5 g for FI) were packed into flat plate steel-framed sample holders with vanadium windows and measured at 300 K and 1.5 K. Structural refinements were performed using the GSAS package [94, 95].

Powder X-ray diffraction (PXRD) data were collected on the I11 beamline at the Diamond Light Source at the Rutherford Appleton Laboratory. Samples were packed into borosilicate glass capillaries and attached to a brass holder. The samples were cooled using a Cryostream, and data were collected using the MAC detector and an X-ray wavelength, $\lambda = 0.826582$ Å, at 90 K and 300 K. For FBr, additional MAC measurements were conducted at 20 K intervals between 90 – 300 K. For FCl and FI, data in 2 K intervals between 90 – 300 K were collected using the PSD detector and an X-ray wavelength, $\lambda = 0.826522$ Å. All

structural refinements were completed using the GSAS package [94, 95]. In all I11 datasets, a broad background feature centred at $\sim 12^\circ$ is present, which is likely due to scattering from air within the sample capillaries. The background in all Rietveld refinements was defined manually with 24 terms to account for this.

Finally, constant wavelength NPD data were collected for each member of the $Cu_4(OH)_6FX$ series on the high-intensity D20 diffractometer at the Institut Laue-Langevin, Grenoble. Samples with masses of 4.2 g (FBr), 3.1 g (FCl) and 1.2 g (FI) were packed into 9 mm (FBr and FCl) or 6 mm (FI) diameter vanadium cans and data collected with a neutron wavelength $\lambda = 2.4188$ Å and monochromator take-off angle 42° at 1.5 K and 20 K (FBr) or 25 K (FCl and FI), with an additional measurement at 10 K for FCl. Magnetic refinements were completed using the FullProf package [96].

3.2.3 Magnetometry

Temperature-dependent DC magnetic susceptibilities of the $Cu_4(OH)_6FX$ series were collected on a Quantum Design Magnetic Properties Measurement System (MPMS) with a SQUID magnetometer. 40 mg samples were packed into gelatin capsules and loaded into clear plastic straw samples holders. Data were collected in an applied field of 1 T between 2 and 300 K in zero-field cooled (ZFC) and field cooled (FC) cycles. Heat capacity data were collected on pressed powders of FBr (26.4 mg), FCl (9.5 mg) and FI (12.4 mg) on a Quantum Design Physical Properties Measurement System (PPMS) in zero field between 2 and 300 K. The addenda for each was measured and subtracted to account for background signal. Two data points per temperature were collected and averaged.

3.3 The Crystal and Magnetic Structures of Barlowite

3.3.1 Crystal Structure Determination Using Time-of-Flight Neutron Powder Diffraction

NPD data collected on Bank 3 of the GEM diffractometer for FBr are shown in Figure 3.3. At room temperature, Rietveld refinement of the $P6_3/mmc$ structural model suggests that samples of barlowite synthesised via the method described in this chapter crystallise in the widely reported hexagonal structure [119, 151, 158, 160, 161]. Here, kagomé layers formed from equilateral triangles of Cu^{2+} (Cu1), bound together by hydroxide anions, lay in the *ab*-plane and are stacked in an eclipsed manner along the *c*-axis, as depicted in Figure 3.2. Between the layers there is a second Cu^{2+} site (Cu2) with a distorted trigonal prismatic coordination which can occupy one of three sites, leading to disorder of this interlayer site where each position is on average one-third occupied. There are two additional sites which lay between the kagomé layers within the barlowite structure; the first is the F^- site, which occupies the centre of the hexagonal motifs formed from the triangular layers, and the second is the Br^- site, which lies directly beneath the equilateral triangle of the kagomé layers, alternating with the Cu2 site. Atomic displacement parameters, in this case, were refined anisotropically for all atoms, which results in a statistically better fit and, in particular, more reasonably accounts for the disorder at the Cu2 site in comparison to isotropic modelling. The final refined structural model is given in Table 3.1. Refinement of the alternatively proposed room temperature $Cmcm$ model [150], which is a subgroup of $P6_3/mmc$, resulted in a significantly poorer fit ($R_{\text{wp}} = 3.04\%$) and placed diffraction intensity in Bank 3 where no scattering is observed in the GEM data.

An important observation to be made from the data collected on GEM is that below 250 K, additional weak diffraction intensity begins to develop which is most evident in the 3.0 – 3.2 Å region of Bank 3 at 1.5 K, as shown in the inset of Figure 3.3. This indicates a structural transition which is likely associated with the ordering of the interlayer Cu2 site of the room temperature model. To determine which model best describes the low temperature data, Le Bail fits of all orthorhombic subgroups of the reported $P6_3/mmc$ and $Cmcm$ models obtained from ISODISTORT [105, 166] were performed on data collected at 1.5 K, and the statistical results obtained are shown in Table 3.2. Le Bail results for the $P6_3/m$ model,

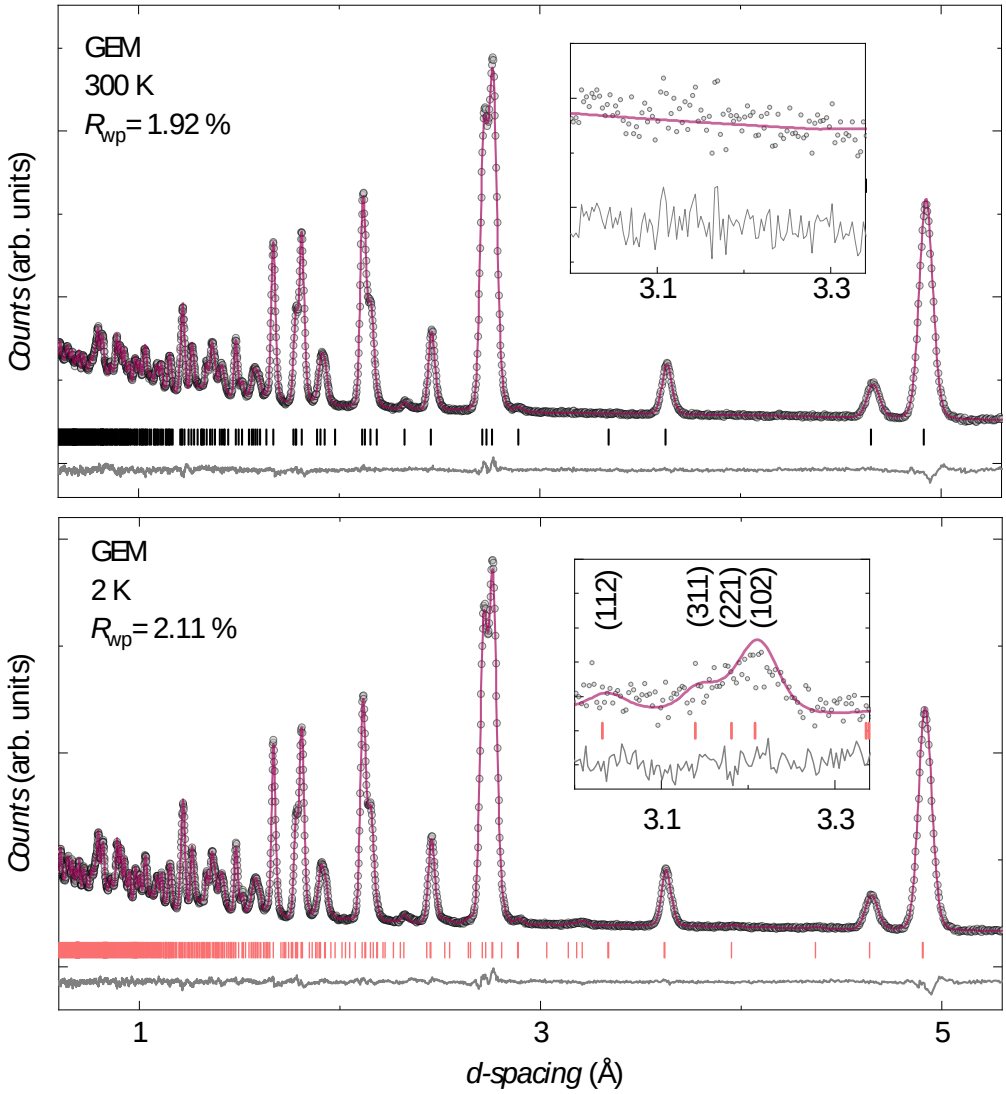

Figure 3.3: NPD data collected for $Cu_4(OD)_6FBr$ at 300 K (top) and 2 K (bottom) in Bank 3 of the GEM diffractometer. Rietveld refinements of the $P6_3/mmc$ and $Pnma$ structural models at 300 K and 2 K, respectively, are shown by the solid lines. The insets show the d-spacing region 3.0 – 3.3 Å, where a (102) reflection is observed in the $Pnma$ structure, along with additional weak (112), (311) and (221) reflections.

also proposed to describe the structure of barlowite at low-temperatures [151], are also shown in Table 3.2. Interestingly, the $Cmcm$ model again places intensity where no scattering is observed in GEM data. In fact, of the groups tested, only $P6_3/m$, $Pbcm$, $Pmmn$, $Pmma$, and $Pnma$ subgroups effectively account for the additional Bragg peaks observed, and of those groups it is the $Pnma$ space group which yields the best Le Bail fit. This is congruent with previous low-temperature studies conducted on barlowite synthesised via a similar route [151, 158]. A Ri-

Table 3.1: Rietveld refinement crystal structure parameters (top) for the $P6_3/mmc$ model of barlowite fitted to NPD data collected on GEM at 300 K. Refined lattice parameters are $a = b = 6.6831(8)$ Å and $c = 9.302(1)$ Å. The refined H/D occupancies indicate that the sample is 96 % deuterated. The refined anisotropic atomic displacement parameters, U_{aniso}, are given in the bottom table. The final statistical factors are $R_{\text{wp}} = 1.92\%$ and $\chi^2 = 1.83$.

Atom	Site	x	y	z	Occupancy
Cu1	$6g$	0.5	0	0	1
Cu2	$6h$	0.62946(8)	0.2589(2)	0.25	$\frac{1}{3}$
F1	$2b$	0	0	0.75	1
Br1	$2c$	0.6667	0.3333	0.75	1
O1	$12k$	0.20160(4)	0.79840(4)	0.90816(4)	1
D1/H1	$12k$	0.12430(4)	0.87570(4)	0.86618(4)	0.959(1)/0.041(1)

	U_{aniso} (10^{-2} Å^2)					
Atom	U_{11}	U_{12}	U_{13}	U_{22}	U_{23}	U_{33}
Cu1	0.72(1)	0.370(8)	−0.228(8)	0.74(2)	−0.46(2)	1.70(2)
Cu2	0.87(4)	0.75(3)	0.0	1.50(6)	0.0	0.24(5)
F1	1.51(3)	0.76(2)	0.0	1.51(3)	0.0	2.87(6)
Br1	1.71(3)	0.854(13)	0.0	1.71(3)	0.0	0.89(4)
O1	0.71(1)	0.27(2)	−0.055(8)	0.71(1)	0.055(8)	1.13(2)
D1	1.92(2)	1.32(2)	−0.239(9)	1.92(2)	0.239(9)	2.64(3)

etveld refinement of the *Pnma* model at 1.5 K is shown in Figure 3.3, and the refined structural parameters are given in Table 3.3. The consequence of this structural transition is presented in Figure 3.2, where there are two key features to be noted. Firstly, the kagomé layers now lay in the *ac*-plane and contain three different bond lengths of 3.344(2) Å, 3.330(2) Å and 3.3438(5) Å within the triangles, which are now formed from two crystallographically distinct copper sites, denoted Cu1 and Cu2. The two Cu2 sites within the triangles are distorted subtly out of plane by approximately 2° relative to the *c*-axis. Secondly, the interlayer copper site (now Cu3) is no longer disordered and occupies a well-defined position shifted towards the Cu2 site. There is no significant movement of the halide anions on going from the hexagonal to the orthorhombic structure, although the F^- and Br^- sites no longer occupy special positions and do, therefore, shift marginally from the centre of the hexagonal and triangular motifs, respectively.

Differences in the *Pnma* model determined here compared to the alternative

Table 3.2: Summary of the R_{wp} and χ^2 values obtained in each bank from Le Bail fits to NPD data collected on GEM for $Cu_4(OD)_6FBr$ at 2 K. The listed space groups are subgroups of $P6_3/mmc$ and $Cmcm$, and were determined using ISODISTORT [105, 166]. The highlighted model, $Pnma$, gives the best fit to the data.

	R_{wp}(%)							
Model	Bank 1	Bank 2	Bank 3	Bank 4	Bank 5	Bank 6	Total	χ^2
$Cmcm$	4.03	2.54	2.27	2.33	2.30	1.76	2.27	2.378
$C222_1$	4.06	2.62	2.40	2.36	2.49	1.66	2.34	2.535
$Cmc2_1$	4.02	2.57	2.48	3.12	4.63	3.36	3.50	5.679
$Pbcm$	4.13	2.55	2.16	2.27	2.26	1.45	2.18	2.201
$Pbcn$	4.05	2.53	2.19	2.24	2.26	1.43	2.17	2.180
$Amm2$	4.19	2.57	2.30	2.27	2.39	1.53	2.25	2.341
$Pmmn$	4.01	2.50	2.00	2.08	2.15	1.31	2.04	1.917
$Ama2$	4.07	2.63	2.42	2.37	2.51	1.67	2.35	2.557
$Pmma$	4.08	2.47	2.11	2.15	2.15	1.31	2.08	2.002
$Pnna$	3.98	2.56	2.15	2.26	2.33	1.49	2.20	2.237
Pnma	**3.97**	**2.49**	**1.98**	**2.09**	**2.15**	**1.30**	**2.03**	**1.914**
$Pnnm$	4.10	2.49	2.07	2.08	2.16	1.32	3.22	1.954
$P6_3/m$	4.06	2.75	2.76	3.30	3.91	2.37	2.06	4.792

$Cmcm$ and $P6_3/m$ models described in the literature lie predominantly in the ordering scheme of the Cu3. In the $Pnma$ structure determined here, the Cu3 ions order cooperatively so that no two move towards each other, whilst in $Cmcm$ they shift towards each other in pairs. Meanwhile, in the $P6_3/m$ structure depicted in Figure 3.2 both equilateral and scalene triangles emerge within the kagomé planes. As a result, there are also two types of interlayer Cu site, one which is disordered over three sites, as in the room temperature structure, and one which has a site preference. The distortion in barlowite could be considered to be driven by a dynamic to static Jahn-Teller effect [161, 167]. Potential energy surface (PES) calculations for the $Pnma$ structure have shown that, of the three possible directions which the distortion can take, the energy barrier is much lower when the interlayer Cu^{2+} shifts in the a-direction away from the Cu1 site of the kagomé planes, meaning that there are two energetically equivalent positions shifted towards the Cu2 site. In $Cmcm$, there is a small preference for the Cu3 to shift solely to one site (towards Cu1) [161]. In the $Pnma$ structure of barlowite determined from the data presented in this chapter, it is not clear why the Cu3 chooses one of the two potential positions over the other. One explanation might lie in a consideration of sterics and/or Coloumbic repulsion, meaning that it is

Table 3.3: Rietveld refinement crystal structure parameters for the *Pnma* model of barlowite fitted to NPD data collected on GEM at 2 K. The deuterium occupancies were fixed to the refined values determined from data collected at room temperature. Refined lattice parameters are $a = 11.551(1)$ Å, $b = 9.280(1)$ Å and $c = 6.6791(8)$ Å ($R_{wp} = 2.11\%$, $\chi^2 = 2.949$).

Atom	Site	x	y	z	Occupancy	U_{iso} (Å^2)
Cu1	4a	0	0	0	1	0.0038(5)
Cu2	8d	0.2504(2)	0.5091(1)	0.2466(2)	1	0.0032(3)
Cu3	4c	0.1863(3)	0.25	0.0563(3)	1	0.0038(2)
F1	4c	0.4979(4)	0.25	0.0034(5)	1	0.0097(2)
Br1	4c	0.3310(3)	0.25	0.4985(4)	1	0.0036(2)
O1	8d	0.2964(2)	0.0965(2)	0.0015(3)	1	0.0025(4)
O2	8d	0.1014(2)	0.0904(2)	0.1998(4)	1	0.0035(4)
O3	8d	0.4007(2)	0.5875(2)	0.3020(4)	1	0.0053(4)
D1/H1	8d	0.3776(2)	0.1268(2)	0.9988(4)	0.959/0.041	0.0121(6)
D2/H2	8d	0.0630(3)	0.13636(2)	0.3130(4)	0.959/0.041	0.0126(8)
D3/H3	8d	0.44052(2)	0.63892(2)	0.19124(3)	0.959/0.041	0.0104(6)

electrostatically favourable for the interlayer Cu^{2+} ions to shift away from each other with a decrease in temperature as the unit cell contracts. The structural distortion which occurs due to this ordering is not a first order transition and is rather a gradual disorder-order transition, based on the observation of a subtle onset of the orthorhombic peaks which occurs over a wide temperature range of approximately 100 K based on the GEM data. Another interesting feature to note at this point is that the orthorhombic peaks are particularly weak and broad, which is demonstrated by the increased peak intensity of the fitted model compared to the observed data presented in Figure 3.3. This point will be returned to in Section 3.4.3.

3.3.2 Magnetic Structure Determination Using Constant Wavelength Neutron Powder Diffraction

The temperature-dependent magnetic susceptibility collected for barlowite in a zero-field cooled cycle is shown in Figure 3.4, and displays an upturn below $T_N = 15$ K, consistent with magnetic ordering at this temperature as determined by several previous studies [114, 119, 158, 160]. Measurement of comparable data in a field-cooled cycle does not lead to a deviation in the temperature dependence of the susceptibility, meaning that the presence of spin glass formation can be ruled

out. The high-temperature inverse susceptibility follows Curie-Weiss behaviour, and a fit of this model to the data yields a Weiss temperature $\theta = -112.3(3)$ K and effective magnetic moment, $\mu_{\text{eff}} = 3.754(8)$ μ_{B} per formula unit. These fitted parameters coincide with the values determined from similar studies and indicate that strong antiferromagnetic exchange interactions dominate within barlowite. However, the nature of the magnetically ordered state has yet to be reported. No magnetic scattering is observed in the GEM data collected for barlowite which was described in Section 3.3.1, indicating that the flux afforded by the instrument is likely insufficient to resolve the small moment magnetism exhibited by the frustrated Cu^{2+} moments. As a consequence, further NPD data, shown in Figure 3.5, were collected on the high-flux constant wavelength diffractometer D20. Rietveld analysis of this dataset was performed by Dr Gøran Nilsen (ISIS Neutron and Muon Source). Corefinement of magnetic and crystal structures is inherently unstable for systems involving small moments, and so here the 20 K data has been subtracted from data collected at 1.5 K, below T_{N}, to isolate the magnetic scattering, resulting in ten resolved magnetic reflections in total. These reflections lie on nuclear allowed and forbidden positions, consistent with antiferromagnetic order with a propagation vector of $\mathbf{k} = (0, 0, 0)$. A full set of symmetry allowed magnetic space groups were determined using $\mathbf{k}$ and *Pbcm*, *Pmmn*, *Pmma*, and *Pnma* space groups—those which could account for the additional nuclear peaks observed in GEM data at 1.5 K—using the MAGMAGN application on the Bilbao Crystallographic Server [106–108]. Of the resulting 32 magnetic space groups, those stemming from *Pbcm*, *Pmmn*, and *Pmma* resulted in a poor fit to the data, leaving eight potential magnetic space groups stemming from the *Pnma* structural space group. Of these, the $Pn'm'a$ model best describes the magnetic scattering observed, and a full Rietveld refinement of this model is shown in Figure 3.5.

The magnetic structure obtained from this analysis is shown in Figure 3.6, where the refined magnetic moments are 0.15(1) μ_{B}, 0.41(1) μ_{B}, and 0.53(1) μ_{B} on the Cu1, Cu2, and Cu3 sites, respectively. Each Cu moment points predominantly along the *a*-direction, but with an antiferromagnetic canting of the Cu2 moments towards the *b*-axis, and a ferromagnetic canting of the Cu3 moments towards the *c*-axis. The latter produces a net ferromagnetic magnetisation of 0.05(1) μ_{B} when averaged over all three Cu sites. Furthermore, this net ferromagnetic moment rationalises previous single crystal magnetisation measurements on barlowite [114]. This study indicated that the magnetic transition corresponds to an antiferromagnetic canted order with a ferromagnetic component ~ 0.1 μ_{B} lying in the *ab*-plane

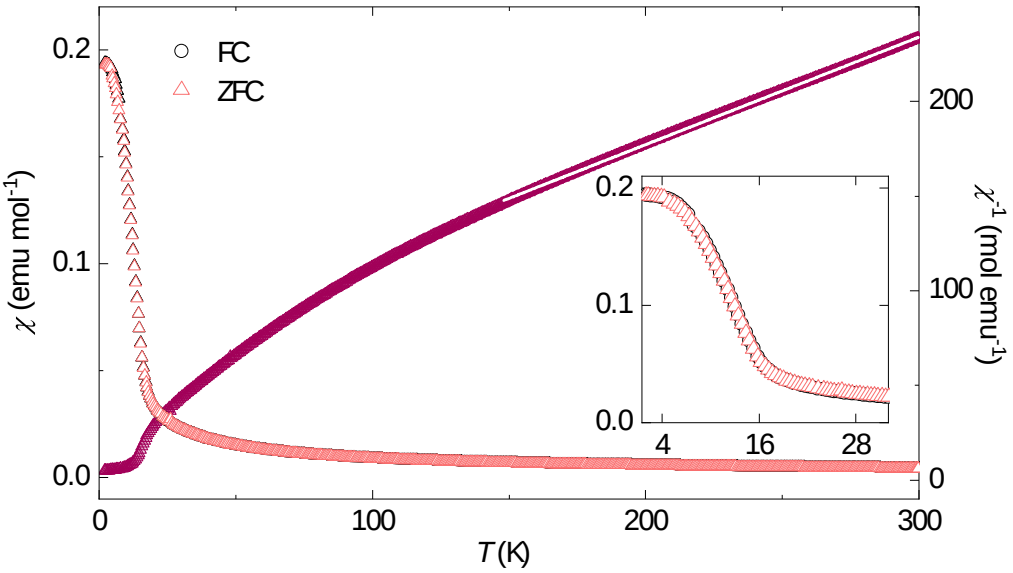

Figure 3.4: Temperature dependence of the magnetic susceptibility collected for barlowite, $Cu_4(OH)_6FBr$, measured in a zero-field cooled (ZFC) and field cooled (FC) cycle in an applied field of 1 T. A Curie-Weiss fit of the inverse susceptibility between 150 – 300 K is also shown, and yields $\theta = 112.3(3)$ K and $C = 1.762(2)$ emu mol^{-1} K.

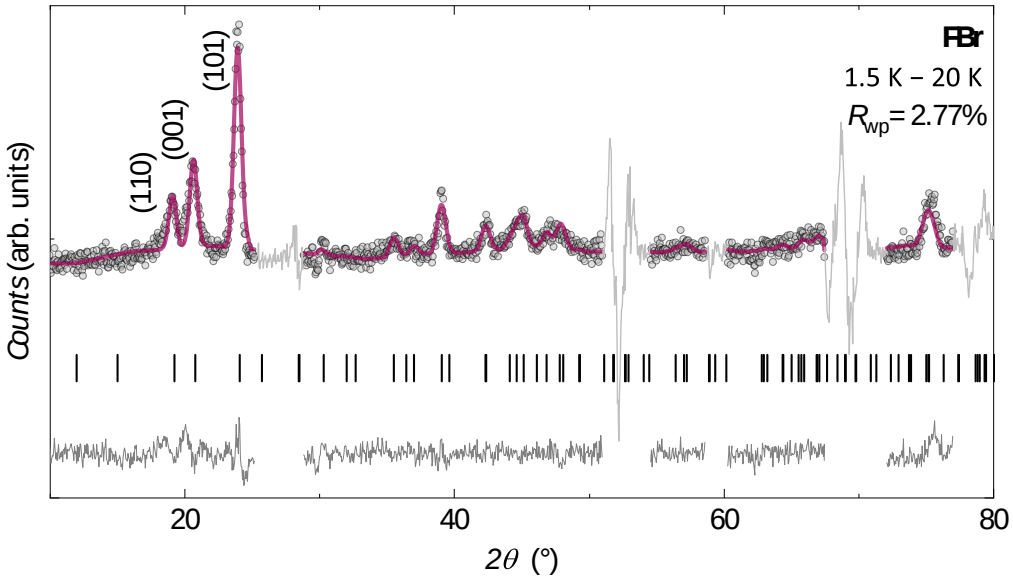

Figure 3.5: Rietveld refinement of the $Pn'm'a$ magnetic structure to subtracted NPD data collected on D20 for barlowite, $Cu_4(OD)_6FBr$. The light grey regions in the collected data were excluded from the refinement because they are the positions of strong nuclear reflections. The final statistical factors are $R_{wp} = 2.77\%$ and $\chi^2 = 2.75$.

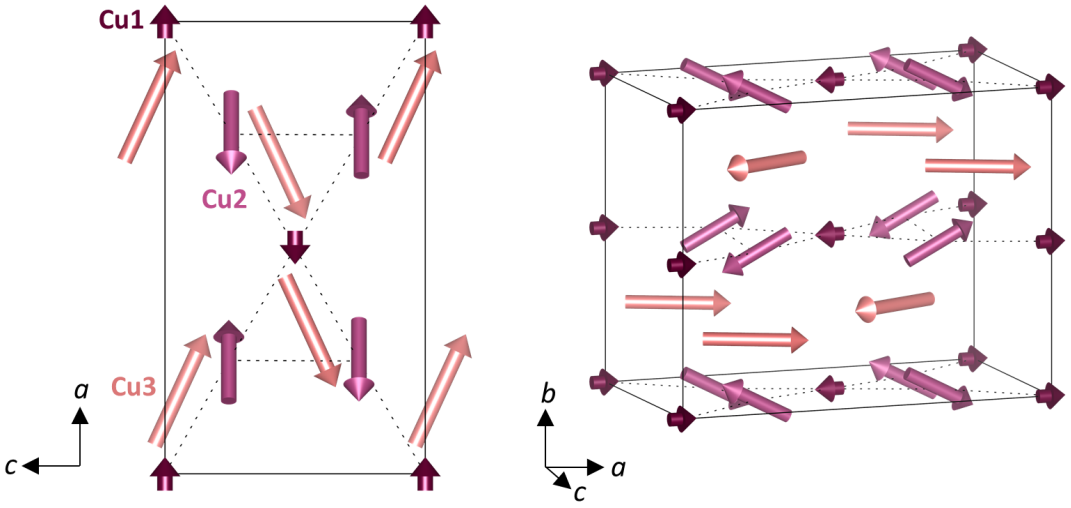

Figure 3.6: The magnetic structure of barlowite, $Cu_4(OD)_6FBr$, which belongs to the $Pn'm'a$ magnetic space group. The dashed lines indicate the kagomé structure formed from the Cu1 and Cu2 sites.

of the $P6_3/mmc$ structure, which corresponds to the ac-plane of the $Pnma$ cell and is indeed what is observed in the fitted structure presented here. This magnetic symmetry is comparable to that described previously [158], in which it was determined that the Cu3 moment magnitude is significantly larger than the average moment of Cu1 and Cu2. However, the high-flux of the D20 diffractometer utilised here has enabled for the precise magnitudes and directions of the Cu1 and Cu2 moments within the kagomé plane to be determined, which was not possible in the previous study which only resolved the most intense (110), (001) and (101) magnetic Bragg peaks.

A full understanding of the origin of the magnetic structure in barlowite is difficult given that there are a total of six possible (three in-plane and three out-of-plane) nearest-neighbour exchange pathways. However, there are several features of the magnetic structure which can be highlighted. Firstly, it is likely that there is a strong antiferromagnetic interaction between the Cu2 moments within the kagomé planes and, secondly, a ferromagnetic exchange between the Cu1 and Cu3 moments is plausible. Interestingly, these are both features that arise in the magnetic structure of the closely related clinoatacamite, $Cu_4(OH)_6Cl_2$, the parent material to the QSL candidate herbertsmithite [69]. Another important point to note is that, like the orthorhombic nuclear Bragg peaks observed on GEM at 1.5 K, the magnetic Bragg peaks observed in D20 data for barlowite are not resolution limited. The full width at half maxima indicates a magnetic correlation length of approxi-

mately 100 Å. Furthermore, the refined moment sizes are heavily suppressed, with an average moment of 0.375(5) μ_B per Cu^{2+} compared to the full $S = \frac{1}{2}$ moment $gS = 1.1$ μ_B, indicating remaining spin frustration or partial order in barlowite, even at 1.5 K. In clinoatacamite, the coexistence of long-range magnetic order and dynamic magnetic moment fluctuations has been observed through muon spin relaxation measurements, again suggesting that there are parallels between these two minerals. Finally, the disparity between the moment sizes across the three Cu^{2+} sites is intriguing, and suggests that the underlying spin Hamiltonian in barlowite is complex.

Whether the structural distortion in barlowite has any relation to the magnetic structure is an intriguing open question. Whilst the temperature at which the onset of the structural distortion takes place (approximately 250 K) is far removed from T_N, it is presumably the exchange between the intra- and interlayer magnetic moments which facilitates magnetic ordering. Consequently, the position of the interlayer Cu^{2+} in relation to the kagomé layers is an important driving force for this interaction. How this may be tuned chemically through halide substitution in the interplane sites is explored in the next section.

3.4 Exploring the Effects of Halide Substitution

The unusual structural distortion in barlowite and the relation that this may have to its magnetic structure was motivation to explore further ways that the structure-property behaviour in barlowite could be systematically tuned. Inspection of the crystal structure of barlowite yields one possible route, which is to apply chemical pressure through the substitution of the halide ions which occupy positions between the kagomé layers, as depicted in Figure 3.7. In the room temperature $P6_3/mmc$ structure of barlowite, bromide ions sit on a $2c$ Wyckoff position and are covalently bound to three Cu^{2+} above and three Cu^{2+} below, completing the octahedral coordination of the Cu1 sites. Meanwhile, the fluoride ions are hydrogen bonded to six surrounding hydroxide anions in a $2b$ position. Given the large void which the bromide ion occupies, along with the likely significance of the high electronegativity of the fluoride anion in the $2b$ position, substitution at the $2c$ site is the natural choice. In addition, the chloride analogue of barlowite (FBr), $Cu_4(OH)_6FCl$, is already a known mineral named claringbullite (FCl) [20, 164]. Meanwhile, the iodide analogue, $Cu_4(OH)_6FI$ (FI), is not found in nature and this is the first report of this material.

3.4.1 The Room Temperature Structures of the Halide Analogues and Presence of Multiple Phases

High-resolution NPD and PXRD data were collected for the series of halide analogues, $Cu_4(OD)_6FX$, on HRPD and I11, respectively. Initial analysis of the data collected at room temperature suggested that each analogue could be indexed to the hexagonal $P6_3/mmc$ space group, which was discussed in Section 3.3.1 in the context of barlowite. The unit cell is predominantly expanded along the c-axis with increasingly larger halide ions, with only a small increase in the ab-plane when going from Cl^- to I^-, as shown in Figure 3.7. This is intuitive given that the site lies between the kagomé layers which are stacked along c. However, Rietveld refinement of this model to data collected for FI reveals a particularly poor fit, especially to systematic $hk4n$ Bragg peaks. An example of this is shown in the inset of Figure 3.8 for the (004) and (104) peaks of I11 and HRPD Bank 1 data, respectively. Close inspection of this subset of peaks across both datasets reveals an asymmetric peak profile which tails towards high Q, as presented in Figure 3.9.

An asymmetric peak profile of this kind is commonly observed in the powder

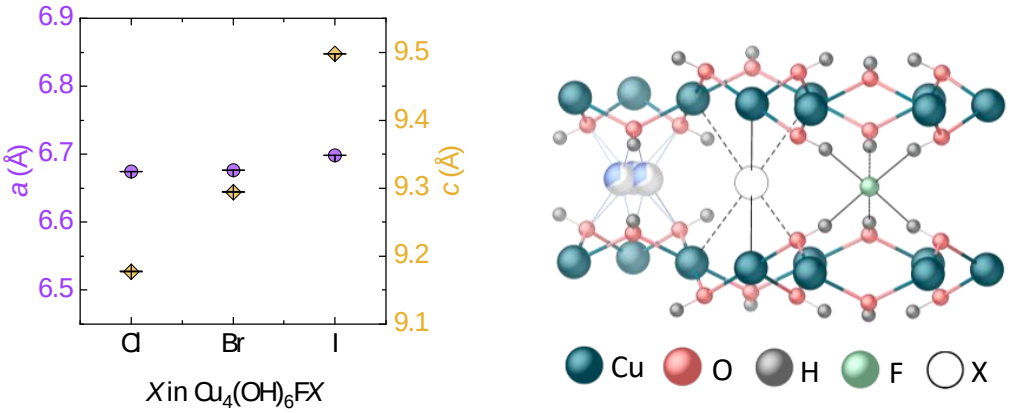

Figure 3.7: The refined room-temperature lattice parameters of the $P6_3/mmc$ model of the $Cu_4(OD)_6FX$ series (left) as a functon of halide site, X, which sits in a $2c$ position between the kagomé layers. The scales of the a- and c-axes have been adjusted to be equal to emphasise the increase in the c-axis across the series. Also between the layers is a disordered copper site and a fluoride site that sits in a $2b$ position in a hydrogen-rich pocket (right).

diffraction data of layered materials which contain stacking faults, where there are irregularities in the stacking sequence of crystal planes which can result in a deviation from the ideal crystal structure, resulting in asymmetric peak broadening and average peak position shifts [84]. In this case, it is proposed that the tail to high Q observed in the data is indicative of a distribution of c-axis parameters, likely driven by deviations from the 1:1 ratio of F^- and I^- anions in the sample composition. To test this, a Rietveld corefinement against I11 and HRPD data at 300 K was conducted using multiple $P6_3/mmc$ phases with differing c-parameters [168]. Several measures were taken to constrain these multiphase refinements. Firstly, the a- and b-axis parameters were fixed to be equal across the phases, so that only the c-axis was allowed to vary. The atom positions and isotropic atomic displacement parameters, U_{iso}, were additionally constrained across phases, along with profile parameters. Additional F^- and I^- sites were added to each model and their occupancies allowed to refine independently for each phase, whilst being constrained so that each site remains fully occupied. A total of four phases could be modelled sensibly using this method, and the refined structural model is given in Table 3.4. The refined phase fractions and F/I occupancies are also given in Table 3.4, and indicate that there are a range of fluoride-rich phases in the measured sample where some F^- occupies the I^- ($2c$) site. Figure 3.9 reveals

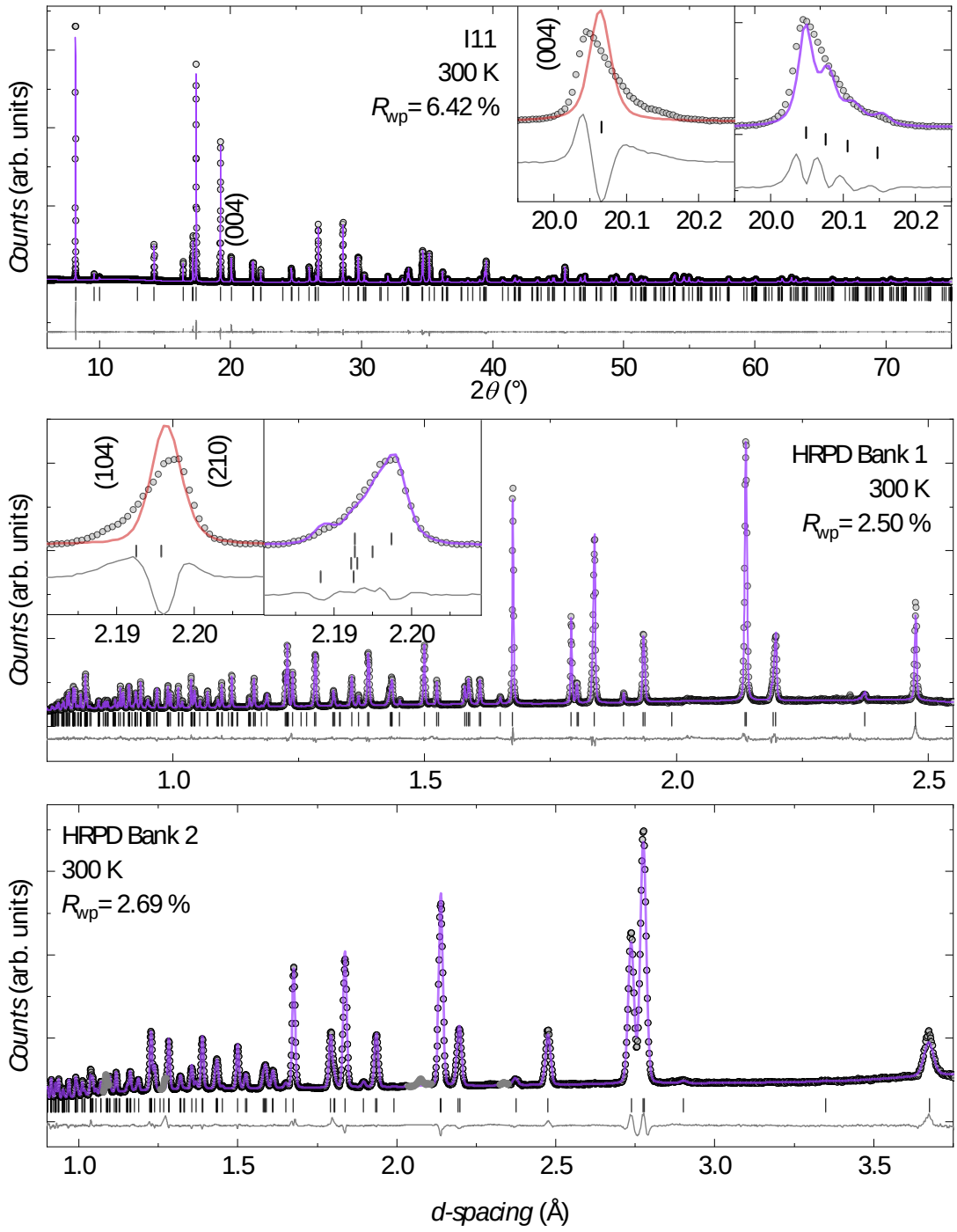

Figure 3.8: Rietveld refinement of four $P6_3/mmc$ models to powder diffraction data collected at 300 K on I11 (top) and HRPD Banks 1 and 2 (middle and bottom) for $Cu_4(OD)_6FI$. Only reflections for the first phase have been included in the main figures. The insets show the most prominent asymmetric peaks in the data with a comparison of single phase and multiphase models. In HRPD Bank 2, the grey regions in the collected data are from steel in the sample environment and were excluded from the refinement.

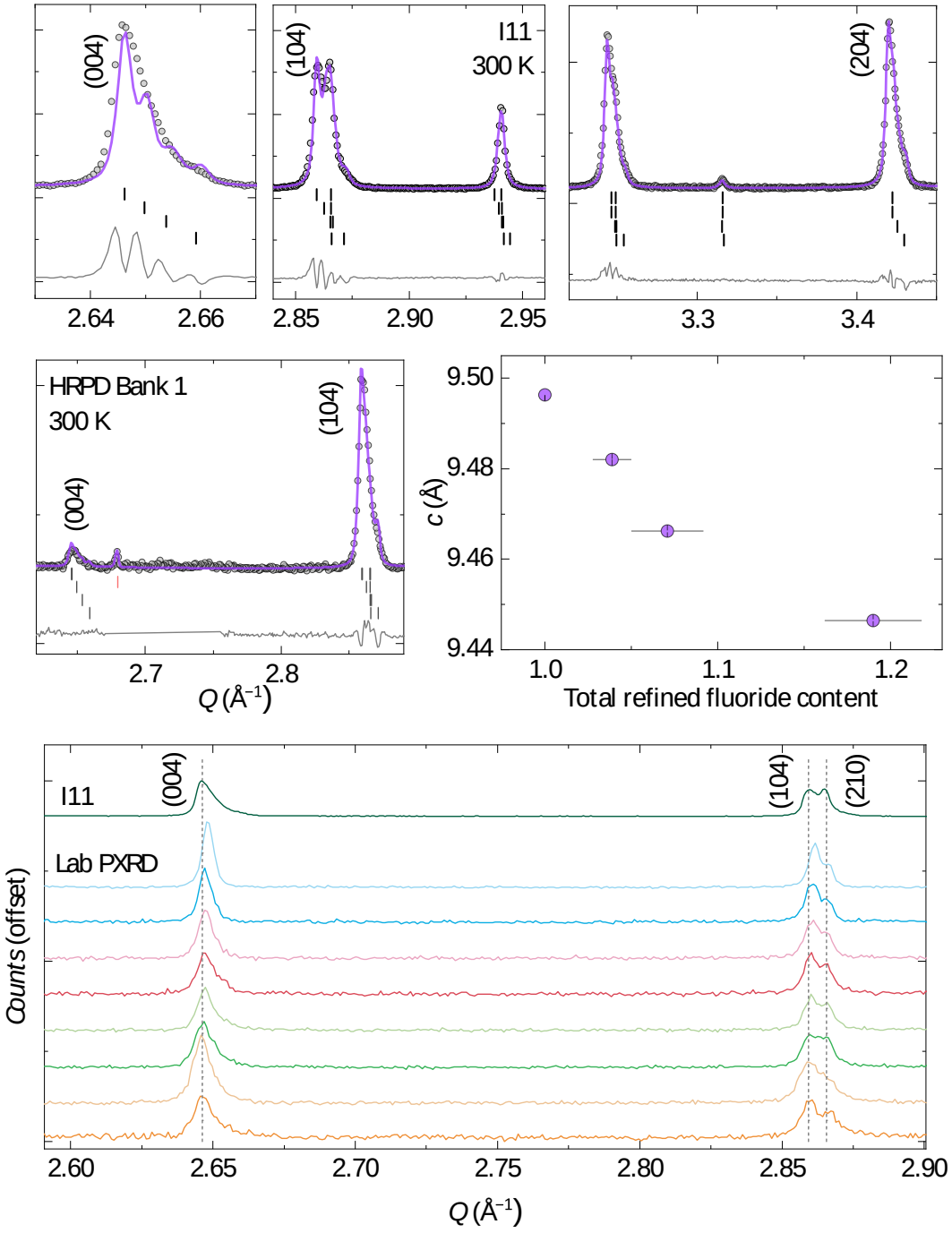

Figure 3.9: Asymmetric peak profiles in PXRD data collected for $Cu_4(OD)_6FI$ at 300 K on I11 (top) and HRPD (middle), with a Rietveld refinement using four *Pnma* phases shown by the solid line, and reflections for each phase shown by black tick marks. The red tick mark represents a vanadium peak from the sample environment. The *c*-axis parameter for each of the four phases is also shown as a function of the total refined fluoride content. The lower panel shows laboratory PXRD data, vertically offset for clarity, for samples synthesised with increasingly more NH_4F in the reaction mixture from bottom to top.

Table 3.4: Structural parameters obtained from the combined Rietveld refinement of the $P6_3/mmc$ model of $Cu_4(OH)_6FI$ fitted to NPD and PXRD data collected on HRPD and I11 at 300 K. The bottom table shows the phase fractions, c-cell parameters and halide occupancies for each of the four refined $P6_3/mmc$ phases. The final statistical parameters are $R_{wp} = 3.40\%$ and $\chi^2 = 5.916$.

Atom	Site	x	y	z	Occupancy	U_{iso} (Å^2)
Cu1	6g	0.5	0	0	1	0.0099(1)
Cu2	6h	0.6304(1)	0.2609(2)	0.25	$\frac{1}{3}$	0.0086(4)
O1	12k	0.20321(7)	0.79679(7)	0.90863(7)	1	0.0095(2)
D1	12k	0.12548(7)	0.87452(7)	0.86814(8)	1	0.0247(2)
F1	2b	0	0	0.75	1	0.0174(4)
I1	2b	0	0	0.75	0	0.0174(4)
F2	2c	0.6667	0.3333	0.75	*	0.0129(1)
I2	2c	0.6667	0.3333	0.75	*	0.0129(1)

	Phase number			
*	1	2	3	4
Phase fraction (%)	46.3(1)	27.2(2)	16.1(2)	10.4(2)
c (Å)	9.49742(4)	9.48472(9)	9.4706(2)	9.4511(1)
F2 occupancy	0	0.04(1)	0.08(2)	0.19(3)
I2 occupancy	1	0.96(1)	0.92(2)	0.82(3)

that the c-axis systematically decreases with increasing total F^- content. To further test the feasibility of this model, additional samples were synthesised using increasingly larger amounts of the fluoride-containing starting material, NH_4F, in the reaction vessel. Inspection of the (004) Bragg peak in laboratory PXRD data, shown in the lower panel of Figure 3.9, reveals a shift in its maximum towards higher Q with increasingly more fluoride in the initial reaction mixture. This is further evidence that it is possible to vary the F:I ratio in this material. However, the presence of Cu(OH)F impurity in some of these samples, along with the difficulty in measuring halides using an elemental analysis method such as ICP-OES, makes quantifying the composition within these systems challenging. Whilst this analytical approach is not necessarily proof of the presence of four distinct phases within the FI sample, this process instead offers an approximation for a phase continuum. Furthermore, it is not clear whether the variation in the lattice spacings is due to a chemical gradient within individual crystallites—which could be considered a type of stacking fault—or a compositional variance between different crystallites.

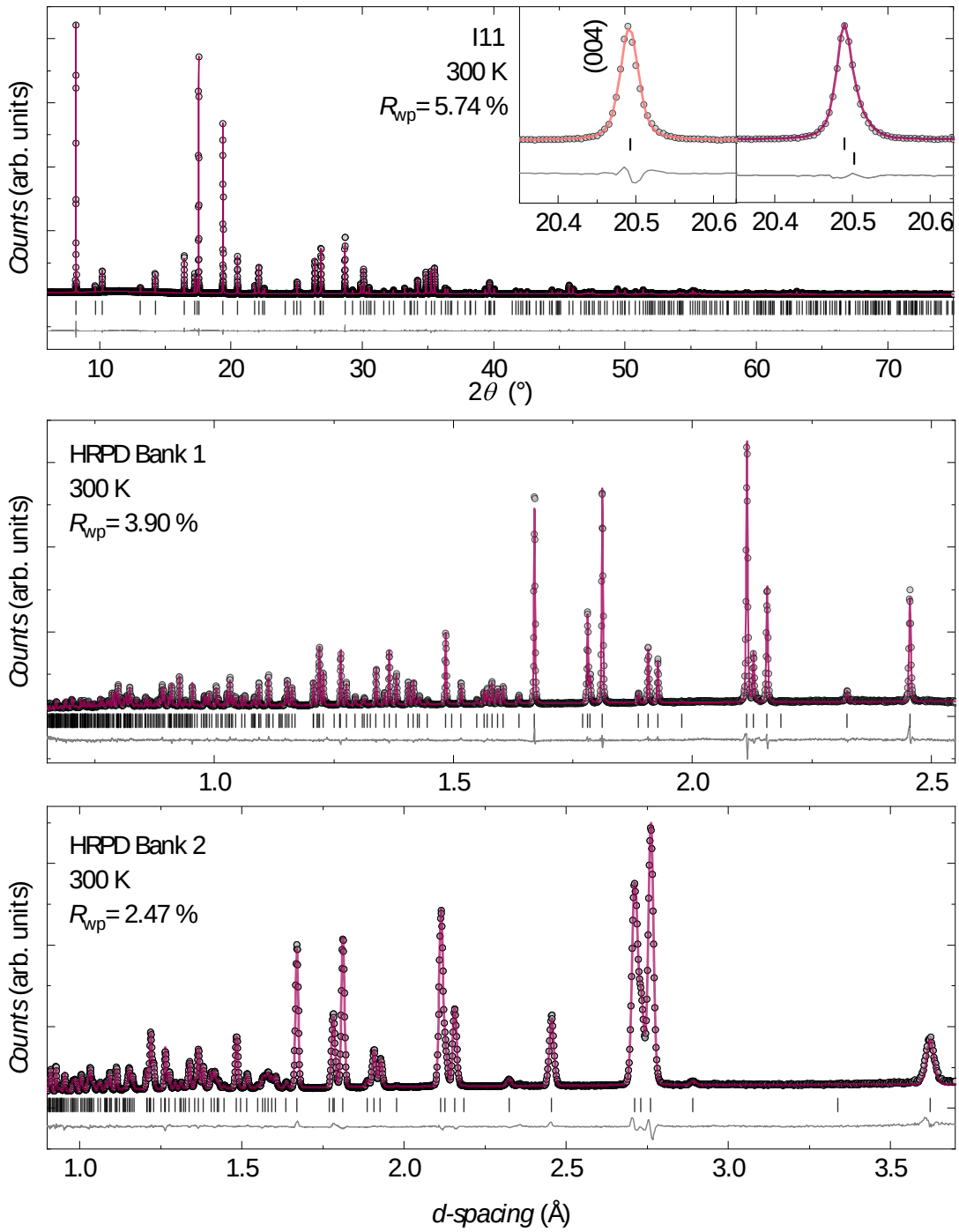

Figure 3.10: Combined Rietveld refinement of two $P6_3/mmc$ models to powder diffraction data collected at 300 K on I11 (top) and HRPD Banks 1 and 2 (middle and bottom) for $Cu_4(OD)_6FBr$. For clarity, only reflections for the first phase have been included in the main figures. The insets show the (004) and (104) peaks with a comparison using single phase and multiphase models.

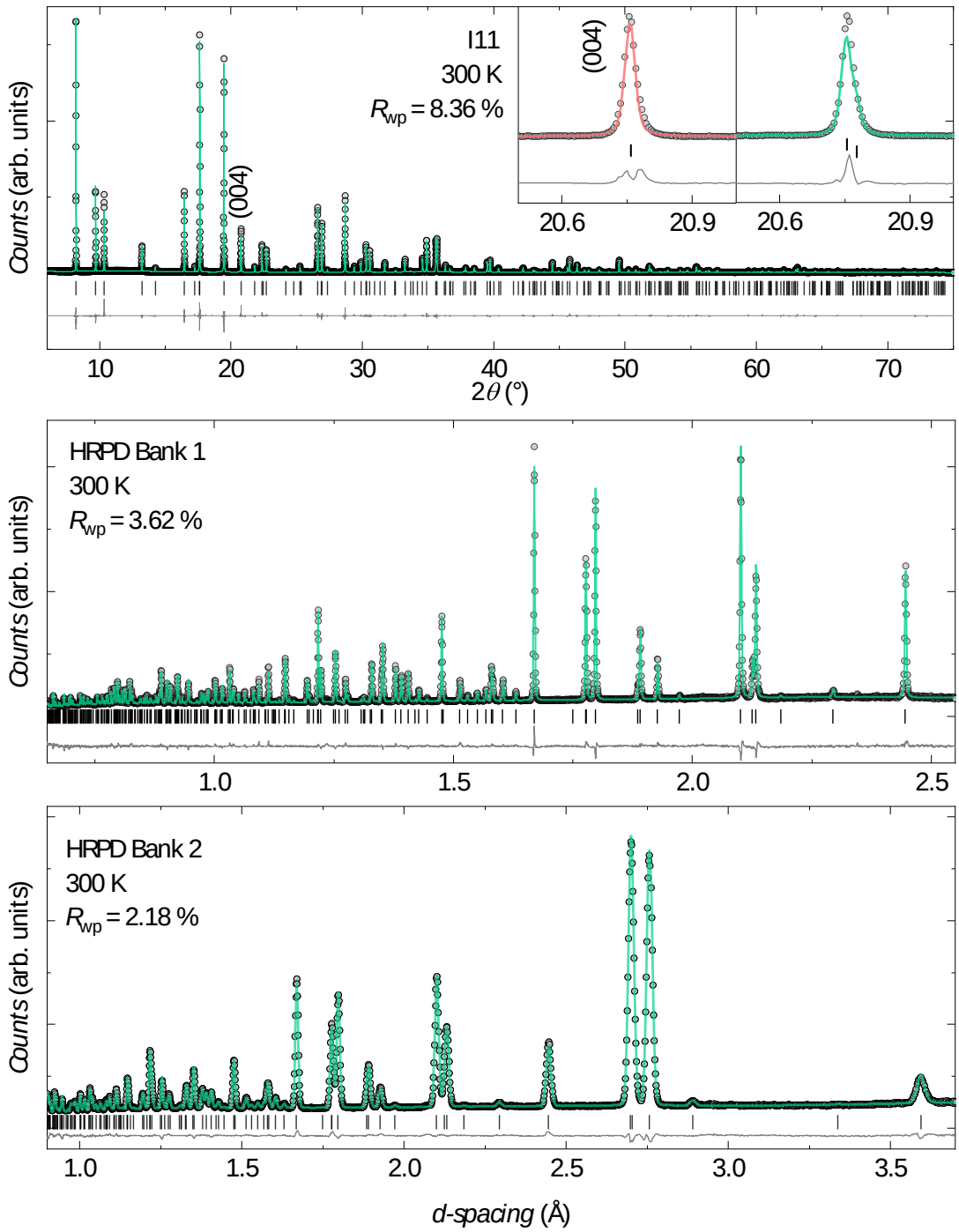

Figure 3.11: Combined Rietveld refinement of two $P6_3/mmc$ models to powder diffraction data collected at 300 K on I11 (top) and HRPD Banks 1 and 2 (middle and bottom) for $Cu_4(OD)_6FCl$. For clarity, only reflections for the first phase have been included in the main figures. The insets show the (004) and (104) peaks with a comparison using single phase and multiphase models.

Table 3.5: Structural parameters obtained from the combined Rietveld refinement of two $P6_3/mmc$ models of $Cu_4(OH)_6FBr$ fitted to NPD and PXRD data collected on HRPD and I11, respectively, at 300 K. Two phases were modelled with refined lattice parameters of $a = 6.676248(8)$ Å and $c = 9.29489(3)$ Å (68.1(5)% wt. frac.) and $c = 9.28944(9)$ Å (32(1)% wt. frac.). Overall $R_{wp} = 3.54\%$.

Atom	Site	x	y	z	Occupancy	U_{iso} (Å^2)
Cu1	6g	0.5	0	0	1	0.0107(1)
Cu2	6h	0.62971(7)	0.2594(1)	0.25	$\frac{1}{3}$	0.0057(3)
O1	12k	0.20243(4)	0.79757(4)	0.90881(4)	1	0.0103(1)
D1	12k	0.12490(4)	0.87511(4)	0.86642(4)	1	0.0262(1)
F1	2b	0	0	0.75	*	0.0218(3)
Br2	2c	0.6667	0.3333	0.75	*	0.0155(2)

	Phase number	
*	1	2
Phase fraction (%)	68.1(5)	32(1)
c (Å)	9.29489(3)	9.28944(9)
F1 occupancy	0.978(2)	1
Br1 occupancy	0.022(2)	0
F2 occupancy	0.040(8)	0.05(2)
Br2 occupancy	0.960(8)	0.95(2)

The discovery of multiple phases in the FI analogue within this family led to the question of whether the same might occur FBr and FCl, in that multiple phases with varying compositions may be present. As such, corefinements of the I11 and HRPD data collected at 300 K for each of these samples were conducted using multiple $P6_3/mmc$ phases, again constraining the model so that only the c-axis and F/X ratios were allowed to vary across the phases. The Rietveld refinements of two $P6_3/mmc$ phases are shown in Figures 3.10 and 3.11 for FBr and FCl, respectively. The (004) peaks are shown in the insets, and do present a subtle asymmetry. In addition, the inclusion of a second phase does significantly improve the R_{wp} values, going from 4.05% and 4.21% to 3.54% and 3.63% for refinements to FBr and FCl datasets, respectively. Refinement of F/Br and F/Cl occupancies was possible, with the former refinement suggesting that a small amount ($\sim 5\%$) of fluoride occupies the bromide site, and that a slight excess of fluoride is present in the phase with a smaller c-axis. In the latter, the converse is suggested, with $\sim 7\%$ chloride anions occupying the fluoride (2b) position. However, the difference between the two phases in both FBr and FCl refinements is subtle and, given the large number of refineable parameters in these fits, it is difficult to make any

Table 3.6: Structural parameters obtained from the combined Rietveld refinement of two $P6_3/mmc$ models of $Cu_4(OH)_6FCl$ fitted to NPD and PXRD data collected on HRPD and I11, respectively, at 300 K. Two phases were modelled with refined lattice parameters of $a = 6.676248(8)$ Å and $c = 9.29489(3)$ Å (68.1(5)% wt. frac.) and $c = 9.28944(9)$ Å (32(1)% wt. frac.). Overall $R_{wp} = 3.54\%$.

Atom	Site	x	y	z	Occupancy	U_{iso} (Å^2)
Cu1	6g	0.5	0	0	1	0.0127(1)
Cu2	6h	0.62850(7)	0.2570(1)	0.25	$\frac{1}{3}$	0.0051(2)
O1	12k	0.20183(4)	0.79817(4)	0.90941(4)	1	0.0100(1)
D1	12k	0.12464(5)	0.87536(5)	0.86670(5)	1	0.0253(1)
F1	2b	0	0	0.75	*	0.0240(4)
Cl2	2c	0.6667	0.3333	0.75	*	0.0225(2)

	Phase number	
*	1	2
Phase fraction (%)	75.3(3)	25(1)
c (Å)	9.17753(4)	9.1677(1)
F1 occupancy	0.929(7)	1
Cl1 occupancy	0.071(7)	0
F2 occupancy	0	0
Cl2 occupancy	1	1

firm conclusions on the halide mixing from these data alone, particularly due to the smaller X-ray scattering contrasts between F/Br and F/Cl pairs than for F/I. Note that including more than two phases led to an unstable refinement in both cases, and thus was deemed unnecessary. The full structural models for FBr and FCl are given in Tables 3.5 and 3.6, respectively. A comparison of selected refined bond lengths and angles across the series at 300 K is given in Table 3.7.

This is, in fact, not the first time that the identity and distribution of the anions in FCl have been called into question. In the original mineralogical study of claringbullite, the formula was reported to be $Cu_4(OH)_7Cl \cdot nH_2O$ [164]. This was subsequently revised to $Cu_4(OH)_6Cl[Cl_{0.29}(OH)_{0.71}]$, meaning that the 2$b$ site was thought to be occupied by a combination of Cl^- and OH^- anions rather than F^- [20], and it was additionally suggested that a solid solution could exist as $Cu_4(OH)_{6+x}Cl_{2-x}$. Following this, work published on the synthetic route to claringbullite determined that a fluoride source is necessary for its successful synthesis, and that the 2b site was solely occupied by F^- based on refinement R-factors [169]. Finally, a recent crystallographic study on mineral samples of claringbullite de-

Table 3.7: Key bond lengths extracted from corefinements against powder diffraction data collected for the $Cu_4(OD)_6FX$ series at room temperature.

	FCl	FBr	FI
	Bond length (Å)		
Cu1–Cu1	3.33723	3.33808	3.34943
Cu1–Cu2	2.7338(5)	2.7686(5)	2.8160(7)
Cu2–Cu2	5.468(1)	5.5372(9)	5.632(1)
Cu1–X	2.99609	3.01886	3.06221
Cu2–X	3.4132(9)	3.4325(9)	3.448(1)
F1–D2	1.7954(5)	1.8056(4)	1.8389(7)
	Bond angle (°)		
Cu1–O–Cu1	118.06(2)	117.63(2)	117.27(4)
Cu1–O–Cu2	87.85(3)	88.91(3)	89.97(4)

termined a Cl:F:OH ratio of 0.98:1.12:5.90 [170]. It is, therefore, not out of the question that there exists a compositional range with a formula $Cu_4(OH)_xF_yCl_z$, where $x+y+z=8$, which may be highly sensitive to synthetic conditions. On the other hand, the first study of the mineral barlowite found the 2*c* and 2*b* sites to be essentially fully occupied by Br^- and F^-, respectively [70]. Halide site selectivity in these systems is likely influenced by both anionic radius and electronegativity. Whilst the comparably large radius and low electronegativity of the bromide anion mean that it is unlikely to occupy the small hydrogen-rich pocket within which the fluoride anions lie, it is plausible that excess fluoride could occupy the large space occupied by the bromide anions in the widely accepted barlowite structure. Meanwhile, in the FI analogue the pronounced variation in the *c*-axis is clear in PXRD data, which is perhaps aided by the disparity between the ionic radii of the F^- and I^- halides which will cause a more pronounced variation in the *c*-axis than in the FBr and and FCl counterparts. Furthermore, the formation of a stoichiometric phase may be energetically unfavourable due to this contrast in ionic radii. Another intriguing observation arises through bond valence analysis of the determined crystal structures across the series. Whilst the bond valences of the Cu^{2+} sites are close to ideal, the halide site X in each analogue is significantly underbonded—with values of 0.41(5) *vu* (valence units), 0.37(3) *vu* and 0.52(5) *vu* determined for Cl^-, Br^- and I^- sites, respectively [171]—indicating that this site is particularly unstable.

3.4.2 Hexagonal to Orthorhombic Structural Distortion

Upon cooling, diffraction data collected on I11 across the $Cu_4(OH)_6FX$ series reveal the development of additional Bragg peaks at approximately 266 K, 220 K and 274 K for FCl, FBr and FI, respectively, which can be indexed to the orthorhombic *Pnma* space group of the low-temperature structure determined for FBr. The distortion to orthorhombic symmetry is driven by displacement of Cu^{2+} ions, as described for FBr in Section 3.3.1, and so the use of X-rays, along with the high resolution of the I11 diffractometer, has enabled the observation of multiple additional peaks which could not be resolved with the GEM data collected previously on FBr. The development of the orthorhombic peaks is presented in Figure 3.12, along with the temperature dependence of the intensity of the most prominent (102) peak. This was extracted by fitting a pseudo-Voigt function to the peak at each temperature for each material, and the fitted height was then taken as a proportion of the most intense (110) peak in the diffraction pattern collected at 90 K for each respective analogue. This analysis suggests that the structural transition occurs over a wide range of temperatures, particularly for FCl and FBr, where the (102) peak intensity does not appear to have plateaued even at 90 K, the lowest temperature of the I11 datasets. For FBr, the peak intensity is so weak that the MAC detector, which requires longer counting times, was necessary to resolve the orthorhombic distortion peaks clearly. This suggests that there is not a straightforward relationship between the halide identity and the temperature at which the structural distortion begins to occur, although it is evident that the substitution at the 2*c* (or 2*b*) site has a significant effect on the nature of the structural transition. A previous study has suggested that the temperature at which the hexagonal to orthorhombic transition begins to occur is related to anisotropic strain, whereby a larger halide at the 2*c* site expands the lattice along the *c*-axis (*b*-axis of the *Pnma* cell), but is constrained by the kagomé lattice to expand along the other cell directions. This supposedly drives the structural transition to higher temperatures in FBr compared to FCl. This conclusion was also supported by PES calculations, discussed in section 3.3.1, which suggest a lower energy barrier for the ordering of the interlayer copper site in FBr compared to FCl [161]. However, in this case it is clear that the opposite is true, indicating that there is a more complex explanation for these observations, perhaps related to synthetic route and/or sample composition.

At 90 K, initial structural refinements to I11 data were completed using a single *Pnma* phase. However, the resulting fit for FCl appeared to place the orthorhom-

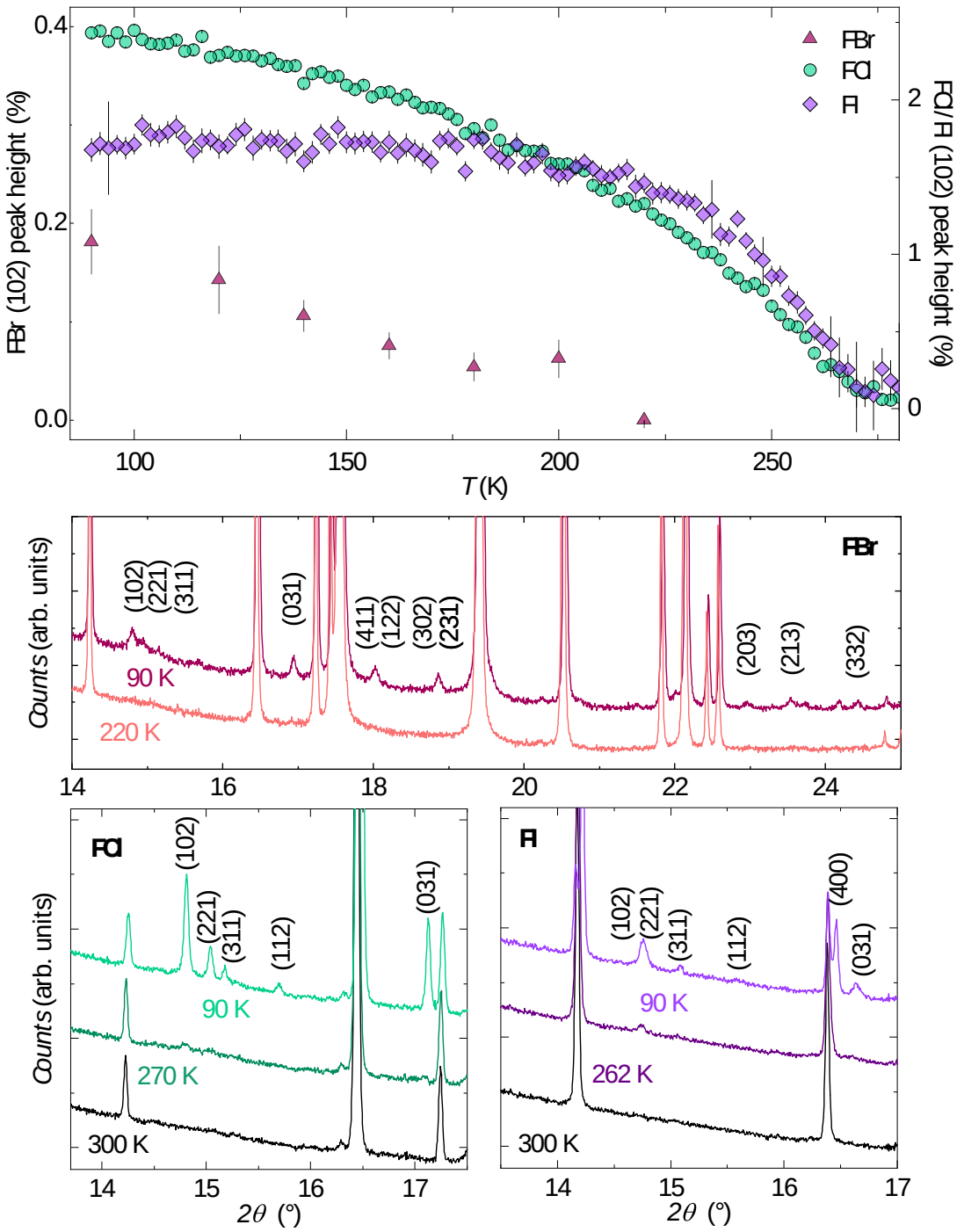

Figure 3.12: The temperature dependence of the intensity (top) of the orthorhombic peaks observed in PSD data collected on I11 for the $Cu_4(OD)_6FX$ series (lower panels). The peak intensities are plotted as a percentage of the most intense (110) Bragg peak at low temperature.

bic peaks, particularly the (102) peak, at slightly higher Q than where they appear in the data, as shown in the lower panel of Figure 3.13(a). The presence of any other orthorhombic phase, such as those tested in Section 3.3.1, also does not account properly for the peak positions. As such, an additional Rietveld refinement was employed with a $P6_3/mmc$ phase as well as a $Pnma$ phase. All structural parameters and profile parameters were allowed to refine independently, but the U_{iso} values were constrained across like-atoms and across phases to simplify the procedure. A significantly better fit is achieved using this approach ($R_{\text{wp}} = 13.57\%$ vs 8.13%), and yields refined $Pnma$ and $P6_3/mmc$ weight fractions of 63.7(2)% and 36.3(3)%, respectively. Moreover, the orthorhombic peak positions are better accounted for using a two-phase refinement, as shown in the middle panel of Figure 3.13(a). Further data were collected for FCl on HRPD at 1.5 K, where the position and intensity of the orthorhombic peaks seen in data collected in Bank 2 are also better described by using both a hexagonal and an orthorhombic model, as presented in Figure 3.13(b). Further evidence that supports this two-phase approach can be found by inspection of the (220) Bragg peak of the hexagonal structure; this peak should split directly into (004) and (602) peaks in the orthorhombic structure, but refinement to HRPD Bank 1 data at 1.5 K indicates that this region is better described by a combination of three Bragg peaks, as shown in Figure 3.13(c).

In the analysis of I11 and HRPD data collected for FBr at 90 K and 1.5 K, respectively, a similar two-phase refinement also leads to a better fit overall ($R_{\text{wp}} = 9.67\%$ vs 6.63%) and $Pnma$ and $P6_3/mmc$ weight fractions of 58.3(2)% and 41.7(2)%, respectively. In particular, whilst the lower two panels of Figure 3.14(a) show that the orthorhombic peak positions and intensities are only marginally improved by a two-phase Rietveld refinement, there is a significant improvement in the fit to the data in the region of the (004) and (602) peaks, and this is presented in Figure 3.14(c).

Conversely, at 90 K and 1.5 K the data collected for FI show two distinct orthorhombic (004) and (602) Bragg peaks, implying that the sample is fully orthorhombic at both temperatures. This rationalises the plateau in the orthorhombic peak heights presented in Figure 3.12. However, there is an intermediate range of temperatures between 250 – 260 K where there appears to be a third peak in this region, as shown in Figure 3.15(c). This is further evidence for multiple phases in the FI sample, and corroborates the multiphase fitting procedure employed at

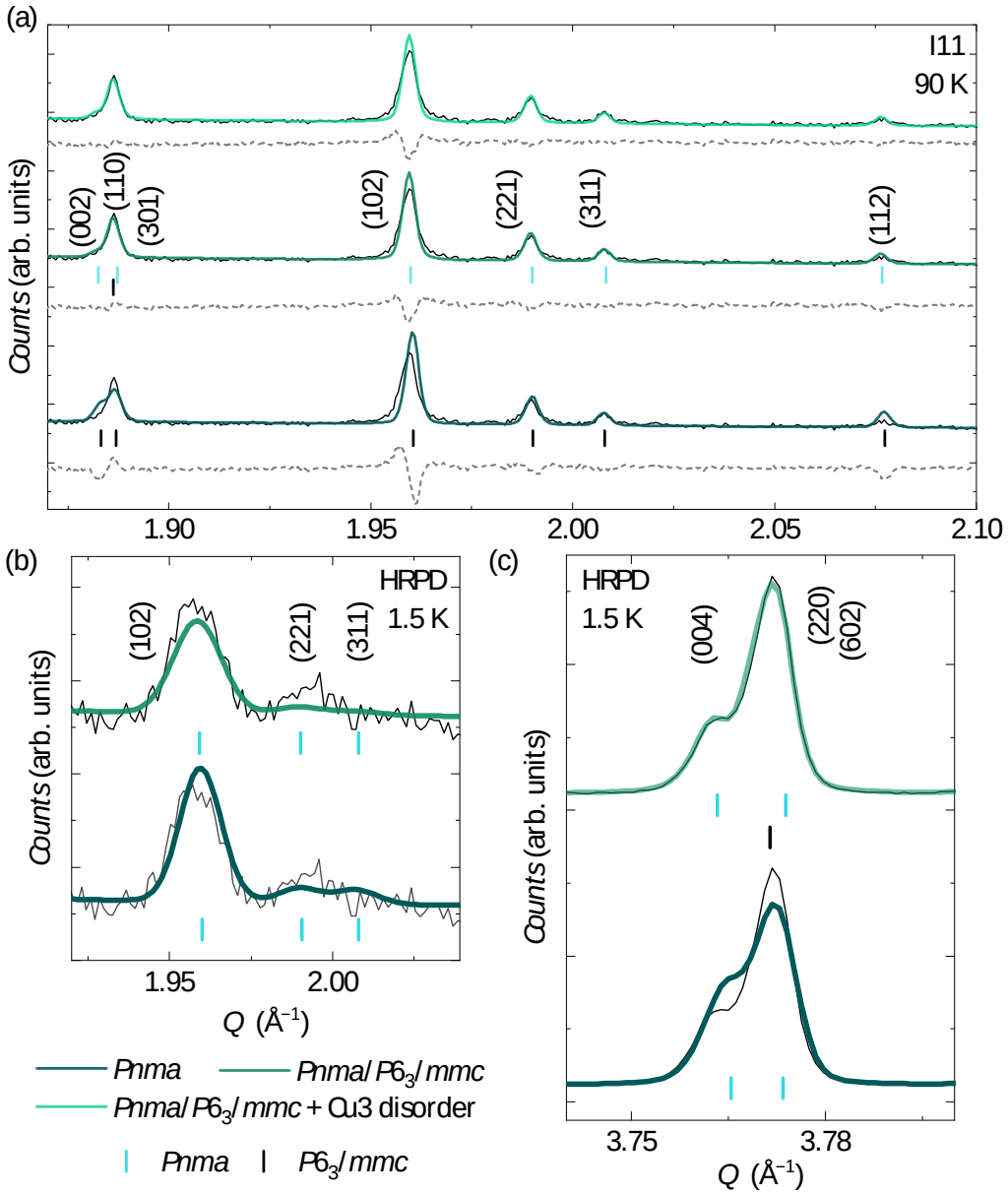

Figure 3.13: The process by which a model was determined to describe the low-temperature orthorhombic Bragg peaks observed in (a) I11 data, (b) HRPD Bank 2 and (c) HRPD Bank 1 data for $Cu_4(OD)_6FCl$. Collected data is shown by black solid lines, and the difference is shown by grey dashed lines. A model incorporating both a $P6_3/mmc$ and a $Pnma$ model is sufficient to describe the data.

room temperature. The same asymmetric peaks observed at 300 K—now $h4nl$ in the orthorhombic notation—are clearly retained at all temperatures, as shown in the insets of Figure 3.19. These data can thus be modelled using four orthorhombic phases with their fluoride and iodide contents fixed to the determined values from 300 K, with correspondingly smaller refined b-axis parameters. In addition,

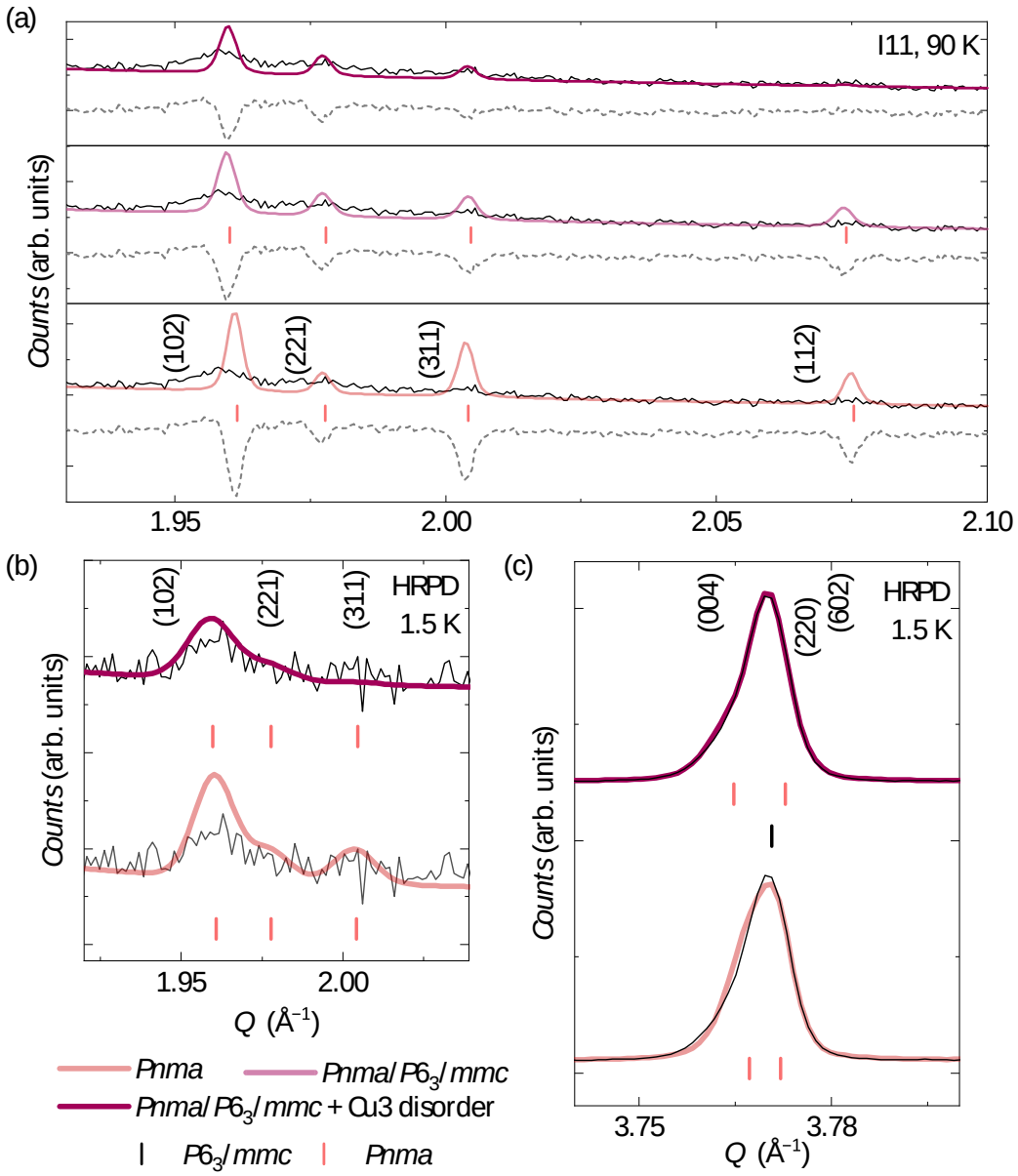

Figure 3.14: The process by which a model was determined to describe the low-temperature orthorhombic Bragg peaks observed in (a) I11 data, (b) HRPD Bank 2 and (c) HRPD Bank 3 data for $Cu_4(OD)_6FBr$. Collected data is shown by black solid lines, and the difference is shown by grey dashed lines. A final model incorporating both a $P6_3/mmc$ and a $Pnma$ model with interlayer copper disorder is shown in the uppermost fit in each panel.

this multiphase approach accounts for the orthorhombic peaks more effectively than a single phase, as shown in the lower two panels of Figure 3.15(a).

It is important to note that at no point in the temperature range measured was it beneficial to use the $Cmcm$ or $P6_3/m$ structures to model data collected for

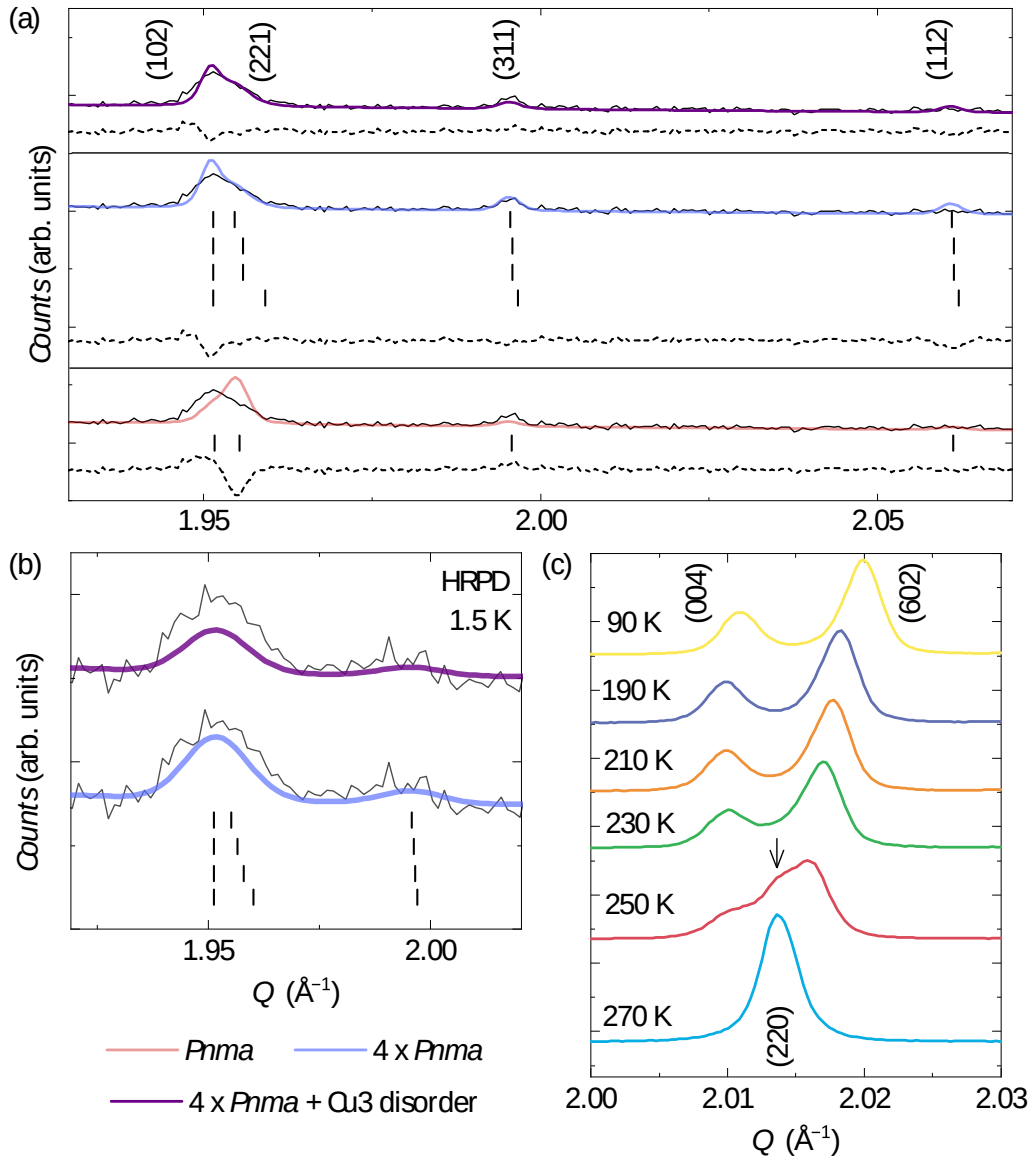

Figure 3.15: The process by which a model was determined to describe the low-temperature orthorhombic Bragg peaks observed in (a) I11 data and (b) HRPD data for $Cu_4(OD)_6FI$. Collected data is shown by black solid lines, and the difference is shown by black dashed lines. A final model incorporating four *Pnma* models with interlayer copper disorder is shown in the uppermost fit in each panel. In (c), the evolution of the (004) and (602) Bragg peaks with decreasing temperature is shown.

any of the $Cu_4(OH)_6FX$ series members, suggesting that there appears to be no significant temperature region in which either of these phases are stable. Instead, it appears that each analogue undergoes a distortion to *Pnma*, but that in FCl and FBr there is some remaining hexagonal phase at low temperatures. This suggests that within each sample there could be a range of different phases which

all undergo the transition at different temperatures, which could explain the soft onset of the transition visualised in Figure 3.12. In FI, the sample appears fully orthorhombic at low temperatures and the orthorhombic peak intensities plateau below around 200 K. In a previous study conducted on FCl, three separate single crystals were found to distort to lower symmetry at different temperatures, whilst another study on FBr also reports two-phase behaviour in polycrystalline samples [151]. However, the former study also found that the transition occurs over a broad temperature range even in single crystals of barlowite, indicating that there is an additional factor contributing to the gradual increase in the intensity of the orthorhombic peaks across this series. In the following section, this additional factor is attributed to the gradual freezing out of the interplane site disorder, which is quantified across the $Cu_4(OH)_6FX$ series through further analysis of high-resolution diffraction data.

3.4.3 Remaining Interlayer Site Disorder

Having determined that all three members of the $Cu_4(OH)FX$ series contain multiple closely related phases, it is clear that the Rietveld refinements still do not fully account for the additional orthorhombic peaks observed at low temperatures, particularly in terms of their broadness, which in turn means that the intensities are not correctly modelled. This is most evident in refinements against data collected for FBr and FI, shown in Figures 3.14(a) and 3.15(a), and indicates residual disorder in their low-temperature structures. In order to account for this disorder, two additional interlayer sites (denoted Cu4 and Cu5) were incorporated into the *Pnma* model and their positions allowed to refine whilst being constrained so that the sum of the interlayer Cu site (Cu3, Cu4, Cu5) remained equal to one. For FI, the interlayer Cu occupancies were constrained to be equal across the four orthorhombic phases. Figure 3.16 shows the interlayer copper occupancies as a function of temperature for each member of the $Cu_4(OH)_6FX$ series. This analysis shows that for all three analogues there is a preference for the interlayer copper to occupy the Cu3 site—one of the two sites which were shown through PES calculations to be energetically more favourable [161] and describe the average *Pnma* structure—but with some remaining Cu^{2+} occupying both of the additional interlayer sites. In FCl, the refined occupancy of Cu3 is 0.950(7) at 90 K and, correspondingly, incorporating this disorder does not significantly improve the Rietveld refinement to I11 data at 90 K, as shown in Figure 3.13(a). In addition, it was not possible to refine the Cu4 and Cu5 occupancies in HRPD data collected at 1.5 K, implying that at this temperature the interlayer copper is fully

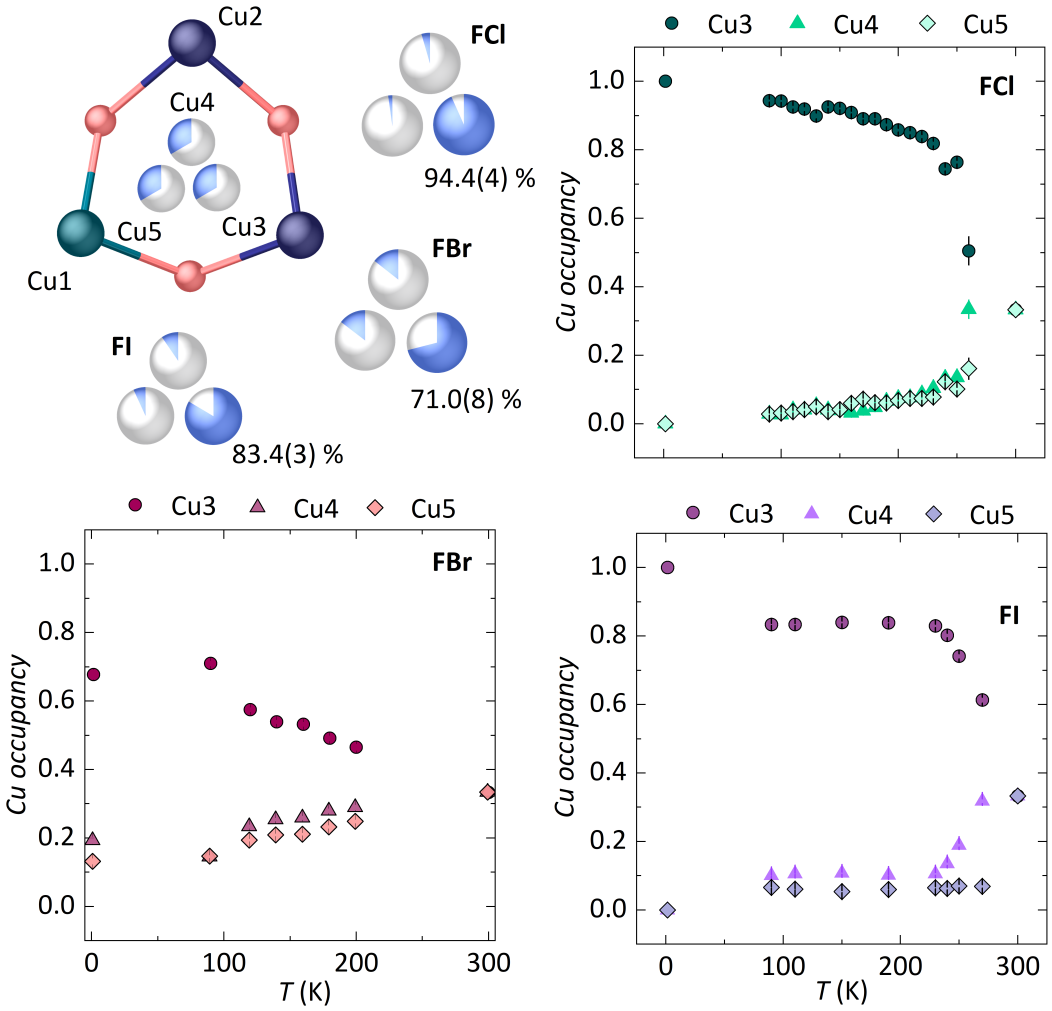

Figure 3.16: The refined interlayer copper occupancies as a function of temperature for the $Cu_4(OD)_6FX$ series, obtained from analysis of data collected on HRPD (1.5 K) and I11 (90 – 300 K). The occupancies presented in the upper left panel are those from 90 K data.

ordered onto the Cu3 site. Conversely, in FBr a model including disorder, leading to Cu4 and Cu5 occupancies of 0.144(5) and 0.146(6) at 90 K, respectively, results in a redistribution of the intensity of the orthorhombic peaks which more closely matches the collected data, as is clear in the difference profile for this refinement shown in the top panel of Figure 3.14(a). Even at 1.5 K, there appears to be some remaining interlayer disorder in FBr which contributes to the low intensity of the orthorhombic peaks in the HRPD data at this temperature, shown in Figure 3.14. Meanwhile, the interlayer copper occupancies appear to plateau in FI, in line with the temperature at which the orthorhombic peak intensities plateau, indicating that the structural transitional is indeed driven by the disorder-order at the interplane sites. In Figure 3.15(b), it can be seen that at 1.5 K refining

the interlayer copper occupancies in FI results in a decrease in the orthorhombic peak intensity to a greater extent than the observed data. This could mean that by this temperature the interlayer copper is fully ordered or, alternatively, could reflect the complexity in modelling this disorder in four phases simultaneously.

Interestingly, inspection of the orthorhombic peaks in Figures 3.13 – 3.15 reveals that there is still a mismatch between the collected data and the model, even having incorporating interlayer disorder. Across the series, the broad orthorhombic peak shapes indicate that modelling these data using the Rietveld method, which evaluates average structure, is insufficient to fully describe the copper displacement at low temperatures. The final Rietveld refinements across the series, incorporating both multiple phases and interlayer copper disorder, are shown in Figures 3.17 – 3.19, and the resulting structural models are given in Tables 3.8 – 3.11, with a summary of refined bond lengths and angles presented in Table 3.12.

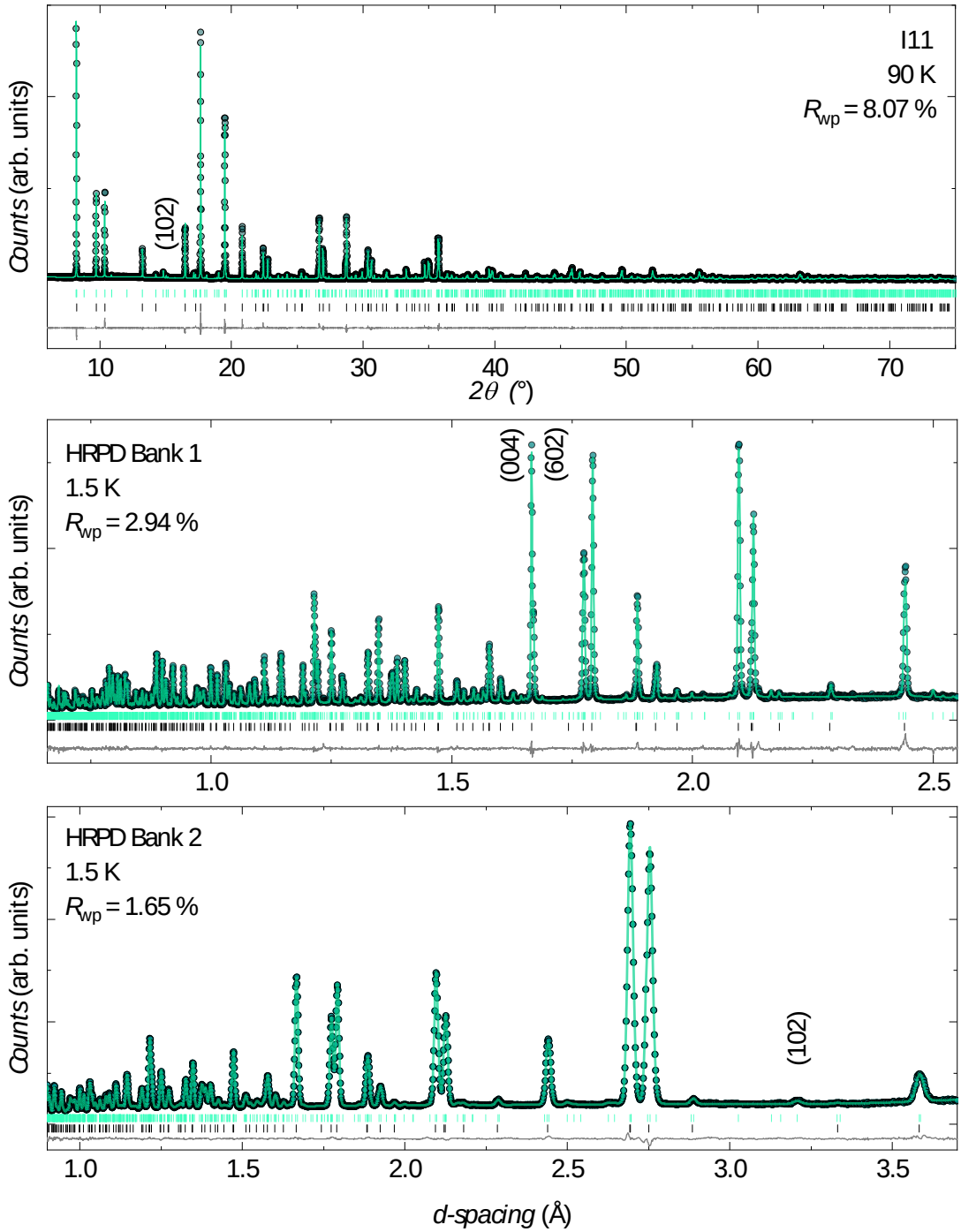

Figure 3.17: Two-phase Rietveld refinement of $Pnma$ and $P6_3/mmc$ structural models to powder diffraction data collected at 90 K on I11 (top) and 1.5 K on HRPD Banks 1 and 2 (middle and bottom) for $Cu_4(OD)_6FCl$. Reflections for $Pnma$ and $P6_3/mmc$ are represented by green and black tick marks, respectively.

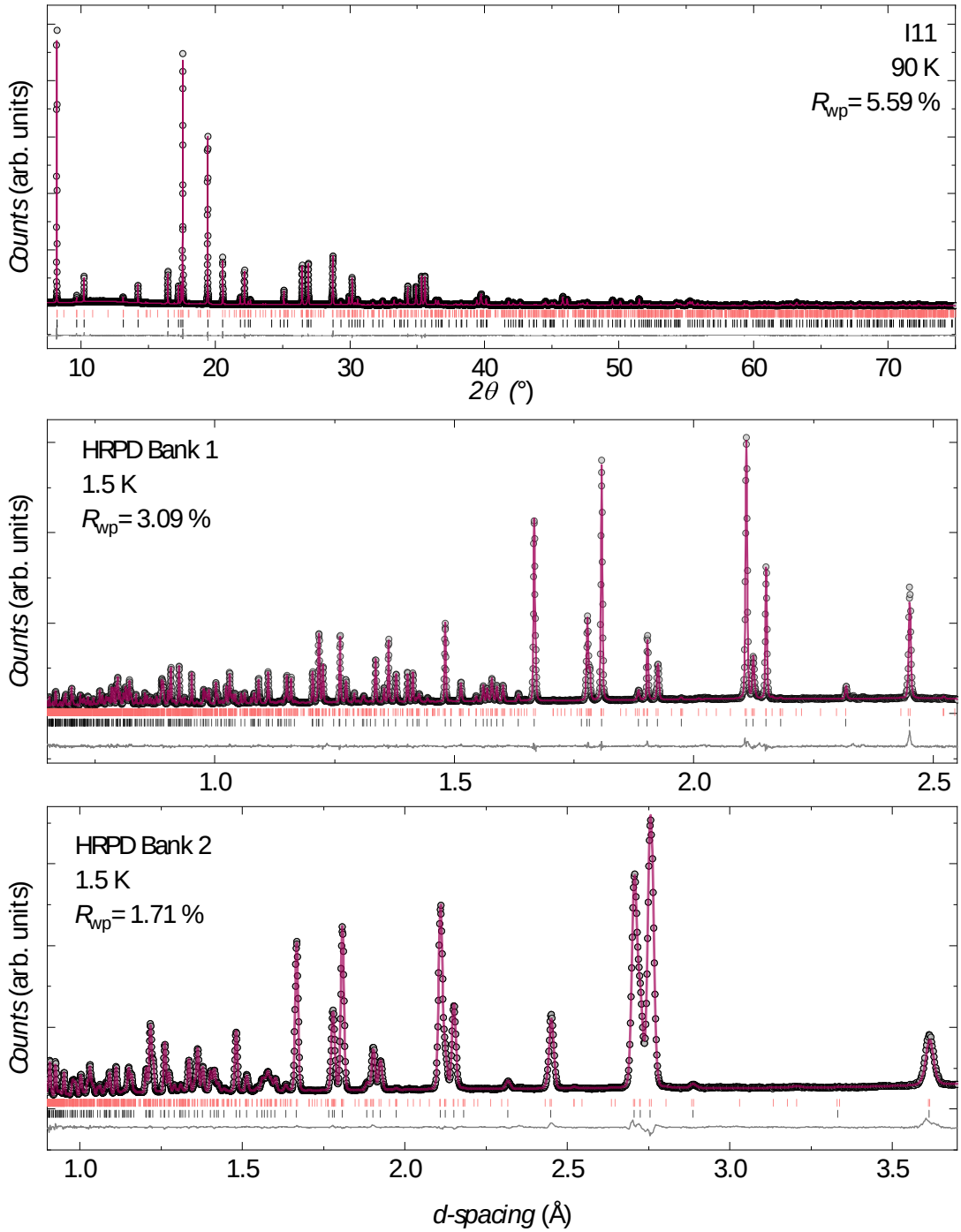

Figure 3.18: Two-phase Rietveld refinement of $Pnma$ and $P6_3/mmc$ structural models to powder diffraction data collected at 90 K on I11 (top) and 1.5 K on HRPD Banks 1 and 2 (middle and bottom) for $Cu_4(OD)_6FBr$. Reflections for $Pnma$ and $P6_3/mmc$ are represented by red and black tick marks, respectively.

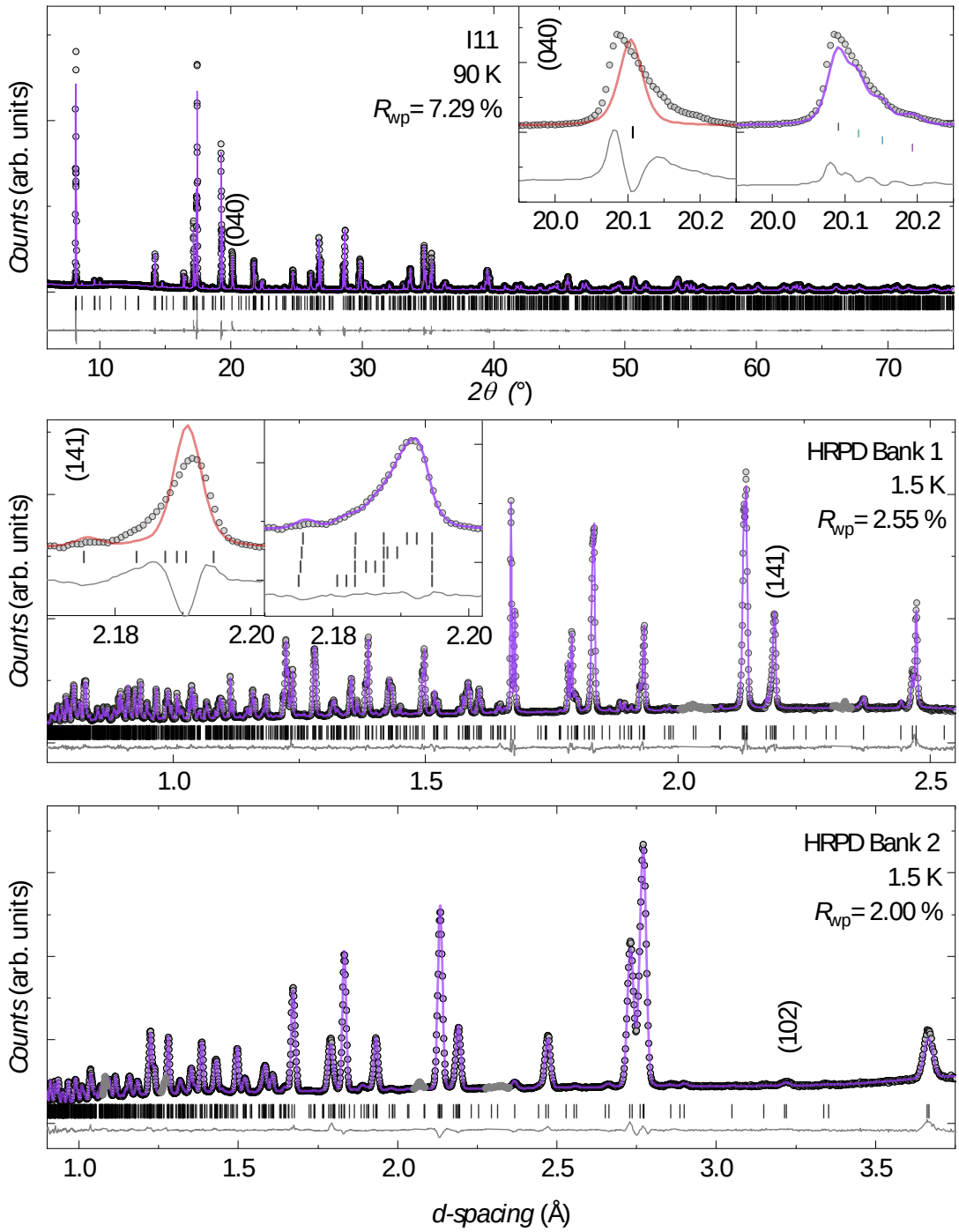

Figure 3.19: Rietveld refinement using four *Pnma* models to powder diffraction data collected at 90 K on I11 (top) and 1.5 K on HRPD Banks 1 and 2 (middle and bottom) for $Cu_4(OD)_6FI$. Only reflections for the first phase have been included in the main figures. The insets show the most prominent asymmetric peaks in the data with a comparison single phase and multiphase models. In HRPD Bank 2, the grey regions in the collected data are from steel in the sample environment and were excluded from the refinement.

Table 3.8: Rietveld refinement crystal structure parameters for the *Pnma* and $P6_3/mmc$ models of $Cu_4(OD)_6FCl$ fitted to PXRD and NPD data collected on I11 at 90 K and HRPD at 1.5 K, respectively. Refined lattice parameters and phase fractions are given in Table 3.11.

	Atom	Site	x	y	z	Occupancy	U_{iso} (Å^2)
Pnma (90 K)	Cu1	4*a*	0	0	0	1	0.00314(7)
	Cu2	8*d*	0.2508(1)	0.5140(1)	0.2450(1)	1	0.00314(7)
	Cu3	4*c*	0.1850(2)	0.25	0.0582(3)	0.950(5)	0.00314(7)
	Cu4	4*c*	0.165(5)	0.25	0.94(1)	0.033(5)	0.00314(7)
	Cu5	4*c*	0.12(1)	0.25	0	0.017(5)	0.00314(7)
	F1	4*c*	0.4928(6)	0.25	0.0054(9)	1	0.017(1)
	Cl1	4*c*	0.3302(3)	0.25	0.5109(4)	1	0.0080(5)
	O1	8*d*	0.2964(2)	0.0965(2)	0.0015(3)	1	0.0013(4)
	O2	8*d*	0.1014(2)	0.0904(2)	0.1998(4)	1	0.0013(4)
	O3	8*d*	0.4007(2)	0.5875(2)	0.3020(4)	1	0.0013(4)
$P6_3/mmc$ (90 K)	Cu1	6*g*	0.5	0	0	1	0.00314(7)
	Cu2	6*h*	0.6278(3)	0.2556(7)	0.25	$\frac{1}{3}$	0.00314(7)
	O1	12*k*	0.2027(4)	0.7973(4)	0.9095(5)	1	0.0013(4)
	F1	2*b*	0	0	0.75	1	0.017(1)
	Cl1	2*c*	0.6667	0.3333	0.75	1	0.0080(5)
Pnma (1.5 K)	Cu1	4*a*	0	0	0	1	0.0044(2)
	Cu2	8*d*	0.2488(2)	0.5173(2)	0.2429(2)	1	0.0044(2)
	Cu3	4*c*	0.1859(3)	0.25	0.0608(4)	1	0.0044(2)
	F1	4*c*	0.4987(4)	0.25	0.0086(8)	1	0.0095(3)
	Cl1	4*c*	0.3274(2)	0.25	0.5106(3)	1	0.0079(2)
	O1	8*d*	0.2963(3)	0.0952(3)	0.0008(4)	1	0.0045(2)
	O2	8*d*	0.1042(3)	0.0907(3)	0.1968(4)	1	0.0045(2)
	O3	8*d*	0.4012(3)	0.5892(3)	0.3032(4)	1	0.0045(2)
	D1	8*d*	0.3770(2)	0.1344(4)	0.0041(5)	1	0.0177(2)
	D2	8*d*	0.0619(3)	0.1282(4)	0.3162(4)	1	0.0177(2)
	D3	8*d*	0.4402(3)	0.6367(3)	0.1927(4)	1	0.0177(2)
$P6_3/mmc$ (1.5 K)	Cu1	6*g*	0.5	0	0	1	0.0044(2)
	Cu2	6*h*	0.6278(4)	0.2557(7)	0.25	$\frac{1}{3}$	0.0044(2)
	O1	12*k*	0.2006(2)	0.7994(2)	0.9103(2)	1	0.0045(2)
	D1	12*k*	0.1244(2)	0.8756(2)	0.8656(2)	1	0.0177(2)
	F1	2*b*	0	0	0.75	1	0.0095(3)
	Cl1	2*c*	0.6667	0.3333	0.75	1	0.0079(2)

Table 3.9: Rietveld refinement crystal structure parameters for the *Pnma* and $P6_3/mmc$ models of $Cu_4(OD)_6FBr$ fitted to PXRD and NPD data collected on I11 at 90 K and HRPD at 1.5 K, respectively. Refined lattice parameters and phase fractions are given in Table 3.11.

	Atom	Site	x	y	z	Occupancy	U_{iso} (Å^2)
Pnma (90 K)	Cu1	4*a*	0	0	0	1	0.00705(7)
	Cu2	8*d*	0.2518(2)	0.5101(1)	0.2496(3)	1	0.00705(7)
	Cu3	4*c*	0.1841(3)	0.25	0.0518(5)	0.710(5)	0.00705(7)
	Cu4	4*c*	0.186(2)	0.25	0.920(3)	0.144(5)	0.00705(7)
	Cu5	4*c*	0.123(2)	0.25	0	0.146(6)	0.00705(7)
	F1	4*c*	0.5041(9)	0.25	0.001(2)	1	0.0112(6)
	Br1	4*c*	0.3326(2)	0.25	0.5037(3)	1	0.0123(1)
	O1	8*d*	0.2986(6)	0.0880(9)	0.011(1)	1	0.0019(3)
	O2	8*d*	0.1059(7)	0.0922(8)	0.196(1)	1	0.0019(3)
	O3	8*d*	0.4076(6)	0.58877(8)	0.304(1)	1	0.0019(3)
$P6_3/mmc$ (90 K)	Cu1	6*g*	0.5	0	0	1	0.00705(7)
	Cu2	6*h*	0.6283(3)	0.2567(5)	0.25	$\frac{1}{3}$	0.00705(7)
	O1	12*k*	0.2016(4)	0.7984(4)	0.9052(6)	1	0.0019(3)
	F1	2*b*	0	0	0.75	1	0.0.0123(1)
	Br1	2*c*	0.6667	0.3333	0.75	1	0.0123(1)
Pnma (1.5 K)	Cu1	4*a*	0	0	0	1	0.0051(1)
	Cu2	8*d*	0.2493(3)	0.5128(2)	0.2455(4)	1	0.0051(1)
	Cu3	4*c*	0.1846(6)	0.25	0.059(1)	0.68(1)	0.0051(1)
	Cu4	4*c*	0.189(2)	0.25	0.942(5)	0.19(1)	0.0051(1)
	Cu5	4*c*	0.128(3)	0.25	0	0.131(9)	0.0051(1)
	F1	4*c*	0.4991(5)	0.25	0.002(1)	1	0.0118(2)
	Br1	4*c*	0.3302(3)	0.25	0.5042(8)	1	0.0055(2)
	O1	8*d*	0.2971(3)	0.0948(4)	0.0050(7)	1	0.0060(1)
	O2	8*d*	0.1044(4)	0.0972(4)	0.1944(6)	1	0.0060(1)
	O3	8*d*	0.3996(4)	0.5874(4)	0.3020(6)	1	0.0060(1)
	D1	8*d*	0.3755(3)	0.1406(4)	0.0040(8)	1	0.0198(1)
	D2	8*d*	0.0608(4)	0.1331(4)	0.3131(6)	1	0.0198(1)
	D3	8*d*	0.4374(4)	0.6364(4)	0.1898(6)	1	0.0198(1)
$P6_3/mmc$ (1.5 K)	Cu1	6*g*	0.5	0	0	1	0.0051(1)
	Cu2	6*h*	0.6291(4)	0.2581(9)	0.25	$\frac{1}{3}$	0.0051(1)
	O1	12*k*	0.2011(2)	0.7988(2)	0.9103(3)	1	0.0060(1)
	D1	12*k*	0.1239(2)	0.8761(2)	0.8693(3)	1	0.0198(1)
	F1	2*b*	0	0	0.75	1	0.0118(2)
	Br1	2*c*	0.6667	0.3333	0.75	1	0.0055(2)

Table 3.10: Rietveld refinement crystal structure parameters for the *Pnma* models of $Cu_4(OD)_6FI$ fitted to PXRD and NPD data collected on I11 at 90 K and HRPD at 1.5 K, respectively. Refined lattice parameters and phase fractions are given in Table 3.11.

	Atom	Site	x	y	z	Occupancy	U_{iso} (Å^2)
Pnma (90 K)	Cu1	4*a*	0	0	0	1	0.0042(3)
	Cu2	8*d*	0.2520(2)	0.5067(2)	0.2484(2)	1	0.0066(2)
	Cu3	4*c*	0.1845(2)	0.25	0.0602(6)	0.835(9)	0.0047(5)
	Cu4	4*c*	0.179(2)	0.25	0.968(4)	0.096(8)	0.0047(5)
	Cu5	4*c*	0.120(2)	0.25	0	0.069(3)	0.0047(5)
	F1	4*c*	0.4973(7)	0.25	0.003(2)	1	0.0112(6)
	I1	4*c*	0.4973(7)	0.25	0.003(2)	1	0.0123(1)
	O1	8*d*	0.2982(4)	0.0926(6)	0.000(1)	1	0.011(2)
	O2	8*d*	0.1010(7)	0.0952(8)	0.195(1)	1	0.011(2)
	O3	8*d*	0.4024(7)	0.5854(8)	0.310(1)	1	0.011(2)
Pnma (1.5 K)	Cu1	4*a*	0	0	0	1	0.0023(4)
	Cu2	8*d*	0.2511(3)	0.5079(2)	0.2484(3)	1	0.0032(3)
	Cu3	4*c*	0.1850(2)	0.25	0.0560(2)	1	0.0049(5)
	F1	4*c*	0.4956(2)	0.25	0.0071(6)	1	0.0031(3)
	I1	4*c*	0.3325(3)	0.25	0.5021(5)	1	0.0031(3)
	O1	8*d*	0.2970(1)	0.0975(2)	0.9993(5)	1	0.0039(4)
	O2	8*d*	0.1039(3)	0.0903(3)	0.1947(4)	1	0.0069(7)
	O3	8*d*	0.4004(3)	0.5872(3)	0.3016(4)	1	0.0017(6)
	D1	8*d*	0.3758(2)	0.1369(2)	0.0011(5)	1	0.0172(5)
	D2	8*d*	0.0627(3)	0.1284(3)	0.3146(4)	1	0.0159(7)
	D3	8*d*	0.4389(3)	0.6336(4)	0.1915(4)	1	0.0192(7)

Table 3.11: Lattice parameters, phase fractions and R-factors obtained from Rietveld refinements against powder diffraction data collected for the $Cu_4(OD)_6FX$ series at 90 K and 1.5 K. Only the parameters for the main $Pnma$ phase of FI are given.

		FCl		FBr		FI	
	T (K)	90 K	1.5 K	90 K	1.5 K	90 K	1.5 K
	R_{wp} (%)	8.07	2.14	5.59	2.25	7.29	2.23
$Pnma$	Phase fraction (%)	66.1(2)	68.1(2)	68.8(1)	65.0(4)	47.5(3)	49.2(3)
	a (Å)	11.52326(5)	11.5240(1)	11.5302(1)	11.5298(2)	11.54775(4)	11.5455(1)
	b (Å)	9.15310(4)	9.14924(6)	9.26978(5)	9.2684(1)	9.47735(9)	9.4725(1)
	c (Å)	6.67509(3)	6.67816(6)	6.67315(6)	6.6756(1)	6.70531(3)	6.70597(7)
	V (Å^3)	704.046(3)	704.117(6)	713.239(6)	713.37(2)	733.843(7)	733.40(2)
$P6_3/mmc$	Phase fraction (%)	33.9(2)	31.9(4)	31.2(3)	35.0(7)		
	a (Å)	6.66240(3)	6.66377(4)	6.66423(2)	6.66524(5)		
	c (Å)	9.14514(8)	9.1407(1)	9.27188(5)	9.2696(1)		
	V (Å^3)	351.546(3)	351.520(7)	356.614(2)	356.635(6)		

Table 3.12: Key bond lengths extracted from refinements against NPD data collected on HRPD for the $Cu_4(OD)_6FX$ series at 1.5 K.

	FCl	FBr	FI
	Bond length (Å)		
Cu1–Cu2 (1)	3.29824(3)	3.311(4)	3.344(3)
Cu1–Cu2 (2)	3.36923(3)	3.354(4)	3.333(3)
Cu2–Cu2	3.35418(3)	3.3462(4)	3.3564(2)
Cu1–Cu3	3.159(4)	3.171(5)	3.211(1)
Cu2–Cu3 (1)	2.826(6)	2.836(6)	2.866(3)
Cu2–Cu3 (2)	3.100(6)	3.129(7)	3.172(3)
Cu1–X	3.033(1)	3.034(3)	3.057(2)
Cu2–X	2.776(1)	2.876(5)	2.987(3)
Cu3–X	3.418(2)	3.41(1)	3.443(4)
F1–D1	1.751(4)	1.749(6)	1.749(3)
F1–D2	1.774(4)	1.788(7)	1.832(4)
F1–D3	1.838(5)	1.814(7)	1.887(7)
	Bond angle (°)		
Cu1–O2–Cu2	114.32(13)	112.9(2)	116.2(2)
Cu1–O3–Cu2	122.77(13)	121.9(3)	119.6(2)
Cu2–O1–Cu2	117.2(1)	116.5(1)	114.9(1)
Cu2–O1–Cu3	91.7(1)	92.1(4)	91.74(1)
Cu2–O2–Cu3	92.3(1)	93.1(3)	92.1(2)
Cu1–O2–Cu3	107.4(1)	108.6(4)	107.2(2)

3.5 The Magnetic Behaviour Across the $Cu_4(OH)_6FX$ Series

3.5.1 Magnetic Susceptibility and Heat Capacity

The zero-field cooled temperature-dependent magnetic susceptibility data collected in a field of 1 T for FBr was presented in Section 3.3.2, and indicated a transition to long-range magnetic order at $T_N = 15$ K. Comparable data have been collected for FCl and FI analogues and are shown in Figure 3.20, along with FBr data for comparison. In the data collected for FCl, there is an upturn in the susceptibility at approximately $T_N = 17$ K, which is corroborated by previous reported magnetometry measurements on this material [172, 173]. In addition, data collected for FI indicates the same is true in this analogue, with an upturn in the data below approximately $T_N = 17$ K. Curie-Weiss fitting of the high-temperature inverse susceptibility yields Weiss constants, θ, which indicate that antiferromagnetic exchange dominates the magnetic behaviour across the series. The value of θ reflects the sum of all exchange interactions within each system, and the magnitude of θ decreases on going from FCl to FI, indicating an increase in a ferromagnetic component of the magnetic ground states of these systems. Note that in previous magnetic susceptibility studies on barlowite in smaller fields, there is a second transition at $T_N = 13.8$ K, which then merges with the high temperature transition with increasing applied fields up to 0.2 T [119].

The heat capacity measured between 2 – 300 K for the $Cu_4(OH)_6FX$ series in zero applied field is shown in Figure 3.21(a). In the absence of suitable non-magnetic analogues of these materials, the lattice contribution to the total heat capacity has been approximated by fitting a function $C_{lat} = \alpha T^2 + \beta T^3$ between 20 – 30 K, following the approach of several previous studies on barlowite and claringbullite [119, 150, 158, 160, 172]. An example of the fitting procedure employed is shown for data collected on FCl in the inset of Figure 3.21(a). Note that it has not been possible to model this contribution using a more sophisticated method entailing the Debye-Einstein model for the lattice specific heat behaviour. In herbertsmithite, this has been ascribed to the bending modes of the OH groups which complicate predicting the lattice behaviour [174]. Whilst the polynomial used here may only provide a first approximation for the lattice contribution, this approach makes for an easy comparison across samples synthesised by various groups, who also used this model.

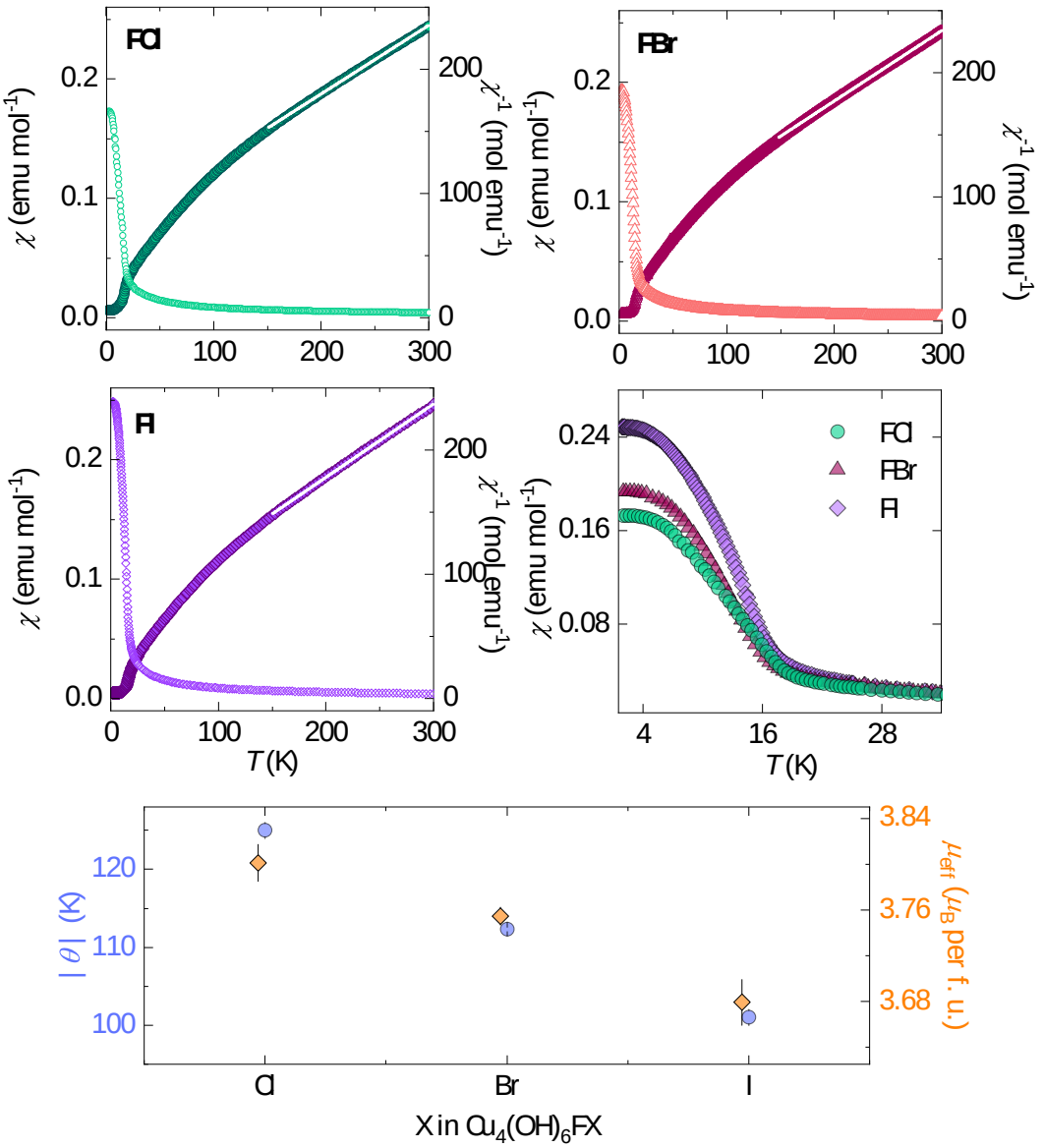

Figure 3.20: Temperature dependence of the magnetic susceptibility measured after zero-field cooling for the $Cu_4(OH)_6FX$ series in an applied field of 1 T. The Curie temperatures, θ, and effective magnetic moments, μ_{eff}, obtained from fitting the Curie-Weiss law to the inverse susceptibility are given in the lower panel.

On subtracting this lattice contribution, the remaining magnetic heat capacity C_{mag}, given in Figure 3.21(b), reveals the presence of broad anomalies below approximately 15 K in all three analogues. In FBr, the anomaly is centred at 6 K, whilst there are clearly two anomalies at 5 K and 15 K in FCl and 7 K and 13 K in FI, with the less prominent feature present at higher temperature. The entropy released across the magnetic transitions observed in the $Cu_4(OH)_6FX$ series has

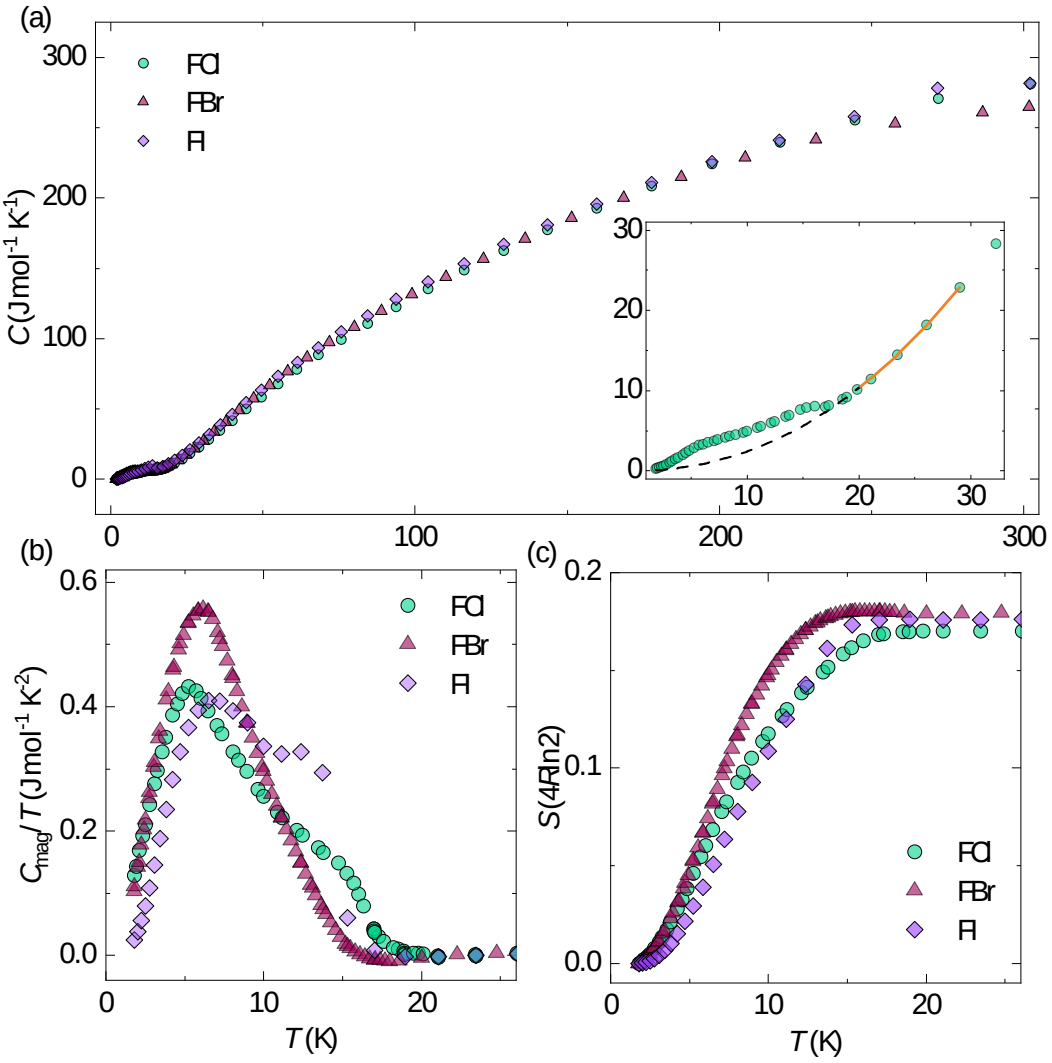

Figure 3.21: The heat capacity measured for the $Cu_4(OH)_6FX$ series in zero field is shown in (a). The inset in (a) shows the fitting procedure for estimating the lattice contribution to the heat capacity. The remaining magnetic specific heat and the recovered entropy are shown in (b) and (c), respectively.

been estimated by integrating each magnetic heat capacity dataset from 2 – 25 K. The magnetic entropy is expected to plateau at $\Delta S = R\ln(2S+1)$ per ion. These systems contain four $S = \frac{1}{2}$ Cu^{2+} ions, and so Figure 3.21(c) presents the entropy as a fraction of the full expected entropy release, $4R\ln 2$, which suggests that the ground state reaches only ~ 18 % of this value in each of the analogues.

Similar results displaying two transitions have been shown in previous studies on barlowite and claringbullite [119, 150, 160, 172]. The recovery of $\sim \frac{1}{4}$ of the expected entropy has led to the hypothesis that this behaviour is associated with

the ordering of interlayer Cu^{2+} ions [150, 160], whilst the missing entropy has been attributed to the formation of dynamic spin correlations, such as those which exist in valence bond solids [119]. Indeed, the reduced moments in the average magnetic structure of barlowite, determined in Section 3.3.2, indicates that the ground state is not fully ordered in this system. Interestingly, the C_{mag} determined for FBr resembles that of the sample reported previously which crystallises in the $P6_3/m$ structure, rather than $Pnma$ [160]. In this case, the gradual incline in C_{mag} was attributed to the short-range ordering of interlayer Cu^{2+} spins, indicating that the magnetic transition at higher temperatures is associated with this site. The $P6_3/m$ structure is characterised by significant remaining disorder on four different interlayer Cu^{2+} sites (see Figure 3.2). In Section 3.4.3, it was revealed that there is remaining disorder within the $Pnma$ structure of the FBr sample measured within this chapter, as well as some remaining $P6_3/mmc$ structure which inherently contains interlayer disorder. In FCl, the $Pnma$ interlayer Cu^{2+} is fully ordered, but there is some remaining $P6_3/mmc$ structure, whilst FI is fully orthorhombic with a small amount of disorder on the interlayer site. Therefore, if the transition at higher temperature in C_{mag} is associated with ordering of the interlayer spins, the prominence of this anomaly across the series correlates with the amount of disorder remaining on these interlayer sites at low temperature. In turn, the differences in the heat capacity data measured across the literature for barlowite, even amongst samples synthesised by similar routes, could indicate that the disorder on the interlayer site, and therefore the magnetic behaviour, is extremely sensitive to even small changes in synthetic conditions.

In the related clinoatacamite, two magnetic transitions are also observed in specific heat and magnetic susceptibility data, although it was discerned that samples with improved crystallinity displayed these transitions more prominently in the specific heat [143]. In vesignieite, the Cu^{2+} within the kagomé planes possess a dynamic Jahn-Teller distortion which is retained down to 4 K, inducing a type of orbital disorder and magnetostructural coupling [100]. However, the magnetic response in vesignieite varies across samples, and it is thought that there is a connection between microstructural defects and the annealing time, which in turn affects the Jahn-Teller behaviour and the prominence of the magnetic transition in magnetometry data. Clearly, this indicates that the synthetic route is likely a crucial factor when considering interlayer disorder and its role in the magnetic response across the $Cu_4(OH)_6FX$ series.

3.5.2 Comparing Magnetic Structures

Further NPD data were collected on the D20 diffractometer for the FCl and FI members of the $Cu_4(OD)_6FX$ series, which are shown in Figure 3.22. Similar to the treatment of data collected for FBr in Section 3.3.2, the high-temperature data have been subtracted from that collected at 1.5 K to isolate the magnetic scattering. In addition, a further dataset was measured for FCl at 10 K, between the two magnetic transitions observed at 5 K and 15 K in heat capacity data. Initial inspection of the subtracted data shows that the magnetic Bragg peaks are largely similar across the series, but with subtle differences in intensities. Indeed, refinement of the $Pn'm'a$ magnetic space group gives good fits to all datasets, as shown in Figure 3.22. Note that, despite the likelihood of there being several structural phases in these samples, only one magnetic phase is necessary to model these data due to the low resolution of D20 which, for example, does not capture the asymmetry of the nuclear Bragg peaks in FI which were observed in HRPD data. As such, the results presented here represent the average magnetic structure within each sample.

The magnetic structures of the $Cu_4(OH)_6FX$ series are given in Figure 3.23. It is clear that each analogue has a largely similar magnetic structure: magnetic moments which point predominantly towards the a-axis, with an antiferromagnetic canting on Cu2 towards b and a ferromagnetic canting on Cu3 towards c. Inclusion of moments along all other crystallographic directions was found to be statistically insignificant in the refinement. However, a comparison of the refined magnetic moments, shown in Figure 3.24, reveals two observations across the series. Firstly, the magnitude of all three Cu moments is significantly larger in the FCl and FI analogues, suggesting that there is no systematic pattern in these parameters on going down the halide series. Instead, the moment magnitudes appear to correlate with the remaining interlayer disorder in each analogue determined in Section 3.4.3. FCl and FI have a higher degree of interlayer site order, which perhaps results in longer-range magnetic order and larger ordered moment sizes. Secondly, whilst the magnetic ground states of each analogue contains the same antiferromagnetic and ferromagnetic cantings, the magnitude of the latter is much larger in the FI sample. This is a consequence of the intense (111) magnetic Bragg peak which is not resolved in data collected for FBr or FCl.

The magnetic structure determined for FCl at 10 K can also be described by the $Pn'm'a$ magnetic model, with even smaller magnetic moments, demonstrating

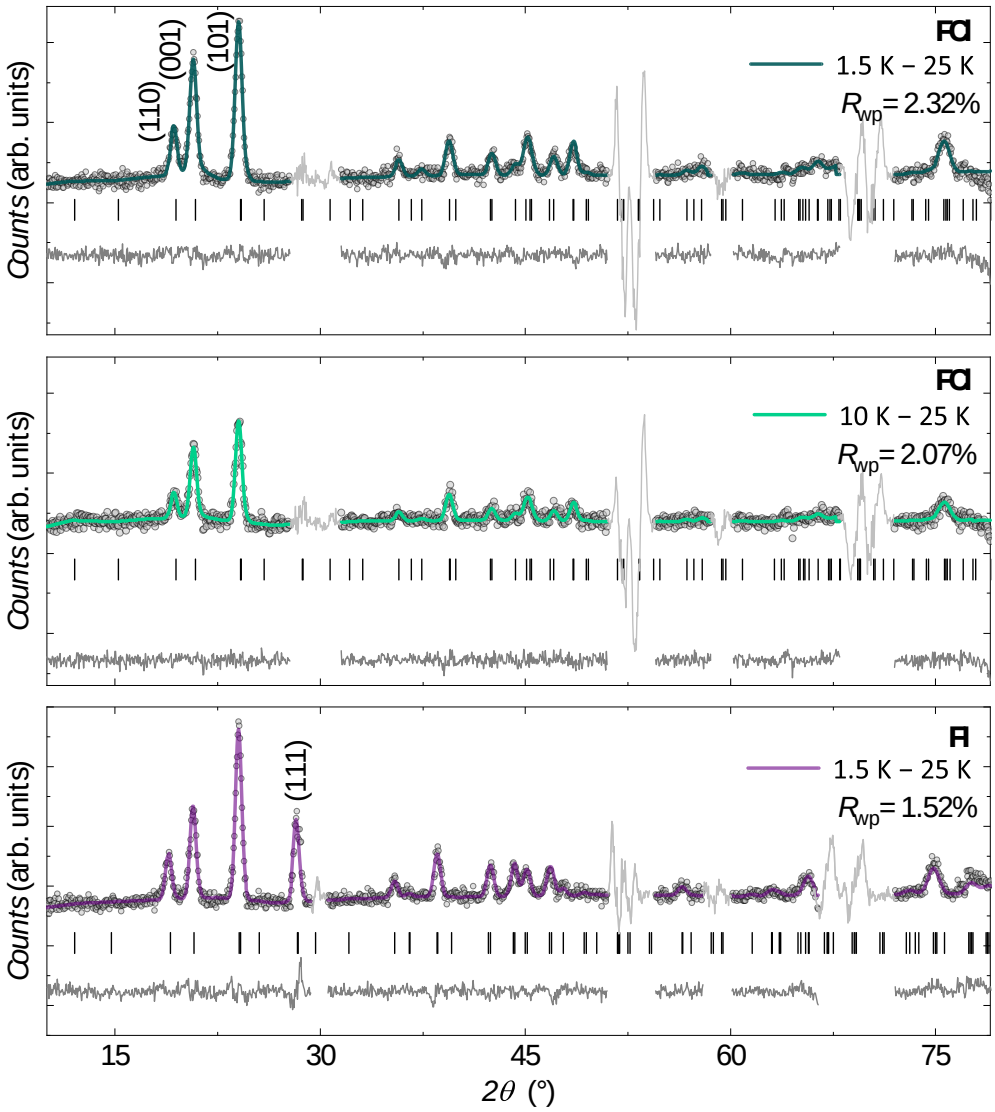

Figure 3.22: Rietveld refinements of the $Pn'm'a$ magnetic structure of $Cu_4(OD)FCl$ to subtracted data collected at 1.5 K (top) and 10 K (middle), and of $Cu_4(OD)FCl$ at 1.5 K (bottom). Grey regions in the collected data were excluded from the refinements.

that the magnetic transition at 15 K in this material is not a sharp transition, as is clear from heat capacity data. Comparing refined moments in FCl at 1.5 K and 10 K, it appears that the magnitude of the refined Cu3 moment along the a-axis significantly jumps on cooling to below the 5 K magnetic transition, indicating that it is the ordering of interlayer copper which characterises this transition, rather than the 15 K transition. The small refined magnetic moments across the series are indicative of remaining spin frustration even at 1.5 K. Magnetic correlation lengths of 149.4(1) Å and 155.4(1) Å have been estimated from the full

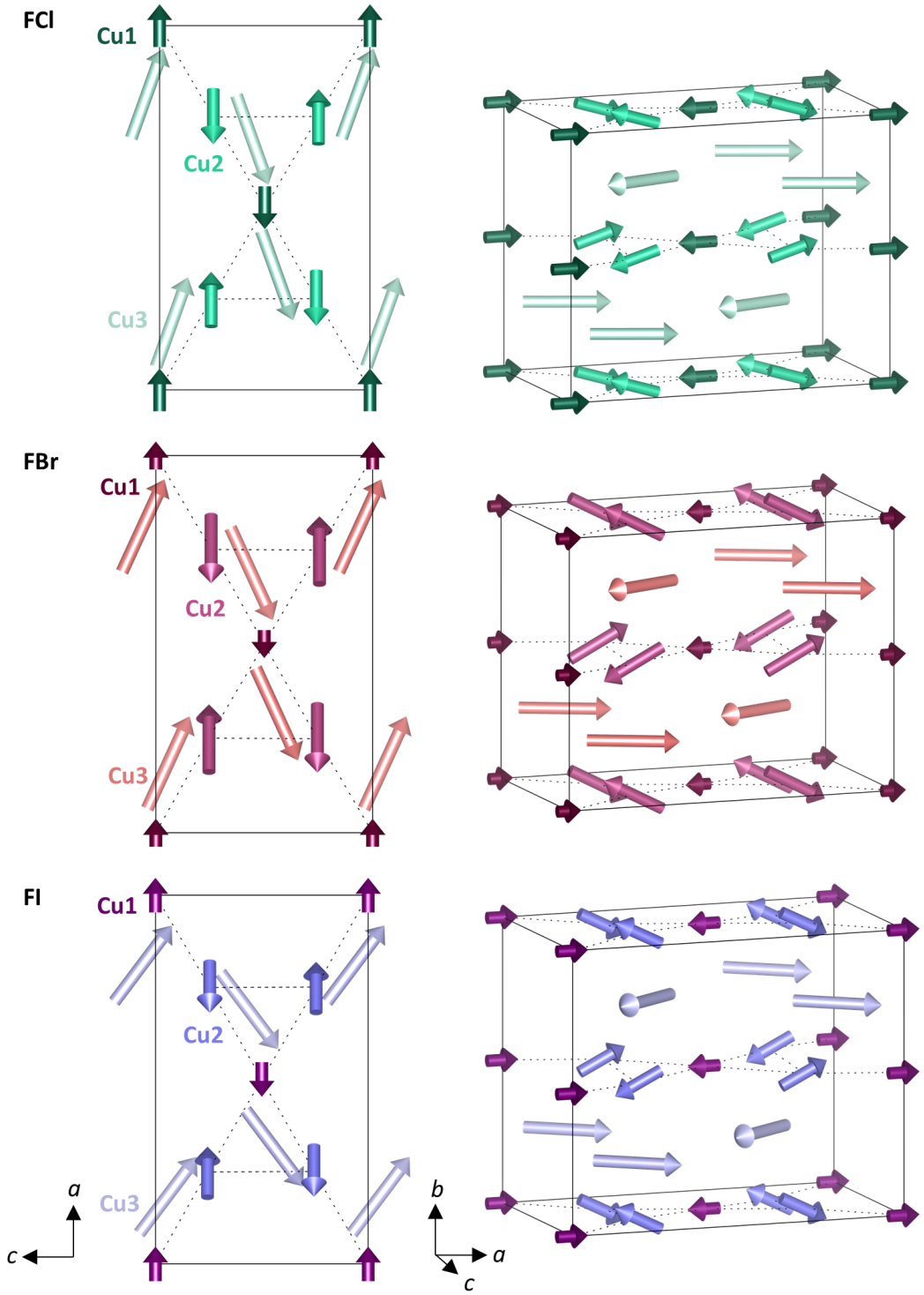

Figure 3.23: Magnetic structures of the $Cu_4(OH)_6FX$ series obtained from refinement of the $Pn'm'a$ magnetic structure against NPD data collected on D20 at 1.5 K. Dashed lines represent the kagomé network formed from Cu1 and Cu2 ions.

width at half maxima of the (001) magnetic Bragg peak in data collected for FCl and FI, respectively, whilst similar analysis for FBr suggests a shorter correlation

length of 119.2(1) Å. This is further indication that there is a correlation between interlayer order and long-range magnetic order in these systems. Previous ^{79}Br NMR measurements on barlowite displayed a weak slowing down of critical fluctuations on cooling below 15 K [159], supporting the findings here that there are significant spin fluctuations persistent in the ordered magnetic state in barlowite and related systems. Indeed, inspection of the bond lengths and angles at 1.5 K presented in Table 3.12 indicates that the distortion of the triangles which make up the kagomé planes across the series is not substantial, meaning these systems likely remain highly frustrated even in the *Pnma* structure. In FI, the remaining frustration may be less pronounced, either due to the more diffuse iodide anion which facilitates a stronger covalent interaction, and therefore stronger exchange than the bromide or chloride counterparts or, alternatively, because of the interlayer Cu^{2+} ions which are ordered at low temperature in FI. Both of these factors may also influence the higher degree of canting on Cu3 observed in the FI sample. The direct relation between the halide identity in $Cu_4(OH)_6FX$, the level of interlayer copper disorder, and the magnetic (dis)order is yet to be determined. What is clear from the results throughout this chapter, however, is that the entire picture is not captured using solely methods which probe long-range crystal and magnetic order.

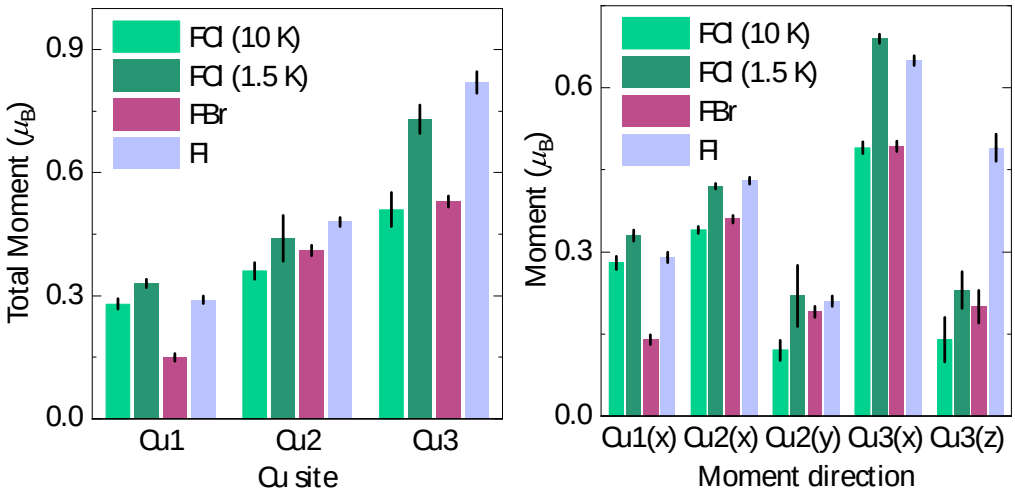

Figure 3.24: A comparison of the refined total magnetic moments (left) and magnetic moment directions (right) across the $Cu_4(OD)_6FX$ series.

3.6 Conclusions

This chapter has provided a comprehensive investigation of the synthesis, structures and magnetic behaviours across a family of frustrated $S = \frac{1}{2}$ kagomé antiferromagnets. Barlowite, $Cu_4(OH)_6FBr$, claringbullite, $Cu_4(OH)_6FCl$, and a novel analogue, $Cu_4(OH)_6FI$, each contain a kagomé network of Cu^{2+} ions, which at room temperature can be described using a hexagonal $P6_3/mmc$ symmetry. Upon cooling, a structural distortion takes place which is characterised by the displacement of interlayer Cu^{2+} ions. The crystal structures of the samples reported here are best described at low temperatures by the orthorhombic $Pnma$ model, although a review of the literature suggests that alternative structures crystallise depending on the synthetic route. There are, however, several further important observations which are summarised below:

- Across the series, there is evidence for multiple structural phases in powder diffraction data. This is particularly prominent for $Cu_4(OH)_6FI$, where asymmetric ($hk4n$) peaks are observed in diffraction data, indicating a range of c parameters within individual samples. This raises the question of the presence of halide compositional disorder within these systems.

- The presence of a combination of hexagonal and orthorhombic phases in $Cu_4(OH)_6FBr$ and $Cu_4(OH)_6FCl$ at low temperatures indicates that the structural distortion which emerges across this series is highly sensitive, perhaps to the presence of small defects.

- Refinement of interlayer Cu^{2+} occupancies within the $Pnma$ phase across the series suggests that there is remaining positional disorder on the interlayer site at 1.5 K, particularly in $Cu_4(OH)_6FBr$.

- Heat capacity measurements, as well as prior magnetic susceptibility measurements, indicate that a two-step process below approximately $T_N < 20$ K is undertaken in the transition to magnetic order across the series. There is evidence to suggest that the extent of magnetic order is related to the interlayer Cu^{2+} disorder, with $Cu(OH)_6FCl$ and $Cu(OH)_6FI$ displaying more prominent magnetic transitions whilst displaying the least interlayer disorder.

- The magnetic structures of the $Cu_4(OH)_6FX$ series belong to the $Pn'm'a$ magnetic space group. The refined structures provide further evidence for correlation between interlayer Cu^{2+} order and long-range magnetic order,

with $Cu(OH)_6FCl$ and $Cu_4(OH)_6FI$ displaying larger ordered moments than their $Cu_4(OH)_6FBr$ counterpart. Across the series, the small magnetic moments and the complex spin ordering is indicative of remaining spin dynamics and an unusual underlying spin Hamiltonian.

However, there are several questions which remain open, and there are many considerations which should be taken into account in future studies:

- The existence of multiple crystal structures, and even of multiple phases within individual samples, is a reminder of the need for careful control of experimental conditions and clear reporting in future studies. Sample dependence appears to be a common theme in the study of copper hydroxide mineral systems, and future work should aim to gain an understanding of how these structures form *in situ*.

- Diffraction data provides an understanding of the long-range crystal and magnetic structures within materials, and in this respect, the limit of what can be extracted from diffraction measurements alone has been reached. Whilst there is value in further single-crystal X-ray, neutron and electron diffraction analysis—both in terms of halide and copper disorder—future studies should also make use of local techniques, such as NMR spectroscopy, alongside total and diffuse scattering. As a result, further insight into the local crystal and magnetic structures can be probed.

- Finally, a deeper understanding of the ground state crystal and magnetic structures, and how they relate to each other, can be gained from computational studies utilising methods such as density-functional theory. This will enable the determination of the relative stability of the proposed structures within barlowite and related analogues, as well as the predicted exchange pathways in their respective magnetic ground states.

Chapter 4

From Magnetic Order to Quantum Disorder: A Study of the Zn-Barlowite Series, $Zn_xCu_{4-x}(OH)_6FBr$

4.1 Introduction

The search for a material bearing a kagomé arrangement of antiferromagnetically interacting $S = \frac{1}{2}$ magnetic ions that, crucially, does not undergo a structural distortion like that discussed in Chapter 3, is an ongoing challenge in the condensed matter community. One material that has garnered considerable attention in this regard is the mineral herbertsmithite, whose "perfect" structure [112] combines the three essential components of a quantum spin liquid (QSL): (i) antiferromagnetically coupled $S = \frac{1}{2}$ Cu^{2+} ions that form (ii) an array of corner-sharing equilateral triangles that, in the ideal crystallographic structure, are (iii) well separated by non-magnetic Zn^{2+} ions leading to a quasi-two-dimensional structure. Whilst the discovery of herbertsmithite is a benchmark in the study of QSL physics, the third point listed is widely contested due to significant antisite disorder which is suspected between the Cu^{2+} within the kagomé layers and the Zn^{2+} sites between the layers. Early studies suggested a dilution of the kagomé layers of 5–7% [175–177], although a later study utilising X-ray anomalous scattering determined that no more than 1% Zn^{2+} occupies the kagomé layers but that approximately 15% of the interlayer site is occupied by Cu^{2+} [71]. The true ground state of herbertsmithite has consequently been called into question as, despite demonstrating the absence of long-range magnetic order down to 50 mK [152], it is not clear whether the presence of disorder obscures the low-temperature signatures of a QSL. For example, the existence or absence of a gap in the spin excitation spectra probed via inelastic

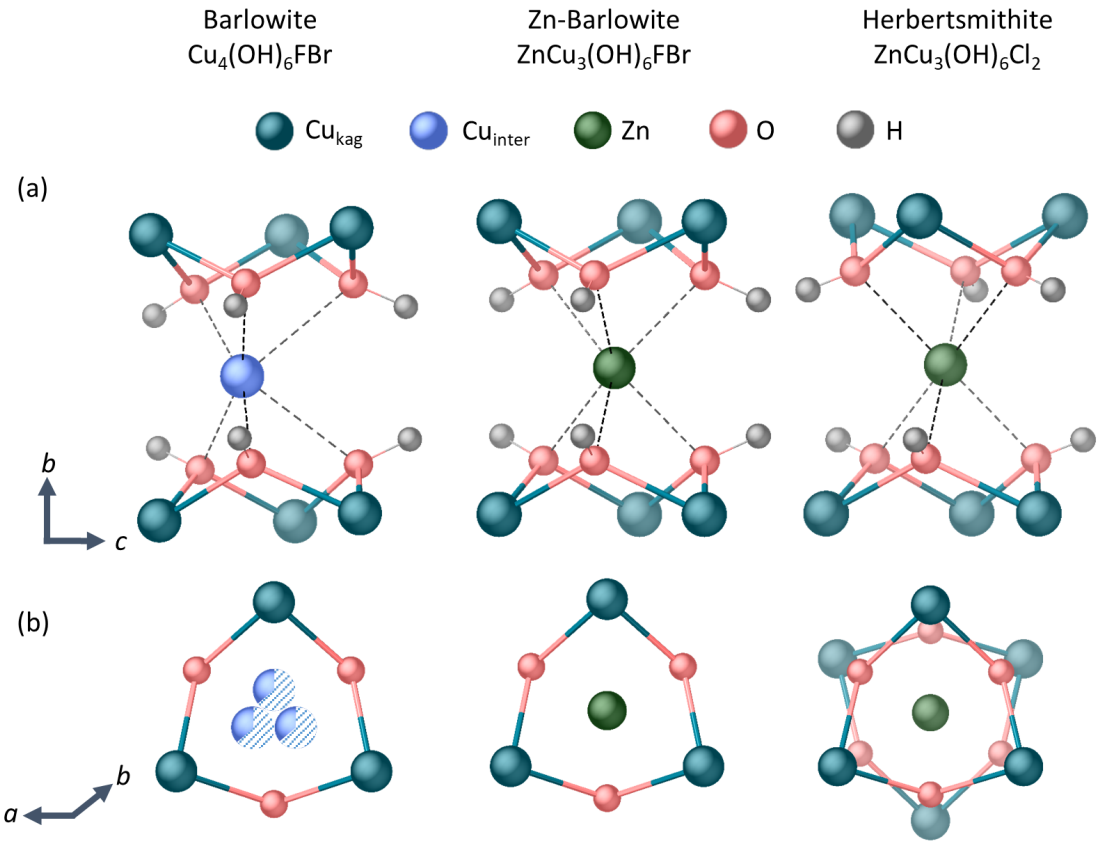

Figure 4.1: (a) A comparison of the coordination environment of the interlayer site viewed along the a-axis, between the kagomé layers, in barlowite (distorted trigonal prismatic), Zn-barlowite (trigonal prismatic) and herbertsmithite (pseudo octahedral) [112]. (b) The same comparison viewed along the b-axis, perpendicular to the kagomé layers. In barlowite, the interlayer site is disordered over three equivalent sites which are one-third occupied. In herbertsmithite, the triangles which form the kagomé layers are staggered along the c-axis.

neutron scattering measurements [114, 153], and the temperature dependence of the Knight shift deduced from ^{17}O NMR spectroscopy measurements [154, 156] are both crucial pieces of information if we are to definitively classify these types of materials.

Following the discovery that barlowite—which is structurally similar to herbertsmithite as described in Chapter 3—does order magnetically, an alternative target material was suggested where the interlayer Cu2 site in barlowite is replaced with diamagnetic isovalent ions [119]. This would result in well-defined kagomé layers of Cu^{2+}, thus relieving the interlayer interactions which presumably facilitate magnetic ordering in the parent material. Promising dopants, determined through den-

sity functional theory (DFT) calculations, included Mg^{2+} and Zn^{2+}, both of which have been successfully doped into clinoatacamite to yield (Zn-)herbertsmithite and Mg-herbertsmithite [178, 179]. It was suggested that the similar ionic radii of Zn^{2+} (74 pm) and Mg^{2+} (72 pm) compared to Cu^{2+} (73 pm) would, in theory, prevent lattice distortion upon substitution. Moreover, the open-shell d^9 electron configuration of Cu^{2+} would preferentially opt for the lower symmetry square planar geometry of the Cu1 site within the kagomé planes (although the coordination of this site is better described as a [4+2] distorted octahedron), leaving the interlayer trigonal prismatic Cu2 position (displayed in Figure 4.1) energetically favoured by Mg^{2+} or Zn^{2+} ions. Larger ions were also originally postulated as potential dopants, including Sn^{2+} (118 pm) and Cd^{2+} (95 pm) [119]. However, later calculations demonstrated that these candidates are energetically more likely to occupy in-plane Cu1 sites than their smaller counterparts, which would in turn have the effect of distorting the kagomé planes [163]. Crucially, substitution of the Cu2 interlayer site in barlowite with Zn^{2+} or Mg^{2+} was predicted to decrease the degree of antisite disorder by at least one order of magnitude when compared to that in herbertsmithite [162]. If this is the case, the effect of disorder on the ground state of the kagomé QSL could be deduced from comparisons to herbertsmithite.

Following these predictions, there have been a handful of studies in which a successful synthesis of the Zn-barlowite series, with formula $Zn_xCu_{4-x}(OH)_6FBr$, has been described. These studies do indeed support the idea of a suppression of the antiferromagnetism in the parent material with increasing x, and are supported by magnetic susceptibility and specific heat measurements [150, 151, 158, 160]. Moreover, probes including ^{19}F NMR spectroscopy, inelastic neutron scattering and Raman spectroscopy appear to point towards a gapless Z_2 QSL ground state in Zn-barlowite [180–182]. Single crystal studies are far fewer, and indeed there is yet to be a successful synthesis of fully-substituted Zn-barlowite ($x = 1$) in single crystal form [150, 151]. It is also interesting to note that there have been no successful reports on Mg-doping, with one attempt presenting the synthesis of α-$MgCu_4(OH)_6Br_2$ instead, which is isostructural to kapellasite [183]. In this case the failure to produce Mg-barlowite was due to the insolubility of the MgF_2 starting material.

The aforementioned studies are predominantly supported by bulk analysis techniques, and the intermediate compositions in the Zn-barlowite series remain largely

unexplored by local techniques, such as muon spectroscopy. The muon is sensitive to magnetic moments as small as 10^{-5} T, which makes it an ideal probe to study materials which exhibit small magnetic moments, such as those observed in quantum systems where the magnetic moments may be suppressed due to effects including magnetic frustration [126]. Additionally, the timescale on which the muon probes matter is suited to the dynamics characteristic of frustrated magnets [130]. Indeed, μSR has proved invaluable in characterising similar families of magnetically frustrated materials. The most relevant example is in the Zn-paratacamite series, $Zn_xCu_{4-x}(OH)_6Cl_2$, the end-member of which is herbertsmithite. In this study, the development from antiferromagnetic order in the $x = 0$ member, clinoatacamite, to quantum disorder for compositions with $x > 0.50$ was demonstrated [134]. Given the similarities in the structural and magnetic responses in the Zn-paratacamite and Zn-barlowite series, the exploration of the latter using a similar experimental approach will be insightful to compare the two systems. Moreover, barlowite is an intriguing system from the perspective of the muon, because it contains both fluoride and hydroxide anions which are known to form μ–F and μ–OH complexes which often result in distinct oscillations in zero field data for systems which contain them [184]. This makes the determination of the muon stopping sites, the ambiguity of which is a major drawback in the quantitative analysis of muon spectroscopy data, more straightforward.

The following chapter presents a comprehensive discussion of the synthesis and characterisation of the Zn-barlowite series, $Zn_xCu_{4-x}(OH)_6FBr$, using DC magnetic susceptibility, neutron powder diffraction (NPD), and muon spin relaxation (μSR) measurements with supporting muon-site DFT calculations. The transition from a magnetically ordered to a dynamically fluctuating ground state, and the intermediate states between these two end-members, is explored using these techniques. The work within this chapter has been published in npj Quantum Materials [185].

4.2 Experimental Methods

4.2.1 Synthesis and Chemical Characterisation

Polycrystalline samples of $Zn_xCu_{4-x}(OH)_6FBr$ were prepared via a hydrothermal synthesis in which $CuCO_3{\cdot}Cu(OH)_2$ (Alfa Aesar, Cu 55%), $CuBr_2$ (Sigma Aldrich, 99%), $ZnBr_2$ (Sigma Aldrich, 99%) and NH_4F (Alfa Aesar, 98%) were combined

with H_2O and sealed in a Teflon-lined stainless steel autoclave. The ratio of $CuBr_2$ to $ZnBr_2$ was varied as shown in Table 4.1. The reaction mixtures were heated at a rate of 10 °C/min to 200 °C and held for 72 hours, and the autoclave allowed to cool to room temperature at 5 °C/min, with the exception of the fully Zn-substituted sample, $x = 0.99$, where the autoclave was heated at 1 °C/min to 210 °C, held for 24 hours and cooled at a rate of 0.1 °C/min to room temperature (following a heating profile similar to that employed in [160]). The resulting products, coloured turquoise to pale blue depending on the level of Zn-substitution, were filtered and washed several times with H_2O, dried in air and ground in an agate pestle and mortar. Deuterated samples were also synthesised for NPD measurements by substituting H_2O for D_2O as outlined in Table 4.1, and deuteration was confirmed using infra-red spectroscopy. The Cu and Zn content was determined using inductively coupled plasma optical emission spectroscopy (ICP-OES) on an Agilent 5110 SVDV. All samples measured were digested in dilute HNO_3. Absolute values obtained from ICP-OES measurements are shown in Table 4.2. The final Zn content, x, was computed via,

$$x = \frac{4}{\mathrm{N_{Cu}}/\mathrm{N_{Zn}} + 1}, \tag{4.1}$$

where $\mathrm{N_{Cu}}$ and $\mathrm{N_{Zn}}$ are the molar quantities of Cu and Zn, respectively, obtained by taking the average of the values in Table 4.2 and dividing by the molar mass of the ion of interest. Errors were obtained by propagating the standard error of the absolute values shown in Table 4.2.

Table 4.1: Summary of the reaction quantities used for the synthesis of $Zn_xCu_{4-x}(OH)_6FBr$. Reaction conditions are detailed in the main text.

	Reagent / mmol				Volume / mL	
x	$CuCO_3 \cdot Cu(OH)_2$	$CuBr_2$	$ZnBr_2$	NH_4F	H_2O/D_2O^a	Autoclave
0	4	8	0	12	20	50
0.153(2)	4	4	4	4	20[a]	50
0.159(3)	2	2	2	2	20	50
0.32(1)	1	1.5	0.5	4	10	23
0.50(1)	4	2	6	4	20[a]	50
0.52(1)	2	2	4	4	20	50
0.60(1)	6	2	6	5	20[a]	50
0.66(1)	2	1	3	4	10	23
0.99(1)	0.5	0.25	0.75	1	2	23

Table 4.2: Absolute values obtained from ICP-OES measurements on samples of $Zn_xCu_{4-x}(OH)_6FBr$. Errors on the average values represent the standard error.

Element label (nm)	Concentration (ppm)							
Cu 222.778	87.35	90.97	86.53	78.56	73.32	12.52	103.78	63.31
Cu 223.009	86.99	87.34	86.74	75.61	72.86	12.59	104.1	62.99
Cu 327.395	88.05	88.69	86.50	78.09	72.79	12.65	103.78	62.85
Cu (average)	87.5(3)	89.0(9)	86.6(1)	77.4(7)	73.0(1)	12.59(3)	103.89(9)	63.1(1)
Zn 334.502	3.87	7.67	13.78	16.32	24.99	0.52	15.92	11.88
Zn 334.557	3.73	8.17	13.78	16.05	24.17	0.52	15.65	11.50
Zn 472.215	3.55	8.04	12.62	15.02	24.44	0.50	14.50	10.64
Zn (average)	3.7(1)	8.0(1)	13.4(3)	15.8(3)	24.5(2)	0.513(5)	15.4(4)	11.3(3)
$\boldsymbol{x}$	**0.159(3)**	**0.32(1)**	**0.52(1)**	**0.66(1)**	**0.99(1)**	**0.153(2)**	**0.50(1)**	**0.60(1)**

Note that the fully-substituted $x = 0.99(1)$ sample was highly irreproducible, with only one successful synthesis in around 50 attempts. Failed attempts either resulted in lower Zn-substitution ($x \approx 0.6$) or significant Zn(OH)F impurity. Lower Zn-dopant levels are reproducible, although there appeared to be no systematic way in which to produce them and synthesis outcomes appeared to be highly dependent on the size of autoclave and overall mass of reactants rather than the ratio of Cu:Zn reactants used (see Table 4.1), indicating that pressure inside the autoclave is an important factor here. Indeed, incorporating $x > 0.66$ Zn^{2+} into the structure was extremely challenging. Even so, this level of interlayer Zn^{2+} means that around 34% of the interlayer sites contain Cu^{2+}, which is approaching that in herbertsmithite when considering the estimated ∼15% of defect Cu^{2+} spins thought to reside on the interlayer site [71]. Whilst another Zn-barlowite study reports similar difficulties, with polycrystalline samples containing Zn levels of $x \approx 0.46$ [150], two studies report polycrystalline samples containing $x > 0.92$ [151, 158] via similar synthetic routes. Meanwhile, single crystal attempts report Zn levels of no more than $x = 0.56$ [151]. This implies that a greater level of control and understanding of the synthesis of Zn-barlowite is still required.

4.2.2 Neutron Powder Diffraction

Time-of-flight NPD data were collected on a deuterated Zn-barlowite sample with Zn content of $x = 0.60(1)$ on the high-resolution powder diffractometer (HRPD) at the ISIS Neutron and Muon Source at the Rutherford Appleton Laboratory. The 1.5 g sample was packed into a flat plate steel-framed sample holder with vanadium windows and data were collected at 300 K and 1.5 K in a helium cryostat. Additional samples with $x = 0.153(2)$ and $x = 0.50(1)$ were measured on the General Materials (GEM) diffractometer at ISIS. 1.5 g samples were packed into cylindrical vanadium cans and data were collected at 200 K and 2 K, again in a helium cryostat. Rietveld refinements were carried out using the GSAS package [94, 95] on data collected in Banks 1 – 2 and Banks 1 – 6 on HRPD and GEM, respectively.

4.2.3 Magnetic Susceptibility

DC magnetic susceptibilities of the $Zn_xCu_{4-x}(OH)_6FBr$ series were measured on a Quantum Design Magnetic Properties Measurement System (MPMS) with a SQUID magnetometer. Samples masses ranging from 6–30 mg were packed into gelatin capsules and mounted in clear plastic straw sample holders. Data were

collected in an applied field of 1 T from 2 – 300 K in a zero-field cooled (ZFC) and field cooled (FC) cycle.

4.2.4 Muon Spin Relaxation

Muon spin relaxation and rotation data were collected on the MuSR spectrometer at the ISIS Neutron and Muon Source. Samples ranging from 60 to 500 mg and $x = 0.00$ to 0.99(1) were packed into silver foil sachets with sizes ranging from 2.25 cm^2 to 4 cm^2, attached to a silver backing plate with vacuum grease and loaded into a ^{4}He cryostat. For $x = 0.99(1)$, the small sample size of 60 mg required that two additional silver sheets were placed in front of the sachet to ensure the muons stopped within the sample. For $x = 0.66(1)$ and 0.99(1), samples were additionally measured in a ^{3}He/^{4}He dilution fridge. Data were collected in zero field (ZF), longitudinal field (LF) and transverse field (TF) geometries and analysed using the MANTID software [186]. Additional data were collected and analysed by Prof Fabrice Bert (Université Paris-Saclay) on a separate sample of $Cu_4(OH)_6FBr$ on the General Purpose Surface-Muon (GPS) instrument of the Swiss Muon Source at Paul Scherrer Institute. The 90 mg sample was contained in an aluminium foil packet, suspended in the muon beam using a silver fork-type holder and measured in VETO mode to reduce background signal.

DFT muon-site calculations were carried out by Prof Tom Lancaster (Durham University) using the MuFinder software [187] and the plane-wave-based code CASTEP [188] using the local density approximation. A supercell consisting of $1 \times 1 \times 2$ unit cells of the *Pnma* low-temperature structural model of barlowite was used in order to minimise the effects of muon self-interaction resulting from the periodic boundary conditions. Muons, modelled by an ultrasoft hydrogen pseudopotential, were initialised in low-symmetry positions and the structure was allowed to relax (keeping the unit cell fixed) until the change in energy per ion was less than 1×10^{-5} eV. A cutoff energy of 544 eV and a $1 \times 2 \times 1$ Monkhorst-Pack grid [189] were selected for k-point sampling.

4.3 Neutron Powder Diffraction and Structural Characterisation

At room temperature, Zn-substituted barlowite with $x = 0.60(1)$ is found to crystallise in the hexagonal $P6_3/mmc$ space group, as in the parent material barlowite, and Rietveld refinements of this structural model to high-resolution NPD data collected on the HRPD instrument are shown in Figure 4.2, with the final refined model shown in Table 4.3. The background was refined using a shifted Chebyschev function with 8 and 10 terms for Bank 1 and Bank 2, respectively. Isotropic atomic displacement parameters (U_{iso}) were refined independently for each distinct site. As described in Chapter 3, the hexagonal model of barlowite is formed from perfect kagomé layers of Cu^{2+} with additional Cu^{2+}/Zn^{2+} ions between the layers. However, whilst in the unsubstituted materials explored in Chapter 3 the interlayer Cu^{2+} ions are disordered over three equivalent sites, in Zn-substituted samples the Zn^{2+} ions, which are not Jahn-Teller active, are found to order onto one site in a trigonal prismatic coordination, shown in Figure 4.1. This is reflected in the R_{wp} values obtained from a Rietveld refinement at 300 K with the Zn^{2+} on a general $6h$ position (2.60%) compared to the special position $2d$ (2.47%) and in the occupancy of the Zn1 site, which refines to be a negative value when Zn2 is in a general position. Meanwhile, any remaining interlayer Cu^{2+} ions remain on $6h$ sites in distorted trigonal prismatic coordination, and their disorder is reflected in the larger refined U_{iso} values obtained for these sites. Deuterium and hydrogen occupancies were refined and indicate a level of deuteration of $> 98\%$ for all samples. An important result from the data is that, upon cooling, the hexagonal structure is retained down to 1.5 K in this sample, and Rietveld refinements and structural parameters at this temperature are shown in Figure 4.3 and Table 4.4, respectively. This suggests that Zn-barlowite does not undergo the symmetry lowering to $Pnma$ that the parent material does, as discussed in Chapter 3, likely due to the aforementioned order on the interlayer Zn^{2+} sites.

Data collected on Bank 3 of GEM for Zn-barlowite samples containing $x = 0.153(2)$ and $x = 0.50(1)$ at 200 K and 2 K are shown in Figure 4.5 and Figure 4.4, respectively, and data collected from all banks are shown in Appendix Figures 1–4. The background for all GEM datasets was refined using a shifted Chebyschev function with 8 terms in each bank. U_{iso} parameters were refined independently for each distinct site. The crystal structure of the lightly-doped $x = 0.152(2)$ sample at 200 K is tentatively assigned to the orthorhombic $Pnma$ structure based on

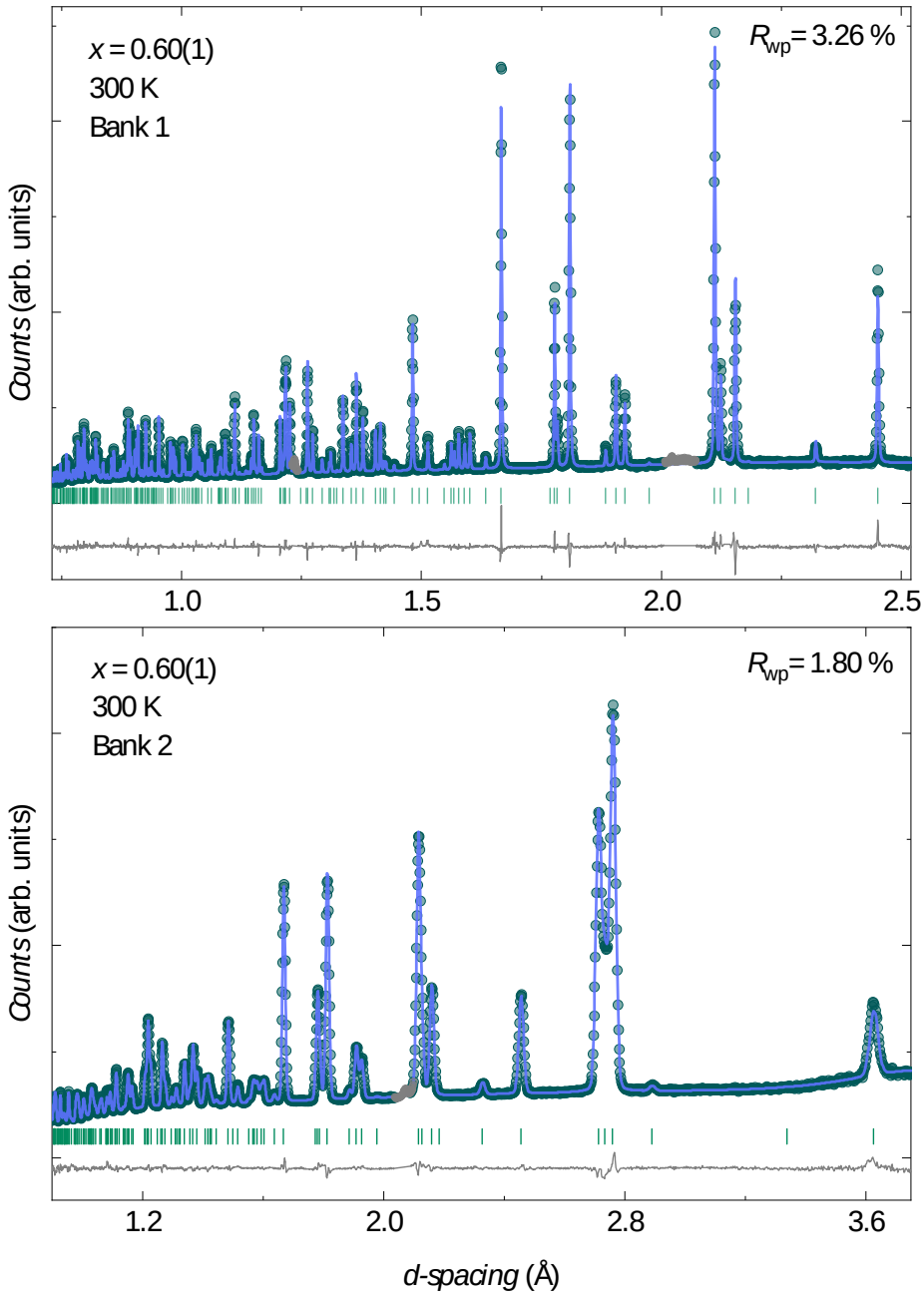

Figure 4.2: Neutron powder diffraction data collected at 300 K for $Zn_{0.60}Cu_{3.40}(OH)_6FBr$ on HRPD. The solid blue line shows Rietveld refinements of the $P6_3/mmc$ structural model to the data. The difference curve is shown in grey, whilst reflections are shown by green tick marks. Data represented by grey points indicate peaks arising due to aluminium and steel from the sample environment, and were excluded from the refinement. Overall $R_{\mathrm{wp}} = 2.47\%$.

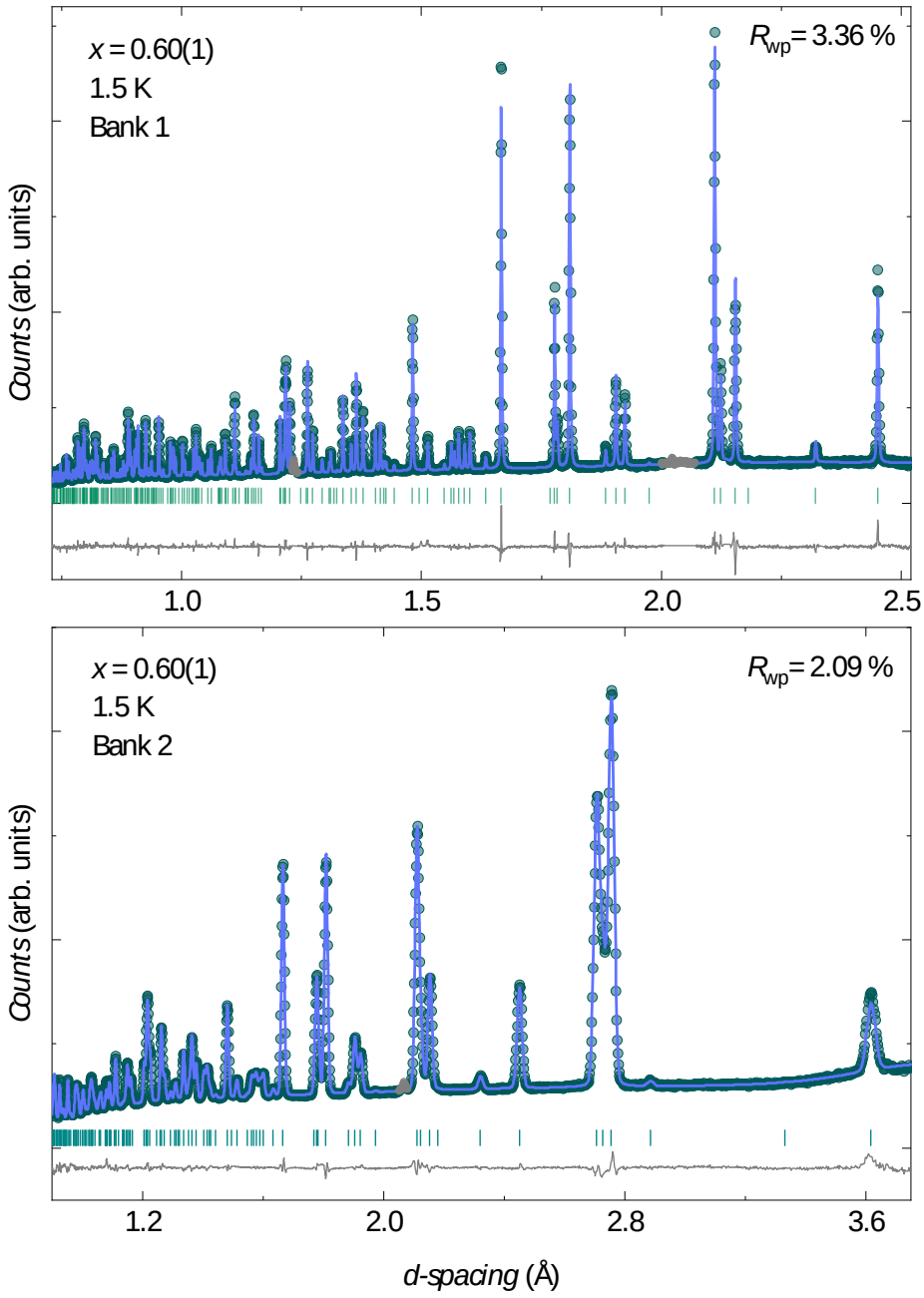

Figure 4.3: Neutron powder diffraction data collected at 1.5 K for $Zn_{0.60}Cu_{3.40}(OH)_6FBr$ on HRPD. The solid blue line shows Rietveld refinements of the $P6_3/mmc$ structural model to the data. The difference curve is shown in grey, whilst reflections are shown by green tick marks. Data represented by grey points indicate peaks arising due to Al and steel from the sample environment, and were excluded from the refinement. Overall $R_{\mathrm{wp}} = 2.65\%$.

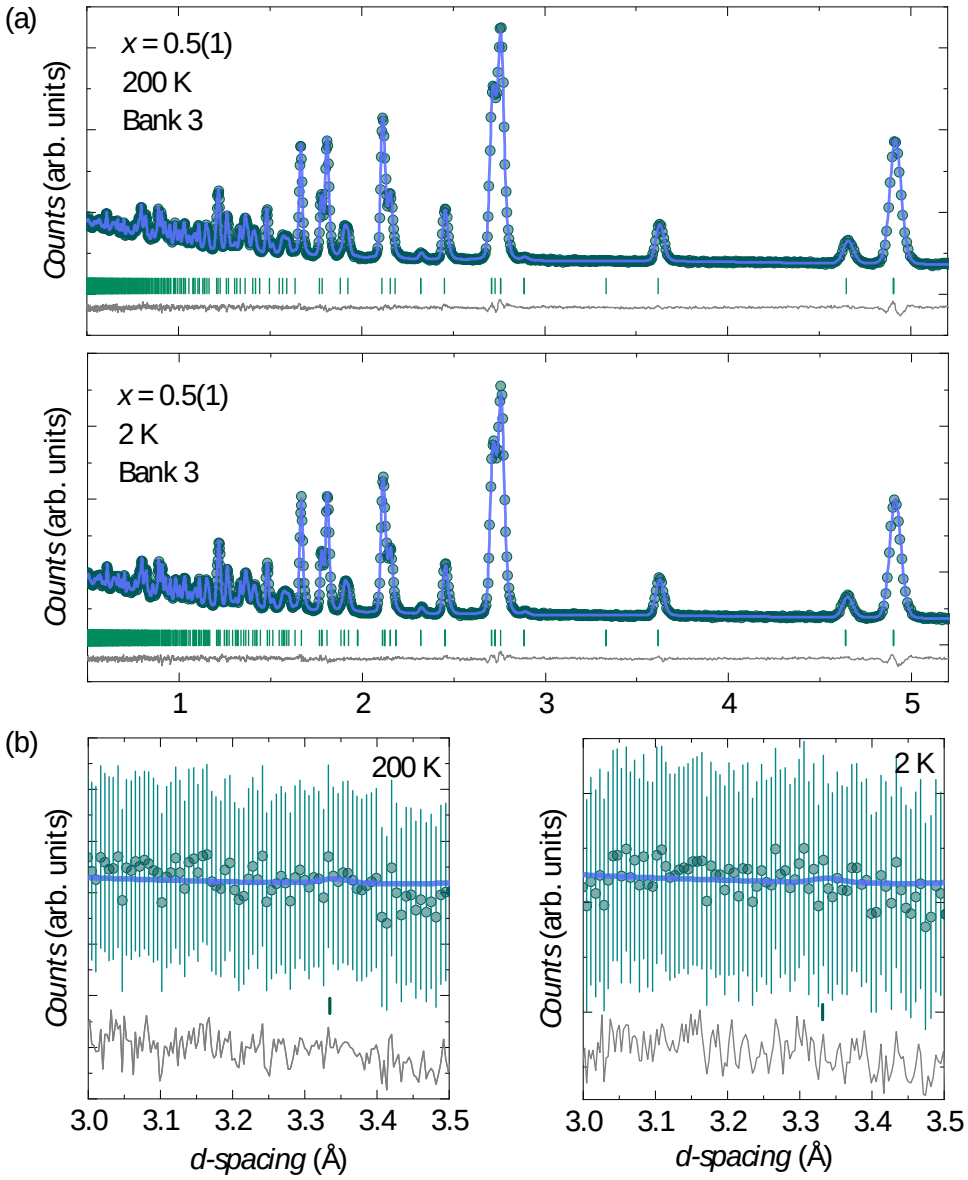

Figure 4.4: (a) Neutron powder diffraction data collected in Bank 3 of the GEM diffractometer at 200 K and 2 K for $Zn_{0.50}Cu_{3.50}(OH)_6FBr$ on HRPD. The solid blue line shows Rietveld refinements of the $P6_3/mmc$ structural model to the data. The difference curve is shown in grey, whilst reflections are shown by green tick marks. Overall $R_{wp} = 2.52\%$ at 200 K and $R_{wp} = 2.63\%$ at 2 K. (b) Expansion of the region in which additional Bragg peaks are expected to occur in the $Pnma$ structural model, where green vertical lines are error bars on the collected data. In this case, the peaks do not appear to be present.

Table 4.3: Rietveld refinement crystal structure parameters for the $P6_3/mmc$ model fitted to neutron powder diffraction data collected on HRPD at 300 K for $Zn_{0.60}Cu_{3.40}(OD)_6FBr$. Refined lattice parameters are $a = b = 6.67521(5)$ Å and $c = 9.31232(8)$ Å.

Atom	Site	x	y	z	Occupancy	U_{iso} (Å^2)
Cu1	6g	0.5	0	0	0.994(7)	0.0117(3)
Zn1	6g	0.5	0	0	0.006(7)	0.0117(3)
Cu2	6h	0.6312(7)	0.262(1)	0.25	0.139(7)	0.015(3)
Zn2	2d	0.6667	0.3333	0.25	0.58(2)	0.006(1)
F	2b	0	0	0.75	1	0.020(5)
Br	2c	0.6667	0.3333	0.75	1	0.0185(4)
O1	12k	0.20221(7)	0.79779(7)	0.90832(6)	1	0.0115(3)
D1	12k	0.12429(3)	0.87533(6)	0.86634(7)	0.982(2)	0.0231(4)
H1	12k	0.12429(3)	0.87533(6)	0.86634(7)	0.018(2)	0.0231(4)

a comparison of the R_{wp} values obtained (2.46% vs 2.73%) for a refinement of this structure compared to the hexagonal structure. However, it is hard to definitively assign a space group to these data given that the statistics make it unclear whether additional weak orthorhombic peaks are present, which were observed in the parent material at low temperature and described in Chapter 3. Even so, at 2 K these additional peaks are visible in the diffraction pattern, indicating that the lightly doped $x = 0.153(2)$ sample does undergo a symmetry lowering with decreasing temperature. The inset in Figure 4.5 shows the region in which these

Table 4.4: Rietveld refinement crystal structure parameters for the $P6_3/mmc$ model fitted to neutron powder diffraction data collected on HRPD at 1.5 K for $Zn_{0.60}Cu_{3.40}(OD)_6FBr$. Refined lattice parameters are $a = b = 6.66277(5)$ Å and $c = 9.28506(7)$ Å.

Atom	Site	x	y	z	Occupancy	U_{iso} (Å^2)
Cu1	6g	0.5	0	0	0.994(7)	0.0067(2)
Zn1	6g	0.5	0	0	0.006(7)	0.0067(2)
Cu2	6h	0.6322(5)	0.265(1)	0.25	0.139(7)	0.014(1)
Zn2	2d	0.6667	0.3333	0.25	0.58(2)	0.004(1)
F	2b	0	0	0.75	1	0.009(4)
Br	2c	0.6667	0.3333	0.75	1	0.0076(3)
O1	12k	0.20202(6)	0.79798(6)	0.90790(1)	1	0.0069(2)
D1	12k	0.12426(5)	0.87574(5)	0.86563(6)	0.982(2)	0.0172(3)
H1	12k	0.12426(5)	0.87574(5)	0.86563(6)	0.018(2)	0.0172(3)

Table 4.5: Rietveld refinement crystal structure parameters for the $P6_3/mmc$ model fitted to neutron powder diffraction data collected on GEM at 200 K for $Zn_{0.50}Cu_{3.50}(OD)_6FBr$. Refined lattice parameters are $a = b = 6.6687(2)$ Å and $c = 9.2964(3)$ Å.

Atom	Site	x	y	z	Occupancy	U_{iso} (Å^2)
Cu1	6g	0.5	0	0	0.991(3)	0.0067(1)
Zn1	6g	0.5	0	0	0.009(3)	0.0067(1)
Cu2	6h	0.6300(3)	0.2600(6)	0.25	0.176(3)	0.0036(7)
Zn2	2d	0.6667	0.3333	0.25	0.473(9)	0.0036(6)
F	2b	0	0	0.75	1	0.0142(3)
Br	2c	0.6667	0.3333	0.75	1	0.0109(2)
O1	12k	0.20194(5)	0.79806(5)	0.90807(4)	1	0.0067(1)
D1	12k	0.12453(4)	0.87547(4)	0.86619(5)	0.992(1)	0.0173(2)
H1	12k	0.12453(4)	0.87547(4)	0.86619(5)	0.008(1)	0.0173(2)

additional peaks are expected. Meanwhile, the $x = 0.50(1)$ sample crystallises in the hexagonal $P6_3/mmc$ space group at 200 K and appears to retain this structure down to 2 K. This is in agreement with another subsequent study [181], and is the first indicator that the $x = 0.50$ composition is a critical point in the Zn-barlowite series, which will be demonstrated throughout this chapter.

A full characterisation of the Zn-barlowite series should take into account the presence or absence of antisite disorder within their crystal structures, given that

Table 4.6: Rietveld refinement crystal structure parameters for the $P6_3/mmc$ model fitted to neutron powder diffraction data collected on GEM at 2 K for $Zn_{0.50}Cu_{3.50}(OD)_6FBr$. Refined lattice parameters are $a = b = 6.6636(2)$ Å and $c = 9.2817(2)$ Å.

Atom	Site	x	y	z	Occupancy	U_{iso} (Å^2)
Cu1	6g	0.5	0	0	0.991(3)	0.00384(8)
Zn1	6g	0.5	0	0	0.009(3)	0.00384(8)
Cu2	6h	0.6295(2)	0.2590(4)	0.25	0.176(3)	0.0024(4)
Zn2	2d	0.6667	0.3333	0.25	0.473(9)	0.0019(4)
F	2b	0	0	0.75	1	0.0081(2)
Br	2c	0.6667	0.3333	0.75	1	0.0039(2)
O1	12k	0.20179(4)	0.79821(4)	0.90791(4)	1	0.00429(8)
D1	12k	0.12426(4)	0.87574(4)	0.86578(4)	0.992(1)	0.0141(1)
H1	12k	0.12426(4)	0.87574(4)	0.86578(4)	0.008(1)	0.0141(1)

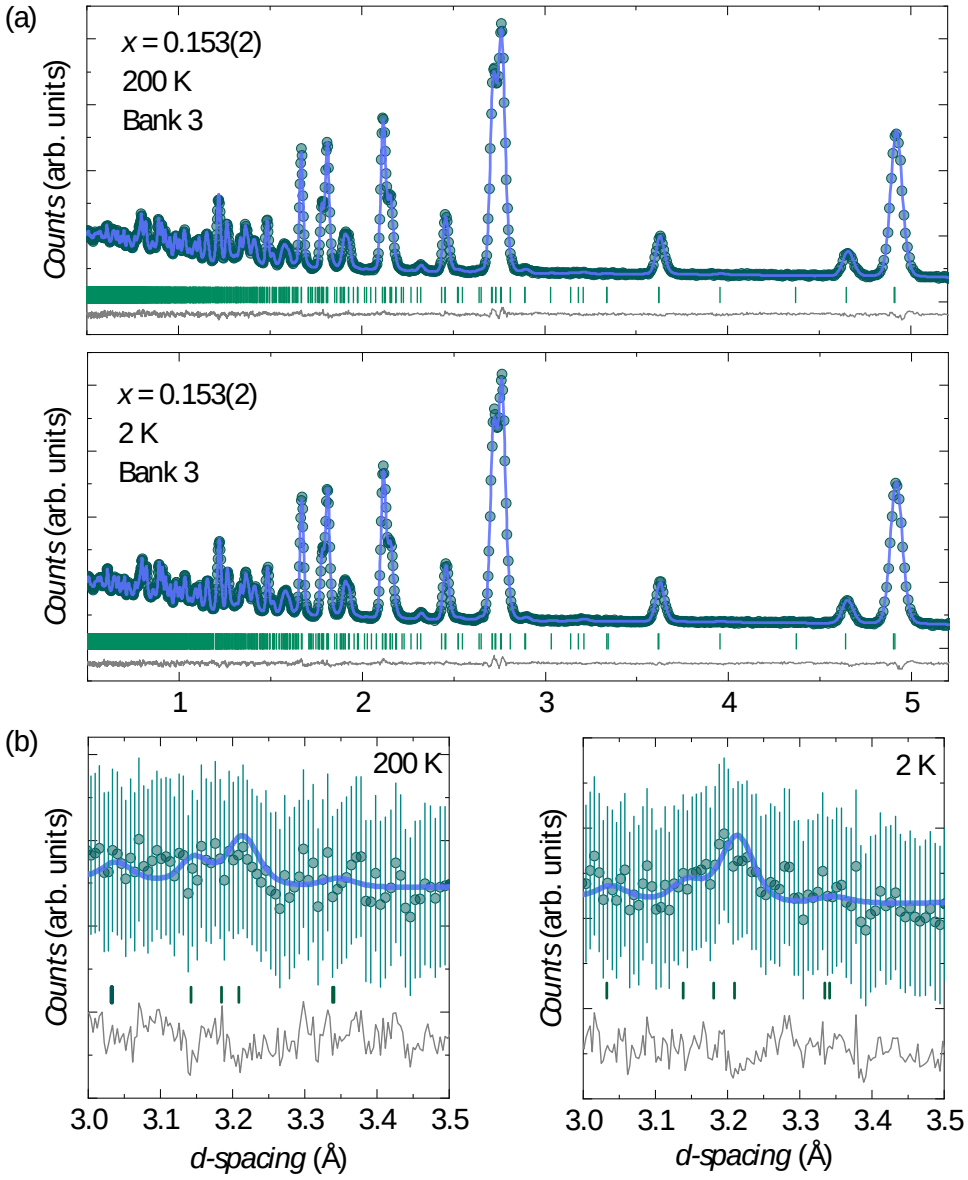

Figure 4.5: (a) Neutron powder diffraction data collected in Bank 3 of the GEM diffractometer at 200 K and 2 K for $Zn_{0.15}Cu_{3.85}(OH)_6FBr$ on HRPD. The solid blue line shows Rietveld refinements of the *Pnma* structural model to the data. The difference curve is shown in grey, whilst reflections are shown by green tick marks. Overall $R_{wp} = 2.46\%$ at 200 K and $R_{wp} = 2.30\%$ at 2 K. (b) Expansion of the region in which additional Bragg peaks are observed in the *Pnma* structural model, where green vertical lines are error bars on the collected data.

Table 4.7: Rietveld refinement crystal structure parameters for the *Pnma* model fitted to neutron powder diffraction data collected on GEM at 200 K for $Zn_{0.15}Cu_{3.85}(OD)_6FBr$. Refined lattice parameters are $a = 11.5640(5)$ Å, $b = 9.2940(3)$ Å and $c = 6.6800(3)$ Å.

Atom	Site	x	y	z	Occupancy	U_{iso} (Å^2)
Cu1	4*a*	0	0	0	1	0.0060(6)
Cu2	8*d*	0.2506(2)	0.5082(2)	0.2462(3)	1	0.0057(3)
Cu3	4*c*	0.1835(3)	0.25	0.0499(4)	0.75(1)	0.005(2)
Zn3	4*c*	0.1835(3)	0.25	0.0499(4)	0.25(1)	0.01(1)
F	4*c*	0.4982(5)	0.25	0.0026(6)	1	0.0143(3)
Br	4*c*	0.3324(4)	0.25	0.4968(4)	1	0.0095(2)
O1	8*d*	0.2957(2)	0.0977(2)	0.0009(4)	1	0.0036(4)
O2	8*d*	0.1005(3)	0.0878(3)	0.0878(3)	1	0.0062(5)
O3	8*d*	0.4009(3)	0.5889(3)	0.3026(5)	1	0.0079(5)
D1	8*d*	0.3783(3)	0.1250(3)	-0.0012(5)	0.988(6)	0.0154(7)
D2	8*d*	0.0639(3)	0.1351(3)	0.3123(4)	0.964(5)	0.0153(9)
D3	8*d*	0.4401(3)	0.6406(2)	0.1925(4)	1	0.0122(5)

this is a widely contested point in the study of herbertsmithite [71, 175–177]. To account for this in structural refinements to NPD datasets, an additional Zn site (Zn1) was placed within the kagomé layers and the occupancies of Zn1/Zn2 and Cu1/Cu2 sites were refined for high-temperature runs with a total Zn:Cu ratio constrained to that obtained from ICP-OES measurements. The coherent neutron scattering lengths of Cu and Zn are sufficiently different to allow for this analysis ($b_{Cu} = 7.718(4)$ fm and $b_{Zn} = 5.680(5)$ fm [190]). The obtained occupancies were then fixed for refinements to low-temperature data. The exception to this procedure is the lightly-doped $x = 0.153(2)$ sample, in which refining a Zn occupancy within the kagomé layers resulted in negative U_{iso} parameters. As a consequence, only the occupancies of the interlayer Zn3/Cu3 sites in the *Pnma* structure were refined, and the resulting structural models are shown in Table 4.7 for 200 K data and Table 4.8 for 2 K data, respectively. The refined Zn3 occupancy of 0.25(1) is higher than the composition obtained from ICP-OES. This is likely an indication that the low-statistics data collected on GEM, which has a much poorer resolution than HRPD, is inadequate for refining such small occupancies. For both GEM data collected for $x = 0.50(1)$ and HRPD data collected for $x = 0.60(1)$, refinements indicate that there is negligible Zn occupancy within the kagomé layers, as shown by Tables 4.3–4.6.

Table 4.8: Rietveld refinement crystal structure parameters for the *Pnma* model fitted to neutron powder diffraction data collected on GEM at 2 K for $Zn_{0.15}Cu_{3.85}(OD)_6FBr$. Refined lattice parameters are $a = 11.5451(3)$ Å, $b = 9.2811(2)$ Å and $c = 6.6818(2)$ Å.

Atom	Site	x	y	z	Occupancy	U_{iso} (Å^2)
Cu1	4*a*	0	0	0	1	0.0031(4)
Cu2	8*d*	0.2507(2)	0.5094(1)	0.2462(2)	1	0.0023(2)
Cu3	4*c*	0.1836(2)	0.25	0.0522(2)	0.75	0.0034(2)
Zn3	4*c*	0.1836(2)	0.25	0.0522(2)	0.25	0.0034(2)
F	4*c*	0.4986(3)	0.25	0.0047(5)	1	0.0080(2)
Br	4*c*	0.3314(2)	0.25	0.4994(3)	1	0.0035(1)
O1	8*d*	0.2966(2)	0.0967(2)	0.0011(3)	1	0.0025(3)
O2	8*d*	0.1007(2)	0.0903(2)	0.1984(3)	1	0.0041(4)
O3	8*d*	0.4015(2)	0.5882(2)	0.3032(3)	1	0.0036(3)
D1	8*d*	0.3779(2)	0.1285(2)	0.0005(4)	0.988	0.0013(5)
D2	8*d*	0.0637(2)	0.1340(2)	0.3139(3)	0.964	0.0121(5)
D3	8*d*	0.4404(2)	0.6395(2)	0.1915(3)	1	0.0112(4)

4.4 Magnetic Susceptibility and Bulk Magnetic Characterisation

The magnetic susceptibility data measured for the $Zn_xCu_{4-x}(OH)_6FBr$ series between 2 – 300 K in an applied field of 1 T are shown in Figure 4.6. No significant splitting between ZFC and FC susceptibilities is observed in data collected for all samples, and thus for the Zn-containing samples only ZFC data are shown. Data for Cu-only barlowite indicate the onset of magnetic ordering at $T_N = 15$ K, and the nature of this magnetic ordering is described in Chapter 3. In Figure 4.7 it can be seen that upon zinc doping the upturn in the magnetic susceptibility gradually shifts to lower temperatures. This likely indicates a suppression of the ferromagnetic coupling between the kagomé layers which was described for the parent material in Chapter 3. No indication of a transition to long-range magnetic order is observed in Zn-barlowite when $x > 0.66(1)$, although a Curie tail is present. This feature has also been observed in herbertsmithite and may indicate copper defects in the structures of both materials [154]. High temperature data follow Curie-Weiss behaviour and can be modelled between 150 – 300 K, as shown by fits of the Curie-Weiss law in Figure 4.6. The Weiss temperatures, θ, along with the effective magnetic moments per formula unit deduced from the Curie constant, C,

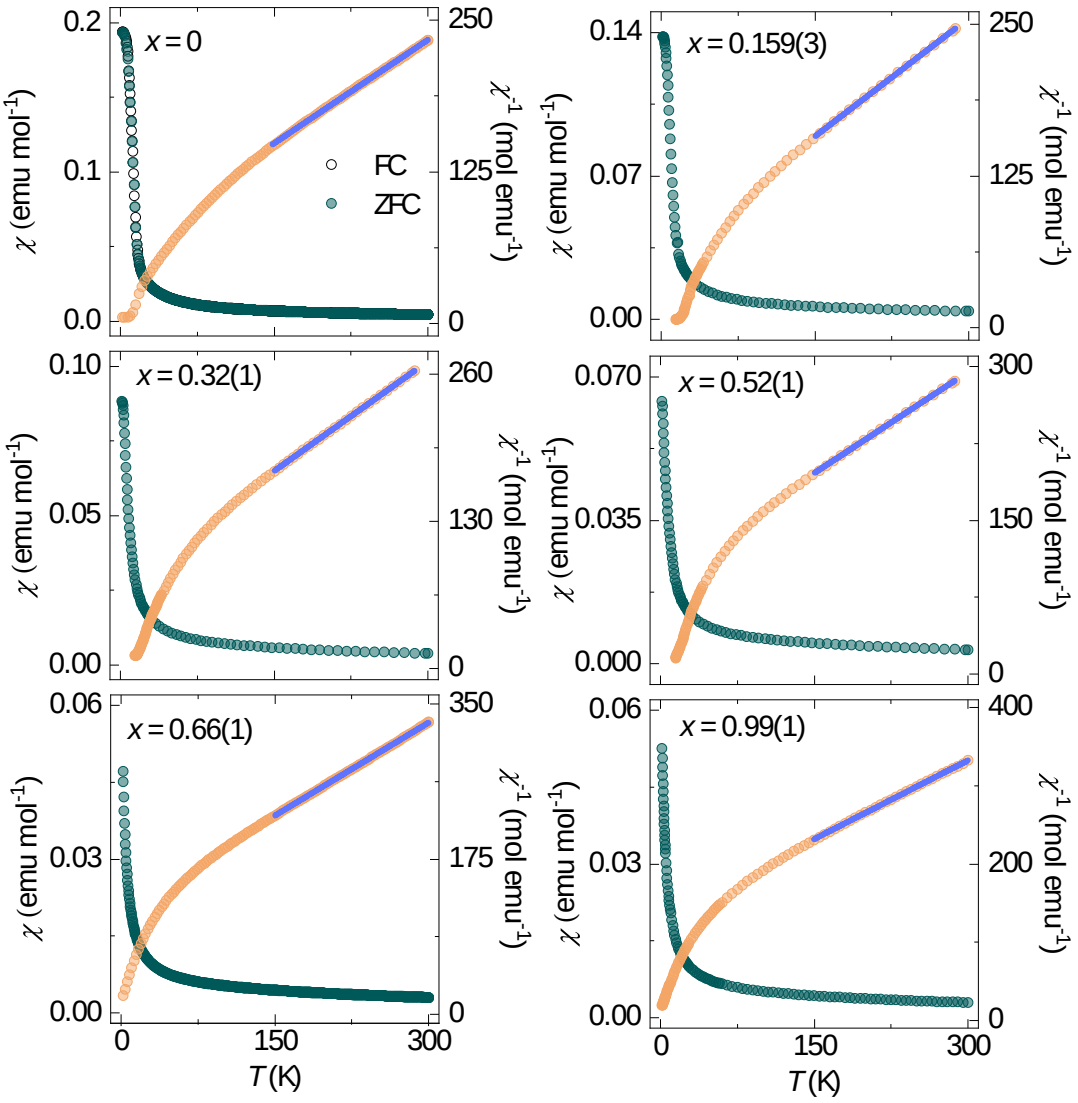

Figure 4.6: Temperature dependence of the magnetic susceptibility measured for the $Zn_xCu_{4-x}(OH)_6FBr$ series, with Curie-Weiss fits to the inverse susceptibility shown on the right hand axes.

are shown in Figure 4.7. θ is negative and increases in magnitude with increasing zinc content, demonstrating the increasingly dominant antiferromagnetic interactions across the series as the ferromagnetic exchange is suppressed. Meanwhile, μ_{eff} per formula unit decreases with increasing Zn content, which is intuitive given the replacement of paramagnetic Cu^{2+} with diamagnetic Zn^{2+} across the series.

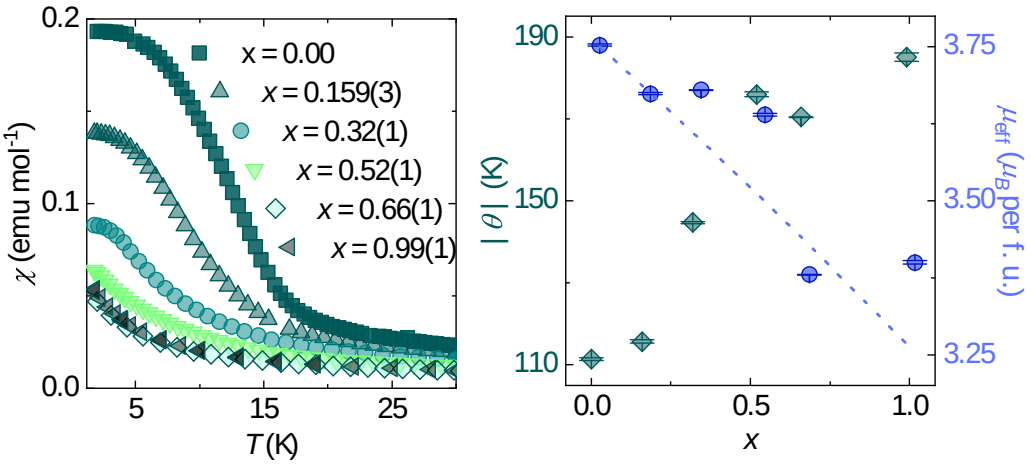

Figure 4.7: The low-temperature magnetic susceptibility for the $Zn_xCu_{4-x}(OH)_6FBr$ series (left) and the Weiss temperature, θ, and effective magnetic moment, μ_{eff}, obtained from Curie-Weiss fits (right). The dashed line indicates the expected variation in μ_{eff} with increasing x.

4.5 Muon Spectroscopy and Local Magnetic Characterisation

4.5.1 Zero Field Measurements

Figure 4.8 shows the muon decay asymmetry measured for barlowite, $Cu_4(OH)_6FBr$, in ZF on the MuSR spectrometer. At 20 K (above T_N), the observed relaxation is a consequence of the muon spin depolarisation due to the randomly oriented and non-interacting nuclear magnetic moments, which are static on the time scale of the muon experiment. Here, any contribution to the relaxation from unpaired electrons, whose spins are assumed to be dynamic at this temperature, is minimal. The long-time oscillations observed in the data indicate the formation of entangled states which are a result of dipolar coupling between the muon and nuclear spins. The most likely stopping sites for the positively charged muons are those in regions of high electron density, in this case, near the F^-, OH^- or Br^- anions. In order to identify the most probable muon stopping sites and assess the degree of perturbation the muon-probe causes in the system, DFT calculations were computed. The results of these calculations show that there are two classes of muon stopping site. The first involves the muon localising approximately 1.0 Å away from the oxygen atoms in the hydroxide groups that connect the Cu^{2+} ions within the kagomé layers of barlowite. This forms a triangular μ–OH complex, with the muon-proton

distance found to be 1.54 Å in the lowest-energy sites, as shown in Figure 4.9. This type of muonium complex has been observed in several copper-hydroxide minerals bearing a kagomé arrangement of magnetic ions [134, 178, 191–193]. A second class of muon stopping sites are found to localise at a distance of 1.1 Å from the fluoride anions which lie between the kagomé layers, as depicted in Figure 4.9. The formation of this class of muon stopping site is unsurprising given the high electronegativity of the fluoride anion and the characteristic oscillations in the data, which are a manifestation of the strong dipole-dipole interaction between the fluoride nuclear spin and the muon spin [133, 194]. However, calculations show that these μ–F sites lie at substantially higher energies above the lowest energy μ–OH sites ($\approx$ 1 eV). This suggests—on purely energetic grounds—that the formation of μ–F complexes in barlowite is unfavourable compared to μ–OH. However, in these types of DFT calculations, the pathway that the muon takes on the journey to its final stopping site is not taken into account, and rather the muon is placed randomly in low-symmetry sites and the structure allowed to relax [136]. In reality it is possible that the muons can be captured in local potential minima during their stopping process.

A model incorporating the two stopping sites predicted from DFT calculations was devised which, as shown in Figure 4.8, successfully describes the time-dependent asymmetry measured in ZF for barlowite in the paramagnetic regime:

$$A(t) = f_{\mathrm{F}} P_{\mathrm{F}}(t) \exp\Big(-\frac{\gamma_\mu^2 \Delta_{\mathrm{F}}^2 t^2}{2}\Big) + f_{\mathrm{OH}} P_{\mathrm{OH}}(t) \exp\Big(-\frac{\gamma_\mu^2 \Delta_{\mathrm{OH}}^2 t^2}{2}\Big) + A_{\mathrm{bg}} \exp(-\lambda_{\mathrm{bg}} t). \tag{4.2}$$

Here, A_{bg} accounts for the background contribution of muons that stop outside the sample, which is weakly relaxing, and the expressions $P_{\mathrm{F}}(t)$ and $P_{\mathrm{OH}}(t)$ describe the dipolar interactions between the nuclear magnetic moments of fluoride and hydroxide groups and the muon spin at each class of stopping site within the sample, given by [184],

$$P_{\mathrm{F(OH)}}(t) = \frac{1}{6} + \frac{1}{3}\cos\Big(\frac{\omega_{\mathrm{F(OH)}} t}{2}\Big) + \frac{1}{6}\cos\Big(\omega_{\mathrm{F(OH)}} t\Big) + \frac{1}{3}\cos\Big(\frac{3\omega_{\mathrm{F(OH)}} t}{2}\Big). \tag{4.3}$$

The oscillation frequencies ω_{F} and ω_{OH} are related to the respective μ–F and μ–H distances, $d_{\mathrm{F(H)}}$, through,

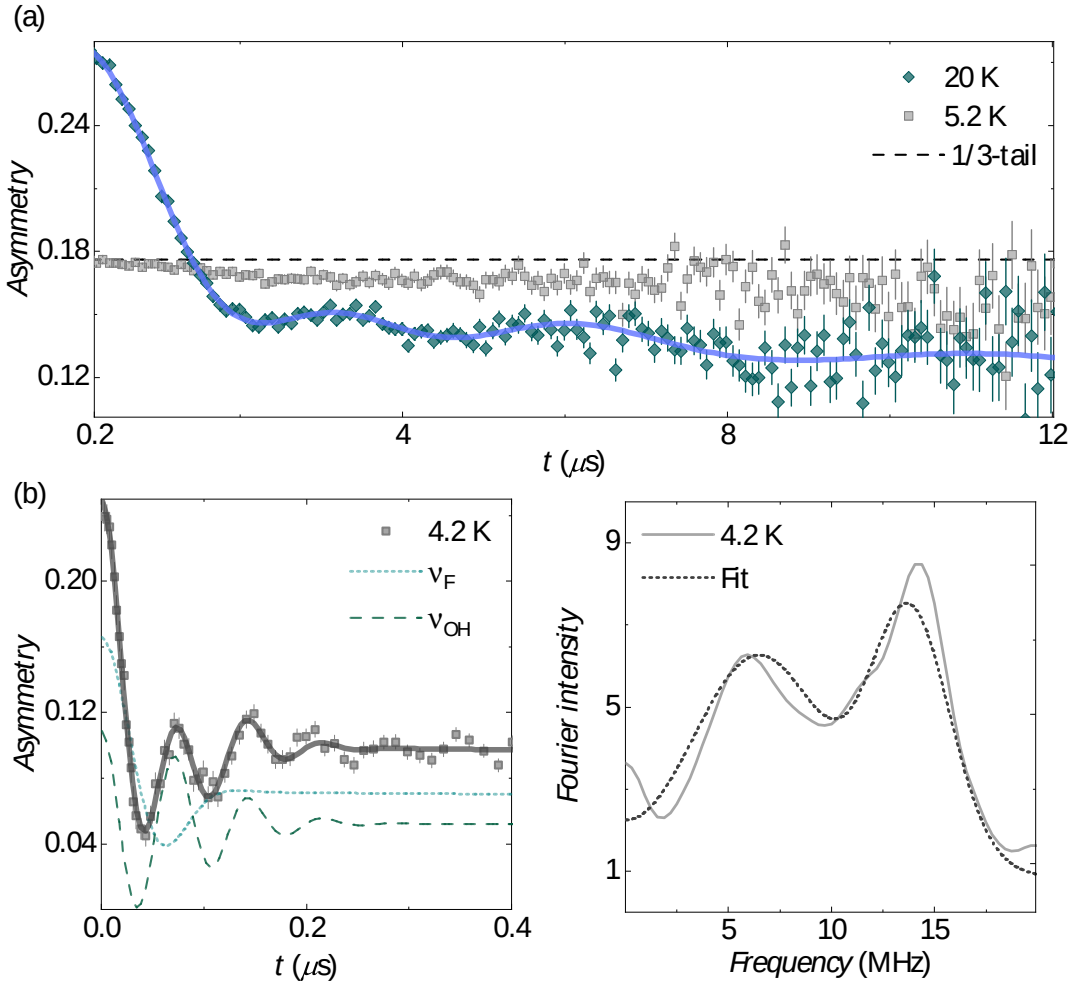

Figure 4.8: (a) The time-dependent muon decay asymmetry measured in zero field at 20 K and 5.2 K on the MuSR spectrometer for barlowite, $Cu_4(OH)_6FBr$. The solid line is a fit of Equation 4.3 to the 20 K data, and parameters obtained from this fit are shown in Table 4.10. The dashed horizontal line is a prediction for the position of the "one-third tail" at 5.2 K, deduced from subtracting the background from the initial asymmetry in the 20 K data and dividing by three. (b) The analogous data at short times measured on the GPS spectrometer at 4.2 K, where the solid line is a fit of Equation 4.6 to the data (left). The dashed lines indicate the two oscillating components contributing to the data. A Fourier transform of the time-dependent data (right) reveals two distinct frequencies. A comparison of the parameters obtained from the fits in parts (a) and (b) is shown in Table 4.9.

$$\omega_{\mathrm{F(OH)}} = \frac{\mu_0 \hbar \gamma_\mu \gamma_{\mathrm{F(H)}}}{4\pi d^3_{\mathrm{F(H)}}}, \tag{4.4}$$

where μ_0 is the permeability of free space and $\gamma_\mu = 2\pi \times 135.5$ MHz T^{-1}, $\gamma_\mathrm{F} = 2\pi \times 40.1$ MHz T^{-1} and $\gamma_\mathrm{H} = 2\pi \times 42.6$ MHz T^{-1} are the gyromagnetic ratios of the muon spin and the fluorine and hydrogen nuclear spins, respectively. The DFT calculations indicate that the muon can come to rest at the oxygen site of the OH^- in several different configurations, but which are separated in energy by < 0.1 eV. This is accounted for by the Gaussian damping terms included in Equation 4.3, where Δ_F and Δ_OH describe the distribution of nuclear fields which the muon experiences in each class of stopping site.

The implementation of muon-site calculations here is crucial, given that the lack of information on the location of the muon stopping site is a common limitation of μSR experiments, and that typically these types of data are modelled through a trial-and-error approach. Indeed, the high-temperature data collected here in ZF can be described using, for example, a model which incorporates an F–μ–F type entangled state [133], as shown in Appendix Figure 5. However, this is not supported by DFT calculations and signifies the importance of performing these types of computations. In addition, muon-site calculations using the method decribed in this chapter allow for a prediction of the muon-induced distortion of the crystal structure, which is important given that the muon response at low temperatures will be governed, in the case of magnetically-ordered barlowite, by its interaction with the magnetic fields induced by copper ions both between and within the kagomé layers. In this case, Figure 4.9 demonstrates that the kagomé planes remain largely intact upon muon implantation, with the nearest Cu^{2+} within the planes moving 0.094 Å and 0.149 Å from their original position in the μ–F and μ–OH classes of stopping site, respectively. Meanwhile, the interlayer Cu^{2+} is shifted by 0.0982 Å and 0.0528 Å in μ–F and μ–OH states, respectively.

Figure 4.8 shows the ZF data collected for barlowite below T_N. Here, the spins of the implanted muons are rapidly depolarised due to the internal electronic magnetic fields arising from the ordered Cu^{2+} moments in barlowite. The initial asymmetry in the MuSR measurements is lost owing to the time resolution of the pulsed beam utilised by the MuSR spectrometer. However, a 'one-third tail' is observed in the baseline asymmetry, which arises due to the presence of static magnetic moments in polycrystalline samples. This can be understood by consid-

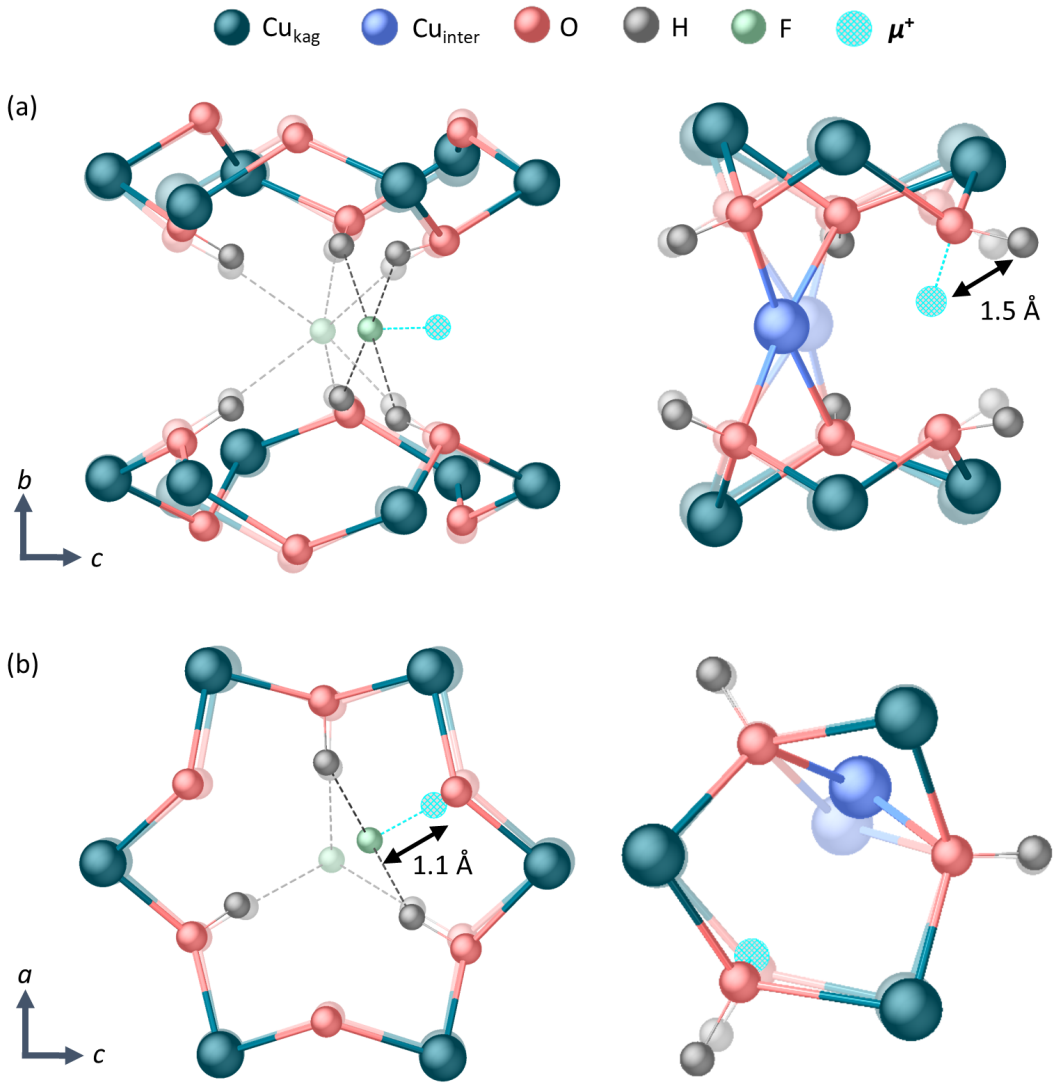

Figure 4.9: The two classes of muon stopping sites, μ–F (left) and μ–OH (right) determined from DFT calculations. The structures are viewed (a) along the a-axis, between the kagomé layers and (b) along the b-axis, perpendicular to the kagomé layers. Faded spheres indicate the unperturbed crystal structure before muon implantation.

ering that, in a sample with randomly oriented crystallites, statistically one-third of the implanted muons have their spin aligned parallel with the local field. The polarisation of one-third of the implanted muons is, therefore, unaffected by the development of internal fields [195]. An estimate for the one-third tail is shown by the dashed line in Figure 4.8(a). The weak relaxation in the tail described by λ_{bg} in Equation 4.3 is due to a fraction of muons interacting with the silver sample holder. Figure 4.8(b) shows ZF data collected on the GPS instrument at PSI, which is a continuous muon source and provides sufficient time-resolution to

capture the spontaneous oscillations apparent below 0.25 μs in the ZF asymmetry signal at 4.2 K, below T_{N}. These oscillations are characteristic of the muon spin precession around static internal fields of electronic origin at a frequency given by $\nu_i = (\gamma_\mu/2\pi)B_i^{\mathrm{loc}}$, where i stands for one muon stopping site and B_i^{loc} is the field at that muon site arising from the neighbouring static Cu^{2+} moments. The spontaneous oscillations in the ZF asymmetry data collected below T_{N} in Figure 4.8 can be modelled in terms of two classes of muon stopping site with the following expression,

$$A(t) = \sum_{i=1}^{2} A_i \Big[\frac{2}{3}\cos(2\pi\nu_i + \phi)\exp(-\sigma_i^2 t^2) + \frac{1}{3}\exp(-\lambda t)\Big] + A_{\mathrm{bg}}, \qquad (4.5)$$

where A_i is the fraction of muons stopping at each stopping site and A_{bg} is a background term. The cosine term describes the resultant oscillations in the data with a gaussian damping described by σ, whilst the second term accounts for the one-third tail. It is important to note that the relaxing term, λ, in the one-third tail is due to the small fraction of muons which stop in the aluminium foil used to hold the sample, and does not indicate residual dynamics in this case. This is unlike what is observed in clinoatacamite, the parent material to herbertsmithite, in which a coexistence between magnetic order and spin fluctuation was demonstrated in the relaxing tail of similar μSR measurements at low temperatures [128]. The results here are consistent with both DFT calculations and the ZF asymmetry above T_{N} which also point towards two muon stopping sites. The two dominant oscillating frequencies from this model, $\nu_1 = 6.3(2)$ MHz and $\nu_2 = 13.7(2)$ MHz, are clearly resolved in the Fourier transform of the GPS data, as shown in Figure 4.8. Additionally, the fitted amplitudes of each component, $a_1 = 64(2)\%$ and $a_2 = 36(2)\%$, are comparable to the stopping site fractions, $f_{\mathrm{F}} = 69(4)\%$ and $f_{\mathrm{OH}} = 31(4)\%$, obtained from fitting the ZF data above T_{N} in Figure 4.8 (see Table 4.9). This comparison can be used to assign the former signal to μ–F and the latter to the μ–OH classes of muon stopping site.

An additional comparison across these datasets can be made by taking the experimentally determined local fields which, from the fitted oscillating frequencies presented in Figure 4.8(b), are $B_{\mathrm{F}}^{loc} = 46$ mT and $B_{\mathrm{OH}}^{\mathrm{loc}} = 101$ mT, and comparing them to estimates for the local electronic magnetic moment dipolar fields of the calculated muon stopping site classes. This calculation is based on the known magnetic structure for barlowite below T_{N} [165], which was described in Chapter

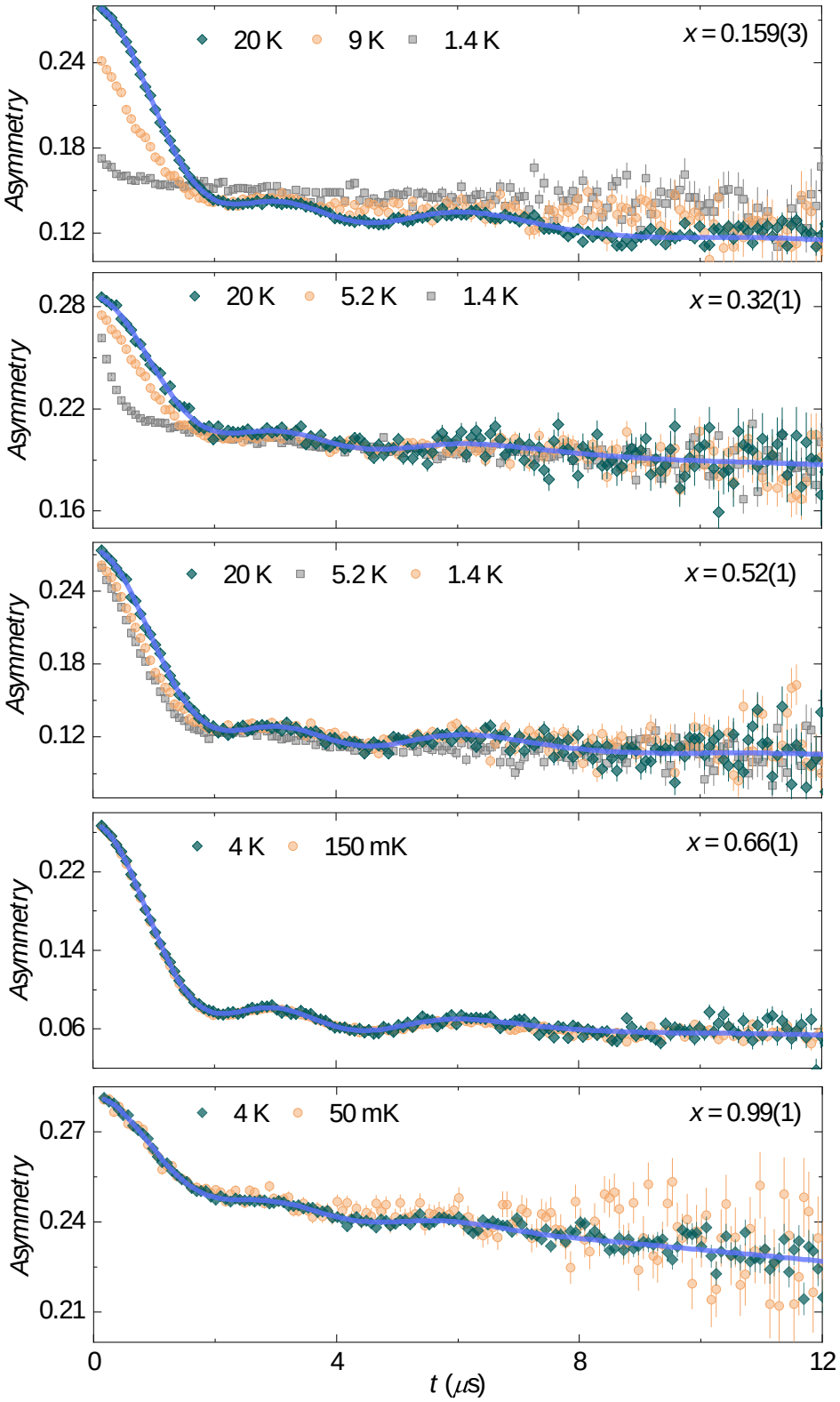

Figure 4.10: The time-dependent muon decay asymmetry measured in zero field on the MuSR spectrometer for the $Zn_xCu_{4-x}(OH)_6FBr$ series. Solid lines are fits of Equation 4.3 to the data, and the fitted parameters are shown in Table 4.10.

Table 4.9: A comparison of the fraction of muons stopping at each site, f, obtained from fits of Equation 4.3 to zero field MuSR data at 20 K and Equation 4.6 to zero field PSI data at 4.2 K, both shown in Figure 4.8, along with a comparison between experiment and calculation of the μ–F(H) bond lengths, d, and their local dipolar fields, B^{loc}, below T_{N}.

	f (%)		d (Å)		B^{loc} (mT)	
μ^+ Stopping Site	MuSR	GPS	MuSR	DFT	GPS	Calculated
F^-	69(4)	64(2)	1.22(1)	1.11	46(2)	55
OH^-	31(4)	36(2)	1.50(3)	1.54	101(2)	120

3. For the lowest-energy μ–OH stopping sites, these calculations yield local fields around 120 mT, along with a few around 75 mT, although this is under the assumption that the crystal structure remains unperturbed by the incoming muon. If the muon-induced distortion is taken into account, in which the closest Cu^{2+} ion within the kagomé planes is moved 0.45 Å away from its original position (see Figure 4.9), even smaller fields are obtained of down to 50 mT. The $B_{\mathrm{OH}}^{\mathrm{loc}}$ fields calculated are, therefore, clearly sensitive to this distortion induced by the muon, although it is likely that the effect is overestimated due to the relatively small supercell size used in these calculations. The average $B_{\mathrm{F}}^{\mathrm{loc}}$ for the μ–F class of stopping sites is around 55 mT, and inclusion of the muon-induced distortion has little effect on the fields obtained. This is logical given that, although the fluoride site is shifted by 0.65 Å away from its original position due to muon implantation, there is negligible distortion of the kagomé planes, as depicted in Figure 4.9. Crucially, however, these calculated fields are comparable to the fields determined from data collected at PSI, and this reinforces the possibility of the formation of μ–F stopping sites in barlowite despite their overall higher energy compared with μ–OH. A comparison of the three datasets *i.e.* MuSR, PSI and calculations, are shown in Table 4.9.

The ZF asymmetry at 20 K measured for $Zn_xCu_{4-x}(OH)_6FBr$, displayed in Figure 4.10, shows a similar response to the parent compound: a slow decrease in asymmetry with time due to depolarisation of the muon spin, and oscillations at long times characteristic of dipolar coupling between the muon and nuclear spins. The background contribution, however, inevitably varies with the different sample sizes implemented in these measurements. DFT calculations have been undertaken in which the inclusion of Zn^{2+} ions and the hexagonal space group symmetry of the Zn-substituted samples yields similar classes of muon stopping sites compared

Table 4.10: Parameters obtained from a fit of Equation 4.3 to data collected in zero field on MuSR for $Zn_xCu_{4-x}(OH)_6FBr$, shown in Figure 4.10. f describes the fraction of muons at each of the two stopping sites, μ–F and μ–OH. ω is the angular frequency used to calculate the μ–F or μ–OH distances, d, and Δ describes the distribution of fields at each site induced by dipolar coupling to nearby nuclei.

	μ–F				μ–OH			
x	f (%)	ω (Mrad s^{-1})	Δ (mT)	d (Å)	f (%)	ω (Mrad s^{-1})	Δ (mT)	d (Å)
0	69(4)	1.23(2)	0.43(3)	1.22(1)	31(4)	0.72(2)	0.18(3)	1.50(3)
0.159(3)	65(2)	1.25(1)	0.44(1)	1.22(1)	35(1)	0.68(1)	0.22(1)	1.52(1)
0.32(1)	70(8)	1.24(4)	0.48(1)	1.22(3)	30(6)	0.63(1)	0.25(9)	1.56(9)
0.52(1)	66(4)	1.25(2)	0.45(3)	1.22(1)	34(2)	0.67(2)	0.23(4)	1.53(4)
0.66(1)[a]	70(2)	1.30(1)	0.48(2)	1.20(1)	30(2)	0.67(1)	0.27(2)	1.54(2)
0.66(1)[b]	72(2)	1.29(1)	0.50(1)	1.20(1)	28(1)	0.65(1)	0.30(2)	1.53(2)
0.99(1)[a]	61(7)	1.32(3)	0.41(5)	1.20(2)	39(6)	0.69(4)	0.31(8)	1.51(7)

with the parent orthorhombic structure. Equation 4.3 can be successfully used to describe these data and is shown in Figure 4.10 with the fitting parameters given in Table 4.10, which do not vary significantly across the series. This further suggests that the muon stopping sites do not alter across the series. Upon cooling, qualitatively it can be seen that the rate of depolarisation of the muon spin decreases as the Zn^{2+} content is increased further, indicating that until $x = 0.52(1)$ dynamic magnetic correlations increasingly dominate the ZF asymmetry at low temperature. Moreover, the one-third tail observed in the parent compound is not recovered in all Zn-containing samples, indicating a dynamic fraction down to the lowest measurable temperatures. Finally, for samples with $x > 0.66(1)$, the asymmetry observed at low temperature is comparable to that at 20 K, and can additionally be modelled using Equation 4.3, again with negligible variation in the fitted parameters (see Table 4.10). It can be inferred from this that there is no development of a static local field at low temperatures, and that the muon spin remains coupled to weak nuclear moments in these samples even at 50 mK in the case of the fully substituted $x = 0.99(1)$ sample.

4.5.2 Transverse Field Measurements

In order to quantitatively track the effect observed in ZF data with increasing Zn content, x, a TF field of 20 G was applied to intermediate samples within the $Zn_xCu_{4-x}(OH)_6FBr$ series and measurements were taken at temperatures spanning the magnetic ordering regime in barlowite. The applied field is deliberately chosen to be weak compared to the magnitude of the internal fields in the magnetically ordered material. This ensures that above T_N the muon spin will precess at a frequency, ν_{TF}, which is characteristic of the applied transverse magnetic field, resulting in oscillations in the measured signal. Below T_N, the development of local internal fields dominates the muon spin depolarisation and can result in a loss of asymmetry and a dephasing of the oscillations. Both of these features are demonstrated for barlowite in Figure 4.11. The observed oscillations can be modelled by,

$$A(t) = [A_p \exp(-\lambda_{TF} t) + A_{bg} \exp(-\sigma_{bg}^2 t^2)] \times \cos(2\pi\nu_{TF} t + \phi) + B, \qquad (4.6)$$

where A_p provides a measure of the paramagnetic volume fraction of the sample and A_{bg} gives the background contribution of muons that stop in the silver sample holder, and is fixed within a given sample to the value at high temper-

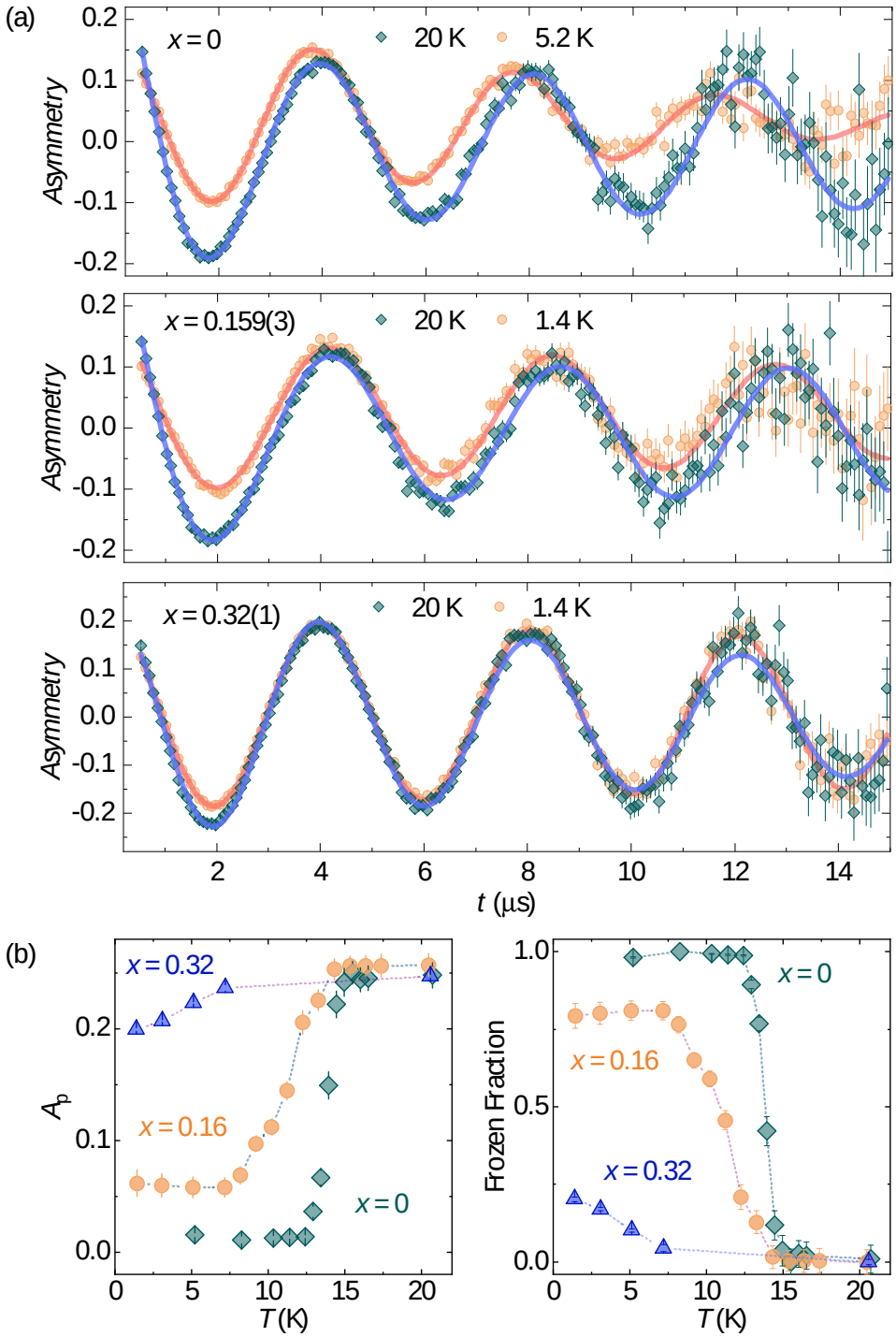

Figure 4.11: (a) The muon decay asymmetry measured in transverse field on the MuSR spectrometer for the $Zn_xCu_{4-x}(OH)_6FBr$ series. (b) The oscillating asymmetry, A_P, as a function of temperature (left), determined from fits of Equation 4.7 to transverse field data, and the resulting frozen fraction in each sample (right).

ature. Both of these components cause a damping of the oscillations described by λ_{TF} and σ_{bg}, respectively. The baseline B accounts for the fraction of muons with their spin polarisation aligned with the local magnetic fields in the ordered state of the sample in question, and can be tracked in a similar manner to the one-third tail described in ZF data. For example, in the $x = 0$ sample below T_{N}, B tends to one-third of the asymmetry we observe in the paramagnetic state and $A_{\mathrm{p}}(5.2\ \mathrm{K}) = 0$, meaning that the observed oscillations at 5.2 K originate from a background contribution. By fitting this model to TF data collected over a range of temperatures, A_{p} can be closely tracked. The normalised inverse of this value [*i.e.* $1 - A_{\mathrm{p}}(T)/A_{\mathrm{p}}(20\ \mathrm{K})$], represents the frozen volume fraction of static magnetic moments within a sample. For example, in data collected for the $x = 0$ sample, a sudden drop in A_{p} at $T_{\mathrm{N}} = 15$ K corresponds to a dramatic increase in the static volume fraction, demonstrated in Figure 4.11. The same analysis can be applied to samples in the Zn-barlowite series upon increasing Zn^{2+} content, and this provides a quantitative analysis which reinforces the observed asymmetry for these samples measured in ZF. Figure 4.11(b) shows the temperature dependence of the frozen volume fraction for $Zn_xCu_{4-x}(OH)_6FBr$ with $x = 0.159(3)$ and 0.32(1). For $x = 0.159(3)$ an extended magnetic ordering regime is calculated, while for the $x = 0.32(1)$ sample, the frozen fraction at base temperature is vastly reduced compared with the parent $x = 0$ compound. Taken together with ZF data, these results suggest a coexistence of static and dynamic magnetic correlations within these intermediate samples.

4.5.3 Longitudinal Field Measurements

A final set of measurements in an applied LF were performed on samples with $x = 0.66(1)$ and $x = 0.99(1)$, where ZF data indicate an absence of ordered internal moments at low temperatures (see Figure 4.10). Such an applied longitudinal field has the effect of decoupling the muon spin from nuclear magnetic moments, which are weak in comparison to moments arising from dynamic or static electron moments, allowing us to track the dynamical correlations within these highly-substituted samples. Initially, a field scan was implemented to determine the strength of field needed to decouple the nuclear moments, which is shown in Figure 4.12 for $x = 0.66(1)$ K at 150 mK. Here, it is clear that an applied LF of 100 G is sufficient to remove the characteristic features of the muon entanglement with nuclear moments which dominate ZF data. Larger applied fields simply result in a modest decrease in the relaxation observed, which can be attributed to a weak decoupling of fluctuating electron moments. LF data, shown in Figure 4.13(a) at

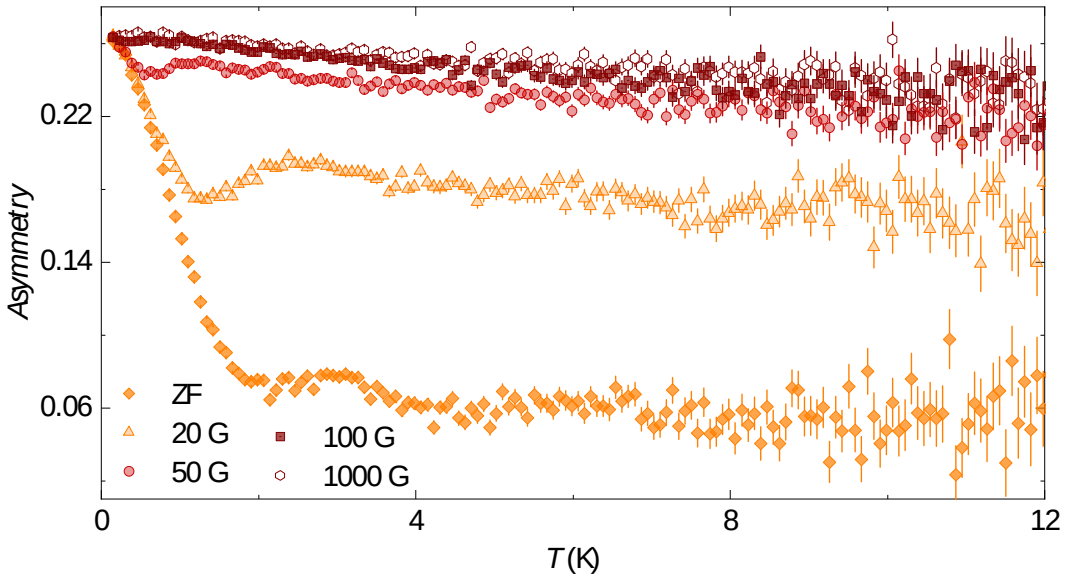

Figure 4.12: The longitudinal field dependence of the muon decay asymmetry measured for $Zn_{0.66}Cu_{0.34}(OH)_6FBr$ at 150 mK. A field of 100 G is sufficient to decouple the muon spin from the nuclear magnetic moments which give rise to oscillations in the ZF data.

various temperatures, can be modelled using an exponential function,

$$A(t) = A_{\mathrm{r}} \exp(-\lambda t) + A_{\mathrm{bg}} \tag{4.7}$$

where λ is the muon spin relaxation rate, A_{r} is the relaxing amplitude and A_{bg} is the background contribution. Figure 4.13(b) shows the fitted parameter λ as a function of temperature for $x = 0.66(1)$ and $x = 0.99(1)$ samples. The magnitude of λ is described by the Redfield equation, given by [196],

$$\lambda = \frac{2\gamma_\mu^2 \Delta^2 \tau}{1 + \gamma_\mu^2 B_{\mathrm{LF}}^2 \tau^2}, \tag{4.8}$$

where B_{LF} is the applied longitudinal-field and Δ and τ are the internal electronic magnetic field distribution and its fluctuation time, respectively. Figure 4.13, therefore, demonstrates a slowing down of dynamic fluctuations below 1 K for both samples with a plateau in λ at low temperature—in the case of $x = 0.99(1)$, down to at least 50 mK—which indicates an absence of ordering or freezing of magnetic moments, and instead suggests the presence of dynamic fluctuations with a temperature-independent fluctuation time. Intuitively, one might expect that Δ will decrease as paramagnetic Cu^{2+} is replaced with diamagnetic Zn^{2+},

and that τ will correspondingly increase as the system approaches a liquid-like state and static magnetic order is suppressed, resulting in a decrease in the overall magnitude of λ with increasing x. This is indeed what was observed in the Zn-paratacamite series, where the magnitude of λ was shown to decrease with increasing Zn^{2+} substitution [134]. It is, therefore, initially intriguing that the opposite is observed in Zn-barlowite. In reality, however, the contributions of Δ and τ to the overall muon spin relaxation rate as we move across the series may not be so straightforward, as it is possible that at low temperatures, the muon is predominantly coupled to the residual interlayer Cu^{2+} moments. The coupling of the muon predominantly to interlayer spins has been demonstrated with an analogous mineral Zn-brochantite, $ZnCu_3(OH)_6SO_4$, where it was additionally shown that the interlayer spins are correlated with the kagomé spins via a Kondo-like effect [197, 198]. If this is the case for Zn-barlowite, there will be a decrease in the dominant dipolar fields coupling to the muon spin as the concentration of these defect spins decreases with increasing x. This may explain the variation in the magnitude of λ between samples shown in Figure 4.13(b) compared with the herbertsmithite series [134].

The plateau observed in the muon spin relaxation rate is a characteristic feature described in the literature and is attributed to the presence of a QSL ground state [47, 134, 139, 199–201], which is characterised by persistent magnetic fluctuations down to $T = 0$ K. However, Equation 4.9 demonstrates that the magnitude of the plateau is dependent on several different sample and experimental factors. For example, it has already been demonstrated that sample composition has a marked effect on this parameter. Additionally, variations in experimental setup such as the background signal and the chosen applied longitudinal field will have an effect on the reported value of λ. A consequence of this is that it is difficult to compare this parameter across different QSL candidates, even within the same family of materials. Instead, by plotting the normalised relaxation rate, λ_{norm}, as a function of temperature, the dynamical moment correlations can be directly compared across datasets. Indeed, for the two compositions explored in applied longitudinal fields, which have already been demonstrated to be magnetically disordered, the magnitude of Δ is expected to be largely temperature-independent within a given sample, meaning λ_{norm} allows for the temperature-dependent parameter τ to be directly probed. Figure 4.13(b) (right) shows λ_{norm} for $x = 0.66(1)$, $x = 0.99(1)$ and for data collected previously for herbertsmithite [134]. The values for λ_{norm} were obtained by normalising the collected data between 0 and 1 with respect to the

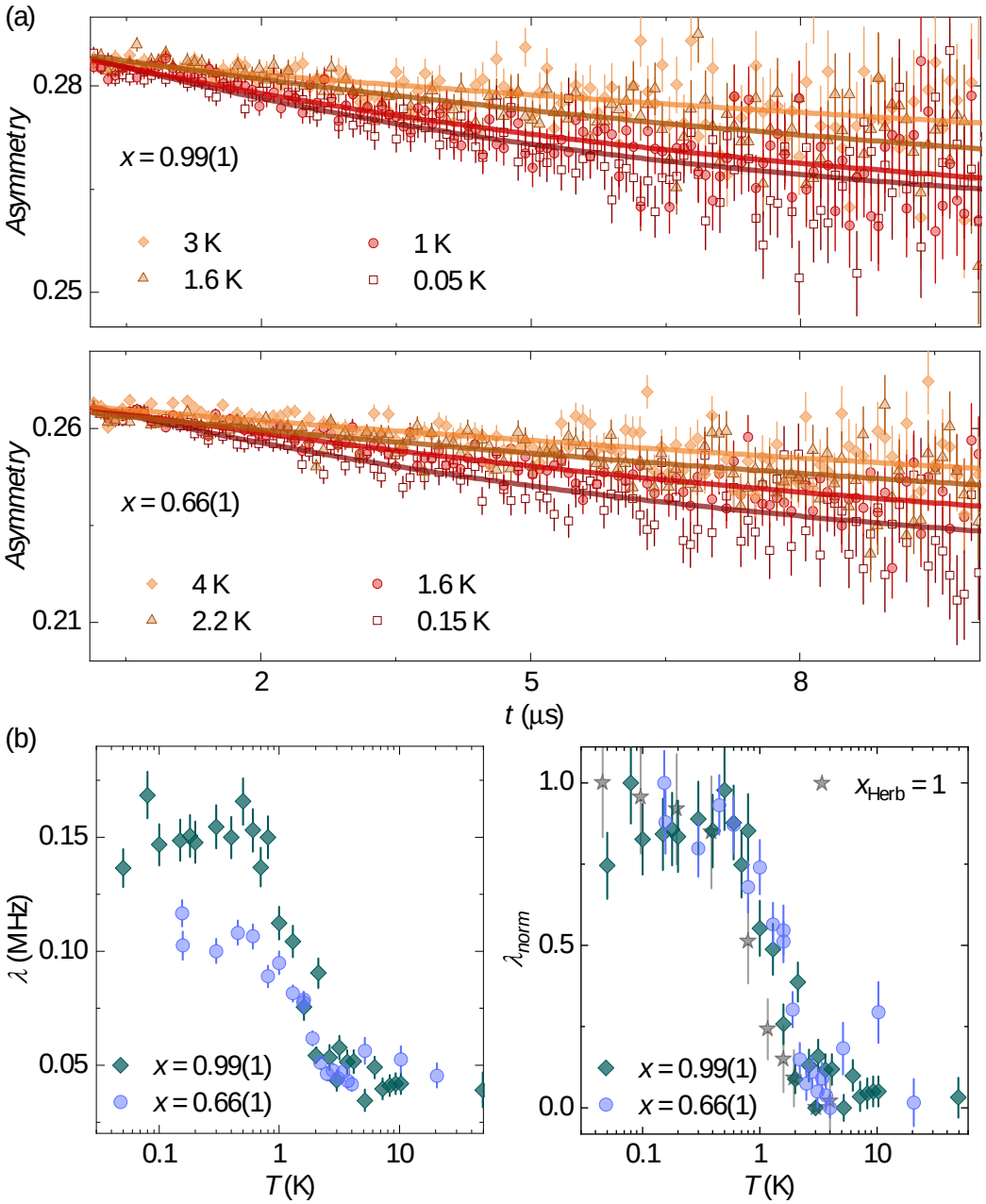

Figure 4.13: (a) The muon decay asymmetry measured in longitudinal fields for $x = 0.99(1)$ (top) and $x = 0.66(1)$ (bottom) samples of the $Zn_xCu_{4-x}(OH)_6FBr$ series. (b) The muon spin relaxation rate, λ, as a function of temperature for $x = 0.66(1)$ and $x = 0.99(1)$ samples, determined from fits to Equation 4.8 (left). The normalised muon spin relaxation rate, λ_{norm}, as a function of temperature for $x = 0.66(1)$ and $x = 0.99(1)$ samples and for herbertsmithite, as deduced from data taken from reference [134] (right).

maximum and minimum values of λ within each data set. The results demonstrate a marked similarity in the temperature dependence of λ_{norm} between $x = 0.66(1)$ and $x = 0.99(1)$ samples. This suggests that the dynamical field fluctuations in the $x = 0.66(1)$ sample are robust to the interlayer exchange interactions which will inevitably be mediated through Cu^{2+} ions which lay between the kagomé planes. Consequently, it follows that fully-substituted Zn-barlowite should also be insensitive to the presence of antisite disorder. Additionally, a plot of comparable data for herbertsmithite reveals further similarity in the temperature dependence of the muon spin relaxation rate in herbertsmithite and Zn-barlowite, perhaps indicating some universality in the progression to the suspected QSL ground state in these hydroxy-halide systems.

4.6 Conclusions

Polycrystalline samples of the Zn-barlowite series, $Zn_xCu_{4-x}(OH)_6FBr$, have been prepared via hydrothermal synthesis techniques, and a comprehensive study combining NPD, magnetic susceptibility and muon spectroscopy measurements is summarised as follows:

- NPD data indicate that the hexagonal $P6_3/mmc$ structure is retained at all temperatures when $x > 0.50$, and refinement of Cu^{2+} and Zn^{2+} occupancies suggests that there is negligible antisite disorder within their crystal structures. This conclusion is important because the maintenance of the kagomé layers within Zn-barlowite is crucial to understanding its low-temperature magnetic behaviour.

- Following the discovery that the $x = 0$ end-member orders antiferromagnetically below $T_N = 15$ K, magnetic susceptibility measurements have revealed that upon replacing the interlayer Cu^{2+} site with diamagnetic Zn^{2+}, the magnetic ordering temperature is suppressed across the series. This is despite strong exchange interactions indicated by Curie-Weiss analysis, where for $x = 0.99(1)$ $\theta = 185(1)$ K and there is no evidence for a transition to long-range magnetic order down to 2 K.

- μSR measurements support these observations, with the parent $x = 0$ material undergoing magnetic ordering below $T_N = 15$ K, as evidenced by both ZF and TF measurements. Modelling of the latter datasets have also allowed for the magnetically frozen fraction to be tracked as a function of temperature for intermediate samples, indicating a coexistence of static and dynamic magnetic moments at low temperatures.

- Finally, an important result from LF measurements is that samples with $x > 0.66$ retain a dynamically fluctuating state down to 50 mK, indicating that Zn-barlowite has a frustration index $f > 3700$. From bulk and local magnetic studies, therefore, it is concluded that the evidence presented in this chapter points towards the presence of a QSL state in highly-substituted Zn-barlowite samples.

The findings within this chapter are illustrated in the low-temperature magnetic phase diagram for the Zn-barlowite series which has been constructed from this study, shown in Figure 4.14. This is notably similar to that deduced for the Zn-paratacamite series [134], and is well-reproduced by another recent μSR study

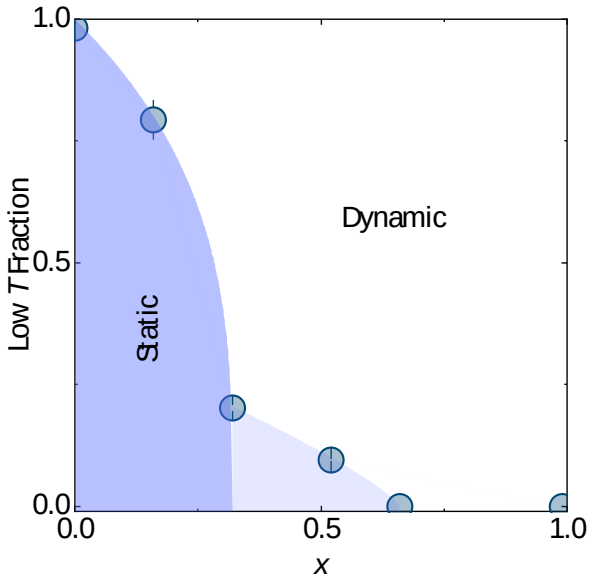

Figure 4.14: Phase diagram for the Zn-barlowite series, $Zn_xCu_{4-x}(OH)_6FBr$, where the low-temperature frozen fraction is obtained from transverse field measurements for $x = 0$, $x = 0.159(1)$ and $x = 0.32(1)$ samples and from longitudinal field measurements for $x = 0.66(1)$ and $x = 0.99(1)$ samples. For $x = 0.52(1)$, an estimate for the low-temperature fraction was made by taking the asymmetry at t_0 in zero field as a proportion of the full asymmetry at high temperature.

[181]. Both systems indicate that the $x \approx 0.50$ composition marks a critical point above which dynamic magnetic moment correlations persist down to the lowest measurable temperatures. These findings are particularly pleasing given a recent study in which single crystals of Zn-barlowite with $x = 0.56$ were found to remain dynamic down to 2 K, as deduced from bulk magnetometry measurements [151]. However, there remain several avenues that may be taken to explore this family of materials further:

- Whilst NPD is a valuable tool for the initial exploration of antisite disorder, further methods which probe different length scales will be required to explore this idea further. Indeed, a comprehensive study implementing site-specific X-ray anomalous diffraction and extended X-ray absorption fine structure (EXAFS) measurements has recently offered convincing evidence that there is no Zn occupancy of the kagomé layers [202], and this supports the present study.

- The nature of this QSL ground state, which can be probed via inelastic neutron and NMR spectroscopies, will make a compelling future study, although the development of reliable synthetic techniques for good-quality

single crystals will be crucial to unravelling the impact of structural defects on the low-temperature magnetic ground state across the series.

- Further direct comparison to similar systems, including Zn-paratacamite and Zn-claringbullite, the latter of which is still largely unexplored [173], will be interesting.

- One additional intriguing viewpoint, which has been predominantly explored in the magnetically ordered barlowite [151, 160], is that there is some sample dependence with respect to the crystal structure and magnetic response observed in this family of materials. It will, therefore, be crucial to investigate if the same is true of the Zn-doped analogues if we are to completely understand this series and the potential QSL state which lies within it.

The conclusions from this chapter are underpinned by complementary muon-site DFT calculations, in which the computed classes of muon stopping sites, μ–F and μ–OH, are confirmed via modelling of the distinct oscillations in ZF data for all samples measured. Moreover, the muon-induced distortion is found to be minimal, providing confidence that the muon is probing the intrinsic magnetism of the Zn-barlowite series. This is further supported by comparisons between experimentally determined local fields in barlowite to those calculated based on the computed muon stopping sites. In this sense, the Zn-barlowite series provides an ideal model in which to test the robustness of these DFT calculations, given that it contains a magnetically ordered analogue with which to perform these types of comparisons. From this we can infer that the quantum disordered ground state in Zn-barlowite is adequately probed by the muon. Overall, this combined study, therefore, illustrates the significance of implementing muon-site DFT calculations in μSR studies more widely, as this approach is a useful tool to guide and interpret the modelling of complex muon data.

Chapter 5

Unconventional Magnetism in a Family of Kagomé Metal-Organic Frameworks

5.1 Introduction

In the discovery of novel quantum materials, a drive towards minimising site disorder has led to increasing interest in hybrid inorganic-organic systems as alternatives to purely inorganic compounds. In this instance, separating the magnetic layers with organic components often diminishes the issue of disorder which is common in purely inorganic systems [71, 72, 151]. The ability to modify this organic component also opens up the possibility of exploring families of closely related materials [86]. Metal-organic frameworks (MOFs) are one class of hybrid materials which are of interest in this regard, and consist of metal-containing nodes linked by multitopic organic ligands. The combinatorial variety of organic linkers and metallic centres available makes MOFs a diverse class of solid state materials with the potential for a number of topological isomers depending on the three-dimensional connectivity. MOFs are of interest for many applications such as gas storage [203], catalysis [204] and sensing [205], in addition to their potential for novel magnetic materials [73]. This versatility has been explored, for example, in multifunctional MOFs which combine magnetic functionality and porosity [206]. However, more recent computational studies [207, 208] which propose the existence of unconventional physical phenomena arising in two-dimensional MOFs has led to growing interest in this class of materials in the field of quantum magnetism [209].

There are numerous examples of MOFs bearing a kagomé arrangement of magnetic ions [210–214], but often these structures are imperfect and are complicated by the

presence of long exchange pathways and interpenetrating lattices [215]. The first example of an ideal kagomé network composed of $S = \frac{1}{2}$ Cu^{2+} ions was a compound exploiting isophthalic acid pillars to separate the kagomé layers, known as Cu(1,3-*bdc*), where 1,3-*bdc* = 1,3-benzenedicarboxylate. The highly symmetric structure, containing half of a crystallographically independent Cu^{2+} ion, was found to exhibit strong antiferromagnetic interactions via Curie-Weiss analysis, but the system orders magnetically at 2 K, indicating the presence of highly frustrated magnetism [211]. However, neutron scattering studies subsequently revealed the presence of ferromagnetic kagomé layers in this system, which are coupled weakly via an antiferromagnetic interaction along a seven-atom superexchange pathway between Cu^{2+} ions in different layers [216]. Whilst not, therefore, a candidate for quantum spin liquid physics, Cu(1,3-*bdc*) has been shown to demonstrate topological magnon bands, a unique physical property from which the quantum Hall effect can emerge. Indeed, there is growing interest in kagomé ferromagnets because they are predicted to display such unique electronic properties, which may have applications in the field of spintronics [217]. Another example of a Cu^{2+} based kagomé MOF is the 2D $Cu_3(HHTP)_2$, where HHTP = hexahydroxytriphenylene, which not only evades long-range magnetic ordering down to 38 mK [213], but is also a semiconductor, demonstrating the potential for multifunctionality in these types of materials. However, even this MOF suffers from disorder via the presence of an observable amount of diamagnetic Cu^{+} cations thought to occur due to structural defects.

Another kagomé MOF that has gained recognition is $Cu_3(CO_3)_2(bpe)_3{\cdot}2ClO_4$, where *bpe* = 1,2-bis(4-pyridyl)ethane [218]. This MOF adopts a structure containing kagomé layers of Cu^{2+} ions that are ligated by CO_3^{2-} and separated by a pillaring ligand, in this case the flexible *bpe* which displays orientational disorder about its alkyl bond, as depicted in Figure 5.1. Initial reports on this MOF sparked intrigue because the heat capacity data does not present a sharp anomaly associated with long-range magnetic order, despite magnetic susceptibility and ^{1}H NMR studies indicating ferromagnetic order below $T_C \approx 12$ K [218–220]. In a more recent study, however, it has been hypothesised that this MOF displays short-range canted antiferromagnetic order, with competing ferromagnetic and antiferromagnetic interactions within the kagomé layers, based on in-field AC magnetic susceptibility and the absence of magnetic scattering in neutron powder diffraction data [92]. As a result of these conflicting models, there is scope for the clarification of the magnetic behaviour in this material. Furthermore, the bidentate *bpe* ligand used

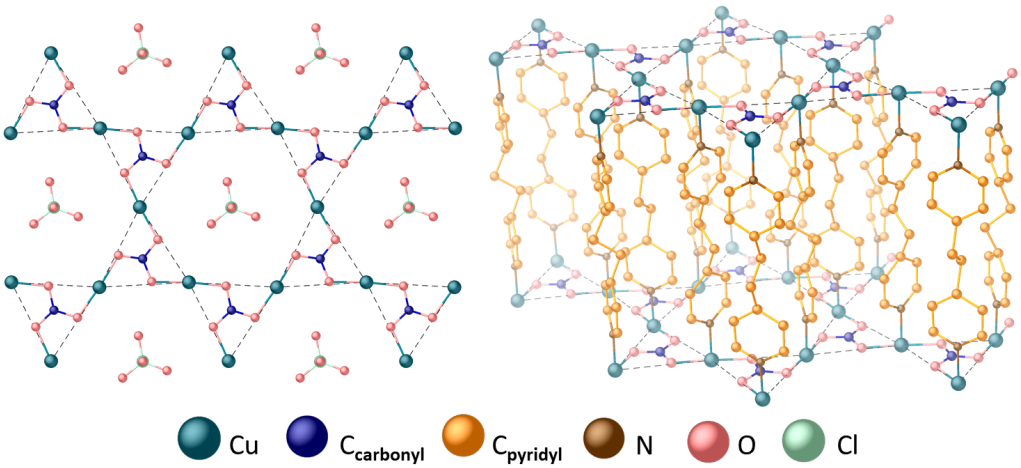

Figure 5.1: The structure of $Cu_3(CO_3)_2(bpe)_3.2ClO_4$, based on the original report by Kanoo *et al* [218], which contains kagomé layers of Cu^{2+}, represented by dashed lines, that are separated by pillaring ligands of *bpe*, whose orientation is randomly disordered. Disordered ClO_4^- occupy the hexagonal channels. For clarity, protons have been excluded.

to pillar the kagomé layers into a three-dimensional MOF (see Figure 5.1) can be varied, which may provide a means to explore a family of related materials whose magnetic exchange interactions and dimensionality can be carefully controlled. Two analogues have already been reported, where the *bpe* linker is replaced by 1,2-bis(4-pyridyl)ethylene (*bpy*) [219] and 4,4'-bipyridylacetylene (*bpa*) [221]. In the former, the more rigid and electronically delocalised *bpy* linker is thought to better facilitate exchange between the kagomé layers, whilst the latter has been described as a metamagnet in which antiferromagnetically coupled kagomé layers align ferromagnetically with the application of a field. This demonstrates that the choice of pillaring linker plays a crucial role in the selected magnetic ground state in this family of MOFs and warrants further investigation.

In this chapter, the syntheses of two previously reported MOFs belonging to a family with formula $Cu_3(CO_3)_2(X)_3{\cdot}2ClO_4$, where X = *bpe, bpy*, are presented, along with a new member of this family where X = 4,4'-azopyridine (*azpy*). Through the combination of bulk magnetometry and powder X-ray and neutron diffraction methods, a comparison across the members of this family is made with an aim to understand the role of the pillaring linker and its orientational disorder on the magnetic properties displayed by these systems. Crucially, some clarification of the nature of the magnetic exchange in this family is gained through neutron powder diffraction and muon spectroscopy measurements.

5.2 Experimental Methods

5.2.1 Synthesis

Samples of $Cu_3(CO_3)_2(X)_3.2ClO_4$, where $X = bpe$ (1,2-bis(4-pyridyl)ethane), *bpy* (1,2-di(4-pyridyl)ethylene) or *azpy* (4,4'-azopyridine) were synthesised using a method based on the Solvay process [79]. $Cu_3(CO_3)_2(bpe)_3.2ClO_4$ (hereafter referred to as MOF–*bpe*) was produced by dissolving 1 mmol of $Cu(ClO_4)_2.6H_2O$ (Sigma Aldrich) in 25 mL aqueous ammonia (Sigma Aldrich, 28–30% NH_3 basis) in a beaker. Next, in a separate beaker 1 mmol of 1,2-bis(4-pyridyl)ethane (Acros Organics, 97%) was stirred with gentle warming in 25 mL distilled H_2O until dissolved. The *bpe* solution was then added dropwise to the copper solution and left to stir for approximately one hour, resulting in a deep blue solution. A similar procedure was followed for $Cu_3(CO_3)_2(bpy)_3{\cdot}2ClO_4$ (MOF–*bpy*) and $Cu_3(CO_3)_2(azpy)_3{\cdot}2ClO_4$ (MOF–*azpy*), except that the $Cu(ClO_4)_2.6H_2O$ was dissolved in 25 mL ammonium hydroxide (14–15% NH_3 basis), and the organics *bpy* (Sigma Aldrich, 97%) and *azpy* (Sigma Aldrich) were dissolved in a mixture of 12 mL ammonium hydroxide (28–30% NH_3 basis), and 12 mL methanol or ethanol for MOF–*bpy* and MOF–*azpy*, respectively. The solutions were covered in parafilm and left for 7 days to allow for slow evaporation of ammonia, leaving polycrystalline purple products alongside a clear solution. The samples were filtered and washed thoroughly with distilled water and acetone. An additional sample of MOF–*bpe* was synthesised using partially deuterated *bpe* ($\sim$ 85% D) synthesised by the ISIS Deuteration Facility, along with D_2O (Sigma Aldrich, 99.9% D). Finally, single crystals were grown by Tristan Dolling, whilst structure solution was performed by Dr Samuel Ivko, both in the School of Chemistry at the University of Birmingham.

5.2.2 Powder X-Ray and Neutron Diffraction

Synchrotron powder X-ray diffraction (PXRD) data were collected for MOF–*bpe*, MOF–*bpy* and MOF–*azpy* on the I11 beamline of the Diamond Light Source at the Rutherford Appleton Laboratory. Samples were packed into borosilicate glass capillaries and attached to a brass holder. Data were collected at 300 K using the PSD detector and X-ray wavelength, $\lambda = 0.826522$ Å. All datasets were analysed using the GSAS package [94, 95]. Backgrounds in each dataset were defined manually using 20 terms.

Neutron powder diffraction (NPD) data were collected on the WISH diffractometer of the ISIS Neutron and Muon Source at the Rutherford Appleton Laboratory. 1 g samples were packed into cylindrical vanadium cans and data were collected at 1.5 K, as well as at 20 K, 30 K and 25 K for MOF–*bpe*, MOF–*bpy* and MOF–*azpy*, respectively. Rietveld analysis for data collected at higher temperatures was conducted using the GSAS-II package [222]. All magnetic Rietveld refinements were completed using FullProf [96].

5.2.3 Magnetometry

Temperature-dependent DC magnetic susceptibilities for MOF–*bpe*, MOF–*bpy* and MOF–*azpy* were collected on a Quantum Design Magnetic Properties Measurement System (MPMS) with a SQUID magnetometer. 20 mg samples were packed into gelatin capsules and loaded into clear plastic straw sample holders. Data were collected in an applied field of 1 T beween 2 – 300 K in zero-field cooled (ZFC) and field cooled (FC) cycles. Heat capacity data were collected on pressed powders with masses of 1.7 mg (MOF–*bpe*), 4.3 mg (MOF–*bpy*) and 1.2 mg (MOF–*azpy*) on a Quantum Design Physical Properties Measurement System (PPMS) in zero field between 2 – 300 K. The addenda for each was measured and subtracted to account for background signal. Two data points per temperature were collected and averaged.

5.2.4 Muon Spin Relaxation

Muon spin relaxation and rotation (μSR) spectra for MOF–*bpe* were collected on the General Purpose Surface-Muon (GPS) instrument of the Swiss Muon Source at Paul Scherrer Institute. A 1 g sample was contained in an aluminium foil packet and loaded into a ^{4}He cryostat. Measurements were taken in zero field (ZF) and transverse field (TF) using the up and down detectors of the GPS instrument, with the initial muon spin rotated upward by 50°. This configuration leads to larger asymmetry and faster counting times compared to the forwards and backwards detectors. All data were analysed using the Musrfit programme [223].

5.3 Results and Discussion

5.3.1 New Crystal Structure Describing Linker Disorder

The crystal structure of MOF–*bpe* was originally reported to crystallise in the $P\bar{6}$ space group, and subsequent studies agreed [92, 218, 219]. Figure 5.2 depicts this structure, which contains distorted kagomé layers of Cu^{2+} that are ligated by CO_3^{2-} anions and stacked along the *c*-axis. The kagomé motif is formed from alternately sized equilateral triangles, forming a so-called "breathing" kagomé network [224, 225]. The kagomé layers are bound together by *bpe* ligands which adopt an *anti* conformation, whilst highly disordered perchlorate counterions, ClO_4^-, are required to charge-balance and occupy the hexagonal channels formed from the kagomé layers. To add further complexity, the carbon atoms within the alkane part of the *bpe* linker, denoted C1 and C2 in Figure 5.2, have orientational disorder and are occupied in a 0.5:0.5 ratio due to the rotational degree of freedom of the linker, which leads to two conformers. The $P\bar{6}$ space group, by definition, contains a three-fold axis and a mirror plane perpendicular to that axis, so that the C1A and C1B, and C2A and C2B sites are equivalent in the model originally proposed. However, considering one of the conformers of the *bpe* linker (*i.e.* removing C1A and C2A in Figure 5.2), there clearly does not exist a mirror plane at its centre. The same space group has been used to describe MOF–*bpy*, an isostructural analogue where the alkane bond in *bpe* is replaced by an alkene bond in *bpy*. However, single crystals of MOF–*bpy* have not been reported to date, and Rietveld analysis of PXRD data have been conducted using a modified CIF from the original Kanoo *et al* report, where C1 and H1 atoms were removed and C2 and H2 occupancies corrected to one, to account for the alkene bond [219]. Figure 5.2, however, clearly demonstrates that this approach does not represent the *trans* configuration of the *bpy* alkene moiety accurately. Furthermore, in the $P\bar{6}$ space group the pyridyl groups of the *bpy* linker would lie perpendicular to the alkene group which links them together, rather than lying planar in the crystal structure as would be expected considering well-established hybridisation rules of carbon atoms.

An improved synthetic approach has made the synthesis of single crystals of MOF–*bpe* and MOF–*bpy* possible, and an alternative model described by the $P3$ space group has been solved at 100 K, which better accounts for the orientational disorder of the organic linkers within these systems. There are two distinct organic

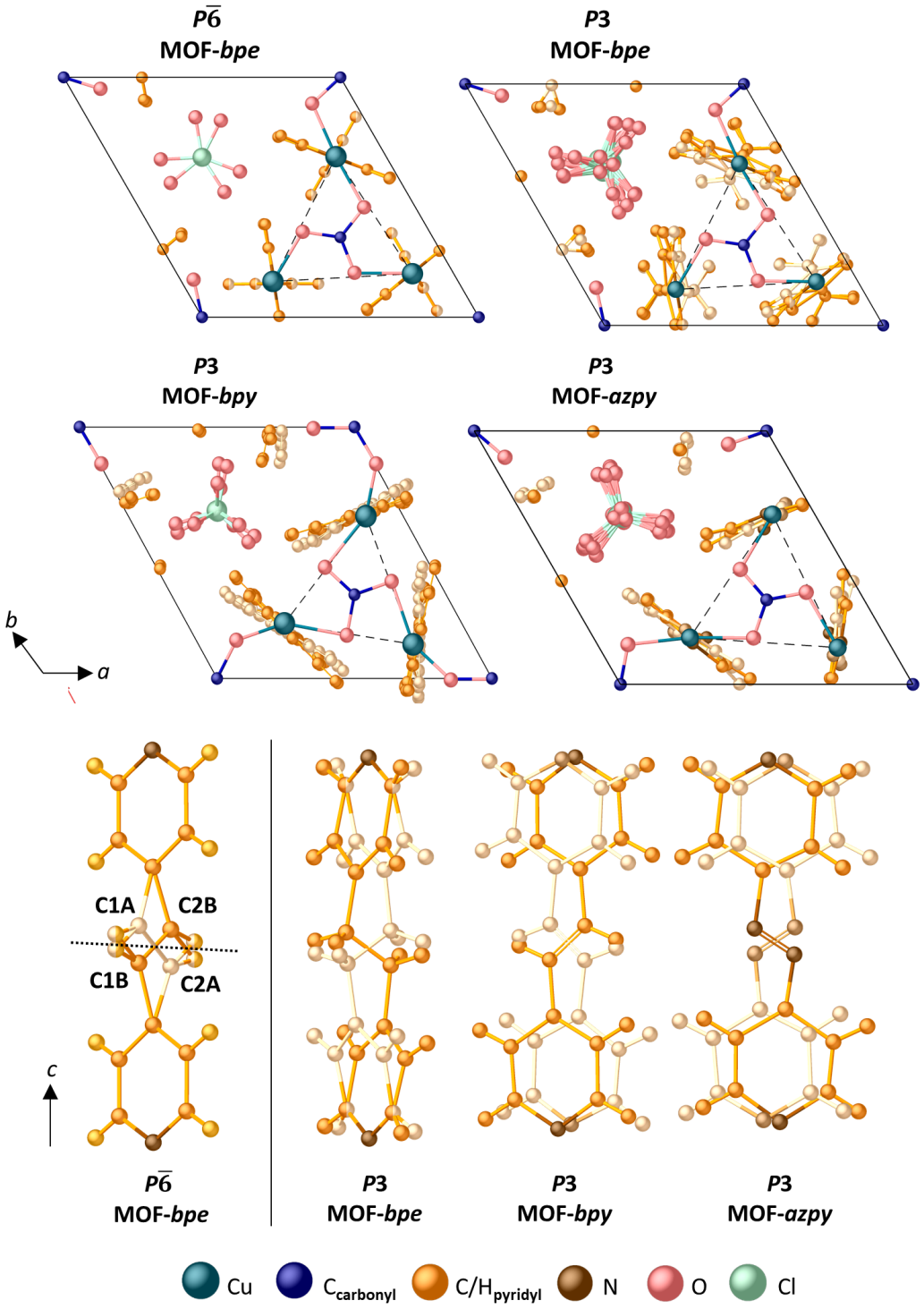

Figure 5.2: A comparison of the $P\bar{6}$ [218] and $P3$ crystal structures of MOF–*bpe*, alongside the $P3$ structures of MOF–*bpy* and MOF–*azpy*. Note that the C1A/C1B and C2A/C2B sites are equivalent in the $P\bar{6}$ *bpe* linker, and the dashed line represents a mirror plane in this space group. The dark and light orange and brown spheres represent the two conformers of the organic linkers which are occupied in a 0.5:0.5 ratio.

linkers in both models, denoted A and B, whose occupancies refine to 0.5 each at 100 K, as depicted in Figure 5.2. In MOF–*bpe*, the pyridyl groups are parallel to each other, but are staggered due to the alkane bond. In MOF–*bpy*, the linkers are planar as would be expected, and in both analogues the linkers are rotated by 180° about the *c*-axis with respect to each other. A third analogue, MOF–*azpy* (where *azpy* = 4,4'-azopyridine), has been synthesised. Here, the double bond of *bpy* is replaced by a N–N double bond, and so this analogue is expected to present similar orientational disorder to MOF–*bpy*. Indeed, analysis of single crystal X-ray diffraction data collected for MOF–*azpy* indicates that its structure is best described by a similar $P3$ model, which is shown in Figure 5.2. In all three MOFs, the Cu^{2+} ion is in a highly distorted octahedral coordination environment, with two Cu–N bonds from the dipyridyl linkers (*trans* to each other) and two Cu–O bonds, as well as two elongated Cu-O bonds. The alternately-sized equilateral triangles within the kagomé planes are retained in in all three of these models, whilst modelling the extreme disorder on the perchlorate anions remains challenging. The full structural parameters for the $P3$ models of all three MOFs at 100 K are given in the appendix.

Synchrotron PXRD data were collected at room temperature for powder samples of MOF–*bpe*, MOF–*bpy* and MOF–*azpy*, and are presented in Figure 5.3. Le Bail fits were conducted using the $P3$ structural model, resulting in refined lattice parameters of $a = 9.41602(8)$ Å and $c = 13.3347(2)$ Å, $a = 9.31744(9)$ Å and $c = 13.4027(2)$ Å, and $a = 9.3117(1)$ Å and $c = 12.9771(2)$ Å for MOF–*bpe*, MOF–*bpy* and MOF–*azpy*, respectively. Further structural refinement using the Rietveld method was unsuccessful, and resulted in negative atomic displacement parameters. A close inspection of the peak shapes in the powder diffraction data goes some way to explaining this. In particular, MOF–*azpy* contains extremely sharp $(00l)$ Bragg peaks in comparison to $(hk0)$ peaks, and this effect is evident, although subtle, in both MOF–*bpe* and MOF–*bpy*, as shown in the insets of Figure 5.3. Fitting a Pseudo-Voigt function to (101) and (002) Bragg peaks across all three materials yields full-width at half maxima values, shown in Table 5.1, which quantify this amplified effect in MOF–*azpy*.

Preferred orientation, where crystallites have a non-random distribution of orientations, is common in layered systems [226], but is unlikely in this case because such an effect normally yields systematically intense peaks, but not such a disparity in peak widths. In addition, measuring the samples in both capillary and

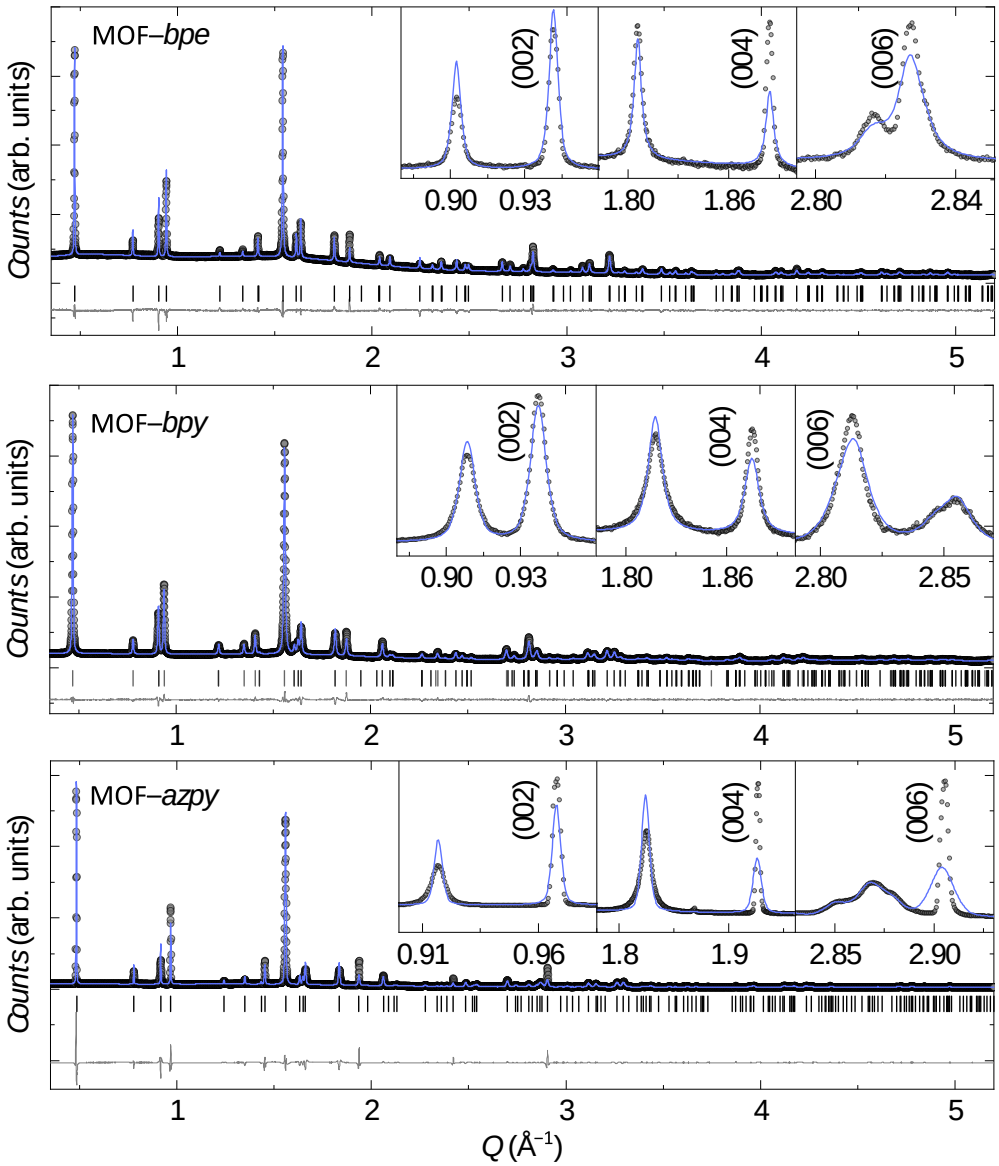

Figure 5.3: Le Bail fits of the $P3$ structural model of MOF–*bpe*, MOF–*bpy* and MOF–*azpy* to PXRD data collected on the I11 instrument at 300 K. The insets reveal the sharp $(00l)$ Bragg peaks which are particularly evident in data collected for MOF–*azpy*.

flat-plate geometries yields similar peak effects, whereas preferred orientation is typically enhanced in the latter geometry. There are several possible alternative explanations for this peak shape behaviour. Sample texture, where there are insufficient crystallites to provide an adequate powder average, is one such example. For instance, if the MOFs crystallise in rod-like formations, the c-axis will have a larger dimension than the a- and b-axes, resulting in sharper $(00l)$ peaks. Conversely, the effect observed may be better explained in terms of broadening of

Table 5.1: The full-width at half maxima of the (101) and (001) peaks in PXRD data collected at 300 K for MOF–*bpe*, MOF–*bpy* and MOF–*azpy*. The (00l) Bragg peaks are sharper than (hk0) Bragg peaks across the series, but this effect is prominent in MOF–*azpy*.

	FWHM (Å)	
	(101)	(001)
MOF–*bpe*	0.00491(5)	0.00439(5)
MOF–*bpy*	0.00834(7)	0.00719(5)
MOF–*azpy*	0.00687(7)	0.00386(7)

peaks in the (hk0) planes, which may occur because of the disorder of the organic linkers which manifests along these directions. This type of phenomenon has been observed in paracrystalline materials, where the lattice is highly disordered and unit cells with variable sizes emerge [227, 228]. In the data presented here, the disorder of the organic linkers could cause a local distortion of the unit cell along the a- and b-axes, resulting in a distribution of cell lengths and broadening of peaks describing planes along these directions. Crucially, the disorder in paracrystals is not random, and this raises the question of whether the disorder present in this family of MOFs is correlated.

5.3.2 Bulk Magnetic Properties

The temperature-dependent magnetic susceptibility data collected for MOF–*bpe*, MOF–*bpy* and MOF–*azpy* are shown in Figure 5.4. A temperature-independent diamagnetic contribution, χ_{D}, was subtracted from each dataset (5.16×10^{-4} emu mol^{-1}, 4.98×10^{-4} emu mol^{-1} and 4.41×10^{-4} emu mol^{-1} for MOF–*bpe*, MOF–*bpy* and MOF–*azpy*, respectively), which were calculated using tabulated values of Pascal's constants [229]. In an applied field of 1 T, the data for MOF–*bpe* and MOF–*bpy* reveal an upturn below approximately 20 K. The inverse susceptibility follows Curie-Weiss behaviour at high temperatures, and modelling the 100 – 300 K region using the Curie-Weiss law yields parameters that are summarised in Table 5.2, where the positive values of the Weiss temperature, θ, indicate that ferromagnetic exchange dominates the magnetic ground states in these two MOFs. On the other hand, the magnetic susceptibility for MOF–*azpy* displays an upturn below approximately 15 K, and Curie-Weiss analysis yields a small negative θ. This indicates that there is a significant change in the interplay between antiferromagnetic and ferromagnetic interactions upon changing the organic linker, and that the modification in the strength or type of exchange does not scale simply with

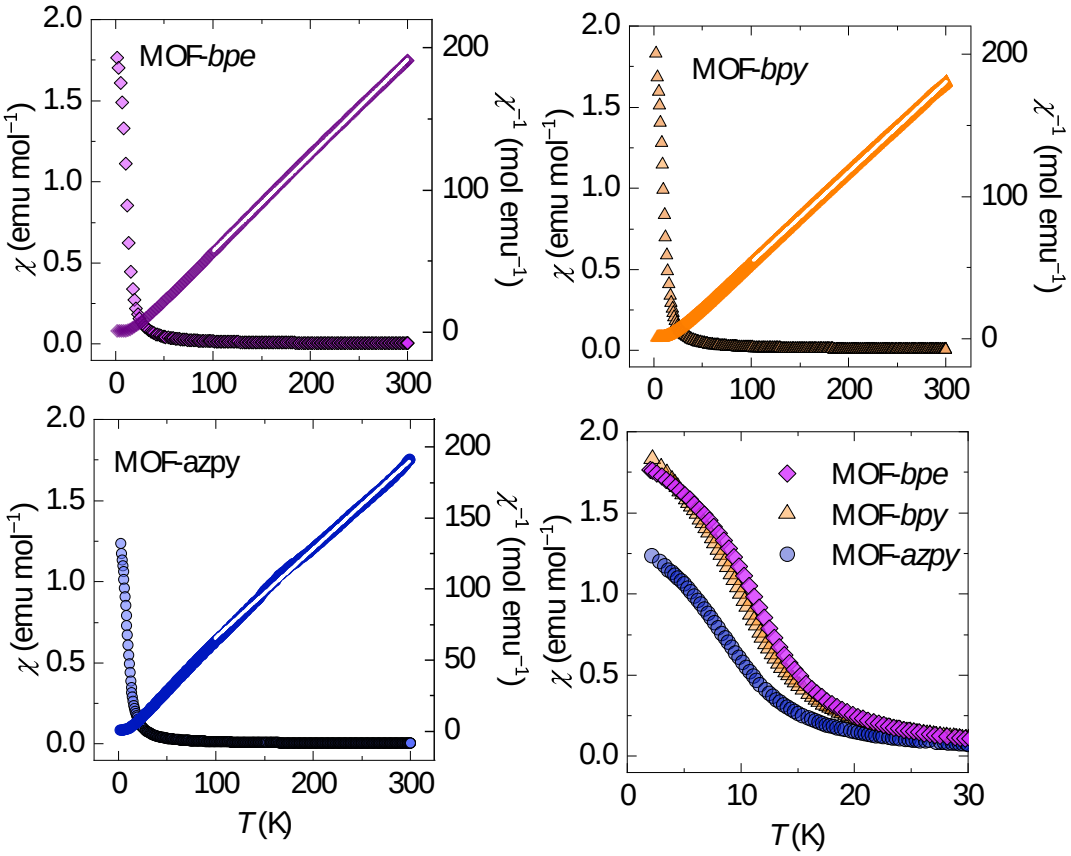

Figure 5.4: Temperature-dependent magnetic susceptibility measured in an applied field of 1 T for MOF–*bpe*, MOF–*bpy* and MOF–*azpy* in a zero-field cooled cycle. Curie-Weiss fits of the inverse susceptibility are shown on the right-hand axes, and the lower right panel is a comparison of the low-temperature magnetic susceptibility across the series. Note that the anomaly in the inverse susceptibility data for MOF–*azpy* at $\sim$ 150 K is an instrumental error.

the separation of the kagomé layers. In previous studies on MOF–*bpe*, θ varies from -2.13 K to 60 K [218–220]. Furthermore, the coercive field obtained from hysteresis loops for this material varies from 8.5 Oe to 600 Oe [218, 219]. These discrepancies indicate that the magnetic susceptibility may vary from sample to sample. The origin of the ferromagnetic and antiferromagnetic contributions to the magnetic susceptiblity is also unclear, with one of the aforementioned studies suggesting a dominant ferromagnetic interlayer exchange [219], and another suggesting weak interlayer exchange and competitive ferromagnetic and antiferromagnetic exchange within the kagomé layers [92]. Meanwhile, analogues of these MOFs with alternative organic components have been proposed as containing dominant ferromagnetic exchange within the planes [221, 230]. As a consequence, an understanding of the magnetic structures of these systems is crucial to eluci-

Table 5.2: Parameters obtained from fits of the Curie-Weiss law to magnetic susceptibility data between 100 – 300 K, shown in Figure 5.4, and T_C obtained from muon spectroscopy data (MOF–*bpe*) or estimated from heat capacity data (MOF–*bpy* and MOF–*azpy*).

	θ (K)	C (emu mol^{-1} K)	μ_{eff} (μ_B per f. u.)	T_C (K)
MOF–*bpe*	26.86(4)	1.481(1)	3.442(4)	5.99(1)
MOF–*bpy*	15.2(3)	1.572(3)	3.55(1)	7.5
MOF–*azpy*	−5.1(1)	1.603(1)	3.581(4)	5.5

dating the bulk magnetic behaviour observed.

Heat capacity data measured in zero applied field from $2 - 300$ K are shown for all three MOFs in Figure 5.5(a). Data collected for MOF–*bpe* and MOF–*bpy* do not evidence an inflection point which would be indicative of long-range magnetic order. The absence of a sharp magnetic anomaly is one of the intriguing characteristics of MOF–*bpe* which has drawn attention to this family of materials [92, 218, 220]. Instead, there are broad features centred at ~ 7 K. Conversely, the temperature-dependent heat capacity for MOF–*azpy* displays a sharper anomaly. A clearer look at the magnetic contribution to the heat capacity can be found by subtracting an estimate for the lattice specific heat. Jain *et al* previously accounted for this using a non-magnetic cadmium analogue of MOF–*bpe*, the data for which was modelled using four Debye functions,

$$C^{\text{D}} = \sum_{i=1}^{4} \left[9NR \left(\frac{\theta_i^{\text{D}}}{T} \right)^3 \int_0^{\frac{T_{\text{D}}}{T}} \frac{x^4 e^x}{(e^x - 1)^2} dx \right], \tag{5.1}$$

where each Debye function accounts for the four types of atoms in the unit cell, grouped together via mass (Cd, C/N/O, Cl and H). N is the number of atoms in the formula unit for each group, and θ_i^{D} is the Debye temperature. The fitted Debye temperature for cadmium was then scaled down to account for the difference in masses between cadmium and copper [92]. Using the Debye model and parameters determined by Jain *et al*, a similar approach has been taken here to estimate the lattice contribution, with N in Equation 3.1 adjusted accordingly between MOFs. The magnetic heat capacity, C_{mag}, is then determined by subtracting the lattice contribution from the total heat capacity, as displayed in Figure 5.5(b). Here, the differences in the variation of C_{mag} with temperature across the three MOFs is clear; MOF–*bpe* and MOF–*bpy* display features peaking at ~ 7 K, with the former noticeably broader than the latter. Meanwhile, C_{mag} for MOF–*azpy* displays a

much sharper anomaly at $T_C = 5.5$ K. The magnetic entropy released across these transitions can be estimated by integrating C_{mag} for each MOF between 2 – 20 K. Figure 5.5(d) presents the entropy as a fraction of the total expected entropy for three $S = \frac{1}{2}$ ions, $\Delta S = 3R\ln(2S+1)$. MOF–*bpy* and MOF–*azpy* appear to reach the full entropy expected, whereas MOF–*bpe* reaches just $\frac{1}{2}$ of the full entropy, suggesting the presence of only a partially ordered magnetic ground state in this system. Of course, the lattice behaviours of MOF–*bpy* and MOF–*azpy* are likely to deviate from that measured for the cadmium analogue of MOF–*bpe*, meaning that the entropy change presented here is merely an estimate.

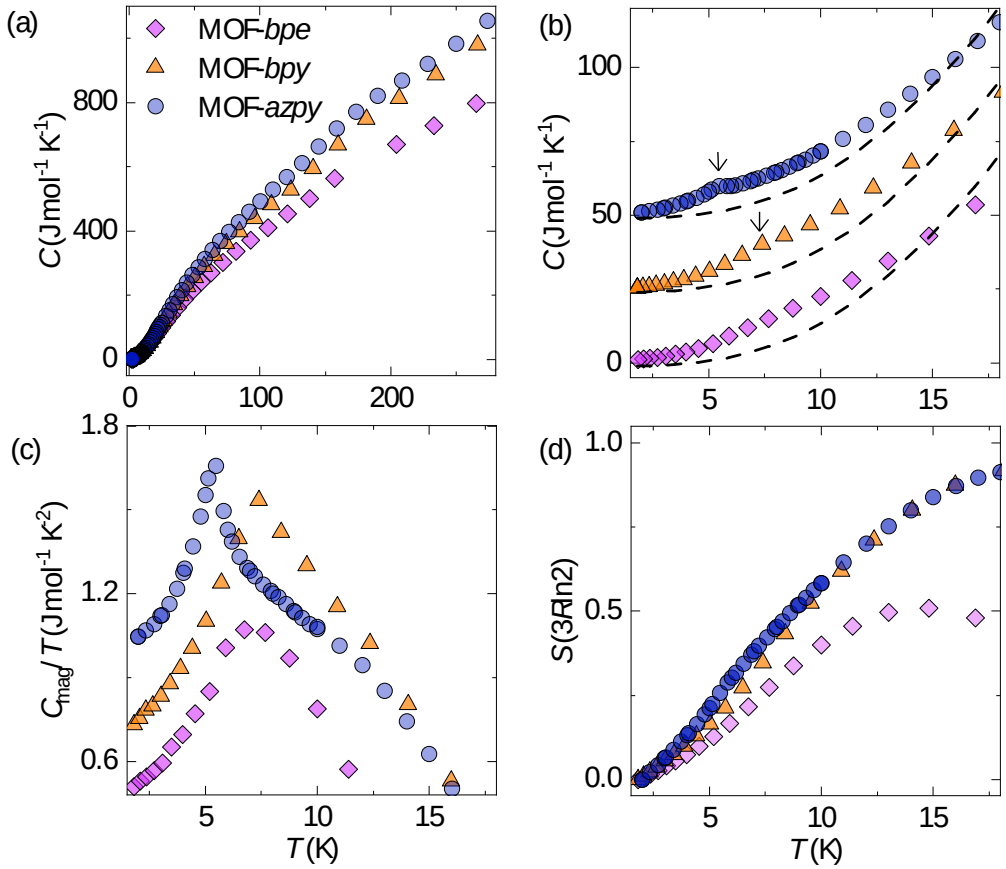

Figure 5.5: (a) The total heat capacity measured between 2 – 300 K for MOF–*bpe*, MOF–*bpy* and MOF–*azpy* in zero field. (b) The weak magnetic anomalies observed at low temperatures, and estimates for the lattice contribution to the heat capacity represented as dashed lines, determined as described in the text. (c) The magnetic contribution to the measured heat capacity. (d) The entropy released through the magnetic transitions as a fraction of the total expected entropy release, $3R\ln 2$.

5.3.3 Magnetic Structure Determination Using Neutron Powder Diffraction

NPD data were collected on the WISH diffractometer for samples of MOF–*bpe*, MOF–*bpy* and MOF–*azpy*. The MOF–*bpe* sample measured was partially deuterated, which makes conducting a full Rietveld refinement on data collected at 20 K difficult due to the inability to determine which proton sites are substituted with deuterium. MOF–*azpy*, on the other hand, whilst fully protonated suffers from sharp (00l) Bragg peaks, as described in PXRD data in Section 3.3.1 and shown in WISH data in Figure 5.6. As a result, full Rietveld analysis of data collected for these two materials was not possible and, particularly for MOF–*bpe*, the scale factor deduced when conducting a magnetic Rietveld refinement is inaccurate (for example, an $R_{\mathrm{wp}} = 9.53\%$ was obtained for a fit of the $P3$ model to high resolution data in Bank 5). For MOF–*bpy*, however, the sample was fully protonated and the resolution of the data produced by the WISH diffractometer precludes

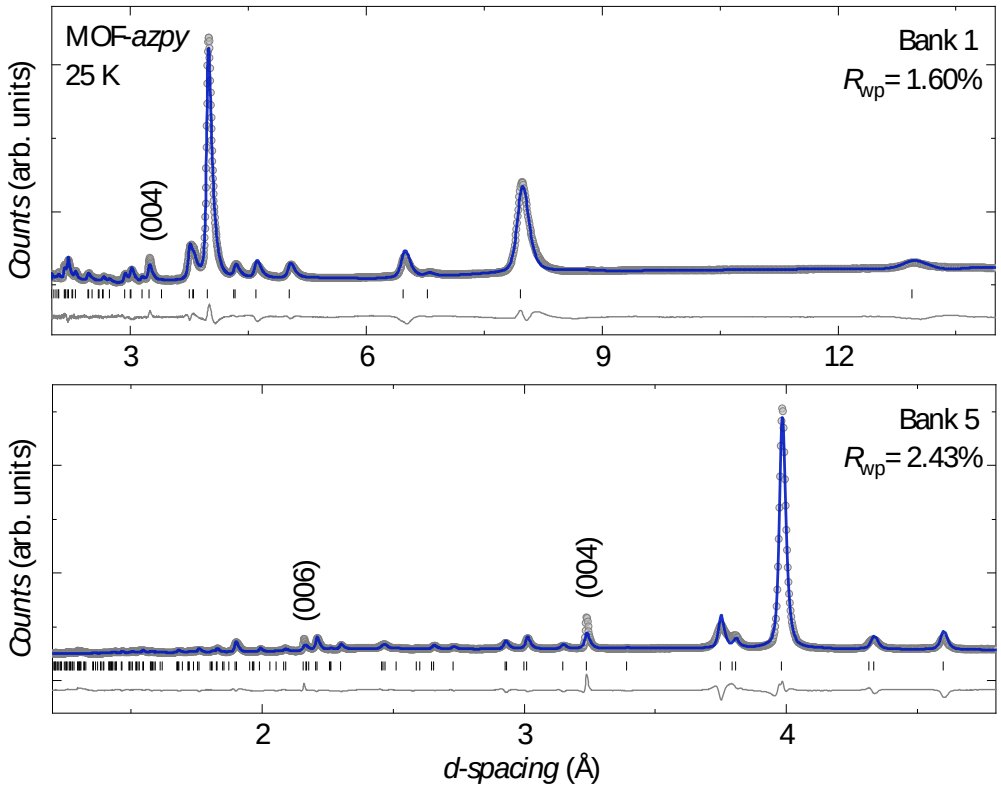

Figure 5.6: Rietveld refinement of the $P3$ structure of MOF–*azpy* against data collected on WISH at 30 K in banks 1 and 5, where sharp (004) and (006) Bragg peaks are evident. Refined lattice parameters are $a = 9.20444(9)$ Å and $c = 12.9574(6)$ Å. The final statistical factor across all five banks is $R_{\mathrm{wp}} = 2.68\%$.

the observation of sharp $(00l)$ peaks, meaning that a full Rietveld refinement of the $P3$ crystal structure to data collected at 30 K was possible. Here, the two *bpy* linkers (A and B) were defined as rigid bodies within the GSAS-II software, and their respective origins and rotation angles, defined as a vector and azimuthal rotation angle, were allowed to refine freely within the unit cell. The thermal motion was refined isotropically and constrained across the atoms in each rigid body. Atomic positions and U_{iso} values for the perchlorate moieties were also fixed due

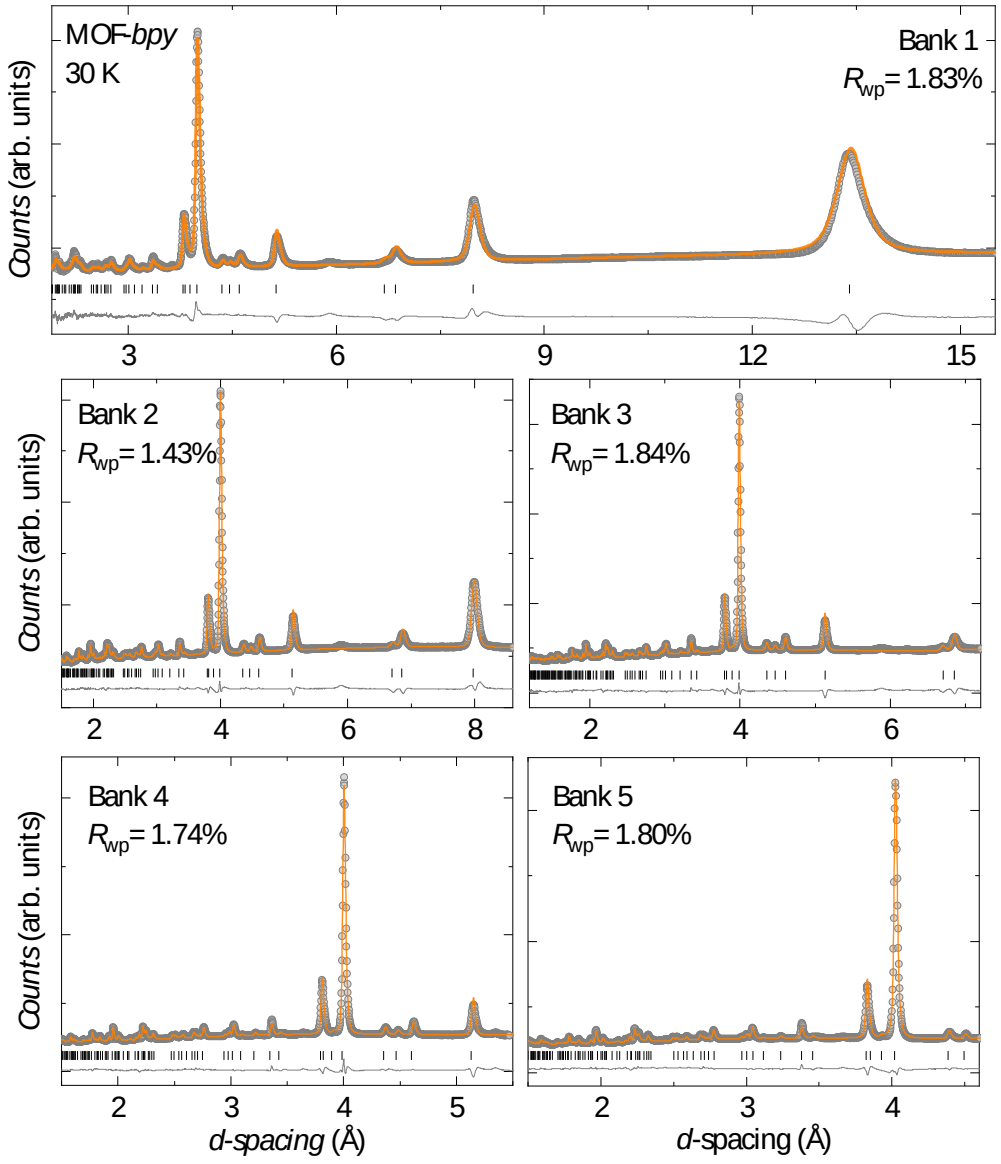

Figure 5.7: Rietveld and rigid body refinement of the $P3$ structure of MOF–*bpy* against data collected on WISH at 30 K. Refined lattice parameters are a = 9.194(2) Å and c = 12.944(3) Å. The final statistical factor across all five banks is $R_{\mathrm{wp}} = 2.38\%$.

to the significant disorder that they display. To further simplify the refinement, the isotropic atomic displacement parameters, U_{iso}, were constrained across the carbonate ligands. The resultant structural parameters of MOF–*bpy* at 30 K are shown in Table 2. Note that the refined U_{iso} values for the Cu1 and carbonate sites are unphysically large. This may relate to the broadening of the ($hk0$) Bragg peaks which were observed in PXRD data; the disorder of the *bpy* linkers—which are well defined in the rigid body model—could locally distort the kagomé layers, and therefore the carbonate linkers, which may then be manifested in the Rietveld refinement via large displacement parameters. Importantly, the $P3$ structure describes the data well, as shown in Figure 5.7, and there is no evidence for any symmetry lowering at this temperature or at 1.5 K.

Table 5.3: Rietveld refinement crystal structure parameters for the $P3$ model of MOF–*bpy* fitted to NPD data collected on WISH at 30 K. Atoms denoted A and B were defined as two separate rigid bodies with refined origins of [0.155(1), 0.804(1), 0.957(1)] and [0.149(1), 0.810(1), 0.950(1)] for A and B linkers, respectively. Refined lattice parameters are $a = b = 9.2069(5)$ Å and $c = 13.3964(6)$ Å. The final statistical factors are $R_{wp} = 1.85\%$ and $\chi^2 = 1.83$.

Atom	Site	x	y	z	Occupancy	U_{iso}
Cu1	3d	0.136(2)	0.781(1)	0.454(2)	1	0.041(3)
			Carbonate			
C13	1a	0	1	0.451(3)	1	0.033(2)
C14	1b	0.33333	0.66667	0.452(3)	1	0.033
O9	3d	0.386(2)	0.828(2)	0.452(3)	1	0.033
O10	3d	0.994(2)	0.848(2)	0.451(3)	1	0.033
			Linker A			
N1A	3d	0.11391	0.76832	0.30777	0.5	0.020(4)
C1A	3d	0.97421	0.67254	0.25648	0.5	0.020
H1A	3d	0.87467	0.60478	0.29303	0.5	0.020
C2A	3d	0.25664	0.86387	0.25456	0.5	0.020
H2A	3d	0.35781	0.93151	0.28980	0.5	0.020
C3A	3d	0.65980	0.66707	0.15427	0.5	0.020
H3A	3d	0.86278	0.59435	0.12222	0.5	0.020
C4A	3d	0.25911	0.86733	0.15055	0.5	0.020
H4A	3d	0.36056	0.93512	0.11531	0.5	0.020
C5A	3d	0.10509	0.76667	0.09768	0.5	0.020

Continued on next page

Table 5.3 – continued from previous page

Atom	Site	x	y	z	Occupancy	U_{iso}
C6A	3d	0.09185	0.75845	0.98857	0.5	0.020
H6A	3d	0.84830	0.68502	0.96090	0.5	0.020
C7A	3d	0.21745	0.84576	0.92391	0.5	0.020
H7A	3d	0.32587	0.91743	0.95078	0.5	0.020
C8A	3d	0.19935	0.83773	0.81240	0.5	0.020
C9A	3d	0.05175	0.73621	0.76266	0.5	0.020
H9A	3d	0.95218	0.66452	0.79823	0.5	0.020
C10A	3d	0.34692	0.94524	0.75779	0.5	0.020
H10A	3d	0.44823	0.01776	0.79122	0.5	0.020
C11A	3d	0.33737	0.94050	0.65795	0.5	0.020
H11A	3d	0.43617	0.01063	0.62087	0.5	0.020
C12A	3d	0.05391	0.74151	0.65935	0.5	0.020
H12A	3d	0.95283	0.67338	0.62391	0.5	0.020
N2A	3d	0.19499	0.84059	0.60731	0.5	0.020
			Linker B			
N1B	3d	0.16690	0.81972	0.30015	0.5	0.018(3)
C1B	3d	0.02772	0.74792	0.24534	0.5	0.018
H1B	3d	0.92184	0.69321	0.27803	0.5	0.018
C2B	3d	0.31533	0.89799	0.25211	0.5	0.018
H2B	3d	0.41342	0.94987	0.29203	0.5	0.018
C3B	3d	0.03374	0.75054	0.14154	0.5	0.018
H3B	3d	0.93256	0.69910	0.10385	0.5	0.018
C4B	3d	0.33565	0.91057	0.15202	0.5	0.018
H4B	3d	0.44338	0.96926	0.12214	0.5	0.018
C5B	3d	0.18596	0.82842	0.82842	0.5	0.018
C6B	3d	0.20651	0.83842	0.98344	0.5	0.018
H6B	3d	0.31808	0.89350	0.95902	0.5	0.018
C7B	3d	0.08560	0.77845	0.91535	0.5	0.018
H7B	3d	0.97388	0.72285	0.93965	0.5	0.018
C8B	3d	0.10662	0.78951	0.80703	0.5	0.018
C9B	3d	0.96626	0.71486	0.74728	0.5	0.018
H9B	3d	0.85804	0.65659	0.77638	0.5	0.018
C10B	3d	0.26639	0.86655	0.75963	0.5	0.018
H10B	3d	0.36619	0.91299	0.79817	0.5	0.018

Continued on next page

Table 5.3 – continued from previous page

Atom	Site	x	y	z	Occupancy	U_{iso}
C11B	3d	0.27379	0.87332	0.65409	0.5	0.018
H11B	3d	0.37894	0.92686	0.62149	0.5	0.018
C12B	3d	0.98470	0.72770	0.64580	0.5	0.018
H12B	3d	0.88628	0.67820	0.60597	0.5	0.018
N2B	3d	0.13197	0.80392	0.59923	0.5	0.018
			Perchlorates			
Cl1	3d	0.66400	0.33100	0.97070	0.333	0.005
O1	3d	0.55300	0.18600	0.91500	0.333	0.005
O2	3d	0.59200	0.29200	0.07400	0.333	0.005
O3	3d	0.65330	0.47720	0.95440	0.333	0.005
O4	3d	0.82120	0.35350	0.00350	0.333	0.005
Cl2	3d	0.66300	0.33300	0.47070	0.333	0.005
O5	3d	0.84300	0.45700	0.46800	0.333	0.005
O6	3d	0.61400	0.22400	0.38200	0.333	0.005
O7	3d	0.56600	0.41900	0.47600	0.333	0.005
O8	3d	0.63400	0.24400	0.56740	0.333	0.005

Upon cooling below T_{C}, weak magnetic intensity develops in all three datasets which is most evident in subtracted data collected in Bank 1 of the WISH diffractometer, as shown in Figure 5.8. In all three analogues, a magnetic Bragg peak is present at twice the length of the c-axis, implying a doubling of the magnetic unit cell along c and a propagation vector $\mathbf{k} = (0, 0, 0.5)$ with respect to the crystal structure. Another peak is observed at one third of the expanded cell, corresponding to the (003) magnetic Bragg peak. In MOF–*bpe*, additional intensity is present at ~ 13.3 Å, corresponding to the (002) magnetic Bragg peak. A small amount of scattering is observed at the corresponding position in MOF–*bpy*, although the intensity is within error of the background and may be due to peak shift due to thermal contraction. Magnetic structure determination for all three datasets using the Bilbao Crystallographic Server [106–108] suggests just one possible magnetic space group—namely $Pc3$—consistent with a $P3$ crystal structure (or even $P\bar{6}$, the space group originally proposed to describe these systems) and $k = (0, 0, 0.5)$. However, inspection of the systematic absences reveals that all $(00l)$ magnetic peaks are forbidden within this space group. The $Pc3$ magnetic structure contains one magnetic site, a three-fold axis, and magnetic

moments which are antiparallel between adjacent planes. This means that a ferromagnetic component is not permitted by $Pc3$ symmetry, which is inconsistent with the magnetic susceptibility data presented for these materials. Instead, the low-temperature magnetic structures must be described by the lower symmetry $P1$ magnetic space group—the only subgroup of $Pc3$—which breaks the symmetry of the underlying crystal structure.

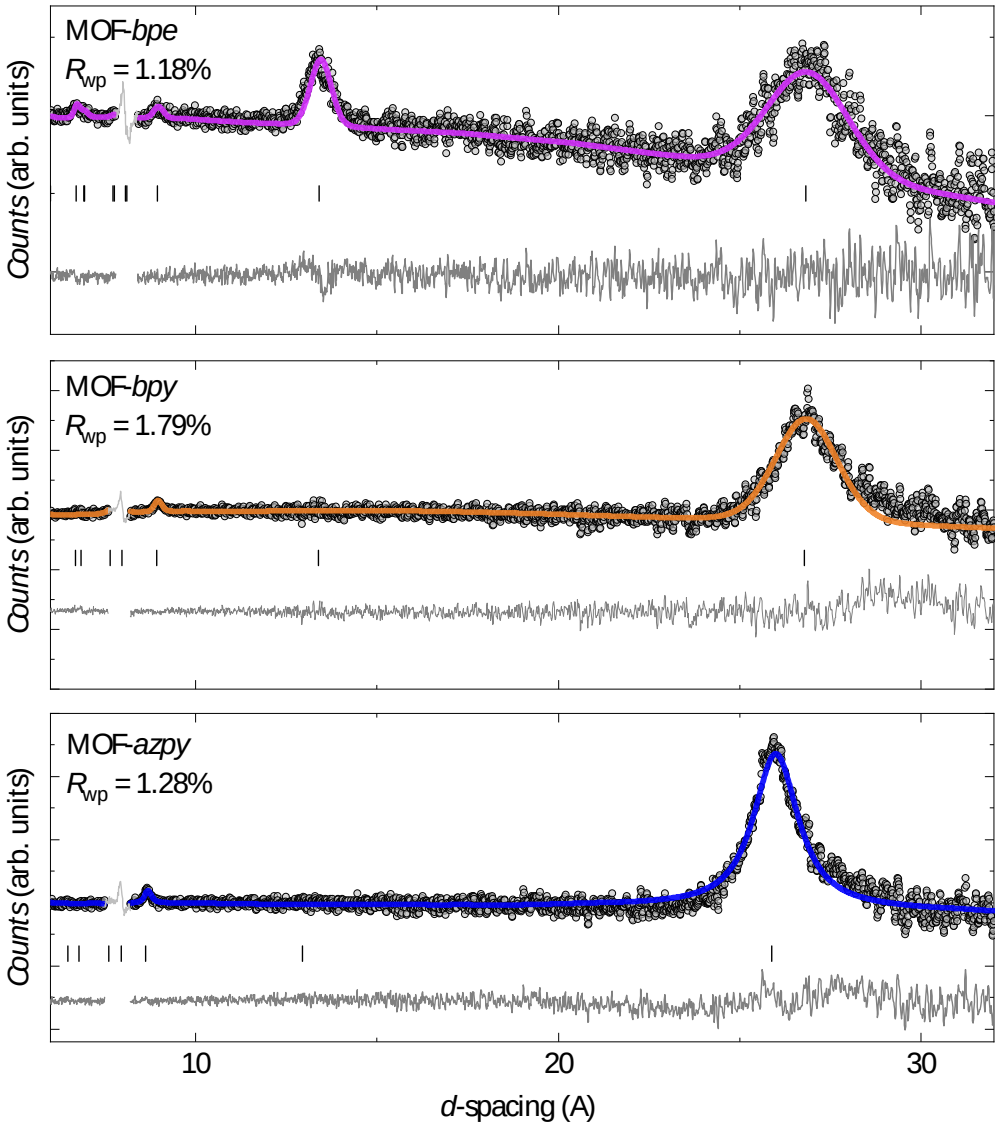

Figure 5.8: Magnetic Rietveld refinements of the constrained $P1$ model to NPD data at 1.5 K, from which data collected at 20 K (MOF–*bpe*), 30 K (MOF–*bpy*) and 25 K (MOF–*azpy*) has been subtracted. The grey regions in the data were excluded from the fits because they are positions of strong nuclear positions.

The $P1$ magnetic structure contains no symmetry constraints, so that each of the six magnetic moments within the magnetic unit cell are free to point in any direction. As a result, a refinement of this model against the data presented here, where very few magnetic Bragg peaks are visible, requires several constraints. Firstly, only $(00l)$ peaks are observed, and so the moments along the z-direction can be fixed to zero, as the $(00l)$ peaks do not yield information about the moment directions out of the bc plane. In MOF–*bpy* and MOF–*azpy*, where there is negligible magnetic intensity at the (002) position, the moments on adjacent layers must be equal and opposite, *i.e.* the magnetic moments must be completely antiferromagnetically aligned between kagomé layers, such as shown in Figure 5.9. Within the kagomé layers, determining where the three magnetic moments point is impossible with so few Bragg peaks, although the simplest solution is one where the intralayer exchange is fully ferromagnetic. In MOF–*bpy* and MOF–*azpy*, the magnetic moments were constrained to be equal and opposite within the adjacent planes, and only the moments along the x-direction were refined, resulting in total refined magnetic moments of 0.497(4) μ_{B} and 0.495(3) μ_{B} on each Cu^{2+} for MOF–*bpy* and MOF–*azpy*, respectively, and yielding a good fit to each dataset, as shown in Figure 5.8. In contrast, in MOF–*bpe* there is a (002) magnetic peak, suggesting there is a difference in the moment magnitudes or spin directions on going from one layer to the next within the doubled unit cell. One solution, shown in Figure 5.9(a), is where the intraplane exchange is ferromagnetic, the interplane exchange is predominantly antiferromagnetic, but there is some misalignment between the moments on adjacent layers, which yields magnetic moments of approximately 0.5 μ_{B} per Cu^{2+} site. This larger ferromagnetic component is in agreement with the hysteresis loop determined in MOF–*bpe*, which displayed a coercive field of $H_{\mathrm{c}} = 600$ Oe, compared to $H_{\mathrm{c}} = 60$ Oe for MOF–*bpy* [219]. In addition, both NMR and ESR studies suggest ferromagnetic order prevails in MOF–*bpe* [220].

In a previous study, the small magnitude of θ from Curie-Weiss analysis of magnetic susceptibility data was attributed to a competition between nearest-neighbour ferromagnetic and next-nearest-neighbour antiferromagnetic exchange *within* the frustrated kagomé layers, under the assumption that the large distance between the planes does not facilitate strong exchange. Instead, a weak interplane ferromagnetic exchange was proposed, which is sensitive to applied fields of 125 Oe or higher [92]. Interestingly, in the same study the absence of magnetic scattering in NPD data was reported, likely due to insufficient range in d-spacing in the collected data. However, reports of similar framework systems containing kagomé

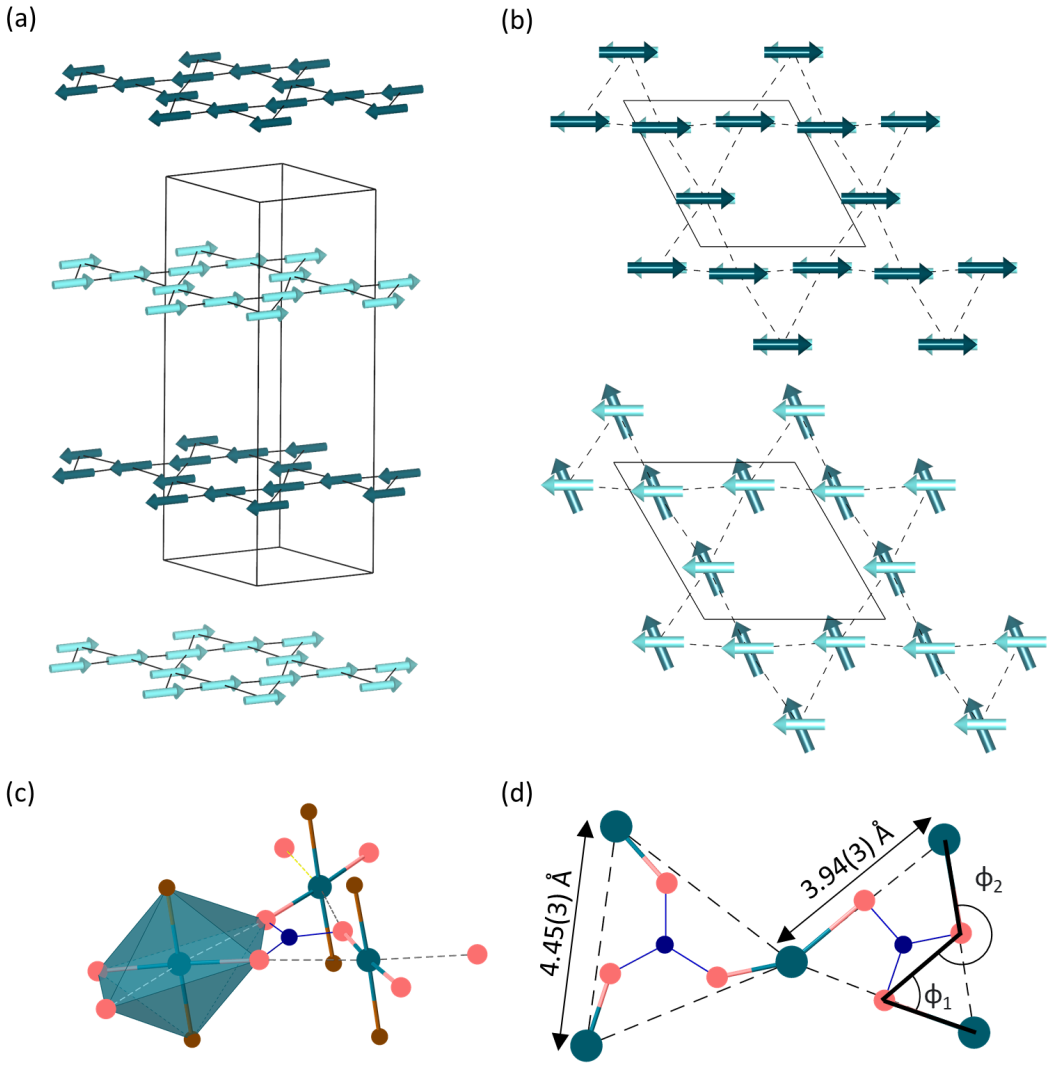

Figure 5.9: (a) In the proposed magnetic structures of MOF–*bpe*, MOF–*bpy* and MOF–*azpy*, ferromagnetically aligned magnetic moments of Cu^{2+} within the kagomé layers are aligned antiferromagnetically along *c*. (b) In MOF–*bpy* and MOF–*azpy* (top), the magnetic moments are perfectly aligned between adjacent layers, whilst in MOF–*bpe* (bottom) one proposed structure is where the moments are misaligned, which leads to (002) magnetic peak intensity. (c) The magnetic exchange is likely mediated through $d_{x^2-y^2}$ orbitals which lie in the equatorial plane of the distorted octrahedra (solid bonds), whilst the lower energy d_{z^2} orbitals lie along the longer Cu-O bonds, represented by a dashed line. (d) The strength and nature of the magnetic exchange along the short Cu-O bonds can be predicted using the CuOO bond angles defined by ϕ_1 and ϕ_2, here shown for MOF–*bpy* at 1.5 K, and the DFT model implemented by Mateus *et al* [231].

layers chelated by CO_3^{2-}, this time with 4,4'bipyridylacetylene and 2,4'-bipyridine as the organic components, indicate that ferromagnetic exchange between the Cu^{2+} within the kagomé layers dominates, as deduced from modelling magnetic susceptibility data [221, 230]. One DFT study, which looked at Cu^{2+} bridged by carbonate in a macrocycle, has explored the effect of the orientation of the $d_{x^2-y^2}$ orbitals of the Cu^{2+}—which are oriented along the short Cu-O bonds within the *ab*-plane and along the Cu-N bonds, but perpendicular to the long Cu-O bonds within the kagomé layers, see Figure 5.9—via the angles depicted in Figure 5.9(c), on the sign and magnitude of the magnetic exchange in such systems. This study suggests that when the orbitals are in a *syn-anti* conformation—*i.e.* where the Cu–O angles are orthogonal to each other—ferromagnetic exchange dominates. In the model for MOF–*bpy*, which could be fully refined against WISH data, the alternating equilateral triangles which form the distorted kagomé networks have sizes of 3.94(3) Å and 4.45(3) Å at 1.5 K, and the bond angles defined in Figure 5.9(c) are $\phi_1 = 61.13(2)^\circ$ and $\phi_1 = 238.87^\circ$, and $\phi_2 = 106.31^\circ$ and $\phi_2 = 193.85^\circ$. This places the exchange firmly in the ferromagnetic region according to the calculations undertaken by Mateus *et al*, but indicates that there will be significant modifications to the strength of exchange in each of the triangles. This DFT model, however, was designed for discrete triangles within a complex, rather than an extended solid, which would require a more in-depth approach.

Although the magnetic structure within the kagomé planes in the materials presented here is preliminary and will await further single crystal magnetometry and NPD measurements, the doubling of the unit cell along *c* observed in WISH data confirms that antiferromagnetic exchange along this direction emerges. The breaking of the underlying crystal symmetry may be due to local distortions of the kagomé network due to disorder within the organic linkers, which in turn will cause subtle changes in the kagomé bond lengths and angles and modify the exchange both within and between the planes. On the other hand, it cannot be ruled out that there is a subtle structural symmetry lowering which is not observed in the present data. The overall angle between the Cu^{2+} ions in adjacent kagomé layers will vary considerably considering the orientational disorder of the linker, implying that subtle changes in the magnetic ground states are likely to occur depending on the identity of the organic linker and the level of disorder which it displays. The identity of the linker which separates two-dimensional magnetic planes has been demonstrated to have a profound effect on the magnetic ground states in coordination polymers, even in the presence of shorter intralayer exchange path-

ways [232]. In the materials discussed here, the extended π-systems in MOF–*bpy* and MOF–*azpy* makes these linkers more rigid and electronically delocalised than their *bpe* counterpart, and can enable spin-spin coupling mechanisms which better facilitate interplane antiferromagnetic exchange. This may explain the trend in θ values across the analogues, which demonstrate increasingly dominant antiferromagnetic interactions with increasing π conjugation. Previously, the raising of T_C from 5.7 K to 9.3 K on replacing *bpe* with *bpy* was attributed to this stronger interlayer exchange, and so it is intriguing that MOF–*azpy* appears to have a lower T_C. This indicates that there is a more complex relationship between the identity of the organic linker and the magnetic ground state. Another factor to consider at this point is the role of the ClO_4^- counterions, whose orientation in relation to the metal centre and the pillaring ligands have been demonstrated via first-principles computations to play a role in increasing the spin density along the magnetic exchange pathway between metal centres, perhaps through hydrogen bonding to the organic linker [233].

5.3.4 Probing Long-Range Order Using Muon Spectroscopy

The magnetic heat capacity presented in Section 5.3.2 indicates that there is a fraction of missing entropy released across the magnetic transition in MOF–*bpe*. Moreover, the refined magnetic moments for all three MOFs from WISH data presented in Section 5.3.3 are roughly 0.5 μ_B per Cu^{2+}. Both of these observations point towards a partially ordered magnetic ground state in these systems. To understand whether MOF–*bpe* undergoes long-range magnetic order, muon spin relaxation data were collected on the GPS instrument at PSI. Initially, data were collected in a transverse field (TF) to determine the calibration parameter, α, which corrects for count mismatch between the two detectors. At 40 K, the data display an oscillation with a frequency, ν_{TF}, proportional to the applied field. However, the full asymmetry expected for this instrumental configuration (~ 0.282) is not displayed at this temperature, indicating that there is an additional process which influences the muon spin polarisation. In zero field data at 25 K, still well into the paramagnetic regime, the value of the full initial asymmetry is also low compared to the instrumental value, and there is an unusual fast relaxing component present in the data at short times. One explanation for this behaviour may be the formation of muonium, which is a neutral state where the muon picks up an electron and the spins of each particle are bound by a hyperfine interaction [126, 234]. For this reason, α cannot be determined accurately, and therefore it is noted that the corrected asymmetry for subsequent measurements cannot be

determined.

Further measurements in a transverse field of 50 G were collected in order to track T_C. As the sample is cooled and an internal magnetic field develops, the muon spin is preferentially depolarised by this local internal field, so that by 1.5 K there is only a weak background signal from muons which stop in the aluminium sample holder and precess in the external field. The data can be modelled at all temperatures using,

$$A(t) = A_p \exp(-\lambda_{TF} t) \cos(2\pi\nu_{TF} t + \phi) + A_{bg}, \tag{5.2}$$

where A_p represents the paramagnetic volume fraction of the sample and λ_{TF} accounts for any damping of the oscillating signal. The baseline A_{bg} encompasses the background signal from the aluminium sample holder ($A_{bg} \approx 0.05$) as well as the fraction of muons which have their spin polarisation initially aligned with the local magnetic fields in the sample. A plot of A_p as a function of temperature, shown in Figure 5.10, demonstrates a clear drop off between 5 – 10 K, indicating that magnetic ordering takes place in this region. This is in agreement with the temperature at which the broad magnetic anomaly is observed in heat capacity data presented in Section 5.3.2. However, it is intriguing that the transition regime appears extended via analysis of these transverse field data.

Next, data were collected in zero field across the magnetic transition regime. In all zero field datasets, the fast-relaxing component with unknown origin persists at all temperatures. At 25 K, there is an additional slowly relaxing component which is indicative of muon spin relaxation in the presence of weak nuclear magnetic moments. Upon cooling, spontaneous oscillations at short times are evident in the data, indicative of muon spin precession in an internal field with a frequency proportional to that field. By 1.5 K, the asymmetry of the tail at longer times begins to recover and is flat, indicating that MOF–*bpe* undergoes long-range magnetic order. However, the presence of a one-third tail is ambiguous in this case because an accurate α was unable to be determined. In order to quantify these observations, a model was devised which describes the muon spin precession about an external field,

$$A(t) = A_s \cos(2\pi\nu + \phi) \exp(-\sigma_s^2 t^2) + A_f \exp(-\lambda_f) + A_{bg}. \tag{5.3}$$

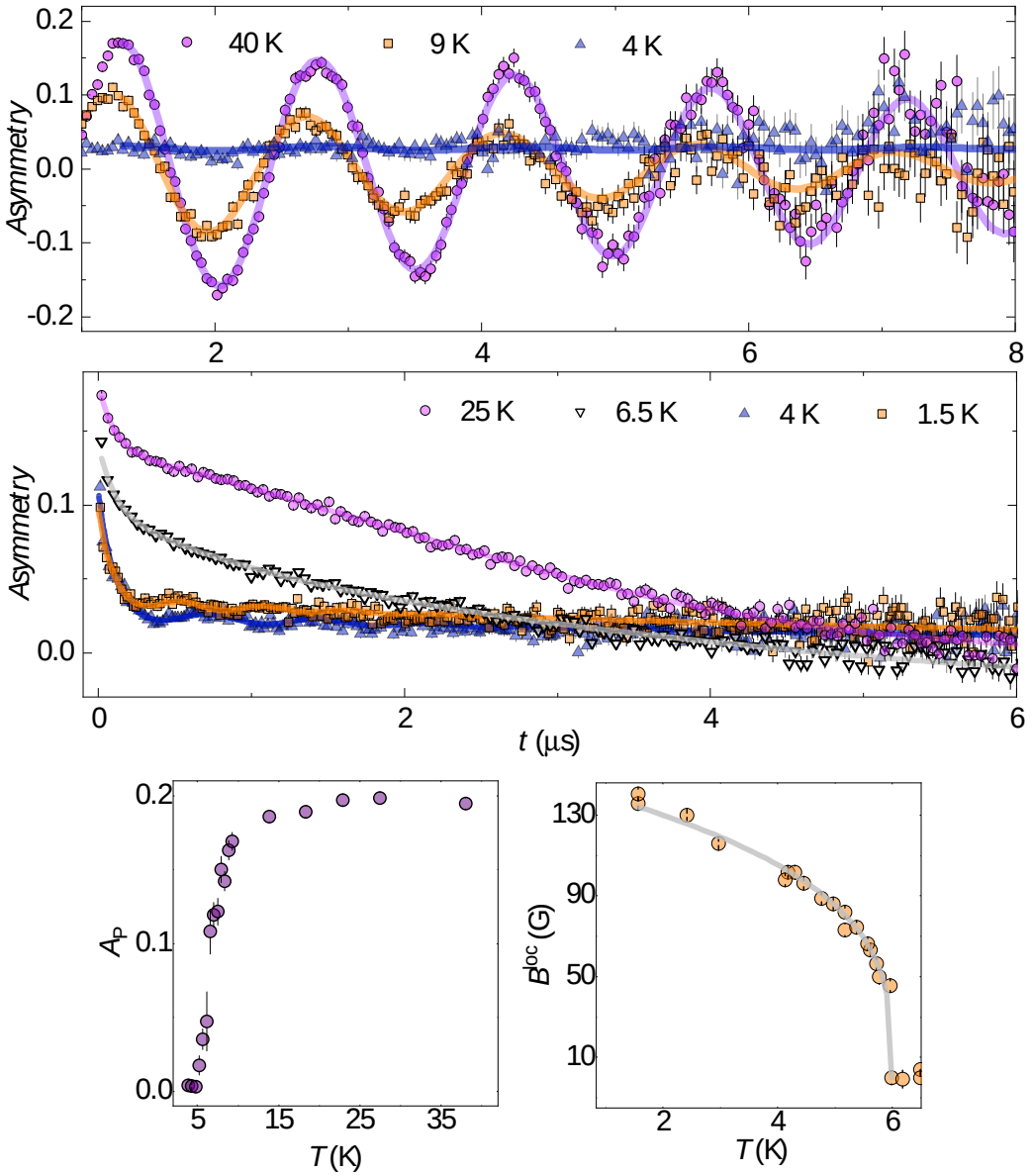

Figure 5.10: The temperature-dependent muon decay asymmetry measured for MOF–*bpe* in transverse field (top) and zero field (middle), from which the paramagnetic asymmetry, A_{P}, and the local magnetic field, B^{loc}, can be determined, respectively. The solid line on the lower right panel is from a fit of Equation 5.4 to the data.

Here, A_{f} represents the fast exponential decay present in all datasets, with a relaxation rate, λ_{f}, which appears to increase with decreasing temperature. A_{s} represents the amplitude of the spontaneous oscillations which have a frequency, ν, proportional to the local magnetic field at the muon stopping site, B^{loc}, which arises from static Cu^{2+} moments, with a relation $\nu = (\gamma_{\mu}/2\pi)B^{\mathrm{loc}}$. A plot of B^{loc} as a function of temperature, shown in Figure 5.10, can be modelled using a

critical law function,

$$B^{\mathrm{loc}} = B_0^{\mathrm{loc}}[1 - (T/T_{\mathrm{C}})]^{\beta}, \tag{5.4}$$

which yields $B_0^{\mathrm{loc}} = 147(3)$ G and $T_N = 5.99(1)$ K, as well as a critical exponent $\beta = 0.30(2)$, which is typical of three-dimensional magnetic ordering [15].

At 1.5 K, the internal field reaches a relatively small ~ 137 G. The small internal field is, therefore, an explanation for the extended transition regime evident from analysis of data collected in transverse field. The chosen applied field of 50 G is, in this case, comparable to the internal field within the sample close to the transition temperature, and so it is challenging to distinguish between the two contributions to the data around this temperature region. The small internal field also coincides with the recent AC magnetic susceptibility study on MOF–*bpe* which demonstrated the fragile nature of the magnetic ground state in weak applied fields of 125 G [92]. However, only tentative conclusions can be made from the muon spin relaxation data described here, due to the fast exponential component in the data which may be contributing to the damping of the spontaneous oscillations, which could disguise components with higher frequencies.

What can certainly be gleaned from the analysis of zero field data, however, is that MOF–*bpe* undergoes long-range, three-dimensional ordering at $T_{\mathrm{C}} = 5.99(1)$ K, and that there are no residual dynamics present at 1.5 K based on the absence of a relaxing tail in the asymmetry data. This, alongside the magnetic scattering presented in Section 3.3.3, contradicts the recent report on this material which describes the magnetic ground state of MOF–*bpe* as a short-range canted antiferromagnet which lacks conventional long-range magnetic order [92]. Instead, the weak magnetic scattering observed, alongside the broad magnetic anomaly in heat capacity data, is possibly a consequence of the significant disorder within the crystal structure of MOF–*bpe*, alongside the two-dimensionality of the crystal structure which may disguise the magnetic transition in heat capacity data [124]. Further muon spectroscopy measurements on MOF–*bpy* and MOF–*azpy* will elucidate whether long-range magnetic ordering also characterises their magnetic ground states.

5.4 Conclusions

The synthesis of a family of metal-organic frameworks which contain a kagomé network of Cu^{2+} ions bound by an organic pyridyl linker has been described. Two of these, MOF–*bpe* and MOF–*bpy*, are already known, but due to a new synthetic route to single crystals, a new crystal structure, described by space group $P3$, has been proposed for these systems which more accurately represents the geometry and orientational disorder present in the organic linkers. A third, novel member of this family has also been synthesised, where the organic linker has been replaced by 4,4'-azopyridine to create MOF–*azpy*. A combination of powder diffraction, bulk magnetometry and muon spectroscopy studies has led to several key findings:

- Synchrotron powder diffraction data exhibit systematically sharp $(00l)$ Bragg peaks, which may be due to correlated disorder of the organic linkers in these systems. The effect is particularly pronounced for MOF–*azpy*.

- Bulk magnetometry measurements indicate that there is a profound variation in the magnetic behaviour within this family of MOFs, indicating that the identity of the organic linker binding the kagomé layers together influences the interplay between ferromagnetic and antiferromagnetic exchange within and between the layers. Heat capacity data for MOF–*bpe* and MOF–*bpy* reveal weak magnetic anomalies, whilst MOF–*azpy* exhibits a stronger transition.

- The high flux and long d-spacing range of the WISH diffractometer has enabled the observation of magnetic Bragg peaks in NPD data which, crucially, disputes a recent study [92]. The magnetic unit cells of all three MOFs are doubled along the c-axis with respect to the underlying crystal structures, and indicate that antiferromagnetic exchange between the kagomé layers is facilitated by the organic linkers. Again, this is in contrast to several studies which postulated ferromagnetic exchange between the layers [92, 218, 219]. Interestingly, the magnetic structure of MOF–*bpe* contains a ferromagnetic component which is not observed in the other analogues, which perhaps is related to the increased linker flexibility in this system.

- The magnetic structures break the symmetry of the underlying crystal structures, suggesting that there is either a subtle structural distortion which is unobservable with current data, or that the disorder within these systems causes local distortions which may explain this symmetry breaking.

- Finally, muon spectroscopy measurements on MOF–*bpe* indicate that this system undergoes long-range, three-dimensional magnetic ordering at T_C = 5.99(1) K. This implies that the weak magnetic transition observed by many in heat capacity measurements is likely a result of structural disorder and the two-dimensional nature of these materials.

Whilst the materials presented here are unlikely models for the kagomé antiferromagnet, these results are reminiscent of the first proposed kagomé MOF, Cu-(1,3-*bdc*), whose magnetic structure was also ultimately found to contain antiferromagnetically coupled ferromagnetic layers [211]. As a result, there is building interest in kagomé ferromagnets, with the aforementioned material displaying signs of a magnon Hall effect [216]. Thus, whether the dominant exchange in the family of MOFs discussed within this chapter is ferromagnetic or antiferromagnetic, they do provide potential to uncover unconventional physics, and pose many interesting questions which should be addressed in future studies:

- The disorder in this family of materials is particularly interesting as it appears to affect the magnetic response observed across the series. An interesting comparison can be made to MOF–*bpa*, where *bpa* = 4,4'-bipyridylacetylene, in which the two-fold rotational symmetry of the linear *bpa* linker precludes the orientational disorder observed in the other members of this family.

- Careful analysis of single crystal X-ray diffraction data as a function of temperature will provide information on whether the structural disorder in these systems is a dynamic effect, and whether the disorder is correlated in some way. In addition, such measurements could reveal subtle symmetry lowering which may occur in this family of MOFs.

- Furthermore, the growth of large single crystals may enable a more detailed insight into the magnetic structures of these systems and elucidate the nature of the exchange within the distorted kagomé layers. Further DFT calculations, leading on from Mateus *et al* [231], will also provide crucial understanding in this regard.

- The synthesis of new members of this family will provide further insight into the role of the organic linker in these systems. Synthetic routes to new analogues should utilise control over the pH [230], as well as post-synthetic modification routes such as ligand exchange [235, 236]. There also exist two more related materials, where the unidentate organic linkers 4-aminopyridine [237] and 2,4'-bipyridine [230] are incorporated. These systems are truly

two-dimensional as the distinct layers are not covalently bonded, and so an in-depth exploration of the magnetic behaviour of these analogues will provide an interesting comparison to the ones studied within this chapter to elucidate the role of the linker.

Chapter 6

Geometrically Frustrated Magnetism and Low-Dimensionality in a Hybrid Coordination Framework, $KFe(C_2O_4)F$

6.1 Introduction

The conception of the quantum spin liquid was originally hypothesised in the context of Heisenberg spins on the triangular lattice [49]. Whilst the presence of a spin liquid ground state in such materials with these characteristics was later shown to be false—Heisenberg spins with purely nearest-neighbour interactions adopt a non-collinear configuration where each is aligned at 120 degrees with respect to its neighbour [32]—perturbations to the ideal model which cause interactions beyond the nearest neighbour can indeed lead to the formation of spin liquid states. For example, the family of organic salts related to κ-(BEDT-TTF)$_2$Cu$_2$(CN)$_3$ contain dimers of BEDT-TTF (bis(ethylenedithio)-tetrathiafulvalene), which each contain a $S = \frac{1}{2}$ source and form an anisotropic triangular network [238]. Members of this family are not only quantum spin liquid candidates [63, 64], but also display superconducting behaviour under pressure [239]. Additionally, the presence of anisotropic exchange in triangular systems can result in intriguing magnetic ground states. For example, in the triangular material Cs_2CuCl_4 [240, 241] the formation of spinons above T_N in the inelastic neutron scattering spectrum was originally proposed to be due to an underlying two-dimensional QSL state [242]. However, this was subsequently attributed to the one-dimensional chains which characterise its crystal structure [243]. These examples, depicted in Figure 6.1,

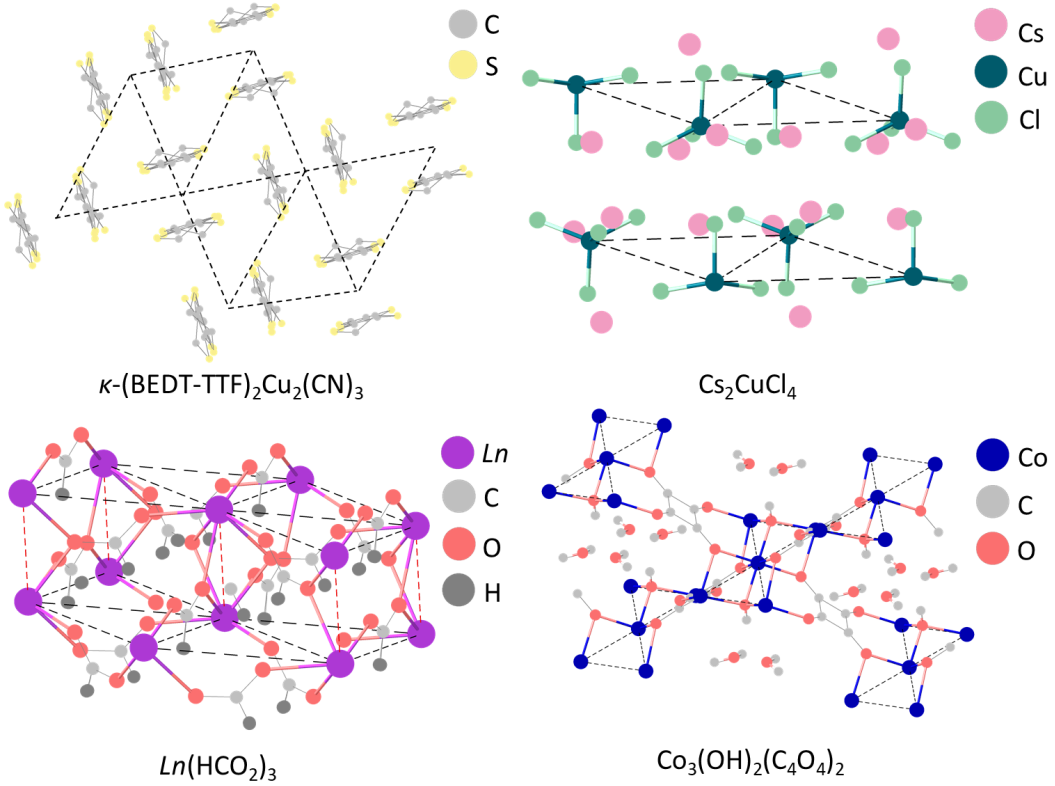

Figure 6.1: The key structural features of materials discussed in the text which bear a triangular arrangement of spins, represented by dashed lines. In κ-(BEDT-TTF)$_2$Cu$_2$(CN)$_3$ [238], partially oxidised dimers of BEDT-TTF represent triangular layers, which are separated by $[Cu_2(CN_3)]^-$ anionic layers (not shown). In Cs_2CuCl_4 [240], triangular layers form in the *bc*-plane, although the magnetic ground state is described by a one-dimensional chain of Cu^{2+} spins along the *b*-axis [243]. In *Ln*(HCO$_2$)$_3$ [244], one-dimensional behaviour (red dashed line) has been observed along the stacking direction of the triangular planes [98]. Meanwhile, in Co$_3$(OH)$_2$(C$_4$O$_4$)$_2$ [245] strong exchange dominates through the short Co-O-Co pathway [246].

illustrate that a triangular arrangement of magnetic ions offers the potential for a rich variety of unusual magnetic ground states, and that new material realisations of such triangular and low-dimensional systems are worthwhile pursuits.

In this regard, hybrid coordination frameworks offer a great deal of versatility in which to explore the synthesis of new magnetically frustrated systems. As was introduced in Chapter 5, the diversity of organic linkers available to the synthetic chemist offers a wealth of new potential materials with a breadth of topologies. Whilst the metal-organic frameworks explored in Chapter 5 utilised organic parts to separate the quasi-two-dimensional layers, organic components can also

be utilised to control the topology *within* the two-dimensional layers. In coordination frameworks, for example, the organic linkers are typically shorter compared to those in metal-organic frameworks, and thus are ideal for controlling intralayer topology and for facilitating superexchange [247]. Indeed, there are several examples of coordination frameworks that contain geometrically frustrated arrays of magnetic ions. One example is the family of lanthanide-based $Ln(HCO_2)_3$ materials, in which the formate linkers bind the lanthanide centres into a triangular arrangement, shown in Figure 6.1 [248]. In this case, analysis of diffuse neutron scattering data indicates these materials resemble a one-dimensional chain just above their magnetic ordering temperatures, which is thought to contribute to their enhanced magnetocaloric properties [98]. Other examples of frustrated coordination frameworks include kagomé structures [211, 249], three-dimensional structures composed of frustrated subunits [250], mixed triangular-kagomé [251] and even more elusive structure types such as star-like arrays, where a recent example is thought to negate long-range magnetic ordering at all temperatures [45, 252]. The resultant topology in these hybrid materials depends on several factors, such as the metal ion used and the binding mode of the organic linker. The latter is demonstrated by the squarate dianion, $(C_4O_4)^{2-}$, in the coordination framework $Co_3(OH)_2(C_4O_4)_2$ [245].xH_2O [253]. Here, the Co^{2+} ions are connected into triangular layers via one-atom (Co-O-Co) and four-atom (Co-O-C-C-O-Co) bridges, also shown in Figure 6.1, and one-dimensional behaviour has been demonstrated depending on the level of hydration [246].

The oxalate linker, $(C_2O_4)^{2-}$, is another example where the binding modes adopted facilitate the formation of one topology over another as well as the nature of the superexchange, and its versatility in this regard has been exploited in several examples of magnetically frustrated and low-dimensional frameworks [254–257]. For example, a recent report presenting a hybrid material in which oxalate linkers bind Cu^{2+} ions into a honeycomb arrangement shows promise as a QSL candidate [257]. Another example is in the $KTi(C_2O_4)_2{\cdot}xH_2O$ polymorphs, the structures of which vary from frustrated square to diamond-type structures depending on the synthetic conditions [122]. A family of materials composed of triangular layers of $[Fe(C_2O_4)]_\infty$ are also of interest, because the chosen coordination of the oxalate linker—either through *cis* or *syn-anti* modes, or a combination of the two—connects the Fe^{2+} ions into either a distorted kagomé [123, 258–260] or a distorted triangular structure [123, 261], as depicted in Figure 6.2. The resulting topology is ultimately dictated by the chosen ion which separates the magnetic layers.

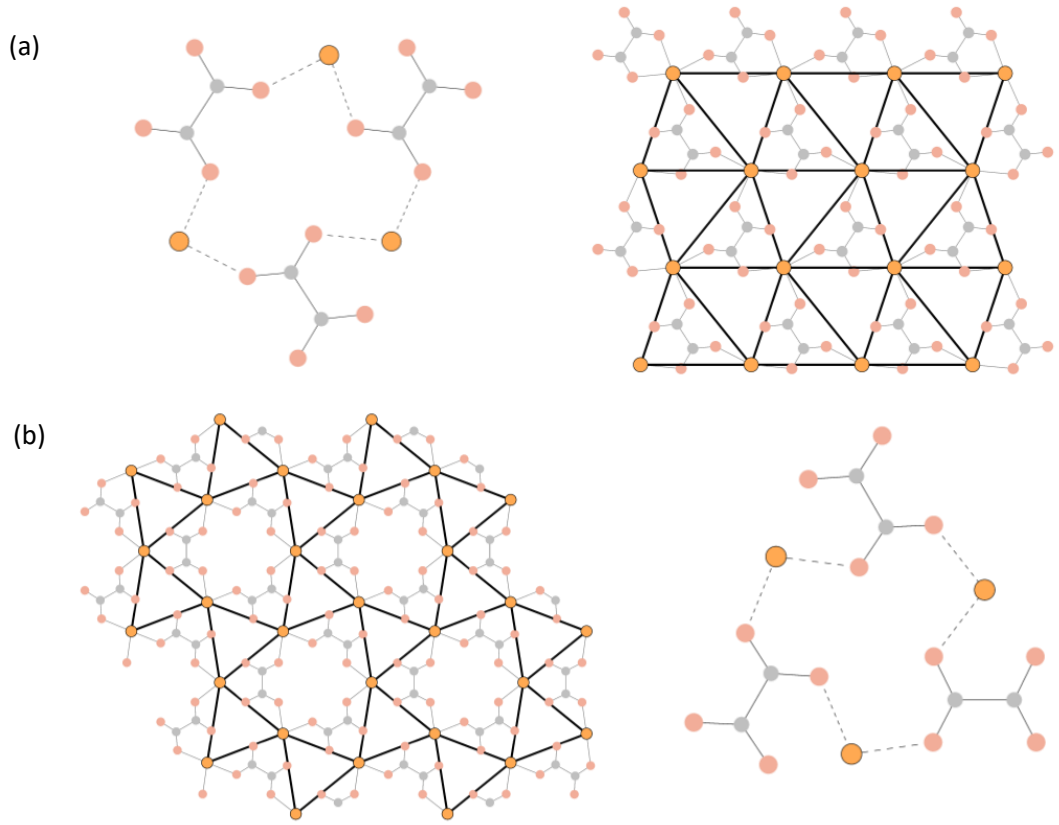

Figure 6.2: (a) The distorted triangular magnetic sublattice, represented by orange circles, formed from two *syn-anti* and one *cis* binding mode of the oxalate linker, shown by grey and red circles. This type of bonding results in three different bond lengths within the triangles. (b) An alternative magnetic sublattice, where the oxalate linkers bind in all *syn-anti* conformations, results in equilateral triangles in a distorted kagomé array.

One particularly intriguing material in this family of oxalates is $KFe(C_2O_4)F$, in which fluoride anions connect together distorted triangular layers of $[Fe(C_2O_4)]_\infty$. The initial report of this material by Yao *et al* [123] presented magnetic susceptibility data that demonstrate a broad maximum below 100 K, indicative of the onset of short-range magnetic correlations. Meanwhile, a sharp upturn in the susceptibility below 20 K indicates a transition to long-range magnetic order. It was hypothesised that this may indicate a crossover from a one-dimensional to a three-dimensional magnetic sublattice. As a result of this intriguing magnetic behaviour, further investigation into the magnetic properties of this system is required to determine the relationship between the crystal structure of $KFe(C_2O_4)F$ and the magnetic features previously observed. This chapter reports a comprehensive neutron powder diffraction (NPD) study to understand the nature of the

magnetic ground state in $KFe(C_2O_4)F$, which is supported by additional muon spectroscopy data. This work is published in Inorganic Chemistry [262].

6.2 Experimental Methods

6.2.1 Synthesis

The sample of $KFe(C_2O_4)F$ characterised throughout this chapter was prepared by Dr Wenjiao Yao in the School of Chemistry at the University of St Andrews via a hydrothermal method [123]. Commercially sourced $Fe(C_2O_4) \cdot 2H_2O$, $C_2H_2O_4$, KBF_4 and K_2CO_3 in a 1:3:2:4 ratio were sealed in a 23 mL stainless steal Teflon-lined autoclave. The autoclave was heated to 160 °C, held at this temperature for 48 hours, and then removed from the oven to allow to cool to room temperature. The product, a 1 g yellow-orange polycrystalline sample, was collected by filtration and washed with distilled water and acetone.

6.2.2 Neutron Powder Diffraction

Time-of-flight NPD data were collected on the same 1 g sample of $KFe(C_2O_4)F$ on the General Materials (GEM) diffractometer of the ISIS Neutron and Muon Source. The sample was packed into a cylindrical vanadium can and cooled to 2 K in a helium cryostat. Data were collected from 2 – 150 K at regular temperature intervals. Rietveld refinements were conducted against data collected in all six banks simultaneously at each temperature using the GSAS [94, 95] and FullProf [96] packages for nuclear and magnetic structure refinements, respectively.

6.2.3 Muon Spectroscopy

Muon spin relaxation data were collected on the 1 g sample of $KFe(C_2O_4)F$ on the MuSR instrument of the ISIS Neutron and Muon Source. The powder sample was packed to a density of 170 mg/cm^2 in an aluminium sample plate, and data were measured between 10 – 200 K in zero field and in an applied longitudinal field of 100 G. Data were analysed by Lewis Farrar in the Department of Chemistry at the University of Liverpool in the Windows Muon Data Analysis (WiMDA) program [263].

6.3 Results and Discussion

6.3.1 Crystal Structure Characterisation Using Neutron Powder Diffraction

The NPD patterns for $KFe(C_2O_4)F$ collected on the GEM diffractometer at 150 K are displayed in Figure 6.3, and a Rietveld refinement of the orthorhombic $Cmc2_1$ structural model confirms the crystal structure solved previously through single-crystal X-ray diffraction [123]. Backgrounds for each bank were modelled using a shifted Chebyschev function with 12 background terms. It was possible to refine all atomic coordinates independently, and atomic displacement parameters were refined isotropically with constraints across like-atoms. The final structural model at 150 K is shown in Table 6.1. This crystal structure is retained down to 2 K with an isotropic reduction in the lattice parameters and atomic displacement parameters with decreasing temperature, as presented in Figure 6.4.

The resulting crystal structure of $KFe(C_2O_4)F$ is shown in Figure 6.5. From the perspective of frustrated magnetism, the structure possesses two interesting features. The first is the presence of laterally slanted triangles of Fe^{2+} ions that are connected via *cis* and *syn-anti* bonding modes of the oxalate linker and that lay

Table 6.1: Crystal structure parameters obtained from Rietveld refinement of the $Cmc2_1$ model to NPD data collected at 150 K. Refined lattice parameters are $a = 7.739(2)$ Å, $b = 11.863(3)$ Å and $c = 10.407(3)$ Å. The final statistical factors are $R_{\mathrm{wp}} = 3.21\%$ and $\chi^2 = 2.480$.

Atom	Site	x	y	z	U_{iso}
Fe	8*b*	0.2533(2)	0.42631(7)	0.1544(2)	0.0048(2)
K1	4*a*	0.5	0.3326(6)	0.8691(5)	0.0139(7)
K2	4*a*	0.0	0.6620(5)	0.3473(6)	0.0139
O1	8*b*	0.2427(3)	0.5121(2)	0.4574(2)	0.0082(2)
O2	8*b*	0.2668(3)	0.3533(2)	0.3417(2)	0.0082
O3	8*b*	0.2782(3)	0.3912(2)	0.6744(2)	0.0082
O4	8*b*	0.2903(3)	0.2340(2)	0.5571(3)	0.0082
C1	8*b*	0.2557(3)	0.4077(1)	0.4449(1)	0.0055(3)
C2	8*b*	0.2781(3)	0.3367(2)	0.5703(2)	0.0055
F1	4*a*	0.0	0.4554(3)	0.1821(4)	0.0240(7)
F2	4*a*	0.5	0.3995(3)	0.1333(4)	0.0240

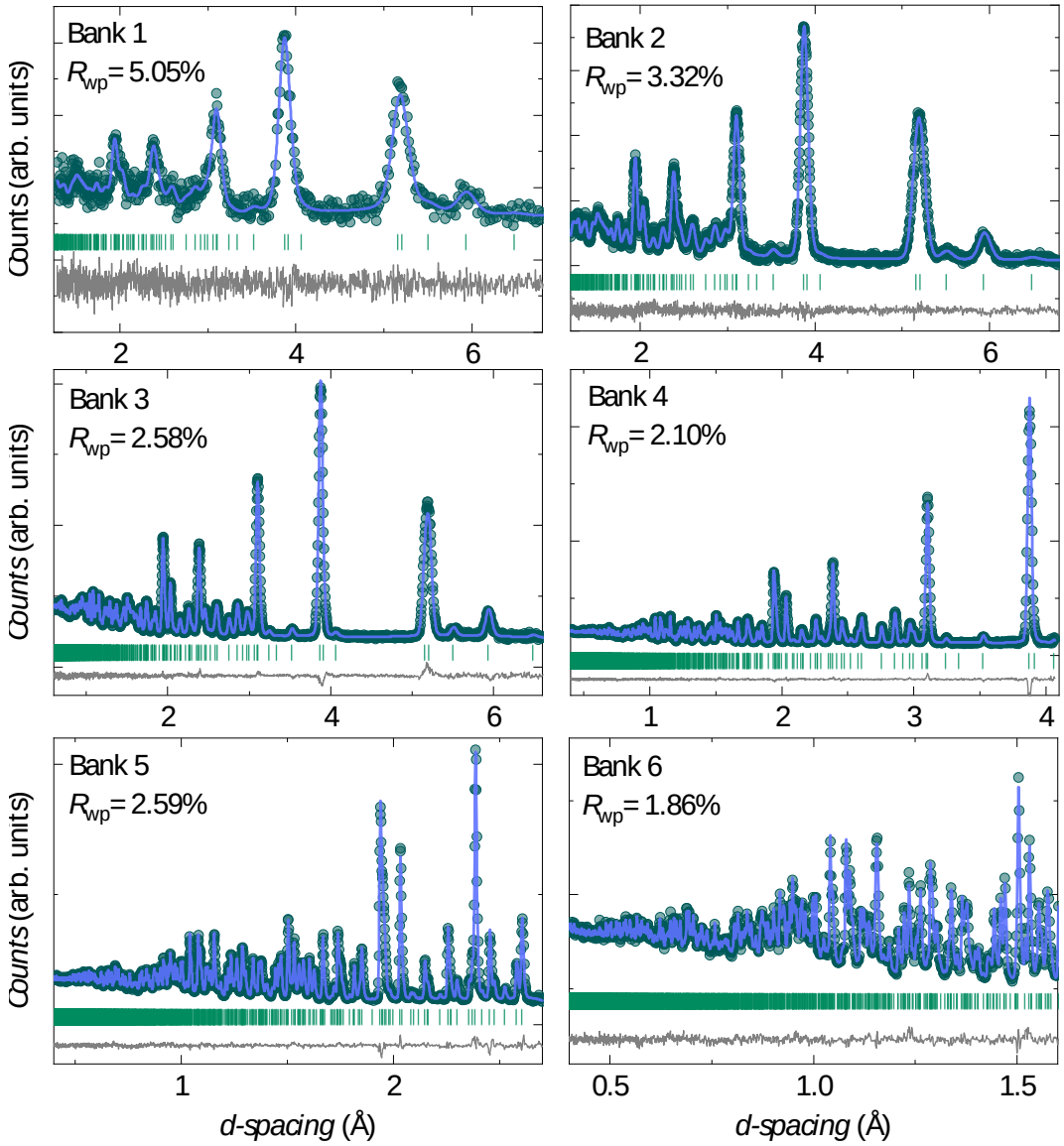

Figure 6.3: Rietveld refinement of the $Cmc2_1$ structural model to NPD data collected on each bank of the GEM diffractometer at 150 K. Data points are shown in green, the fitted curves are shown in blue and Bragg peak positions are represented by light green tick marks.

within the *bc*-plane. The triangular layers are stacked along the *a*-axis and are perfectly eclipsed. The Fe^{2+} ions, which have a d^6 high-spin electron configuration, are octahedrally coordinated with four bonds to oxygen anions of the oxalate linkers and two bonds to fluoride anions. The second notable structural feature, therefore, is the quasi-one-dimensional Fe–F–Fe chains which run along the *a*-axis, perpendicular to the triangular planes. Finally, K^+ cations occupy positions between the triangular layers, within the same plane as the fluoride anions.

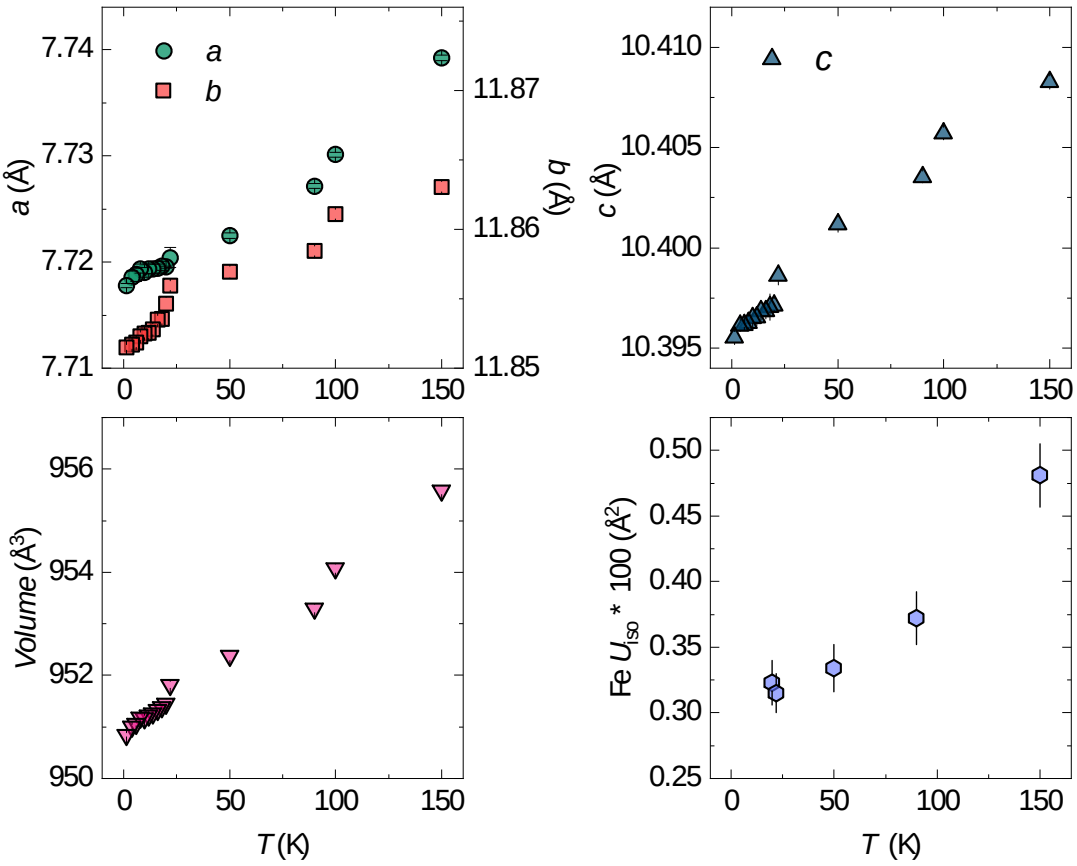

Figure 6.4: The refined lattice parameters (top), volume (bottom left) and isotropic atomic displacement parameters, U_{iso} (bottom right), as a function of temperature for $KFe(C_2O_4)F$, as obtained from Rietveld and Le Bail fits of the $Cmc2_1$ structural model to data collected on GEM.

The oxalate linker adopts a planar conformation with approximate D_{2h} symmetry and a dihedral angle in the region of 3.2°, as expected for bidentate coordination in the absence of particularly large cations or bulky counterions [264]. The combination of *cis* and *syn-anti* conformations results in three different Fe–Fe bond lengths within the triangular planes: 6.680(1) Å through the Fe–O–C–C–O–Fe *cis* linkage and 5.489(2) Å and 5.932(2) Å via two Fe–O–C–O–Fe *syn-anti* bonding modes. The Fe^{2+} octahedra are slightly distorted, with four Fe–O bond lengths ranging from 2.129 – 2.200 Å and Fe–F1 and Fe–F2 bond lengths of 1.982(2) Å and 1.983(2) Å, respectively, and bond angles within the octahedra ranging from 75.6° – 93.4°. A consideration of Goodenough-Kanamori rules [23–25] implies that strong antiferromagnetic exchange interactions are predicted to dominate along the *a*-axis due to the Fe–F–Fe chains, which contain angles of 153.6(2)° for Fe–F1–Fe and 156.1(2)° for Fe–F2–Fe.

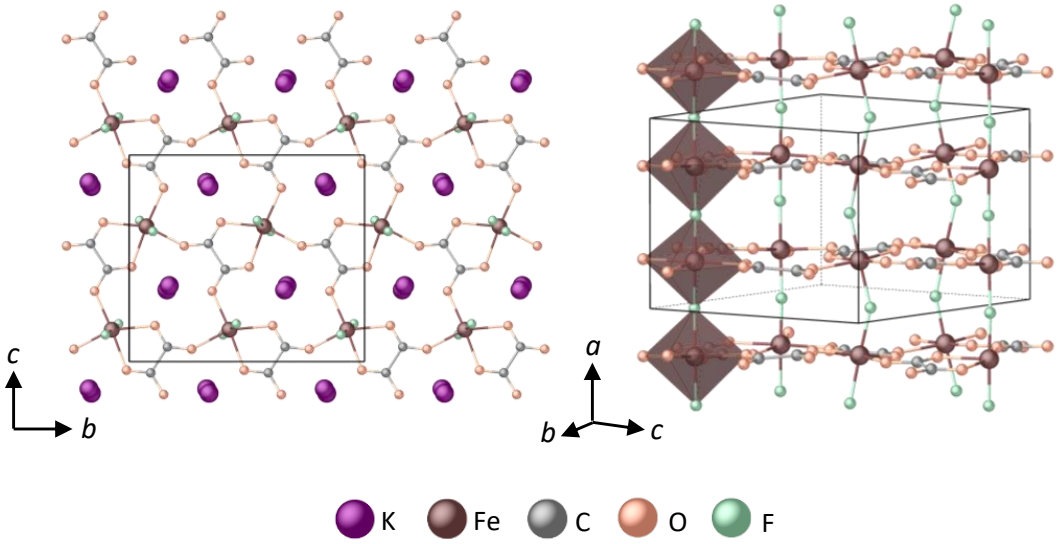

Figure 6.5: The crystal structure of $KFe(C_2O_4)F$, which contains a distorted triangular network of Fe^{2+} in the *bc*-plane (left), whilst K^+ ions occupy interlayer positions. Meanwhile, Fe–F–Fe chains run along the *a*-axis (right).

It is interesting to note that the synthesis of alkali metal analogues of $KFe(C_2O_4)F$ results in significantly different structure types. For example, attempts to replace K^+ in $KFe(C_2O_4)F$ with Na^+ yields $Na_2Fe(C_2O_4)F_2$ instead, which consists of zigzag chains of $[Fe(C_2O_4)F_2]^{2-}$ [265] rather than the triangular structure type presented here. The identity of the bridge which binds the layers together also influences the final crystal structure. For instance, in the two-dimensional materials $Li_2[Fe(C_2O_4)Cl_2][Fe(C_2O_4)(H_2O)_2]\cdot{}_2H_2O$ [123] and $K_2Fe(C_2O_4)(HPO_4)(OH_2)\cdot H_2O$ [261], the same laterally slanted triangular layers appear, but they are staggered because the chloride and hydrogen phosphate anions, respectively, fail to bind the layers together. Clearly, the coordination of the fluoride anion to triangular layers above and below in $KFe(C_2O_4)F$ plays a key role in stabilising the eclipsed stacking of the layers. Meanwhile, $Na_2Fe(C_2O_4)(SO_4)\cdot H_2O$ was previously synthesised using the same route as $KFe(C_2O_4)F$ with the replacement of KBF_4 with sulphuric acid and K_2CO_3 with Na_2CO_3, but yields a distorted kagomé structure instead, where each oxalate linker is bound in a *syn-anti* configuration [123]. In other examples of distorted kagomé structures the oxalate linker plays the additional role of binding the layers together via a *syn-anti* mode, such as in $(NH_4)_2Fe(C_2O_4)_2\cdot H_2O$ [259] and $Na_2K_4(Fe(C_2O_4)_2)_3\cdot 3H_2O$ [260]. These observations demonstrate that the identity of both the alkali metal and the bridging anion dictates the overall symmetry in this family of oxalate materials.

6.3.2 Observation of Magnetic Ordering Using Muon Spin Relaxation

The initial study of $KFe(C_2O_4)F$ by Yao *et al* [123] reported temperature-dependent magnetic susceptibility data which could be modelled using a Curie-Weiss law above 100 K, with a Weiss constant $\theta = -301(2)$ K, indicating dominant antiferromagnetic exchange interactions. The data also demonstrated a broad maximum centred at 100 K which was successfully modelled using a one-dimensional spin chain model with an intrachain coupling constant $J = 8.46(4)$ K. These results are, therefore, consistent with the observation of chains within the crystal structure of $KFe(C_2O_4)F$. Muon spectroscopy has proved to be a key experimental tool in the study of low-dimensional magnetism [266], and is an excellent probe for the presence of any remaining dynamics which may persist in such low-dimensional systems.

The muon decay asymmetry measured in zero field (ZF) at 200 K is shown in Figure 6.6, where the relaxation observed is characteristic of muon depolarisation due to the nuclear magnetic moments of nuclei within the crystal structure of $KFe(C_2O_4)F$. Intriguingly, there are no features indicative of muon entanglement, which might be expected due to the presence of fluoride anions in the system. This suggests that the muon comes to rest at a position away from the F^- sites

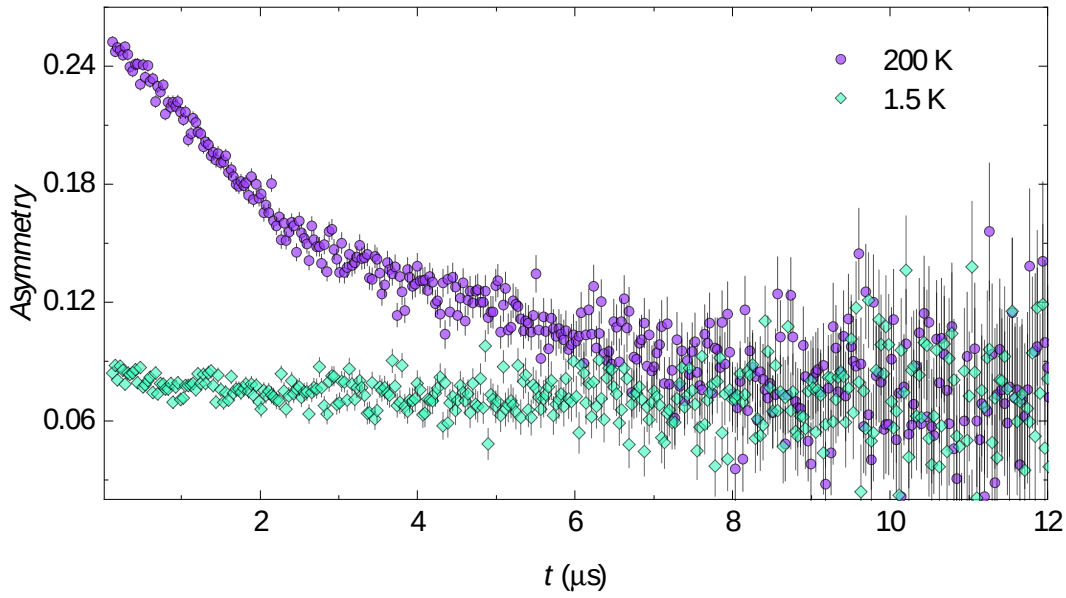

Figure 6.6: The muon decay asymmetry measured in zero field for $KFe(C_2O_4)F$ at 200 K and 1.5 K.

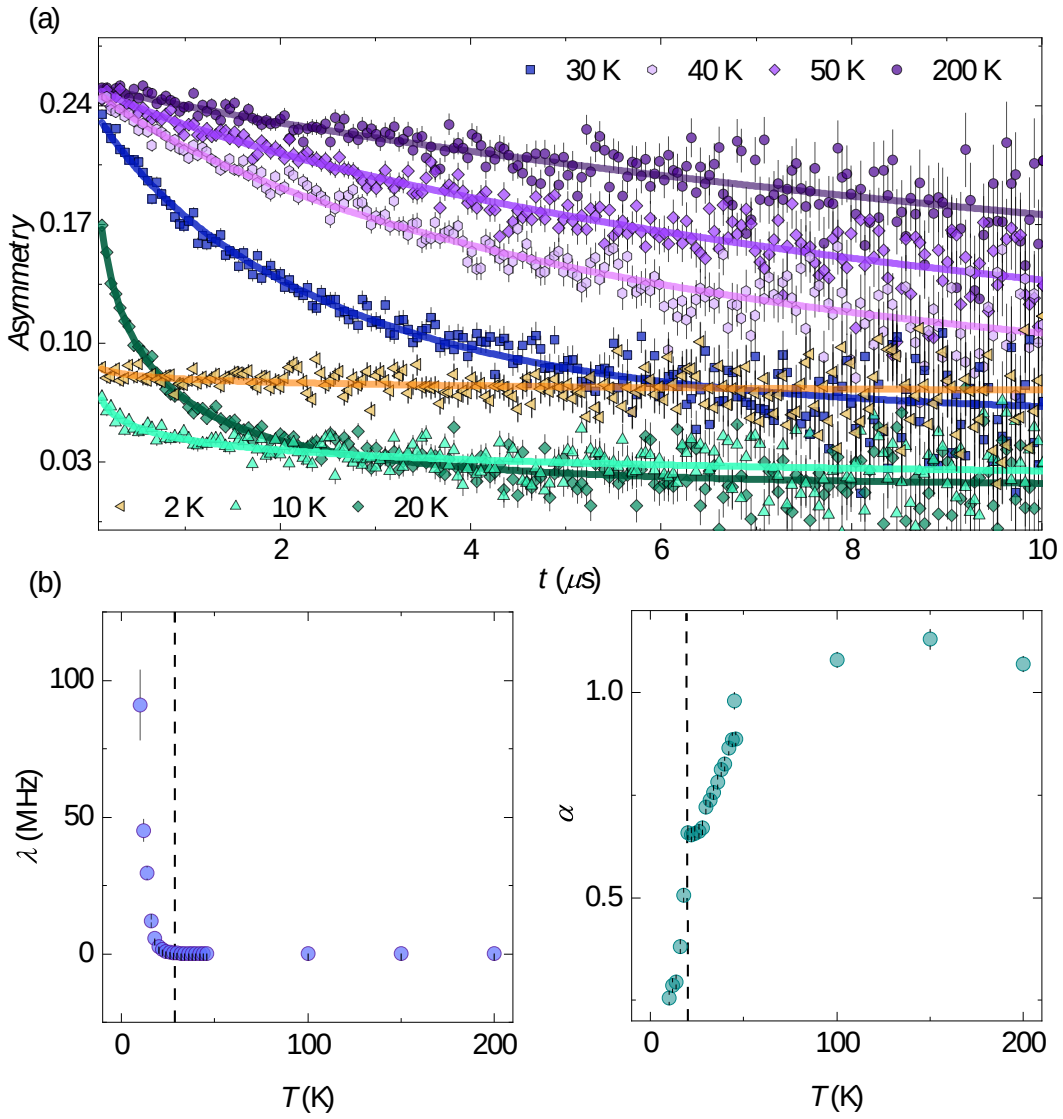

Figure 6.7: (a) The muon decay asymmetry measured for $KFe(C_2O_4)F$ in a longitudinal field of 100 G between 2 – 200 K. Solid lines are fits of Equation 6.1 to the data. (b) The fitted muon spin relaxation rate, λ (left), and stretching component, α (right), as a function of temperature. The dashed line represents T_N.

between the layers. It can be inferred from this that the muon stopping sites are likely near the oxalate linkers, within the triangular planes, and should, therefore, provide an excellent probe for the magnetism within $KFe(C_2O_4)F$. Upon cooling to 1.5 K, a loss of the initial asymmetry indicates a fast depolarisation of the muon spin as internal magnetic fields develop. The characteristic one-third tail commonly observed in polycrystalline samples in the presence of a static internal field is absent here, although the lack of a relaxing component in the tail, clearly shown in Figure 6.6, indicates that there are no residual dynamics present at this

temperature.

A longitudinal field (LF) of 100 G was applied to the sample and the muon decay asymmetry was measured at regular intervals between 1.5 – 200 K, as displayed for selected temperatures in Figure 6.7. The applied field has the effect of decoupling the muon spin from nuclear spins, so that the muon directly probes magnetism arising from unpaired electrons in the system. As a consequence, the increase in the decay of the asymmetry as the temperature is lowered indicates the development of an internal magnetic field which depolarises the muon spin. This is particularly evident below ~ 40 K, where the muon spin is rapidly depolarised at a rate beyond the time resolution of the MuSR spectrometer, leading to a loss of asymmetry at temperatures below this point. By 2 K, a recovery of the baseline to approximately one-third of the initial asymmetry at high temperatures is further evidence for completely static magnetic moments. To quantify these observations, data collected in a LF were modelled using a stretched exponential,

$$A(t) = A_0 \exp(-\lambda t)^{\alpha} + A_{\mathrm{B}}. \tag{6.1}$$

Here, A_0 represents the initial asymmetry, and was fixed at the high temperature fitted value to account for the loss of asymmetry at lower temperatures. A_{B} is a background term accounting for muons stopping in the sample environment, whilst λ is the muon spin relaxation rate and α is a stretching component. The fitted values of λ and α are shown in Figure 6.7. Above 100 K, the data can be modelled by a simple exponential where $\alpha \approx 1$, which is typical of muon spin relaxation caused by electrons in a paramagnetic regime. However, as the sample is cooled below 100 K, α tends towards $\sim \frac{1}{3}$, which suggests that a more complex distribution of internal fields develops at these low temperatures. Meanwhile, the muon relaxation rate, λ, rapidly increases below ~ 20 K. Taken together with the previously reported magnetometry results, in which an upturn in the magnetic susceptibility was observed at the same temperature, it can be concluded that $KFe(C_2O_4)F$ undergoes a transition to long-range magnetic order at $T_{\mathrm{N}} \approx 20$ K.

6.3.3 Magnetic Structure Determination Using Neutron Powder Diffraction

A key question that Yao *et al* discussed in their initial report of $KFe(C_2O_4)F$ is whether the one-dimensional behaviour they observed in magnetic susceptibility measurements stems from the Fe–F–Fe chains within its crystal structure

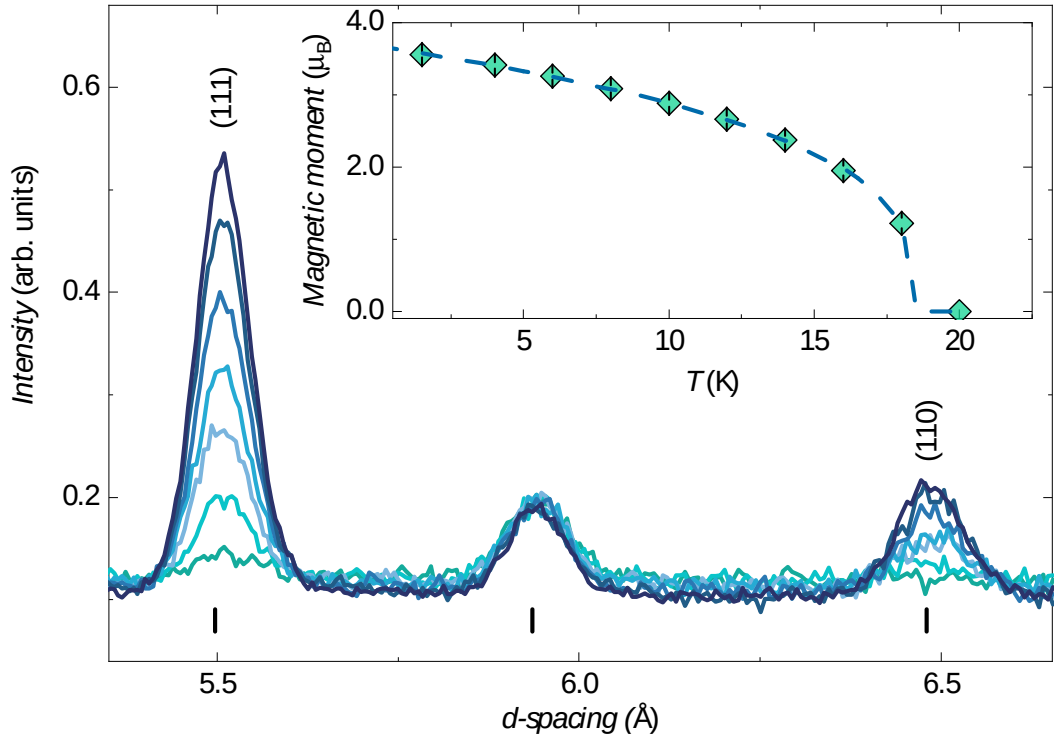

Figure 6.8: The evolution of (111) and (110) magnetic Bragg peaks in NPD data collected for $KFe(C_2O_4)F$ below 20 K. The temperature variation of the refined magnetic moment of Fe^{2+} in $KFe(C_2O_4)F$ is shown in the inset. The dashed line is a guide to the eye to demonstrate the critical behaviour of the magnetic moment, represented by Equation 6.2.

or, alternatively, from a more complex exchange pathway within the triangular layers. In order to address this and understand the nature of the magnetic ordering in $KFe(C_2O_4)F$, NPD data was collected below 20 K. Upon cooling below this temperature, additional magnetic scattering was observed in reflection positions of allowed nuclear Bragg peaks of the $Cmc2_1$ space group, which indicates a magnetic propagation vector $\mathbf{k} = (0, 0, 0)$. The evolution of the (111) and (110) magnetic Bragg peaks are shown in Figure 6.8. Using $\mathbf{k} = (0, 0, 0)$ and the nuclear space group $Cmc2_1$, a set of possible magnetic space groups was determined using the *BasIreps* and ISODISTORT [267] programmes. There are four possible symmetry-allowed irreducible representations from this search ($m\Gamma_1$, $m\Gamma_2$, $m\Gamma_3$, $m\Gamma_4$ in Miller-Love notation [268]), which correspond to $Cmc2_1$, $Cm'c'2_1$, $Cmc'2'_1$ and $Cm'c2'_1$ magnetic space groups.

Magnetic structure refinements were implemented by fixing the scale factor and

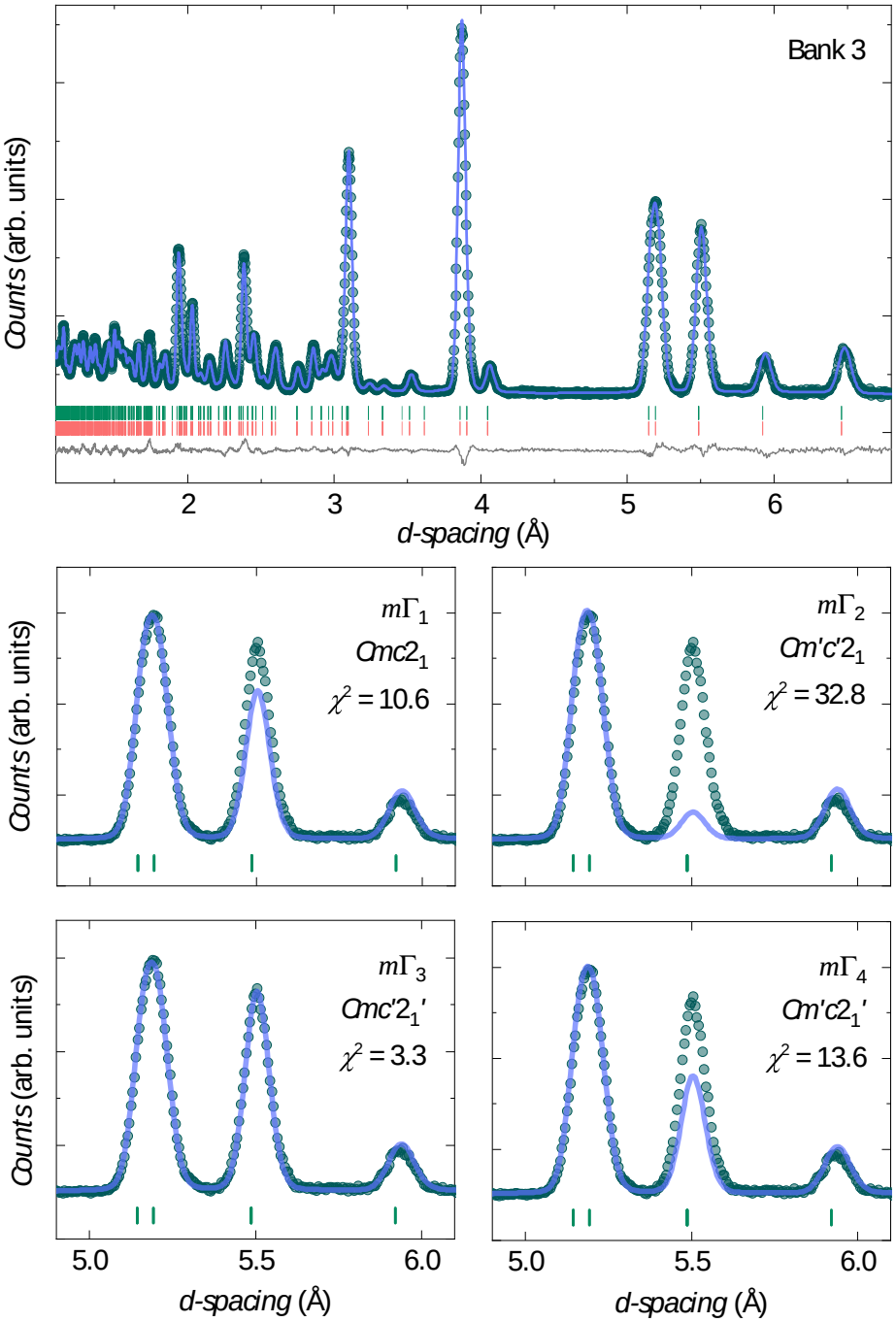

Figure 6.9: Corefinement of the nuclear ($Cmc2_1$, top ticks) and magnetic ($Cmc'2'_1$, bottom ticks) structures of $KFe(C_2O_4)F$ to NPD data collected on bank 3 of GEM at 1.5 K ($R_{wp} = 6.28\%, \chi^2 = 3.281$). The lower four panels show a comparison of the Rietveld refinements of the four magnetic space groups compatible with the $Cmc2_1$ nuclear space group, along with corresponding χ^2 values.

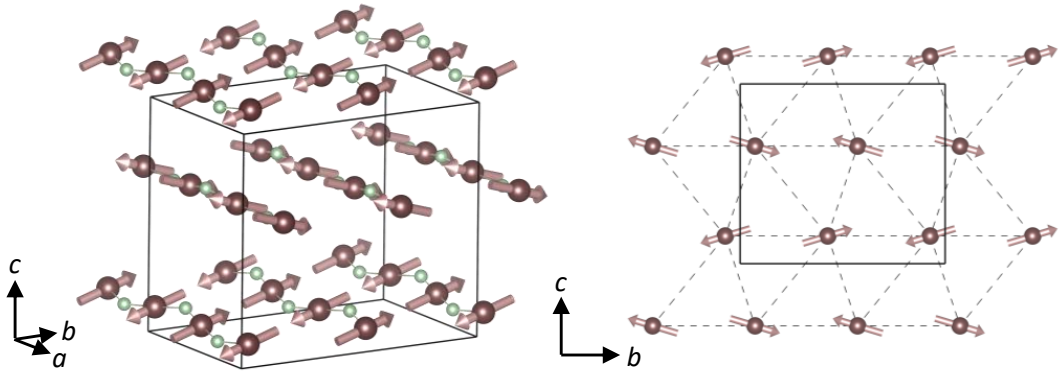

Figure 6.10: The magnetic structure of $KFe(C_2O_4)F$ at 1.5 K, which belongs to the $Cmc'2'_1$ magnetic space group. The structure is formed from antiferromagnetically coupled chains which run along the a-axis and are mediated by fluoride anions (green spheres). The chains are packed onto the distorted triangular layers in the bc-plane.

profile parameters from a refinement of the $Cmc2_1$ structural model at 20 K. The lattice parameters were then allowed to refine at 1.5 K, along with the magnetic moments along each crystallographic axis for each of the proposed magnetic space groups in turn. A comparison of each of these fits to the magnetic (111) Bragg peak is given in Figure 6.9. Here, it is clear that $Cmc'2'_1$ is the most appropriate model to describe the magnetic scattering, and a fit of this to the full diffraction pattern collected at 1.5 K in Bank 3, where the magnetic scattering is most evident, is also shown in Figure 6.9. In the final fitted model, the magnetic moments along the b- and c-axes were refined, yielding $m_y = 3.41(4)$ μ_B and $m_z = 1.02(8)$ μ_B, respectively. The fit was not significantly improved with the inclusion of refinement of the moment along the a-axis ($\chi^2 = 3.22$ vs $\chi^2 = 3.28$), and resulted in unstable refinements for temperatures larger than 16 K. Therefore, this component was fixed to zero for all subsequent refinements. The total moment magnitude at 1.5 K is 3.56(4) μ_B, which is comparable to the saturisation magnetisation, μ_{sat}, expected for Fe^{2+}. The temperature dependence of the refined total magnetic moment is shown in Figure 6.8. A critical law, given by,

$$\mu(T) = \mu_0[1 - (T/T_N)]^{\beta}, \tag{6.2}$$

can be used to model this temperature dependence. Given that there are so few data points around the suspected ordering temperature, this fit provides an estimate of $T_N \approx$ 18.5 K and $\beta \approx 0.3$, which is typical of three-dimensional ordering [15].

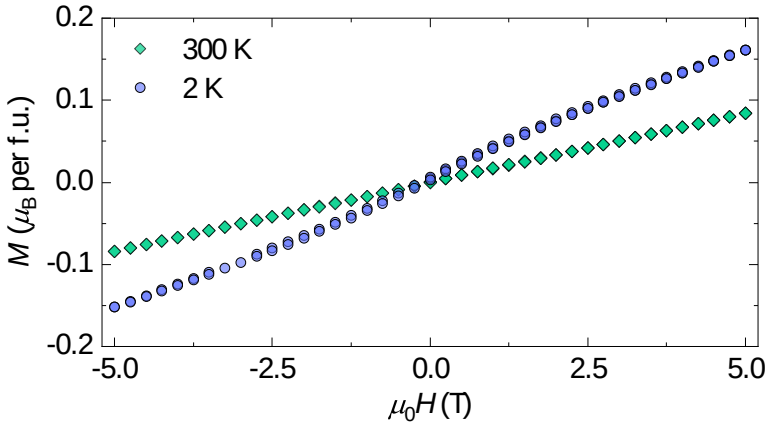

Figure 6.11: The isothermal magnetisation of $KFe(C_2O_4)F$ measured at 300 K and 2 K. At 2 K, no significant hysteresis is observed, indicating antiferromagnetic ordering.

The resulting magnetic structure at 1.5 K consists of antiferromagnetically coupled Fe^{2+} ions that run along the *a*-axis, shown in Figure 6.10(a), and that are packed onto the triangular layers that form in the *bc*-plane. The magnetic moments point predominantly towards the *b*-axis, with a small antiferromagnetic canting towards *c*, as depicted in Figure 6.10(b). This structure is consistent with isothermal magnetisation data at 2 K, which do not provide evidence for any significant hysteresis, and instead give a response typical of three-dimensional antiferromagnetic ordering, as shown in Figure 6.11. The magnetic structure depicted in Figure 6.10 is also consistent with the presence of one-dimensional antiferromagnetic chains, which were predicted through the spin chain modelling of magnetic susceptibility data [123]. This dominant antiferromagnetic interaction is likely mediated through Fe–F–Fe superexchange.

6.4 Conclusions

The crystal and magnetic structures of an oxalate fluoride framework, $KFe(C_2O_4)F$, have been determined via a comprehensive NPD study. As previously reported, the crystal structure is described by the $Cmc2_1$ space group and is composed of Fe–F–Fe chains which run along the a-axis, perpendicular to distorted triangular planes which lay in the bc-plane. Further key findings are summarised below, alongside the directions which future studies should take:

- Consistent with previous magnetometry measurements, $KFe(C_2O_4)F$ undergoes a transition to long-range three-dimensional magnetic ordering at $T_N \approx 18.5$ K, as confirmed by muon spin relaxation and temperature-dependent NPD measurements. The magnetic structure belongs to the $Cmc'2'_1$ magnetic space group, and has the prominent feature of antiferromagnetic chains of Fe–F–Fe running along the a-axis, presumably mediated by exchange through the fluoride anions.

- The findings within this work confirm the presence of quasi-one-dimensional behaviour within $KFe(C_2O_4)F$. This observation in triangular magnets is common [98, 243, 246], and raises the question of whether the low magnetic ordering temperature in $KFe(C_2O_4)F$ in comparison to its calculated Weiss temperature is a result of the geometric frustration stemming from triangular layers, or simply due to the low-dimensional features within its crystal structure.

- Calculation of the various nearest-neighbour exchange couplings along with inelastic neutron scattering to determine the spin Hamiltonian will be a crucial future study to investigate the interplay between these two contributions in $KFe(C_2O_4)F$ further.

- Future synthetic routes to related members of this oxalate family could include the incorporation of organics with longer alkyl chains, which would have the effect of increasing the size of the triangular layers and consequently separating the one-dimensional chains. On the other hand, the synthesis of analogues with larger separating halide ions, perhaps under different synthetic conditions, may assist in increasing the frustration within the triangular layers.

Aside from the structural interest in $KFe(C_2O_4)F$ from a frustrated magnetism perspective, this coordination framework, along with several analogues utilising dif-

ferent separating counterions and alkali metals [260, 269], are promising in terms of their potential electrochemical properties. This is due to the large channels within the structure through which alkali metals may diffuse, combined with the variable oxidation state of Fe. Indeed, $KFe(C_2O_4)F$ has already proven to be a promising cathode material in potassium-ion batteries [270], along with the compositionally similar (although structurally rather different) $Na_2Fe(C_2O_4)F_2$ [265] and $Li_2Fe(C_2O_4)_2$ [271] in sodium- and lithium-ion batteries, respectively.

Chapter 7

Summary and Outlook

This thesis has explored the structural and magnetic properties of several systems that contain a frustrated arrangement of magnetic ions. In each chapter a comprehensive outlook has already been provided, and the most important conclusions from each study are summarised below:

- **Barlowite, $Cu_4(OH)_6FBr$, and its halide analogues:** In Chapter 3, the unusual structural distortion in a family of kagomé antiferromagnets—where a Jahn-Teller distorted interlayer Cu^{2+} ion orders to varying extents at low temperature across the series—was shown to be closely linked to their magnetically ordered states and the levels of disorder that they display. In turn, it was also hypothesised that the synthetic route is anticipated to give rise to varying levels of sample defects, and therefore goes some way to explaining the variation in the reported crystal structures of barlowite across different research groups [119, 150, 151]. This is a theme that is resonated in the study of similar copper hydroxide minerals [100], and indeed, in all Cu^{2+} systems Jahn-Teller distortion is likely to play a role in the deviation from the ideal kagomé structure. Even so, the work contained herein has advanced our understanding of the structural and magnetic behaviour in barlowite, and lays the groundwork for future local structure studies on barlowite and related Cu-based minerals.

- **Zn-barlowite, $Zn_xCu_{4-x}(OH)_6FBr$:** The Zn-barlowite series, where the aforementioned interlayer Cu^{2+} is replaced by diamagnetic Zn^{2+}, was explored in Chapter 4 via muon spectroscopy, which has provided insight into the dynamics that emerge through ion substitution. Importantly, members of this series with $x > 0.66$ show evidence for persistent dynamics at 50 mK, which points towards a quantum spin liquid state in these samples. This is the first step towards confirming that the early DFT calculations which predicted this behaviour are reasonable, and that the quest for realising a QSL state in Zn-barlowite with reduced disorder is a rational one [162, 163]. Cer-

tainly, it will be interesting to uncover the effects of ion substitution on the dynamic behaviour in the halide analogues of barlowite. Furthermore, this chapter demonstrated how the use of complementary DFT muon-site calculations can aid in the interpretation of complex muon data, and that this is an approach that should be routinely adopted to support claims stemming from muon spectroscopy experiments.

- **$Cu_3(CO_3)_2(X)_3{\cdot}2ClO_4$, *X* = *bpe*, *bpy*, *azpy*:** The metal-organic frameworks studied in Chapter 5 demonstrate the diversity afforded by incorporating organic components into frustrated magnets. In this study, the use of neutron powder diffraction has progressed our understanding of the nature of the exchange within these kagomé MOFs, whose magnetic ground states are characterised by antiferromagnetic exchange between the quasi-two-dimensional layers. However, it is evident that predicting the magnetic behaviour through organic components is not as straightforward as that in, for example, simple oxides. Moreover, this work has demonstrated that features such as low-dimensionality and disorder can have a profound effect on the structural and magnetic features anticipated in many analytical procedures, and so the selection of appropriate instruments and techniques is crucial to our understanding of the complex behaviour prominent in magnetic hybrid systems.

- **$KFe(C_2O_4)F$:** The hybrid coordination framework $KFe(C_2O_4)F$ contains distorted triangles of Fe^{2+} magnetic ions, but it is in fact the one-dimensional Fe–F–Fe chains also present in the crystal structure which are likely pertinent to the low T_N observed in this material in comparison to the scale of its exchange interactions. This was shown in Chapter 6 through a neutron powder diffraction study, where the resultant magnetic structure indicates that strong antiferromagnetic exchange along these chains is likely a crucial feature of the magnetic ground state of this material. In particular, this study demonstrates that a triangular arrangement of magnetic ions is not always indicative of frustration, and other features such as low dimensionality should be considered too.

A theme that runs throughout this thesis is that of structural disorder, which ultimately results in deviations from the desired structure types relevant to magnetic frustration that were introduced in Chapter 1. For instance, in Chapter 3, both compositional and occupational disorder are present in barlowite and its halide analogues, and this is thought to influence the ensuing structural distortion,

which in turn impacts the observed magnetic properties in this family of materials. Meanwhile, whilst this work and other studies suggest that site disorder is minimal in Zn-barlowite, it is still ambiguous how even small amounts of Cu^{2+}/Zn^{2+} disorder may affect the (disordered) magnetic ground state in this QSL candidate. In the MOFs discussed in Chapter 5, orientational disorder of the counterions and linkers makes gaining a full understanding of the crystal structure, and therefore an understanding of the magnetic behaviour, difficult to elucidate. There are two approaches towards tackling this ongoing issue. The first is through aiming to minimise disorder, and for this to be achieved a clear understanding of the factors that cause this disorder must be attained. The development of methods that observe the formation of solid state materials *in situ* will be an important contribution to this issue, alongside the ability to carefully control the experimental environment, both of which will also circumvent the sample dependence issues seen across the field. Of course, the synthesis of single crystals is also an important focus in this regard. Even so, real materials will always contain some level of defects, and advances in using computational methods to understand the cause and effect of disorder is crucial. An alternative approach is to use disorder to our advantage. The experimental methods used within this thesis are predisposed to investigate long-range order, but there is increasingly more interest in using diffuse scattering to detect correlated disorder, which is found to be essential for many functional properties [272, 273]. On the other hand, there are ever more theoretical and experimental studies that propose the possibility of a disorder-induced quantum spin liquid state [274, 275]. Perhaps finding the "perfect" frustrated magnet is an unrealistic goal, and aspiring to understand and harness the disorder in materials that already exist is crucial to the future of quantum materials.

Appendix

I Full Rietveld Analysis of GEM data for $Zn_{0.50}Cu_{3.50}(OH)_6FBr$ and $Zn_{0.15}Cu_{3.85}(OH)_6FBr$

Table 1 shows the structural parameters obtained from a refinement of the $P6_3/mmc$ structural model to GEM data collected for $Zn_{0.15}Cu_{3.85}OH_6FBr$. The lower symmetry $Pnma$ model, described in Chapter 4, gives a better fit to the data. Figures 1 – 4 show the full Rietveld analysis of data collected in all six banks of GEM for $Zn_{0.15}Cu_{3.85}(OH)_6FBr$ and $Zn_{0.5}Cu_{3.5}(OH)_6FBr$ at 200 K and 2 K.

Table 1: Rietveld refinement structure parameters for the alternative $P6_3/mmc$ model fitted to neutron powder diffraction data collected on GEM at 200 K for $Zn_{0.15}Cu_{3.85}(OD)_6FBr$. Refined lattice parameters are $a = b = 6.6740(2)$ Å and $c = 9.2883(3)$ Å. The overall $R_{wp} = 2.73\%$, whilst the overall $R_{wp} = 2.46\%$ for a refinement of the $Pnma$ model, which is shown in the main text.

Atom	Site	x	y	z	Occupancy	U_{iso} (Å^2)
Cu1	6g	0.5	0	0	0.991(3)	0.00384(8)
Cu2	6h	0.6284(2)	0.2569(3)	0.25	0.281(2)	0.0020(3)
Zn2	2d	0.6667	0.3333	0.25	0.156(7)	0.0020(3)
F	2b	0	0	0.75	1	0.0152(3)
Br	2c	0.6667	0.3333	0.75	1	0.0113(2)
O1	12k	0.20178(4)	0.79822(4)	0.90835(4)	1	0.0072(1)
D1	12k	0.12447(4)	0.87553(4)	0.86622(4)	0.982(1)	0.0166(1)
H1	12k	0.12447(4)	0.87553(4)	0.86622(4)	0.008(1)	0.0166(1)

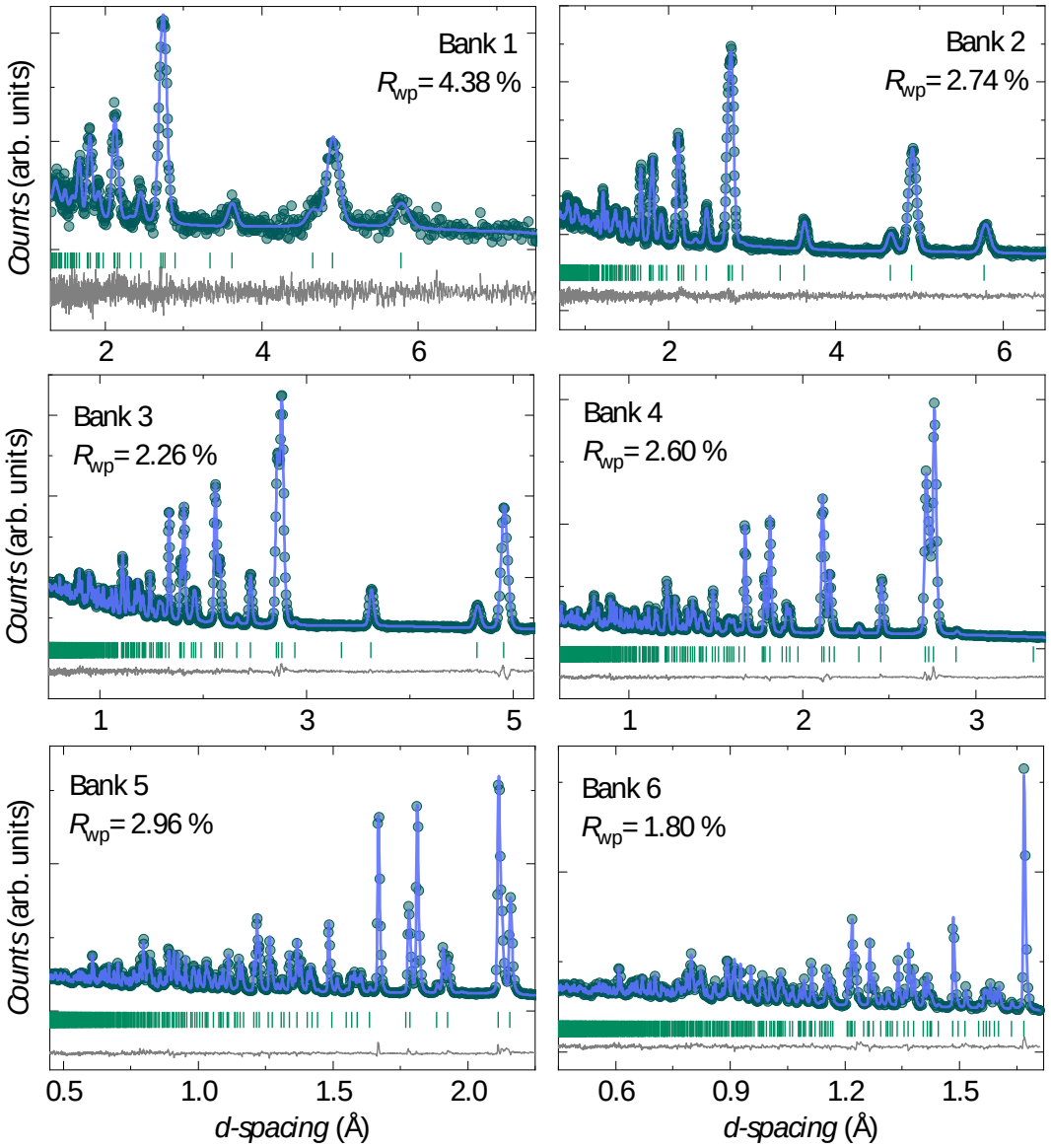

Figure 1: Neutron powder diffraction data collected at 200 K for $Zn_{0.50}Cu_{3.50}(OH)_6FBr$ on the GEM diffractometer. The solid blue line shows Rietveld refinements of the $P6_3/mmc$ structural model to the data. The difference curve is shown in grey, whilst reflections are shown by green tick marks. Overall $R_{wp} = 2.52\%$.

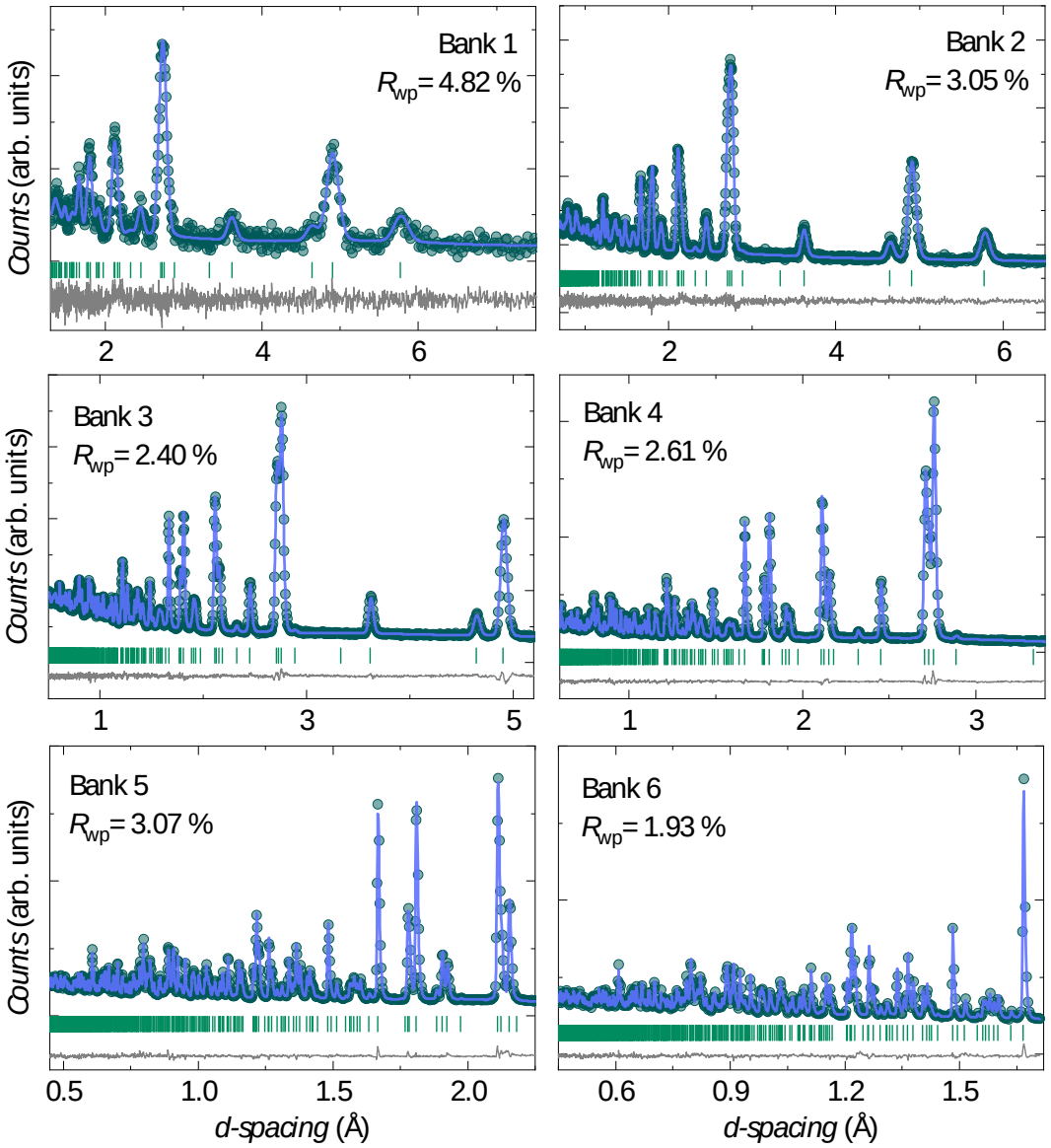

Figure 2: Neutron powder diffraction data collected at 2 K for $Zn_{0.50}Cu_{3.50}(OH)_6FBr$ on the GEM diffractometer. The solid blue line shows Rietveld refinements of the $P6_3/mmc$ structural model to the data. The difference curve is shown in grey, whilst reflections are shown by green tick marks. Overall $R_{wp} = 2.63\%$.

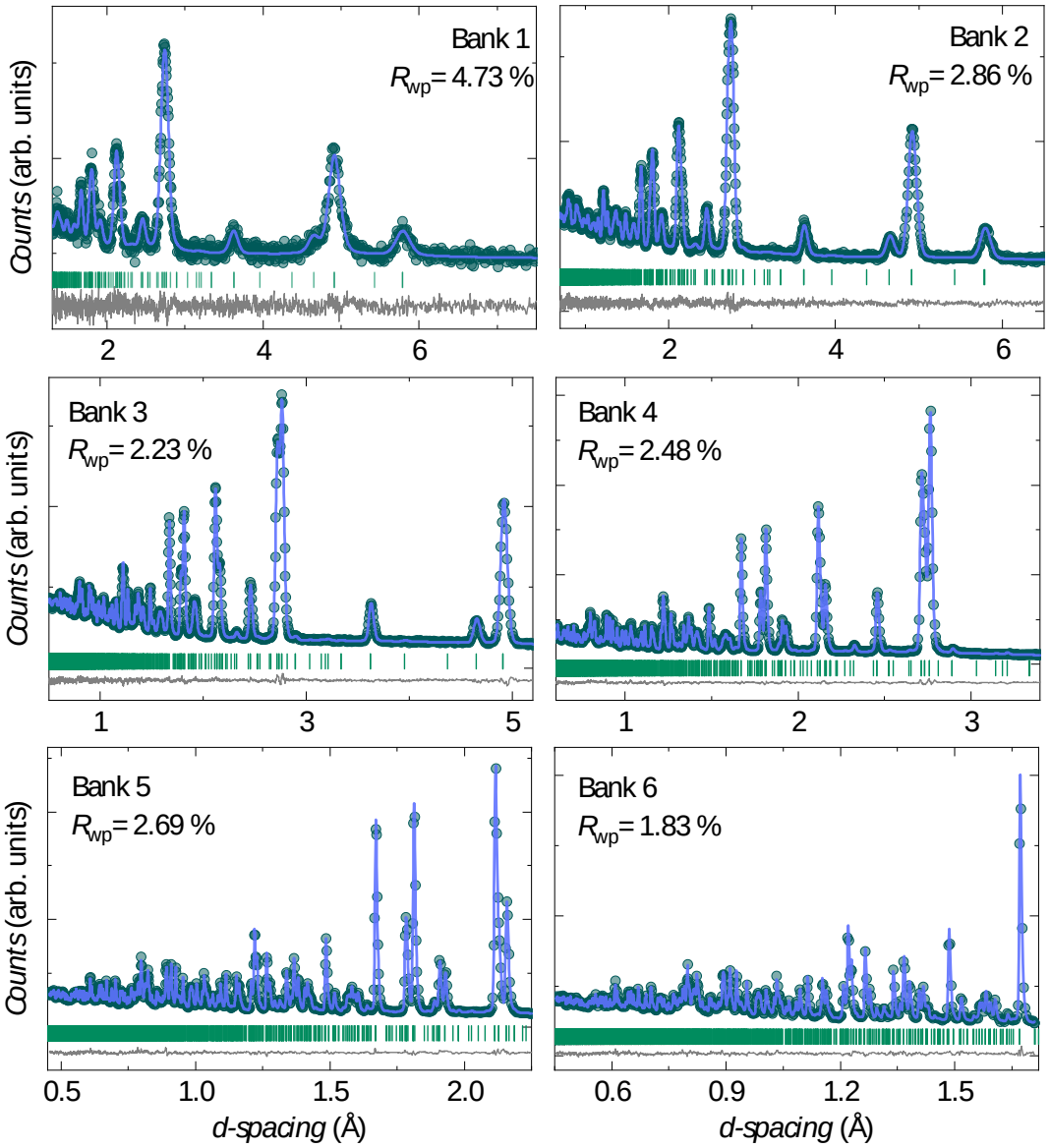

Figure 3: Neutron powder diffraction data collected at 200 K for $Zn_{0.15}Cu_{3.85}(OH)_6FBr$ on the GEM diffractometer. The solid blue line shows Rietveld refinements of the $P6_3/mmc$ structural model to the data. The difference curve is shown in grey, whilst reflections are shown by green tick marks. Overall $R_{wp} = 2.46\%$.

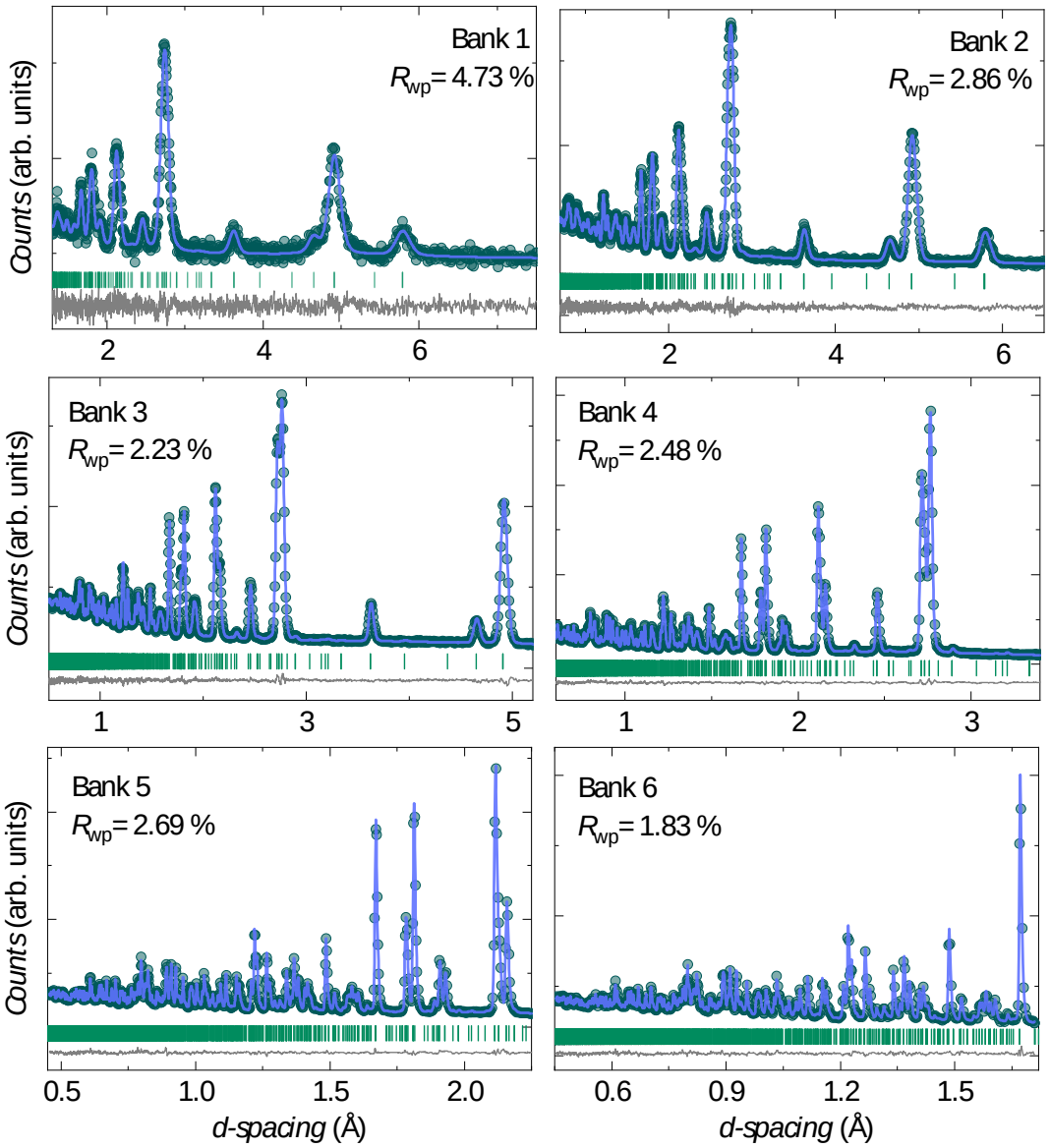

Figure 4: Neutron powder diffraction data collected at 2 K for $Zn_{0.15}Cu_{3.85}(OH)_6FBr$ on the GEM diffractometer. The solid blue line shows Rietveld refinements of the $P6_3/mmc$ structural model to the data. The difference curve is shown in grey, whilst reflections are shown by green tick marks. Overall $R_{wp} = 2.30$ %.

II Alternative Zero Field μSR Model

Figure 5 shows the muon decay asymmetry measured in zero field for barlowite, $Cu_4(OH)_6FBr$, at 20 K. Initial observation of the oscillations in the data, described in the main text in Chapter 4, pointed towards the formation of an F–μ–F entangled state which is commonly observed in fluoride containing materials. Indeed, it is possible to model the observed oscillations by a combination of expressions describing the formation of a muon complex involving protons (from the hydroxide groups) and fluorine:

$$A(t) = \left[f_{\mathrm{F}} P_{\mathrm{F}\mu\mathrm{F}} + f_{\mathrm{F}} P_{\mathrm{OH}}(t) \exp\left(\frac{-\Delta_{\mathrm{OH}}^2 t^2}{2}\right) + f_{\mathrm{Br}} P_{\mathrm{KB}}(t)\right] A \exp^{-\lambda t^{\beta}} + A_{\mathrm{bg}}, \quad (1)$$

where $P_{\mathrm{F}\mu\mathrm{F}}$ is described by Equation 2.13, and $P_{\mathrm{KB}}(t)$ is the Kubo-Toyabe function and accounts for muons stopping near the Br^- anions. Here, the Gaussian damping accounts for the distribution of muons stopping near nuclei in a μ–OH complex. A small dynamical relaxation is allowed through the exponential multiplying factor. A fit of this model to ZF data collected barlowite is shown in Figure 5. However, upon close inspection of the low-temperature crystal structure of barlowite, it is unclear where exactly the muon could stop, especially given that the above model

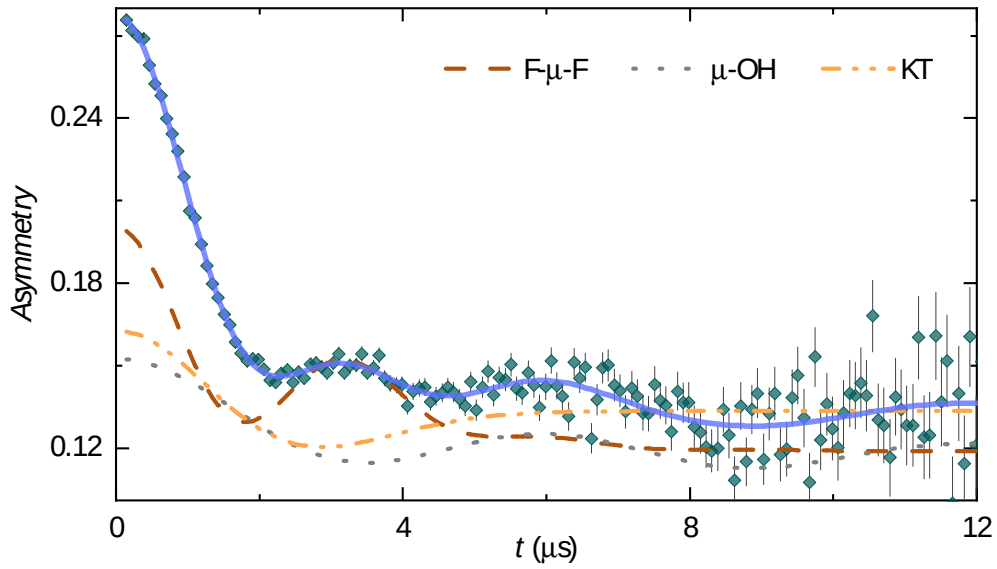

Figure 5: The time-dependent muon decay asymmetry measured in zero field at 20 K on the MuSR spectrometer for barlowite, $Cu_4(OH)_6FBr$. The solid line is an alternative fit to the data than that presented in the main text, using Equation 1. The dashed lines represent the contributions from F–μ–F and μ–OH entangled states, as well as a Kubo-Toyabe term which accounts for μ–Br formation.

suggests a μ–F distance of 2.80(2) Å, which would result in a highly distorted crystal structure. This example demonstrates the importance of performing muon-site calculations to guide the analysis of these types of data, as was demonstrated in Chapter 4.

III Single Crystal Structure Solution for the $Cu_3(CO_3)_2(X)_3{\cdot}2ClO_4$ Metal-Organic Frameworks

Structural solutions for MOF–*bpe*, MOF–*bpy* and MOF–*azpy* single crystal X-ray diffraction data measured at 100 K are given in Tables 2 – 4. Data were collected on an Agilent Supernova with an AtlasS2 CCD detector, and the structures were solved and refined using ShelXS and ShelXL in Olex2, respectively.

Table 2: Crystal structure parameters for the $P3$ model of MOF–*bpy* from structure solution of single crystal XRD data collected at 100 K. Refined lattice parameters are $a = b = 9.2297(2)$ Å and $c = 13.3817(4)$ Å. The final R-factor = 4.58%.

Atom	Site	x	y	z	Occupancy	U_{iso}
Cu1	3*d*	0.1850(1)	0.3300(1)	0.47082(8)	1	0.0353(3)
			Carbonate			
C13	1*a*	0	0	0.4712(7)	1	0.032(2)
C14	1*b*	0.33333	0.66667	0.4711(6)	1	0.028(2)
O9	3*d*	0.1844(5)	0.5413(5)	0.4707(3)	1	0.0370(9)
O10	3*d*	0.1578(5)	0.1043(4)	0.4707(3)	1	0.0296(8)
			Linker A			
N1A	3*d*	0.171(3)	0.327(4)	0.615(3)	0.502(5)	0.030(3)
C1A	3*d*	0.297(2)	0.271(2)	0.274(1)	0.502	0.033(2)
H1A	3*d*	0.354909	0.230234	0.313256	0.502	0.040
C2A	3*d*	0.136(2)	0.395(2)	0.265(1)	0.502	0.034(2)
H2A	3*d*	0.0781	0.4435	0.2964	0.502	0.041
C3A	3*d*	0.304(2)	0.263(2)	0.172(8)	0.502	0.030(1)
H3A	3*d*	0.3666	0.2180	0.1418	0.502	0.036
C4A	3*d*	0.136(2)	0.389(2)	0.161(1)	0.502	0.031(1)
H4A	3*d*	0.0791	0.4330	0.1237	0.502	0.037
C5A	3*d*	0.219(2)	0.318(1)	0.112(1)	0.502	0.027(1)

Continued on next page

Table 2 – continued from previous page

Atom	Site	x	y	z	Occupancy	U_{iso}
C6A	3*d*	0.228(1)	0.306(1)	0.004(1)	0.502	0.026(1)
H6A	3*d*	0.2879	0.2549	0.9785	0.502	0.031
C7A	3*d*	0.159(1)	0.360(1)	0.937(1)	0.502	0.026(1)
H7A	3*d*	0.1015	0.4142	0.9616	0.502	0.031
C8A	3*d*	0.164(2)	0.344(1)	0.829(1)	0.502	0.026(1)
C9A	3*d*	0.254(2)	0.282(2)	0.780(1)	0.502	0.030(1)
H9A	3*d*	0.3151	0.2435	0.8170	0.502	0.036
C10A	3*d*	0.074(1)	0.398(1)	0.769(1)	0.502	0.031(1)
H10A	3*d*	0.0095	0.4400	0.7989	0.502	0.037
C11A	3*d*	0.082(2)	0.389(2)	0.668(1)	0.502	0.034(2)
H11A	3*d*	0.0214	0.4273	0.6303	0.502	0.041
C12A	3*d*	0.254(2)	0.276(2)	0.674(1)	0.5	0.033(2)
H12A	3*d*	0.3169	0.2321	0.6423	0.502	0.040
N2A	3*d*	0.170(3)	0.327(4)	0.320(4)	0.502	0.030(3)
			Linker B			
N1B	3*d*	0.211(3)	0.337(3)	0.324(3)	0.498(5)	0.030(3)
C1B	3*d*	0.253(2)	0.275(2)	0.267(1)	0.498	0.034(1)
H1B	3*d*	0.3154	0.2323	0.3000	0.498	0.041
C2B	3*d*	0.080(2)	0.388(2)	0.273(1)	0.498	0.033(2)
H2B	3*d*	0.0189	0.4246	0.3127	0.498	0.040
C3B	3*d*	0.252(2)	0.282(2)	0.164(1)	0.498	0.031(1)
H3B	3*d*	0.3128	0.2428	0.1258	0.498	0.037
C4B	3*d*	0.075(2)	0.399(1)	0.172(1)	0.498	0.030(1)
H4B	3*d*	0.0120	0.4427	0.1417	0.498	0.036
C5B	3*d*	0.165(2)	0.346(1)	0.115(1)	0.498	0.027(1)
C6B	3*d*	0.160(1)	0.360(1)	0.004(1)	0.498	0.026(1)
H6B	3*d*	0.1011	0.4126	0.7873	0.498	0.031
C7B	3*d*	0.229(1)	0.307(1)	0.938(1)	0.498	0.026(1)
H7B	3*d*	0.2892	0.2560	0.9626	0.498	0.031
C8B	3*d*	0.221(2)	0.319(1)	0.829(1)	0.498	0.027(1)
C9B	3*d*	0.304(2)	0.263(2)	0.770(1)	0.498	0.031(1)
H9B	3*d*	0.3662	0.2176	0.7997	0.498	0.037
C10B	3*d*	0.136(2)	0.389(2)	0.781(1)	0.498	0.030(1)
H10B	3*d*	0.0794	0.4333	0.8186	0.498	0.036

Continued on next page

Table 2 – continued from previous page

Atom	Site	x	y	z	Occupancy	U_{iso}
C11B	3d	0.136(2)	0.394(2)	0.677(1)	0.498	0.033(2)
H11B	3d	0.0782	0.4413	0.6438	0.498	0.040
C12B	3d	0.299(2)	0.272(2)	0.667(2)	0.498	0.034
H12B	3d	0.3569	0.2325	0.6287	0.498	0.041
N2B	3d	0.212(3)	0.337(4)	0.624(3)	0.498	0.030(3)
			Perchlorates			
Cl1	3d	0.659(3)	0.327(3)	0.975(1)	0.333	0.024(1)
O1	3d	0.541(4)	0.167(3)	0.933(2)	0.333	0.027(4)
O2	3d	0.607(3)	0.325(4)	0.078(1)	0.333	0.042(4)
O3	3d	0.663(4)	0.465(3)	0.920(2)	0.333	0.032(5)
O4	3d	0.822(4)	0.339(5)	0.975(3)	0.333	0.027(3)
Cl2	3d	0.650(4)	0.326(3)	0.471(5)	0.333	0.034(3)
O5	3d	0.822(4)	0.454(4)	0.467(3)	0.333	0.12(1)
O6	3d	0.626(4)	0.231(4)	0.560(2)	0.333	0.13(1)
O7	3d	0.620(4)	0.232(4)	0.232(4)	0.381(2)	0.13(1)
O8	3d	0.529(4)	0.403(3)	0.473(2)	0.333	0.067(7)

Table 3: Crystal structure parameters for the $P3$ model of MOF–*azpy* from structure solution of single crystal XRD data collected at 100 K. Refined lattice parameters are $a = b = 9.2116(4)$ Å and 12.9467(10) Å. The final R-factor = 11.09%.

Atom	Site	x	y	z	Occupancy	U_{iso}
Cu1	3d	0.6701(3)	0.8152(4)	0.9498(2)	1	0.0561(9)
			Carbonate			
C1	1a	1.0	1.0	0.950(2)	1	0.037(4)
C2	1b	0.33333	0.66667	0.949(2)	1	0.049(5)
O1	3d	0.947(1)	0.104(1)	0.9492(7)	1	0.037(2)
O2	3d	0.363(2)	0.547(2)	0.9500(8)	1	0.060(3)
			Linker A			
N1A	3d	0.671(2)	0.7884(3)	0.795(2)	0.49(1)	0.036(4)
C3A	3d	0.609(3)	0.868(4)	0.741(2)	0.49	0.045(4)
H3A	3d	0.5573	0.9191	0.7755	0.49	0.054

Continued on next page

Table 3 – continued from previous page

Atom	Site	x	y	z	Occupancy	U_{iso}
C4A	3d	0.741(3)	0.711(3)	0.744(2)	0.49	0.044(4)
H4A	3d	0.7850	0.6574	0.7834	0.49	0.052
C5A	3d	0.625(4)	0.875(4)	0.629(3)	0.49	0.053(1)
H5A	3d	0.5849	0.9322	0.5895	0.49	0.064
C6A	3d	0.753(3)	0.706(3)	0.639(2)	0.49	0.045(4)
H6A	3d	0.7956	0.6445	0.6074	0.49	0.054
C7A	3d	0.699(3)	0.797(3)	0.583(2)	0.49	0.038(4)
N2A	3d	0.714(3)	0.794(2)	0.476(3)	0.49	0.036(3)
N3A	3d	0.613(3)	0.816(2)	0.425(2)	0.49	0.034(3)
C8A	3d	0.645(3)	0.821(3)	0.316(3)	0.49	0.039(4)
C9A	3d	0.593(4)	0.924(4)	0.257(3)	0.49	0.051(5)
H9A	3d	0.5471	0.9816	0.2890	0.49	0.061
C10A	3d	0.707(4)	0.731(4)	0.266(2)	0.49	0.047(4)
H10A	3d	0.7458	0.6699	0.3022	0.49	0.056
C11A	3d	0.616(3)	0.928(4)	0.158(2)	0.49	0.046(4)
H11A	3d	0.5924	0.9988	0.1193	0.49	0.056
C12A	3d	0.709(3)	0.736(3)	0.159(2)	0.49	0.042(4)
H12A	3d	0.7372	0.6667	0.1228	0.49	0.050
N4A	3d	0.671(2)	0.838(3)	0.107(2)	0.49	0.032(3)
			Linker B			
N1B	3d	0.672(2)	0.836(3)	0.798(2)	0.51(1)	0.036(4)
C3B	3d	0.616(3)	0.929(3)	0.739(2)	0.51	0.045(4)
H3B	3d	0.5945	0.0028	0.7753	0.51	0.054
C4B	3d	0.711(3)	0.736(3)	0.738(2)	0.51	0.044(4)
H4B	3d	0.7435	0.6685	0.7720	0.51	0.052
C5B	3d	0.594(4)	0.921(4)	0.643(3)	0.51	0.053(5)
H5B	3d	0.5451	0.9771	0.6123	0.51	0.064
C6B	3d	0.705(3)	0.729(3)	0.638(2)	0.51	0.045(4)
H6B	3d	0.7389	0.6629	0.6023	0.51	0.054
C7B	3d	0.646(3)	0.823(3)	0.582(3)	0.51	0.038(4)
N2B	3d	0.613(3)	0.815(2)	0.477(2)	0.51	0.036(3)
N3B	3d	0.712(2)	0.790(2)	0.428(2)	0.51	0.034(3)
C8B	3d	0.696(3)	0.797(3)	0.316(2)	0.51	0.039(4)
C9B	3d	0.620(4)	0.872(4)	0.270(3)	0.51	0.051(5)

Continued on next page

Table 3 – continued from previous page

Atom	Site	x	y	z	Occupancy	U_{iso}
H9B	3d	0.5769	0.9264	0.3092	0.51	0.061
C10B	3d	0.751(3)	0.705(4)	0.261(2)	0.51	0.047(4)
H10B	3d	0.7928	0.6433	0.2929	0.51	0.056
C11B	3d	0.608(3)	0.868(4)	0.159(2)	0.51	0.046(4)
H11B	3d	0.5583	0.9211	0.1250	0.51	0.056
C12B	3d	0.740(3)	0.711(3)	0.155(2)	0.51	0.042(4)
H12B	3d	0.7853	0.6586	0.1153	0.51	0.050
N4B	3d	0.670(2)	0.784(3)	0.105(2)	0.51	0.032(3)
			Perchlorates			
Cl1	3d	0.662(4)	0.342(4)	0.4635(8)	0.2	0.032(3)
O3	3d	0.536(6)	0.394(7)	0.440(5)	0.0.2	0.037(7)
O4	3d	0.65(1)	0.308(8)	0.577(2)	0.2	0.06(2)
O5	3d	0.828(4)	0.490(3)	0.443(2)	0.2	0.009(5)
O6	3d	0.618(5)	0.183(4)	0.412(3)	0.2	0.031(8)
Cl2	3d	0.665(5)	0.336(7)	0.429(1)	0.133	0.032(3)
O7	3d	0.542(8)	0.39(1)	0.449(5)	0.133	0.037(7)
O8	3d	0.692(9)	0.33(1)	0.317(2)	0.133	0.03(2)
O9	3d	0.601(7)	0.166(8)	0.475(6)	0.133	0.031(8)
O10	3d	0.824(5)	0.480(4)	0.009(5)	0.133	0.009(5)
Cl3	3d	0.668(3)	0.327(3)	0.937(1)	0.15	0.017(4)
O11	3d	0.638(7)	0.357(8)	0.833(3)	0.15	0.06(2)
O12	3d	0.872(4)	0.390(5)	0.939(4)	0.15	0.133(7)
O13	3d	0.607(5)	0.143(4)	0.957(3)	0.15	0.024(9)
O14	3d	0.64(1)	0.407(9)	0.020(4)	0.15	0.13(5)
Cl4	3d	0.656(3)	0.306(2)	0.960(1)	0.183	0.017(4)
O15	3d	0.842(4)	0.386(5)	0.968(4)	0.183	0.033(7)
O16	3d	0.578(8)	0.212(7)	0.056(3)	0.183	0.09(2)
O17	3d	0.591(6)	0.190(5)	0.869(3)	0.183	0.06(1)
O18	3d	0.608(6)	0.436(5)	0.941(5)	0.183	0.048(2)

Table 4: Crystal structure parameters for the $P3$ model of MOF–*bpe* from structure solution of single crystal XRD data collected at 100 K. Refined lattice parameters are $a = b = 9.3115(2)$ Å and 13.3034(3) Å. The final R-factor = 4.34$.

Atom	Site	x	y	z	Occupancy	U_{iso}
Cu1	3*d*	0.81879(9)	0.66941(8)	0.84723(8)	1	0.0175(3)
			Carbonate			
C1	1*a*	1.0	1.0	0.8478(6)	1	0.016(2)
C2	1*b*	0.66667	0.33333	0.8477(6)	1	0.018(2)
O1	3*d*	0.1077(4)	0.9515(5)	0.8475(3)	1	0.0167(8)
O2	3*d*	0.5420(5)	0.3571(1)	0.8475(3)	1	0.0227(9)
			Linker A			
N1	3*d*	0.8140(7)	0.6679(5)	0.6985(6)	1	0.024(2)
C3A	3*d*	0.7299(9)	0.7192(9)	0.6480(5)	1	0.0359(7)
H3A	3*d*	0.6458	0.7380	0.6810	0.499(6)	0.043
C4A	3*d*	0.9024(9)	0.6147(8)	0.6460(5)	1	0.0359(7)
H4A	3*d*	0.9444	0.5567	0.6805	0.499(6)	0.043
C5A	3*d*	0.748(2)	0.744(2)	0.5412(9)	0.499	0.038(2)
H5A	3*d*	0.6928	0.7890	0.5067	0.499	0.045
C6A	3*d*	0.935(2)	0.641(2)	0.5430(9)	0.499	0.038(2)
H6A	3*d*	0.0103	0.6180	0.6120	0.499	0.045
C7A	3*d*	0.850(2)	0.704(2)	0.488(1)	0.499	0.039(2)
C8A	3*d*	0.878(3)	0.731(2)	0.377(1)	0.499	0.060(3)
H8AA	3*d*	0.8902	0.8374	0.3603	0.499	0.072
H8AB	3*d*	0.9820	0.7353	0.3608	0.499	0.072
C9A	3*d*	0.752(3)	0.609(2)	0.316(1)	0.499	0.060(3)
H9AA	3*d*	0.6481	0.6006	0.3352	0.499	0.072
H9AB	3*d*	0.7439	0.5030	0.3314	0.499	0.072
C10A	3*d*	0.769(2)	0.631(2)	0.203(1)	0.499	0.039(2)
C11A	3*d*	0.686(2)	0.691(2)	0.147(1)	0.499	0.038(2)
H11A	3*d*	0.6077	0.7121	0.1756	0.499	0.045
C12A	3*d*	0.872(2)	0.587(2)	0.153(1)	0.499	0.038(2)
H12A	3*d*	0.9225	0.5389	0.1888	0.499	0.045
C13A	3*d*	0.7229(9)	0.7189(9)	0.0468(5)	1	0.0359(7)
H13A	3*d*	0.6822	0.7767	0.0110	0.499	0.043
C14A	3*d*	0.9019(9)	0.6135(8)	0.0490(5)	1	0.0359(7)
H14A	3*d*	0.9796	0.5941	0.01722	0.499	0.043

Continued on next page

Table 4 – continued from previous page

Atom	Site	x	y	z	Occupancy	U_{iso}
N2	3d	0.8144(7)	0.6674(5)	0.9975(6)	1	0.022(2)
			Linker B			
H3B	3d	0.6815	0.7766	0.6835	0.501(6)	0.043
H4B	3d	0.9809	0.5961	0.6775	0.501	0.043
C5B	3d	0.687(2)	0.693(2)	0.5480(9)	0.501	0.038(2)
H5B	3d	0.6105	0.7157	0.5186	0.501	0.045
C6B	3d	0.872(2)	0.588(2)	0.542(9)	0.501	0.038(2)
H6B	3d	0.9232	0.5408	0.5059	0.501	0.045
C7B	3d	0.768(2)	0.631(2)	0.492(1)	0.501	0.039(2)
C8B	3d	0.752(3)	0.605(2)	0.380(1)	0.501	0.060(3)
H8BA	3d	0.7493	0.5022	0.3645	0.501	0.072
H8BB	3d	0.6456	0.5918	0.3594	0.501	0.072
C9B	3d	0.874(3)	0.729(2)	0.320(1)	0.501	0.060(3)
H9BA	3d	0.9793	0.7390	0.3377	0.501	0.072
H9BB	3d	0.8796	0.8330	0.3369	0.501	0.072
C10B	3d	0.851(2)	0.705(2)	0.207(1)	0.501	0.039(2)
C11B	3d	0.748(2)	0.745(2)	0.154(1)	0.501	0.038(2)
H11B	3d	0.6930	0.7897	0.1888	0.501	0.045
C12B	3d	0.934(2)	0.642(2)	0.152(1)	0.501	0.038(2)
H12B	3d	0.0093	0.6185	0.1831	0.501	0.045
H13B	3d	0.6460	0.7373	0.0133	0.501	0.043
H14B	3d	0.9432	0.5546	0.0148	0.501	0.043
			Perchlorates			
Cl1	3d	0.335(3)	0.665(3)	0.841(1)	0.2	0.028(2)
O3	3d	0.357(6)	0.720(4)	0.735(2)	0.2	0.059(6)
O4	3d	0.419(4)	0.573(4)	0.851(4)	0.2	0.050(2)
O5	3d	0.164(4)	0.548(4)	0.862(4)	0.2	0.046(4)
O6	3d	0.935(2)	0.641(2)	0.543(1)	0.2	0.038(2)
Cl2	3d	0.344(5)	0.669(4)	0.857(2)	0.133	0.028(2)
O7	3d	0.398(6)	0.814(5)	0.791(3)	0.133	0.048(6)
O8	3d	0.456(7)	0.605(7)	0.834(5)	0.133	0.050(4)
O9	3d	0.176(6)	0.539(6)	0.829(5)	0.133	0.046(4)
O10	3d	0.35(1)	0.711(5)	0.964(2)	0.133	0.056(8)
Cl3	3d	0.352(4)	0.564(4)	0.310(3)	0.133	0.027(3)

Continued on next page

Table 4 – continued from previous page

Atom	Site	x	y	z	Occupancy	U_{iso}
O11	3d	0.222(5)	0.679(6)	0.293(3)	0.133	0.043(7)
O12	3d	0.502(5)	0.831(5)	0.344(4)	0.133	0.035(4)
O13	3d	0.383(4)	0.546(4)	0.310(3)	0.133	0.025(5)
O14	3d	0.302(5)	0.636(6)	0.455(2)	0.133	0.032(7)
Cl4	3d	0.365(3)	0.677(3)	0.345(1)	0.2	0.027(3)
O15	3d	0.532(3)	0.818(3)	0.348(3)	0.2	0.035(4)
O16	3d	0.307(6)	0.633(6)	0.242(1)	0.2	0.057(8)
O17	3d	0.242(5)	0.697(6)	0.400(3)	0.2	0.068(8)
O18	3d	0.378(3)	0.541(4)	0.387(2)	0.2	0.042(5)

Bibliography

[1] West, A. R. *Basic Solid State Chemistry*; John Wiley & Sons Ltd: Trowbridge, UK, 1984.

[2] Xie, J.; Lu, Y.-C. A retrospective on lithium-ion batteries. *Nature Communications* **2020**, *11*, 2499.

[3] Nair, G. B.; Swart, H.; Dhoble, S. A review on the advancements in phosphor-converted light emitting diodes (pc-LEDs): Phosphor synthesis, device fabrication and characterization. *Progress in Materials Science* **2020**, *109*, 100622.

[4] Lustig, W. P.; Mukherjee, S.; Rudd, N. D.; Desai, A. V.; Li, J.; Ghosh, S. K. Metal–organic frameworks: functional luminescent and photonic materials for sensing applications. *Chemical Society Reviews* **2017**, *46*, 3242–3285.

[5] Mills, A. A. The Lodestone: History, Physics, and Formation. *Annals of Science* **2004**, *61*, 273–319.

[6] Cowburn, R. P. The attractions of magnetism for nanoscale data storage. *Philosophical Transactions of the Royal Society of London. Series A* **2000**, *358*, 281–301.

[7] Gossuin, Y.; Hocq, A.; Gillis, P.; Vuong, Q. L. Physics of magnetic resonance imaging: from spin to pixel. *Journal of Physics D: Applied Physics* **2010**, *43*, 213001.

[8] Gottschall, T.; Skokov, K. P.; Fries, M.; Taubel, A.; Radulov, I.; Scheibel, F.; Benke, D.; Riegg, S.; Gutfleisch, O. Making a Cool Choice: The Materials Library of Magnetic Refrigeration. *Advanced Energy Materials* **2019**, *9*, 1901322.

[9] Weiss, P. L'hypothèse du champ moléculaire et la propriété ferromagnétique. *Journal de Physique Théorique et Appliquée* **1907**, *6*, 661–690.

[10] The rise of quantum materials. *Nature Physics* **2016**, *12*, 105–105.

[11] Giustino, F. et al. The 2021 quantum materials roadmap. *Journal of Physics: Materials* **2021**, *3*, 042006.

[12] Broholm, C.; Cava, R. J.; Kivelson, S. A.; Nocera, D. G.; Norman, M. R.; Senthil, T. Quantum spin liquids. *Science* **2020**, *367*, 263.

[13] Tokura, Y.; Kawasaki, M.; Nagaosa, N. Emergent functions of quantum materials. *Nature Physics* **2017**, *13*, 1056–1068.

[14] Gerlach, W.; Stern, O. Der experimentelle Nachweis der Richtungsquantelung im Magnetfeld. *Zeitschrift für Physik* **1922**, *9*, 349–352.

[15] Blundell, S. *Magnetism in Condensed Matter*; Oxford University Press: Oxford, UK, 2001.

[16] McHenry, M. E.; Laughlin, D. E. *Characterization of Materials*; John Wiley & Sons, Inc.: New York, 2012; pp 1–25.

[17] Green, N. J. B. *Quantum Mechanics 1: Foundations*; Oxford University Press: Oxford, UK, 1997.

[18] Shriver, D. F.; Atkins, P. W. *Inorganic Chemistry*; Oxford University Press: Oxford, UK, 2010.

[19] Huisman, R.; de Jonge, R.; Haas, C.; Jellinek, F. Trigonal-prismatic coordination in solid compounds of transition metals. *Journal of Solid State Chemistry* **1971**, *3*, 56–66.

[20] Burns, P. C.; Cooper, M. A.; Hawthorne, F. C. Claringbullite; a Cu^{2+} oxysalt with Cu^{2+} in trigonal-prismatic coordination. *The Canadian Mineralogist* **1995**, *33*, 633–639.

[21] Rodríguez-Carvajal, J.; Bourée, F. Symmetry and magnetic structures. *EPJ Web of Conferences* **2012**, *22*, 00010.

[22] Anderson, P. W. More Is Different. *Science* **1972**, *177*, 393–396.

[23] Goodenough, J. B. Theory of the role of covalence in the perovskite-type manganites [La,M(II)]MnO_3. *Physical Review* **1955**, *100*, 564–573.

[24] Goodenough, J. B. An interpretation of the magnetic properties of the perovskite-type mixed crystals $La_{1-x}Sr_xCoO_{3-\lambda}$. *Journal of Physics and Chemistry of Solids* **1958**, *6*, 287–297.

[25] Kanamori, J. Superexchange interaction and symmetry properties of electron orbitals. *Journal of Physics and Chemistry of Solids* **1959**, *10*, 87–98.

[26] Tokura, Y.; Kanazawa, N. Magnetic Skyrmion Materials. *Chemical Reviews* **2021**, *121*, 2857–2897.

[27] Ruderman, M. A.; Kittel, C. Indirect Exchange Coupling of Nuclear Magnetic Moments by Conduction Electrons. *Physical Review* **1954**, *96*, 99–102.

[28] Zener, C. Interaction between the *d*-shells in the Transition Metals. II. Ferromagnetic Compounds of Manganese with Perovskite Structure. *Physical Review* **1951**, *82*, 403–405.

[29] Anderson, P. W.; Hasegawa, H. Considerations on Double Exchange. *Physical Review* **1955**, *100*, 675–681.

[30] Felsteiner, J.; Misra, S. K. Magnetic order of $RBa_2Cu_4O_8$ (R = rare earth) due to dipole-dipole and exchange interactions. *Physical Review B* **1994**, *50*, 7184–7187.

[31] Ramirez, A. P. Strongly Geometrically Frustrated Magnets. *Annual Review of Materials Science* **1994**, *24*, 453–480.

[32] Greedan, J. E. Geometrically frustrated magnetic materials. *Journal of Materials Chemistry* **2001**, *11*, 37–53.

[33] Balents, L. Spin liquids in frustrated magnets. *Nature* **2010**, *464*, 199–208.

[34] Morris, D. J. P.; Tennant, D. A.; Grigera, S. A.; Klemke, B.; Castelnovo, C.; Moessner, R.; Czternasty, C.; Meissner, M.; Rule, K. C.; Hoffmann, J.-U.; Kiefer, K.; Gerischer, S.; Slobinsky, D.; Perry, R. S. Dirac Strings and Magnetic Monopoles in the Spin Ice $Dy_2Ti_2O_7$. *Science* **2009**, *326*, 411–414.

[35] Fennell, T.; Deen, P. P.; Wildes, A. R.; Schmalzl, K.; Prabhakaran, D.; Boothroyd, A. T.; Aldus, R. J.; McMorrow, D. F.; Bramwell, S. T. Magnetic Coulomb Phase in the Spin Ice $Ho_2Ti_2O_7$. *Science* **2009**, *326*, 415–417.

[36] Matsuhira, K.; Hiroi, Z.; Tayama, T.; Takagi, S.; Sakakibara, T. A new macroscopically degenerate ground state in the spin ice compound $Dy_2Ti_2O_7$ under a magnetic field. *Journal of Physics: Condensed Matter* **2002**, *14*, 559–565.

[37] Fennell, T.; Bramwell, S. T.; McMorrow, D. F.; Manuel, P.; Wildes, A. R. Pinch points and Kasteleyn transitions in kagome ice. *Nature Physics* **2007**, *3*, 566–572.

[38] Zhao, K.; Deng, H.; Chen, H.; Ross, K. A.; Petříček, V.; Günther, G.; Russina, M.; Hutanu, V.; Gegenwart, P. Realization of the kagome spin ice state in a frustrated intermetallic compound. *Science* **2020**, *367*, 1218–1223.

[39] Mydosh, J. Disordered magnetism and spin glasses. *Journal of Magnetism and Magnetic Materials* **1996**, *157-158*, 606–610.

[40] Lundgren, L.; Svedlindh, P.; Nordblad, P.; Beckman, O. Dynamics of the Relaxation-Time Spectrum in a CuMn Spin-Glass. *Physical Review Letters* **1983**, *51*, 911–914.

[41] Sherrington, D.; Kirkpatrick, S. Solvable Model of a Spin-Glass. *Physical Review Letters* **1975**, *35*, 1792–1796.

[42] Ma, Z. et al. Spin-Glass Ground State in a Triangular-Lattice Compound $YbZnGaO_4$. *Physical Review Letters* **2018**, *120*, 087201.

[43] Booth, C. H.; Gardner, J. S.; Kwei, G. H.; Heffner, R. H.; Bridges, F.; Subramanian, M. A. Local lattice disorder in the geometrically frustrated spin-glass pyrochlore $Y_2Mo_2O_7$. *Physical Review B* **2000**, *62*, R755–R758.

[44] Fujihala, M. et al. Gapless spin liquid in a square-kagome lattice antiferromagnet. *Nature Communications* **2020**, *11*, 1–7.

[45] Sorolla, M.; Wang, X.; Koo, H.-J.; Whangbo, M.-H.; Jacobson, A. J. Synthesis of the Elusive $S = \frac{1}{2}$ Star Structure: A Possible Quantum Spin Liquid Candidate. *J. Am. Chem. Soc* **2020**, *13*, 5013–5016.

[46] Perez, J. V.; Sorolla, M.; Wang, X.; Jacobson, A. J. "Stagomé" Lattice: The Missing Member of the Star-Kagomé Family. *Chemistry of Materials* **2021**, *33*, 2173–2177.

[47] Mustonen, O.; Vasala, S.; Sadrollahi, E.; Schmidt, K. P.; Baines, C.; Walker, H. C.; Terasaki, I.; Litterst, F. J.; Baggio-Saitovitch, E.; Karppinen, M. Spin-liquid-like state in a spin-$\frac{1}{2}$ square-lattice antiferromagnet perovskite induced by d^{10}-d^0 cation mixing. *Nature Communications* **2018**, *9*, 1085.

[48] Mustonen, O.; Vasala, S.; Schmidt, K. P.; Sadrollahi, E.; Walker, H. C.; Terasaki, I.; Litterst, F. J.; Baggio-Saitovitch, E.; Karppinen, M. Tuning the $S = \frac{1}{2}$ square-lattice antiferromagnet $Sr_2Cu(Te_{1-x}W_x)O_6$ from Néel order to quantum disorder to columnar order. *Physical Review B* **2018**, *98*, 064411.

[49] Anderson, P. W. Resonating valence bonds: A new kind of insulator? *Mat. Res. Bull* **1973**, *8*, 153–160.

[50] Anderson, P. W. The Resonating Valence Bond State in La_2CuO_4 and Superconductivity. *Science* **1987**, *235*, 1196–1198.

[51] Liu, Q.; Yao, Q.; Kelly, Z. A.; Pasco, C. M.; McQueen, T. M.; Lany, S.; Zunger, A. Electron Doping of Proposed Kagome Quantum Spin Liquid Produces Localized States in the Band Gap. *Physical Review Letters* **2018**, *121*, 186402.

[52] Puphal, P.; Ranjith, K. M.; Pustogow, A.; Müller, M.; Rogalev, A.; Kummer, K.; Orain, J.; Baines, C.; Baenitz, M.; Dressel, M.; Kermarrec, E.; Bert, F.; Mendels, P.; Krellner, C. Tuning of a Kagome Magnet: Insulating Ground State in Ga-Substituted $Cu_4(OH)_6Cl_2$. *Physica Status Solidi B* **2019**, *256*, 1800663.

[53] Huse, D. A.; Elser, V. Simple Variational Wave Functions for Two-Dimensional Heisenberg Spin-$\frac{1}{2}$ Antiferromagnets. *Physical Review Letters* **1988**, *60*, 2531–2534.

[54] Li, Y.; Gegenwart, P.; Tsirlin, A. A. Spin liquids in geometrically perfect triangular antiferromagnets. *Journal of Physics: Condensed Matter* **2020**, *32*, 224004.

[55] Norman, M. R. Colloquium: Herbertsmithite and the search for the quantum spin liquid. *Reviews of Modern Physics* **2016**, *88*, 041002.

[56] Zhou, Y.; Kanoda, K.; Ng, T.-K. Quantum spin liquid states. *Reviews of Modern Physics* **2017**, *89*, 025003.

[57] Moessner, R.; Ramirez, A. P. Geometrical frustration. *Physics Today* **2006**, *59*, 24–29.

[58] Savary, L.; Balents, L. Quantum spin liquids: a review. *Reports on Progress in Physics* **2017**, *80*, 016502.

[59] Clark, L.; Abdeldaim, A. H. Quantum Spin Liquids from a Materials Perspective. *Annual Review of Materials Research* **2021**, *51*.

[60] Chamorro, J. R.; McQueen, T. M.; Tran, T. T. Chemistry of Quantum Spin Liquids. *Chemical Reviews* **2021**, *121*, 2898–2934.

[61] Burch, K. S.; Mandrus, D.; Park, J.-G. Magnetism in two-dimensional van der Waals materials. *Nature* **2018**, *563*, 47–52.

[62] Graham, J. N.; Coak, M. J.; Son, S.; Suard, E.; Park, J.-G.; Clark, L.; Wildes, A. R. Local nuclear and magnetic order in the two-dimensional spin glass $Mn_{0.5}Fe_{0.5}PS_3$. *Physical Review Materials* **2020**, *4*, 084401.

[63] Shimizu, Y.; Miyagawa, K.; Kanoda, K.; Maesato, M.; Saito, G. Spin Liquid State in an Organic Mott Insulator with a Triangular Lattice. *Physical Review Letters* **2003**, *91*, 107001.

[64] Miksch, B.; Pustogow, A.; Rahim, M. J.; Bardin, A. A.; Kanoda, K.; Schlueter, J. A.; Hübner, R.; Scheffler, M.; Dressel, M. Gapped magnetic ground state in quantum spin liquid candidate κ-(BEDT-TTF)$_2$Cu$_2$(CN)$_3$. *Science* **2021**, *372*, 276–279.

[65] Braithwaite, R. S. W.; Mereiter, K.; Paar, W. H.; Clark, A. M. Herbertsmithite, $Cu_3Zn(OH)_6Cl_2$, a new species, and the definition of paratacamite. *Mineralogical Magazine* **2004**, *68*, 527–539.

[66] Ishikawa, H., Yamaura J. Okamoto Y. Yoshida, H. Nilsen, G. J. H. Z.; Ishikawa, H.; Yamaura, J.-I.; Okamoto, Y.; Yoshida, H.; Nilsen, G. J.; Hiroi, Z. A novel crystal polymorph of volborthite, $Cu_3V_2O_7(OH)_2{\cdot}2H_2O$. *Acta Crystallographica C* **2012**, *68*, 41–44.

[67] Zhesheng, M., Ruilin, H., Xiaoling, Z. Redetermination of the Crystal Structure of Vesignieite. *Acta Geologica Sinica* **1991**, *4*, 145–151.

[68] Nocera, D. G.; Bartlett, B. M.; Grohol, D.; Papoutsakis, D.; Shores, M. P. Spin frustration in 2D kagomé lattices: A problem for inorganic synthetic chemistry. *Chemistry - A European Journal* **2004**, *10*, 3850–3859.

[69] Wills, A. S.; Henry, J.-Y. On the crystal and magnetic ordering structures of clinoatacamite, γ-$Cu_2(OD)_3Cl$, a proposed valence bond solid. *J. Phys.: Condens. Matter* **2008**, *20*, 472206.

[70] Elliott, P.; Cooper, M. A.; Pring, A. Barlowite, $Cu_4FBr(OH)_6$, a new mineral isotructural with claringbullite: description and crystal structure. *Mineral. Mag.* **2014**, *78*, 1755–1762.

[71] Freedman, D. E.; Han, T. H.; Prodi, A.; Müller, P.; Huang, Q. Z.; Chen, Y. S.; Webb, S. M.; Lee, Y. S.; McQueen, T. M.; Nocera, D. G. Site specific X-ray anomalous dispersion of the geometrically frustrated kagomé magnet, herbertsmithite, $ZnCu_3(OH)_6Cl_2$. *Journal of the American Chemical Society* **2010**, *132*, 16185–16190.

[72] Zhu, Z.; Maksimov, P. A.; White, S. R.; Chernyshev, A. L. Disorder-Induced Mimicry of a Spin Liquid in $YbMgGaO_4$. *Phys. Rev. Lett.* **2017**, 157201.

[73] Thorarinsdottir, A. E.; Harris, T. D. Metal–Organic Framework Magnets. *Chemical Reviews* **2020**, *120*, 8716–8789.

[74] Saines, P. J.; Bristowe, N. C. Probing magnetic interactions in metal–organic frameworks and coordination polymers microscopically. *Dalton Transactions* **2018**, *47*, 13257–13280.

[75] Paddison, J. A. M.; Jacobsen, H.; Petrenko, O. A.; Fernandez-Diaz, M. T.; Deen, P. P.; Goodwin, A. L. Hidden order in spin-liquid $Gd_3Ga_5O_{12}$. *Science* **2015**, *350*, 179–181.

[76] Wen, J.; Yu, S.-L.; Li, S.; Yu, W.; Li, J.-X. Experimental identification of quantum spin liquids. *npj Quantum Materials* **2019**, *4*, 12.

[77] Rabenau, A. The Role of Hydrothermal Synthesis in Preparative Chemistry. *Angewandte Chemie International Edition in English* **1985**, *24*, 1026–1040.

[78] Feng, S.; Xu, R. New Materials in Hydrothermal Synthesis. *Accounts of Chemical Research* **2001**, *34*, 239–247.

[79] Lackner, K. S. Carbonate Chemistry for Sequestering Fossil Carbon. *Annual Review of Energy and the Environment* **2002**, *27*, 193–232.

[80] Einstein, F. W. B.; Willis, A. C. Crystal and Molecular Structure of p-Carbonato-di-p-chloro-tetrakis(bis(3-aminopropyl)amine) tetracopper (II) Chloride Hydrate. *Inorganic Chemistry* **1981**, *20*, 609–614.

[81] Escuer, A.; Peñalba, E.; Vicente, R.; Solans, X.; Font-Bardía, M. Two new tetranuclear 4-carbonato copper(II) complexes. Syntheses, crystal struc-

ture and magnetic behaviour of $[(\mu_4\text{-}CO_3)(\mu\text{-}Br)_2Cu_4\text{-}(bapa)_4]Br_4$ and $[(\mu_4\text{-}CO_3)(\mu\text{-}Cl)_2Cu_4(bapma)_4]Cl_4{\cdot}12H_2O$. *J. Chem. Soc* **1997**, *34*, 2315–2319.

[82] Fassel, V. A.; Kniseley, R. N. *Encyclopedia of Analytical Chemistry*; John Wiley & Sons Ltd: Chichester, UK, 2000; pp 9468–9485.

[83] Naozuka, J.; Mesquita Silva da Veiga, M. A.; Vitoriano Oliveira, P.; de Oliveira, E. Determination of chlorine, bromine and iodine in milk samples by ICP-OES. *Journal of Analytical Atomic Spectrometry* **2003**, *18*, 917.

[84] McKie, D.; McKie, C. *Essentials of Crystallography*; Blackwell Scientific Publications, 1986.

[85] Sivia, D. S. *Elementary Scattering Theory*; Oxford University Press: Oxford, UK, 2011.

[86] Clark, L.; Aidoudi, F. H.; Black, C.; Arachchige, K. S. A.; Slawin, A. M. Z.; Morris, R. E.; Lightfoot, P. Extending the Family of V^{4+} $S = \frac{1}{2}$ Kagome Antiferromagnets. *Angewandte Chemie International Edition* **2015**, *54*, 15457–15461.

[87] Pynn, R. *Neutron scattering - A Primer*; Los Alamos Neutron Science Center, 1990.

[88] Cockcroft, J. K. http://pd.chem.ucl.ac.uk/pdnn/inst3/diff3.htm (Accessed July 2021).

[89] Young, O.; Balakrishnan, G.; Manuel, P.; Khalyavin, D.; Wildes, A.; Petrenko, O. Field-Induced Transitions in Highly Frustrated $SrHo_2O_4$. *Crystals* **2019**, *9*, 488.

[90] Kozlenko, D. P.; Kusmartseva, A. F.; Lukin, E. V.; Keen, D. A.; Marshall, W. G.; DeVries, M. A.; Kamenev, K. V. From quantum disorder to magnetic order in an $S = \frac{1}{2}$ kagome lattice: A structural and magnetic study of herbertsmithite at high pressure. *Physical Review Letters* **2012**, *108*.

[91] de Vries, M. A.; Stewart, J. R.; Deen, P. P.; Piatek, J. O.; Nilsen, G. J.; Rønnow, H. M.; Harrison, A. Scale-Free Antiferromagnetic Fluctuations in the $s = \frac{1}{2}$ Kagome Antiferromagnet Herbertsmithite. *Physical Review Letters* **2009**, *103*, 237201.

[92] Jain, A.; Yusuf, S. M.; Kanoo, P.; Dhar, S. K.; Kumar Maji, T. Fragile magnetic ground state of a spin-$\frac{1}{2}$ metal-organic kagome lattice. *Physical Review B* **2020**, *101*, 140413.

[93] Lovesy, S. W. *Theory of Neutron Scattering from Condensed Matter*; Oxford University Press: Oxford, UK, 1986.

[94] Larson, A. C.; von Dreele, R. B. *General Structure Analysis System (GSAS) Los Alamos National Laboratory Report LAUR 86-748*; 2000.

[95] Toby, B. H. EXPGUI, a graphical user interface for GSAS. *J. Appl. Cryst.* **2001**, *34*, 210–213.

[96] Rodríguez-Carvajal, J. Recent advances in magnetic structure determination by neutron powder diffraction. *Physica B: Condensed Matter* **1993**, *192*, 55–69.

[97] Bette, S.; Takayama, T.; Duppel, V.; Poulain, A.; Takagi, H.; Dinnebier Powder samples of Ag, R. E.; Dinnebier, R. E. Crystal structure and stacking faults in the layered honeycomb, delafossite-type materials $Ag_3LiIr_3O_6$ and $Ag_3LiRu_2O_6$. *Dalton Transactions* **2019**, *48*, 9250–9259.

[98] Harcombe, D. R.; Welch, P. G.; Manuel, P.; Saines, P. J.; Goodwin, A. L. One-dimensional magnetic order in the metal-organic framework $Tb(HCOO)_3$. *Physical Review B* **2016**, *94*, 174429.

[99] McCusker, L. B.; Von Dreele, R. B.; Cox, D. E.; Louër, D.; Scardi, P. Rietveld refinement guidelines. *Journal of Applied Crystallography* **1999**, *32*, 36–50.

[100] Boldrin, D.; Knight, K.; Wills, A. S. Orbital frustration in the $S = \frac{1}{2}$ kagome magnet vesignieite, $BaCu_3V_2O_8(OH)_2$. *Journal of Materials Chemistry C* **2016**, *4*, 10315–10322.

[101] Posnjak, G. *Magnetic symmetry and determination of magnetic structures (seminar)*; 2012.

[102] Wills, A. *A walk through of the maths behind Bertaut's method of representational analysis of magnetic structures (seminar)*; 2019.

[103] Wills, A. A new protocol for the determination of magnetic structures using simulated annealing and representational analysis (SARAh). *Physica B: Condensed Matter* **2000**, *276-278*, 680–681.

[104] Wills, A. S. Indexing magnetic structures and crystallographic distortions from powder diffraction: Brillouin zone indexing. *Zeitschrift für Kristallographie Supplements* **2009**, *2009*, 39–44.

[105] Stokes, H. T.; Hatch, D. M.; Campbell, B. J. ISODISTORT. *Isotropy Software Suite* 2006.

[106] Aroyo, M. I.; Perez-Mato, J. M.; Orobengoa, E.; Tasci, G.; de la Flor, A.; Kirov, A. Crystallography online: Bilbao Crystallographic Server. *Bulgarian Chemical Communications* **2011**, *43(2)*, 183–197.

[107] Aroyo, M. I.; Perez-Mato, J. M.; Capillas, C.; Kroumova, E.; Ivantchev, S.; Madariaga, G.; Kirov, A.; Wondratschek, H. Bilbao Crystallographic Server: I. Databases and crystallographic computing programs. *Zeitschrift für Kristallographie* **2006**, *221*.

[108] Aroyo, M. I.; Kirov, A.; Capillas, C.; Perez-Mato, J. M.; Wondratschek, H. Bilbao Crystallographic Server. II. Representations of crystallographic point groups and space groups. *Acta Crystallographica A* **2006**, *62*, 115–128.

[109] Feyerherm, R.; Loose, A.; Landsgesell, S.; Manson, J. L. Magnetic Ordering in Iron Tricyanomethanide. *Inorganic Chemistry* **2004**, *43*, 6633–6639.

[110] Dixey, R. J. C.; Stenning, G. B. G.; Manuel, P.; Orlandi, F.; Saines, P. J. Ferromagnetic Ising chains in frustrated $LnODCO_3$: the influence of magnetic structure in magnetocaloric frameworks. *Journal of Materials Chemistry C* **2019**, *7*, 13111–13119.

[111] Fagaly, R. L. Superconducting quantum interference device instruments and applications. *Review of Scientific Instruments* **2006**, *77*, 101101.

[112] Shores, M. P.; Nytko, E. A.; Bartlett, B. M.; Nocera, D. G. A Structurally Perfect $S = \frac{1}{2}$ Kagomé Antiferromagnet. *Journal of the American Chemical Society* **2005**, *127*, 13462–13463.

[113] Guchhait, S.; Arjun, U.; Anjana, P. K.; Sahoo, M.; Thirumurugan, A.; Medhi, A.; Skourski, Y.; Koo, B.; Sichelschmidt, J.; Schmidt, B.; Baenitz, M.; Nath, R. Case study of bilayered spin-$\frac{1}{2}$ square lattice compound $VO(HCOO)_2{\cdot}(H_2O)$. *Physical Review Materials* **2019**, *3*, 104409.

[114] Han, T. H.; Isaacs, E. D.; Schlueter, J. A.; Singleton, J. Anisotropy: Spin order and magnetization of single-crystalline $Cu_4(OH)_6FBr$ barlowite. *Phys. Rev. B* **2016**, *93*, 214416.

[115] Amoretti, G.; Fournier, J. On the interpretation of magnetic susceptibility data by means of a modified Curie-Weiss law. *Journal of Magnetism and Magnetic Materials* **1984**, *43*, L217–L220.

[116] Nag, A.; Ray, S. Misjudging frustrations in spin liquids from oversimplified use of Curie-Weiss law. *Journal of Magnetism and Magnetic Materials* **2017**, *424*, 93–98.

[117] Sereni, J. *Encyclopedia of Materials: Science and Technology*; Elsevier, 2001; pp 4986–4993.

[118] Kittel, C. *Introduction to Solid State Physics*, 8th ed.; John Wiley & Sons, Inc.: New York, NY, 2005.

[119] Han, T. H.; Singleton, J.; Schlueter, J. A. Barlowite: A spin-$\frac{1}{2}$ antiferromagnet with a geometrically perfect kagome motif. *Physical Review Letters* **2014**, *113*, 227203.

[120] Gamsjäger, E.; Wiessner, M. Low temperature heat capacities and thermodynamic functions described by Debye–Einstein integrals. *Monatshefte für Chemie* **2018**, *149*, 357–368.

[121] Scheie, A.; Ross, K.; Stavropoulos, P. P.; Seibel, E.; Rodriguez-Rivera, J. A.; Tang, J. A.; Li, Y.; Kee, H.-Y.; Cava, R. J.; Broholm, C. Counterrotating magnetic order in the honeycomb layers of $NaNi_2BiO_{6-\delta}$. *Physical Review B* **2019**, *100*, 214421.

[122] Abdeldaim, A. H.; Li, T.; Farrar, L.; Tsirlin, A. A.; Yao, W.; Gibbs, A. S.; Manuel, P.; Lightfoot, P.; Nilsen, G. J.; Clark, L. Realizing square and diamond lattice $S = \frac{1}{2}$ Heisenberg antiferromagnet models in the α and β phases of the coordination framework, $KTi(C_2O_4)_2{\cdot}xH_2O$. *Physical Review Materials* **2020**, *4*, 104414.

[123] Yao, W.; Clark, L.; Xia, M.; Li, T.; Lee, S. L.; Lightfoot, P. Diverse Family of Layered Frustrated Magnets with Tailorable Interlayer Interactions. *Chemistry of Materials* **2017**, *29*, 6616–6620.

[124] Blundell, S. J.; Lancaster, T.; Pratt, F. L.; Baker, P. J.; Brooks, M. L.; Baines, C.; Manson, J. L.; Landee, C. P. μ^+SR as a probe of anisotropy in low-dimensional molecular magnets. *Journal of Physics and Chemistry of Solids* **2007**, *68*, 2039–2043.

[125] Ramirez, A. P. Quantum spin liquids: A flood or a trickle? *Nature Physics* **2008**, *4*, 442–443.

[126] Blundell, S. J. Spin-polarized muons in condensed matter physics. *Contemporary Physics* **1999**, *40*, 175.

[127] Carretta, P.; Keren, A. *Introduction to Frustrated Magnetism*; Springer: Berlin, Germany, 2011; Chapter 4.

[128] Zheng, X. G.; Kubozono, H.; Nishiyama, K.; Higemoto, W.; Kawae, T.; Koda, A.; Xu, C. N. Coexistence of Long-Range Order and Spin Fluctuation in Geometrically Frustrated Clinoatacamite $Cu_2Cl(OH)_3$. *Physical Review Letters* **2005**, *95*, 057201.

[129] Berlie, A. *Muon Instrumentation (International Advanced School in Muon Spectroscopy, ISIS Neutron and Muon Source)*; 2019.

[130] Bert, F. Local probes of magnetism, NMR and μSR: A short introduction. *Collection SFN* **2014**, *13*, 03001.

[131] King, P. J. C.; De Renzi, R.; Cottrell, S. P.; Watts, I. D.; Carling, S. G.; Day, P.; Visser, D. Muon spin relaxation studies of magnetic ordering in the molecular-based ferrimagnets $PPh_4Mn^{II}Fe^{III}(C_2O_4)_3$ and $(n\text{-}C_4H_9)_4NFe^{II}Fe^{III}(C_2O_4)_3$. *J. Phys.: Condens. Matter* **2001**, *13*, 2225–2233.

[132] Hayano, R. S.; Uemura, Y. J.; Imazato, J.; Nishida, N.; Yamazaki, T.; Kubo, R. Zero-and low-field spin relaxation studied by positive muons. *Physical Review B* **1979**, *20*, 850–859.

[133] Brewer, J. H.; Kreitzman, S. R.; Noakes, D. R.; Ansaldo, E. J.; Harshman, D. R.; Keitel, R. Observation of muon-fluorine "hydrogen bonding" in ionic crystals. *Physical Review B* **1986**, *33*, 7813.

[134] Mendels, P.; Bert, F.; De Vries, M. A.; Olariu, A.; Harrison, A.; Duc, F.; Trombe, J. C.; Lord, J. S.; Amato, A.; Baines, C. Quantum Magnetism in the Paratacamite Family: Towards an Ideal Kagomé Lattice. *Physical Review Letters* **2007**, *98*, 077204.

[135] Martin, D. Z. C.; Haworth, A. R.; Schmidt, W. L.; Baker, P. J.; Boston, R.; Johnston, K. E.; Reeves-McLaren, N. Evaluating lithium diffusion mechanisms in the complex spinel $Li_2NiGe_3O_8$. *Physical Chemistry Chemical Physics* **2019**, *21*, 23111–23118.

[136] Huddart,; Benjamin, M. Muon stopping sites in magnetic systems from density functional theory. Ph.D. thesis, 2020.

[137] Foronda, F. R.; Lang, F.; Möller, J. S.; Lancaster, T.; Boothroyd, A. T.; Pratt, F. L.; Giblin, S. R.; Prabhakaran, D.; Blundell, S. J. Anisotropic Local Modification of Crystal Field Levels in Pr-Based Pyrochlores: A Muon-Induced Effect Modeled Using Density Functional Theory. *Phys. Rev. Lett.* **2015**, *114*, 017602.

[138] Wilkinson, J. M.; Blundell, S. J. Information and Decoherence in a Muon-Fluorine Coupled System. *Physical Review Letters* **2020**, *125*, 087201.

[139] Clark, L.; Orain, J. C.; Bert, F.; De Vries, M. A.; Aidoudi, F. H.; Morris, R. E.; Lightfoot, P.; Lord, J. S.; Telling, M. T. F.; Bonville, P.; Attfield, J. P.; Mendels, P.; Harrison, A. Gapless Spin Liquid Ground State in the $S = \frac{1}{2}$ Vanadium Oxyfluoride Kagome Antiferromagnet $[NH_4]_2[C_7H_{14}N][V_7O_6F_{18}]$. *Physical Review Letters* **2013**, *110*, 207208.

[140] Clark, L.; Sala, G.; Maharaj, D. D.; Stone, M. B.; Knight, K. S.; Telling, M. T. F.; Wang, X.; Xu, X.; Kim, J.; Li, Y.; Cheong, S.-W.; Gaulin, B. D. Two-dimensional spin liquid behaviour in the triangular-honeycomb antiferromagnet $TbInO_3$. *Nature Physics* **2019**, *15*, 262–268.

[141] Bisson, W. G.; Wills, A. S. Anisotropy-driven spin glass transition in the kagome antiferromagnet hydronium jarosite, $(H_3O)Fe_3(SO_4)_2(OH)_6$. *Journal of Physics: Condensed Matter* **2008**, *20*, 452204.

[142] Mills, S. J.; Nestola, F.; Kahlenberg, V.; Christy, A. G.; Hejny, C.; Redhammer, G. J. Looking for jarosite on Mars: The low-temperature crystal structure of jarosite. *American Mineralogist* **2013**, *98*, 1966–1971.

[143] Zheng, X. G.; Kawae, T.; Kashitani, Y.; Li, C. S.; Tateiwa, N.; Takeda, K.; Yamada, H.; Xu, C. N.; Ren, Y. Unconventional magnetic transitions in the mineral clinoatacamite $Cu_2Cl(OH)_3$. *Physical Review B* **2005**, *71*, 052409.

[144] https://www.mindat.org/ (Accessed May 2021).

[145] Lafontaine, M.; Le Bail, A.; Férey, G. Copper-containing minerals—I. $Cu_3V_2O_7(OH)_2$, $2H_2O$: The synthetichomolog of volborthite; crystal structure determination from X-ray and neutron data; structural correlations. *Journal of Solid State Chemistry* **1990**, *85*, 220–227.

[146] Hiroi, Z.; Ishikawa, H.; Yoshida, H.; Yamaura, J.-i.; Okamoto, Y. Orbital Transitions and Frustrated Magnetism in the Kagome-Type Copper Mineral Volborthite. *Inorganic Chemistry* **2019**, *58*, 11949–11960.

[147] Yoshida, H.; Yamaura, J. I.; Isobe, M.; Okamoto, Y.; Nilsen, G. J.; Hiroi, Z. Orbital switching in a frustrated magnet. *Nature Communications* **2012**, *3*, 1–5.

[148] Malcherek, T.; Welch, M. D.; Williams, P. A. The atacamite family of minerals – a testbed for quantum spin liquids. *Acta Crystallographica B* **2018**, *74*, 519–526.

[149] Zenmyo, K.; Kubo, H.; Tokita, M.; Hamasaki, T.; Hagihala, M.; Zheng, X. G.; Kawae, T.; Takeuchi, Y.; Matsumura, M. Proton NMR study of atacamite $Cu_2Cl(OH)_3$. *Journal of the Physical Society of Japan* **2013**, *82*.

[150] Pasco, C. M.; Trump, B. A.; Tran, T. T.; Kelly, Z. A.; Hoffmann, C.; Heinmaa, I.; Stern, R.; Mcqueen, T. M. Single-crystal growth of $Cu_4(OH)_6BrF$ and universal behavior in quantum spin liquid candidates synthetic barlowite and herbertsmithite. *Physical Review Materials* **2018**, *2*, 44406.

[151] Smaha, R. W. et al. Materializing rival ground states in the barlowite family of kagome magnets: quantum spin liquid, spin ordered, and valence bond crystal states. *npj Quantum Materials* **2020**, *5*, 1.

[152] Helton, J. S.; Matan, K.; Shores, M. P.; Nytko, E. A.; Bartlett, B. M.; Yoshida, Y.; Takano, Y.; Suslov, A.; Qiu, Y.; Chung, J. H.; Nocera, D. G.; Lee, Y. S. Spin dynamics of the spin-$\frac{1}{2}$ kagome lattice antiferromagnet $ZnCu_3(OH)_6Cl_2$. *Physical Review Letters* **2007**, *98*, 107204.

[153] Nilsen, G. J.; De Vries, M. A.; Stewart, J. R.; Harrison, A.; Rønnow, H. M. Low-energy spin dynamics of the $S = \frac{1}{2}$ kagome system herbertsmithite. *Journal of Physics: Condensed Matter* **2013**, *25*, 106001.

[154] Fu, M.; Imai, T.; Han, T.-H.; Lee, Y. S. Evidence for a gapped spin-liquid ground state in a kagome Heisenberg antiferromagnet. *Science* **2015**, *350*, 655–658.

[155] Han, T. H.; Norman, M. R.; Wen, J. J.; Rodriguez-Rivera, J. A.; Helton, J. S.; Broholm, C.; Lee, Y. S. Correlated impurities and intrinsic spin-

liquid physics in the kagome material herbertsmithite. *Physical Review B* **2016**, *94*, 060409.

[156] Khuntia, P.; Velazquez, M.; Barthélemy, Q.; Bert, F.; Kermarrec, E.; Legros, A.; Bernu, B.; Messio, L.; Zorko, A.; Mendels, P. Gapless ground state in the archetypal quantum kagome antiferromagnet $ZnCu_3(OH)_6Cl_2$. *Nature Physics* **2020**, *16*, 469–474.

[157] Jeschke, H. O.; Salvat-Pujol, F.; Gati, E.; Hoang, N. H.; Wolf, B.; Lang, M.; Schlueter, J. A.; Valentí, R. Barlowite as a canted antiferromagnet: Theory and experiment. *Physical Review B* **2015**, *92*, 094417.

[158] Feng, Z.; Wei, Y.; Liu, R.; Yan, D.; Wang, Y. C.; Luo, J.; Senyshyn, A.; Cruz, C. D.; Yi, W.; Mei, J. W.; Meng, Z. Y.; Shi, Y.; Li, S. Effect of Zn doping on the antiferromagnetism in kagome $Cu_{4-x}Zn_x(OH)_6FBr$. *Physical Review B* **2018**, *98*, 155127.

[159] Ranjith, K. M.; Klein, C.; Tsirlin, A. A.; Rosner, H.; Krellner, C.; Baenitz, . M. Magnetic resonance as a local probe for kagome magnetism in Barlowite $Cu_4(OH)_6FBr$. *Sci. Rep.* **2018**, *8*, 10851.

[160] Smaha, R. W.; He, W.; Sheckelton, J. P.; Wen, J.; Lee, Y. S. Synthesis-dependent properties of barlowite and Zn-substituted barlowite. *Journal of Solid State Chemistry* **2018**, *268*, 123–129.

[161] Henderson, A.; Dong, L.; Biswas, S.; Revell, H. I.; Xin, Y.; Valenti, R.; Schlueter, J. A.; Siegrist, T.; Li, R.; Chemcomm, .; Communication, C. Order-disorder transition in the $S = \frac{1}{2}$ kagome antiferromagnets claringbullite and barlowite. *Chem. Commun* **2019**, *55*, 11587–11590.

[162] Liu, Z.; Zou, X.; Mei, J.-W.; Liu, F. Selectively doping barlowite for quantum spin liquid: A first-principles study. *Physical Review B* **2015**, *92*, 220102.

[163] Guterding, D.; Valentí, R.; Jeschke, H. O. Reduction of magnetic interlayer coupling in barlowite through isoelectronic substitution. *Physical Review B* **2016**, *94*, 125136.

[164] Fejer, E. E.; Clark, A. M.; Couper, A. G.; Elliott, C. J. Claringbullite, a new hydrated copper chloride. *Mineralogical Magazine* **1977**, *41*, 433–436.

[165] Tustain, K.; Nilsen, G. J.; Ritter, C.; da Silva, I.; Clark, L. Nuclear and magnetic structures of the frustrated quantum antiferromagnet barlowite, $Cu_4(OH)_6FBr$. *Physical Review Materials* **2018**, *2*, 111405.

[166] Campbell, B. J.; Stokes, H. T.; Tanner, D. E.; Hatch, D. M. ISODISPLACE: a web-based tool for exploring structural distortions. *J. Appl. Cryst* **2006**, *39*, 607–614.

[167] Burns, P. C.; Hawthorne, F. C. Static and dynamic Jahn-Teller effects in Cu^{2+} oxysalt minerals. *The Canadian Mineralogist* **1996**, *34*, 1089–1105.

[168] David, W. I. F.; Jones, M. O.; Gregory, D. H.; Jewell, C. M.; Johnson, S. R.; Walton, A.; Edwards, P. P. A Mechanism for Non-stoichiometry in the Lithium Amide/Lithium Imide Hydrogen Storage Reaction. *Journal of the American Chemical Society* **2007**, *129*, 1594–1601.

[169] Nytko, E. A. Synthesis, Structure, and Magnetic Properties of Spin-1/2 Kagomé Antiferromagnets. Ph.D. thesis, 2008.

[170] Welch, M. D.; Najorka, J.; Rumsey, M. S.; Spratt, J. The Hexagonal to Orthorhombic Structural Phase Transition in Claringbullite, $Cu_4FCl(OH)_6$. *The Canadian Mineralogist 00*, 1–21.

[171] Wills, A. S., Brown, I. D. *VaList v. 4.0.7 VaList-bond valence calculation and listing Program available from www.ccp14.ac.uk*; 2010.

[172] Yue, X. Y.; Ouyang, Z. W.; Wang, J. F.; Wang, Z. X.; Xia, Z. C.; He, Z. Z. Magnetization and ESR studies on $Cu_4(OH)_6FCl$: An antiferromagnet with a kagome lattice. *Physical Review B* **2018**, *97*, 54417.

[173] Feng, Z.; Yi, W.; Zhu, K.; Wei, Y.; Miao, S.; Ma, J.; Luo, J.; Li, S.; Yang Meng, Z.; Shi, Y. Express Letter From Claringbullite to a New Spin Liquid Candidate $Cu_3Zn(OH)_6FCl$. *Chinese Physics Letters* **2019**, *36*, 017502.

[174] de Vries, M. A. Iron jarosite and zinc paratacamite as models of the classical and the quantum kagomé. Ph.D. thesis, 2007.

[175] Lee, S. H.; Kikuchi, H.; Qiu, Y.; Lake, B.; Huang, Q.; Habicht, K.; Kiefer, K. Quantum-spin-liquid states in the two-dimensional kagome antiferromagnets $Zn_xCu_{4-x}(OD)_6Cl_2$. *Nature Materials* **2007**, *6*, 853–857.

[176] De Vries, M. A.; Kamenev, K. V.; Kockelmann, W. A.; Sanchez-Benitez, J.; Harrison, A. Magnetic ground state of an experimental $S = \frac{1}{2}$ kagome antiferromagnet. *Physical Review Letters* **2008**, *100*, 157205.

[177] Bert, F.; Olariu, A.; Zorko, A.; Mendels, P.; Trombe, J. C.; Duc, F.; De Vries, M. A.; Harrison, A.; Hillier, A. D.; Lord, J.; Amato, A.;

Baines, C. Frustrated magnetism in the quantum Kagome Herbertsmithite $ZnCu_3(OH)_6Cl_2$ antiferromagnet. *Journal of Physics Conference Series* **2008**, *145*, 1–8.

[178] Kermarrec, E.; Mendels, P.; Bert, F.; Colman, R. H.; Wills, A. S.; Strobel, P.; Bonville, P.; Hillier, A.; Amato, A. Spin-liquid ground state in the frustrated kagome antiferromagnet $MgCu_3(OH)_6Cl_2$. *Physical Review B* **2011**, *84*, 100401.

[179] Colman, R. H.; Sinclair, A.; Wills, A. S. Magnetic and Crystallographic Studies of Mg-Herbertsmithite, γ-$Cu_3Mg(OH)_6Cl_2$ —A New $S = \frac{1}{2}$ Kagome Magnet and Candidate Spin Liquid. *Chem. Mater* **2011**, *23*, 1811–1817.

[180] Feng, Z. et al. Gapped spin-$\frac{1}{2}$ spinon excitations in a new kagome quantum spin liquid compound $Cu_3Zn(OH)_6FBr$. *Chinese Physics Letters* **2017**, *34*, 077502.

[181] Wei, Y.; Ma, X.; Feng, Z.; Adroja, D.; Hillier, A.; Bitwas, P.; Senyshyn, A.; Hoser, A.; Mei, J.-W.; Yang Meng, Z.; Luo, H.; Shi, Y.; LI, S. Magnetic Phase Diagram of $Cu_{4-x}Zn_x(OH)_6FBr$ Studied by Neutron-Diffraction and μSR Techniques. *Chinese Physics Letters* **2020**, *37*, 107503.

[182] Fu, Y. et al. Dynamic fingerprint of fractionalized excitations in single-crystalline $Cu_3Zn(OH)_6$ FBr. **2020**, Preprint at http://arxiv.org/abs/2010.07900.

[183] Wei, Y.; Feng, Z.; dela Cruz, C.; Yi, W.; Yang Meng, Z.; Mei, J.-W.; Shi, Y.; Li, S. Antiferromagnetism in kagome α-$Cu_3Mg(OH)_6Br_2$. *Physical Review B* **2019**, *100*, 155129.

[184] Lord, J. S.; Cottrell, S. P.; Williams, W. G. Muon spin relaxation in strongly coupled systems. *Physica B Condens. Matter* **2000**, *289*, 495–498.

[185] Tustain, K.; Ward-O'Brien, B.; Bert, F.; Han, T.; Luetkens, H.; Lancaster, T.; Huddart, B. M.; Baker, P. J.; Clark, L. From magnetic order to quantum disorder in the Zn-barlowite series of $S = \frac{1}{2}$ kagomé antiferromagnets. *npj Quantum Materials* **2020**, *5*.

[186] Arnold, O. et al. Mantid—Data analysis and visualization package for neutron scattering and μSR experiments. *Nuclear Instruments and Methods in Physics Research A* **2014**, *764*, 156–166.

[187] Huddart, B. M. *https://gitlab.com/BenHuddart/mufinder/*; 2020.

[188] Clark, S. J.; Segall, M. D.; Pickard Ii, C. J.; Hasnip, P. J.; Probert, M. I. J.; Refson, K.; Payne, M. C. First principles methods using CASTEP. *Zeitschrift für Kristallographie* **2005**, *220*, 567–570.

[189] Monkhorst, H. J.; Pack, J. D. Special points for Brillouin-zone integrations. *Physical Review B* **1976**, *13*, 5188–5192.

[190] Sears, V. F. Neutron scattering lengths and cross sections. *Neutron News* **1992**, *3*, 26–37.

[191] Fåk, B.; Kermarrec, E.; Messio, L.; Bernu, B.; Lhuillier, C.; Bert, F.; Mendels, P.; Koteswararao, B.; Bouquet, F.; Ollivier, J.; Hillier, A. D.; Amato, A.; Colman, R. H.; Wills, A. S. Kapellasite: A Kagome Quantum Spin Liquid with Competing Interactions. *Physical Review Letters* **2012**, *109*, 037208.

[192] Barthélemy, Q.; Puphal, P.; Zoch, K. M.; Krellner, C.; Luetkens, H.; Baines, C.; Sheptyakov, D.; Kermarrec, E.; Mendels, P.; Bert, F. Local study of the insulating quantum kagome antiferromagnets $YCu_3(OH)_6O_xCl_{3-x} (x = 0, \frac{1}{3})$. *Physical Review Materials* **2019**, *3*, 74401.

[193] Zorko, A.; Pregelj, M.; Klanjšek, M.; Gomilšek, M.; Jagličić, Z.; Lord, J. S.; Verezhak, J. A. T.; Shang, T.; Sun, W.; Mi, J.-X. Coexistence of magnetic order and persistent spin dynamics in a quantum kagome antiferromagnet with no intersite mixing. *Physical Review B* **2019**, *99*, 214441.

[194] Lancaster, T.; Blundell, S. J.; Baker, P. J.; Brooks, M. L.; Hayes, W.; Pratt, F. L.; Manson, J. L.; Conner, M. M.; Schlueter, J. A. Muon-Fluorine Entangled States in Molecular Magnets. *Physical Review Letters* **2007**, *99*, 267601.

[195] Yaouanc, A.; Dalmas de Réotier, P. *Muon Spin Rotation, Relaxation, and Resonance*; Oxford University Press, 2010.

[196] Slichter, C. P. *Principles of Magnetic Resonance*; Springer Verlag, 1978.

[197] Gomilšek, M.; Klanjšek, M.; Pregelj, M.; Luetkens, H.; Li, Y.; Zhang, Q. M.; Zorko, A. μSR insight into the impurity problem in quantum kagome antiferromagnets. *Physical Review B* **2016**, *94*, 24438.

[198] Gomilšek, M.; Žitko, R.; Klanjšek, M.; Pregelj, M.; Baines, C.; Li, Y.; Zhang, Q. M.; Zorko, A. Kondo screening in a charge-insulating spinon metal. *Nature Physics* **2019**, *15*, 754–760.

[199] Gardner, J. S.; Dunsiger, S. R.; Gaulin, B. D.; Gingras, M. J. P.; Greedan, J. E.; Kiefl, R. F.; Lumsden, M. D.; Macfarlane, W. A.; Raju, N. P.; Sonier, J. E.; Swainson, I.; Tun, Z. Cooperative Paramagnetism in the Geometrically Frustrated Pyrochlore Antiferromagnet $Tb_2Ti_2O_7$. *Physical Review Letters* **1999**, *82*, 1012–1015.

[200] Li, Y.; Adroja, D.; Biswas, P. K.; Baker, P. J.; Zhang, Q.; Liu, J.; Tsirlin, A. A.; Gegenwart, P.; Zhang, Q. Muon Spin Relaxation Evidence for the U(1) Quantum Spin-Liquid Ground State in the Triangular Antiferromagnet $YbMgGaO_4$. *Physical Review Letters* **2016**, *117*, 097201.

[201] Kenney, E. M. et al. Coexistence of static and dynamic magnetism in the Kitaev spin liquid material Cu_2IrO_3. *Physical Review B* **2019**, *100*, 094418.

[202] Smaha, R. W.; Boukahil, I.; Titus, C. J.; Jiang, J. M.; Sheckelton, J. P.; He, W.; Wen, J.; Vinson, J.; Wang, S. G.; Chen, Y.-S. S.; Teat, S. J.; Devereaux, T. P.; Das Pemmaraju, C.; Lee, Y. S. Site-specific structure at multiple length scales in kagome quantum spin liquid candidates. *Physical Review Materials* **2020**, *4*, 124406.

[203] Li, H.; Wang, K.; Sun, Y.; Lollar, C. T.; Li, J.; Zhou, H.-C. Recent advances in gas storage and separation using metal-organic frameworks. *Materials Today* **2018**, *21*, 108–121.

[204] Huang, Y.-B.; Liang, J.; Wang, X.-S.; Cao, R. Multifunctional metal–organic framework catalysts: synergistic catalysis and tandem reactions. *Chemical Society Reviews* **2017**, *46*, 126–157.

[205] Amini, A.; Kazemi, S.; Safarifard, V. Metal-organic framework-based nanocomposites for sensing applications – A review. *Polyhedron* **2020**, *177*, 114260.

[206] Mínguez Espallargas, G.; Coronado, E. Magnetic functionalities in MOFs: From the framework to the pore. *Chemical Society Reviews* **2018**, *47*, 533–557.

[207] Yamada, M. G.; Soejima, T.; Tsuji, N.; Hirai, D.; Dincă, M.; Aoki, H. First-principles design of a half-filled flat band of the kagome lattice in two-dimensional metal-organic frameworks. *Physical Review B* **2016**, *94*, 081102.

[208] Yamada, M. G.; Fujita, H.; Oshikawa, M. Designing Kitaev Spin Liquids in Metal-Organic Frameworks. *Physical Review Letters* **2017**, *119*, 057202.

[209] Chakraborty, G.; Park, I.-H.; Medishetty, R.; Vittal, J. J. Two-Dimensional Metal-Organic Framework Materials: Synthesis, Structures, Properties and Applications. *Chemical Reviews* **2021**, *121*, 3751–3891.

[210] Barthelet, K.; Marrot, J.; Férey, G.; Riou, D. $V^{III}(OH)(O_2C{-}C_6H_4{-}CO_2)\cdot(HO_2C{-}C_6H_4{-}CO_2H)_x(DMF)_y(H_2O)_z$ (or MIL-68), a new vanadocarboxylate with a large pore hybrid topology. *Chemical Communications* **2004**, *4*, 520–521.

[211] Nytko, E. A.; Helton, J. S.; Müller, P.; Nocera, D. G. A Structurally Perfect $S = \frac{1}{2}$ Metal-Organic Hybrid Kagome Antiferromagnet. *Journal of the American Chemical Society* **2008**, *130*, 2922–2923.

[212] H. Mohideen, M. I.; Lei, C.; Tuček, J.; Malina, O.; Brivio, F.; Kasneryk, V.; Huang, Z.; Mazur, M.; Zou, X.; Nachtigall, P.; Čejka, J.; Morris, R. E. Magneto-structural correlations of novel kagomé-type metal organic frameworks. *Journal of Materials Chemistry C* **2019**, *7*, 6692–6697.

[213] Misumi, Y.; Yamaguchi, A.; Zhang, Z.; Matsushita, T.; Wada, N.; Tsuchizu, M.; Awaga, K. Quantum Spin Liquid State in a Two-Dimensional Semiconductive Metal–Organic Framework. *Journal of the American Chemical Society* **2020**, *142*, 16513–16517.

[214] Hua, M.; Xia, B.; Wang, M.; Li, E.; Liu, J.; Wu, T.; Wang, Y.; Li, R.; Ding, H.; Hu, J.; Wang, Y.; Zhu, J.; Xu, H.; Zhao, W.; Lin, N. Highly Degenerate Ground States in a Frustrated Antiferromagnetic Kagome Lattice in a Two-Dimensional Metal–Organic Framework. *The Journal of Physical Chemistry Letters* **2021**, *12*, 3733–3739.

[215] Liu, Y.; Kravtsov, V. C.; Beauchamp, D. A.; Eubank, J. F.; Eddaoudi, M. 4-Connected metal-organic assemblies mediated via heterochelation and bridging of single metal ions: Kagome lattice and the M_6L_{12} octahedron. *Journal of the American Chemical Society* **2005**, *127*, 7266–7267.

[216] Chisnell, R.; Helton J. S.,; Freedman, D. E.; Singh, D. K.; Bewley, R. I.; Nocera, D. G.; Lee, Y. S. Topological Magnon Bands in a Kagome Lattice Ferromagnet. *Physical Review Letters* **2015**, *115*, 147201.

[217] Jiang, W.; Ni, X.; Liu, F. Exotic Topological Bands and Quantum States in Metal–Organic and Covalent–Organic Frameworks. *Accounts of Chemical Research* **2021**, *54*, 416–426.

[218] Kanoo, P.; Madhu, C.; Mostafa, G.; Maji, T. K.; Sundaresan, A.; Pati, S. K.; Rao, C. N. R. A planar Cu^{2+} ($S = 1/2$) kagome network pillared by 1,2-bis(4-pyridyl) ethane with interesting magnetic properties. *Dalton Transactions* **2009**, *9226*, 5062–5064.

[219] Ajeesh, M. O.; Yogi, A.; Padmanabhan, M.; Nath, R. Tuning of magnetic frustration in $S = 1/2$ Kagome lattices $[Cu_3(CO_3)_2(bpe)_3](ClO_4)_2]_n$ and $[Cu_3(CO_3)_2(bpy)_3(ClO_4)]_{2n}$ through rigid and flexible ligands. *Solid State Communications* **2015**, *207*, 16–20.

[220] Kikuchi, H.; Fujii, Y.; Nakata, H.; Taniguchi, T.; Zhang, W.; Okubo, S.; Ohta, H. Unusual Magnetic Phase Transition of 2D Kagomé Compound $Cu_3(CO_3)(bpe)_3.2ClO_4$. *JPS Conf. Proc.* **2014**, *1*, 0120191–0120194.

[221] Keene, T. D.; Murphy, M. J.; Price, J. R.; Sciortino, N. F.; Southon, P. D.; Kepert, C. J. Multifunctional MOFs through CO_2 fixation: a metamagnetic kagome lattice with uniaxial zero thermal expansion and reversible guest sorption. *Dalton Transactions* **2014**, *43*, 14766–14771.

[222] Toby, B. H.; Von Dreele, R. B. GSAS-II : the genesis of a modern open-source all purpose crystallography software package. *Journal of Applied Crystallography* **2013**, *46*, 544–549.

[223] Suter, A.; Wojek, B. Musrfit: A Free Platform-Independent Framework for μSR Data Analysis. *Physics Procedia* **2012**, *30*, 69–73.

[224] Orain, J.-C.; Bernu, B.; Mendels, P.; Clark, L.; Aidoudi, F. H.; Lightfoot, P.; Morris, R. E.; Bert, F. Nature of the Spin Liquid Ground State in a Breathing Kagome Compound Studied by NMR and Series Expansion. *Physical Review Letters* **2017**, *118*, 237203.

[225] Schaffer, R.; Huh, Y.; Hwang, K.; Kim, Y. B. Quantum spin liquid in a breathing kagome lattice. *Physical Review B* **2017**, *95*, 054410.

[226] Ergun, S.; Berman, M. X-ray diffraction profiles of defective layered lattices showing preferred orientation. *Acta Crystallographica Section A* **1973**, *29*, 12–17.

[227] Cervellino, A.; Maspero, A.; Masciocchi, N.; Guagliardi, A. From Paracrystalline $Ru(CO)_4$ 1D Polymer to Nanosized Ruthenium Metal: A Case of Study through Total Scattering Analysis. *Crystal Growth & Design* **2012**, *12*, 3631–3637.

[228] Marisa, M. E.; Zhou, S.; Melot, B. C.; Peaslee, G. F.; Neilson, J. R. Paracrystalline Disorder from Phosphate Ion Orientation and Substitution in Synthetic Bone Mineral. *Inorganic Chemistry* **2016**, *55*, 12290–12298.

[229] Bain, G. A.; Berry, J. F. Diamagnetic Corrections and Pascal's Constants. *Journal of Chemical Education* **2008**, *85*, 532.

[230] Mulrooney, D. Z.; Clements, J. E.; Ericsson, D. J.; Price, J. R.; Kühne, I. A.; Coles, S. J.; Kepert, C. J.; Keene, T. D. Phase Control of Ferromagnetic Copper(II) Carbonate Coordination Polymers through Reagent Concentration. *European Journal of Inorganic Chemistry* **2018**, *2018*, 5223–5228.

[231] Mateus, P.; Delgado, R.; Lloret, F.; Cano, J.; Brandão, P.; Félix, V. A trinuclear copper(II) cryptate and its μ_3-CO_3 cascade complex: Thermodynamics, structural and magnetic properties. *Chemistry - A European Journal* **2011**, *17*, 11193–11203.

[232] Kenny, E. P.; Jacko, A. C.; Powell, B. J. The princess and the pea: on the outsized role of inter-layer ligands in copper-pyrazine antiferromagnets. **2021**, Preprint at http://arxiv.org/abs/2102.09699v1.

[233] Vela, S.; Jornet-Somoza, J.; Turnbull, M. M.; Feyerherm, R.; Novoa, J. J.; Deumal, M. Dividing the Spoils: Role of Pyrazine Ligands and Perchlorate Counterions in the Magnetic Properties of Bis(pyrazine)diperchloratecopper(II), $[Cu(pz)_2](ClO_4)_2$. *Inorganic Chemistry* **2013**, *52*, 12923–12932.

[234] Prando, G.; Perego, J.; Negroni, M.; Riccò, M.; Bracco, S.; Comotti, A.; Sozzani, P.; Carretta, P. Molecular Rotors in a Metal–Organic Framework: Muons on a Hyper-Fast Carousel. *Nano Letters* **2020**, *20*, 7613–7618.

[235] Burnett, B. J.; Barron, P. M.; Hu, C.; Choe, W. Stepwise synthesis of metal - Organic frameworks: Replacement of structural organic linkers. *Journal of the American Chemical Society* **2011**, *133*, 9984–9987.

[236] Li, T.; Kozlowski, M. T.; Doud, E. A.; Blakely, M. N.; Rosi, N. L. Stepwise ligand exchange for the preparation of a family of mesoporous MOFs. *Journal of the American Chemical Society* **2013**, *135*, 11688–11691.

[237] Majumder, A.; Choudhury, C. R.; Mitra, S.; Rosair, G. M.; El Fallah, M. S.; Ribas, J. Isolation of a new two-dimensional honeycomb carbonato-bridged copper(ii) complex exhibiting long-range ferromagnetic ordering. *Chemical Communications* **2005**, 2158.

[238] Bu, X.; Frost-Jensen, A.; Allendoerfer, R.; Coppens, P.; Lederle, B.; Naughton, M. J. Structure and properties of a new κ-phase organic metal: (BEDT-TTF)$_2$Cu$_2$(CN)$_3$. *Solid State Communications* **1991**, *79*, 1053–1057.

[239] H Edema, J. J.; Gambarotta, S.; Kin, O.; Shoukang Hao Corinne Bensimon, C.; Crouch, S. Superconductivity at 2.8 K and 1.5 kbar in κ-(BEDT-TTF)$_2$Cu$_2$(CN)$_3$: The First Organic Superconductor Containing a Polymeric Copper Cyanide Anion. *Inorganic Chemistry* **1991**, *30*, 2586–2588.

[240] Morosin, B.; Lingafelter, E. C. The configuration of the tetrachlorocuprate(II) ion. *The Journal of Physical Chemistry* **1961**, *65*, 50–51.

[241] Carlin, R. L.; Burriel, R.; Palacio, F.; Carlin, R. A.; Keij, S. F.; Carnegie, D. W. Linear chain antiferromagnetic interactions in Cs_2CuCl_4. *Journal of Applied Physics* **1985**, *57*, 3351–3352.

[242] Coldea, R.; Tennant, D. A.; Tsvelik, A. M.; Tylczynski, Z. Experimental Realization of a 2D Fractional Quantum Spin Liquid. *Physical Review Letters* **2001**, *86*, 1335–1338.

[243] Kohno, M.; Starykh, O. A.; Balents, L. Spinons and triplons in spatially anisotropic frustrated antiferromagnets. *Nature Physics* **2007**, *3*, 790–795.

[244] Lorusso, G.; Sharples, J. W.; Palacios, E.; Roubeau, O.; Brechin, E. K.; Sessoli, R.; Rossin, A.; Tuna, F.; McInnes, E. J. L.; Collison, D.; Evangelisti, M. A Dense Metal-Organic Framework for Enhanced Magnetic Refrigeration. *Advanced Materials* **2013**, *25*, 4653–4656.

[245] Kurmoo, M.; Kumagai, H.; Chapman, K. W.; Kepert, C. J. Reversible ferromagnetic–antiferromagnetic transformation upon dehydration–hydration of the nanoporous coordination framework, $[Co_3(OH)_2(C_4O_4)_2]\cdot 3H_2O$. *Chemical Communications* **2005**, 3012.

[246] Mole, R. A.; Rule, K. C.; Yu, D.; Stride, J. A.; Nadeem, M. A.; Wood, P. T. Dynamics of the frustrated spin in the low dimensional magnet $Co_3(OH)_3(C_4O_4)_2$. *Journal of Physics: Condensed Matter* **2016**, *28*, 126005.

[247] Harrison, A. First catch your hare: the design and synthesis of frustrated magnets. *Journal of Physics: Condensed Matter* **2004**, *16*, 553–572.

[248] Saines, P. J.; Paddison, J. A. M.; Thygesen, P. M. M.; Tucker, M. G. Searching beyond Gd for magnetocaloric frameworks: magnetic properties and interactions of the $Ln(HCO_2)_3$ series. *Materials Horizons* **2015**, *2*, 528–535.

[249] Manson, J. L.; Ressouche, E.; Miller, J. S. Spin Frustration in $M^{II}[C(CN)_3]_2$ (M = V, Cr). A Magnetism and Neutron Diffraction Study. *Inorganic Chemistry* **2000**, *39*, 1135–1141.

[250] Ding, B.; Zhang, S.; Liu, Z. Y.; Yang, E. C.; Zhao, X. J. A spin-frustrated (4, 12)-connected metal-organic framework with unusual $[Co_8(\mu_4\text{-}OH)_6^{10+}]$ cubes. *Inorganic Chemistry Communications* **2017**, *83*, 27–30.

[251] Wang, X.-Y.; Sevov, S. C. A Manganese Carboxylate with Geometrically Frustrated Magnetic Layers of Novel Topology. *Chemistry of Materials* **2007**, *19*, 3763–3766.

[252] Zheng, Y. Z.; Tong, M. L.; Xue, W.; Zhang, W. X.; Chen, X. M.; Grandjean, F.; Long, G. J. A "Star" Antiferromagnet: A Polymeric Iron(III) Acetate That Exhibits Both Spin Frustration and Long-Range Magnetic Ordering. *Angewandte Chemie - International Edition* **2007**, *46*, 6076–6080.

[253] Mole, R. A.; Nadeem, M. A.; Stride, J. A.; Peterson, V. K.; Wood, P. T. Switchable Magnetism: Neutron Diffraction Studies of the Desolvated Coordination Polymer $Co_3(OH)_2(C_4O_4)_2$. *Inorganic Chemistry* **2013**, *52*, 13462–13468.

[254] Price, D. J.; Powell, A. K.; Wood, P. T. A new series of layered transition metal oxalates: hydrothermal synthesis, structural and magnetic studies. *Dalton Transactions* **2003**, 2478–2482.

[255] Hursthouse, M. B.; Light, M. E.; Price, D. J. One-Dimensional Magnetism in Anhydrous Iron and Cobalt Ternary Oxalates with Rare Trigonal-Prismatic Metal Coordination Environment. *Angewandte Chemie* **2004**, *43*, 472–475.

[256] Rousse, G.; Rodríguez-Carvajal, J. Oxalate-mediated long-range antiferromagnetism order in $Fe_2(C_2O_4)_{3\cdot 4}H_2O$. *Dalton Transactions* **2016**, *45*, 14311–14319.

[257] Zhang, B.; Baker, P. J.; Zhang, Y.; Wang, D.; Wang, Z.; Su, S.; Zhu, D.; Pratt, F. L. Quantum Spin Liquid from a Three-Dimensional Copper-Oxalate Framework. *Journal of the American Chemical Society* **2018**, *140*, 122–125.

[258] Lhotel, E.; Simonet, V.; Ortloff, J.; Canals, B.; Paulsen, C.; Suard, E.; Hansen, T.; Price, D.; Wood, P.; Powell, A.; Ballou, R. Magnetic properties of a family of quinternary oxalates. *The European Physical Journal B* **2013**, *86*, 248.

[259] Li, J.-H.; Liu, H.; Wei, L.; Wang, G.-M. Two novel Fe II-oxalate architectures: Solvent-free synthesis, structures, thermal and magnetic studies. *Solid State Sciences* **2015**, *48*, 225–229.

[260] Wang, X.; Kurono, R.; Nishimura, S. I.; Okubo, M.; Yamada, A. Iron-oxalato framework with one-dimensional open channels for electrochemical sodium-ion intercalation. *Chemistry - A European Journal* **2015**, *21*, 1096–1101.

[261] Yang, X.; Li, J.; Hou, Y.; Shi, S.; Shan, Y. $K_2Fe(C_2O_4)(HPO_4)(OH_2)\cdot H_2O$: A layered oxalatophosphate hybrid material. *Inorganica Chimica Acta* **2008**, *361*, 1510–1514.

[262] Tustain, K.; Farrar, L.; Yao, W.; Lightfoot, P.; da Silva, I.; F Telling, M. T.; Clark, L. Materialization of a Geometrically Frustrated Magnet in a Hybrid Coordination Framework: A Study of the Iron(II) Oxalate Fluoride Framework, $KFe(C_2O_4)F$. *Inorganic Chemistry* **2019**, *58*, 11971–11977.

[263] Pratt, F. WIMDA: a muon data analysis program for the Windows PC. *Physica B: Condensed Matter* **2000**, *289-290*, 710–714.

[264] Dean, P. A. W. The Oxalate Dianion, $C_2O_4{}^{2-}$: Planar or Nonplanar? *Journal of Chemical Education* **2012**, *89*, 417–418.

[265] Yao, W.; Sougrati, M.-T.; Hoang, K.; Hui, J.; Lightfoot, P.; Armstrong, A. R. $Na_2Fe(C_2O_4)F_2$: A New Iron-Based Polyoxyanion Cathode for Li/Na Ion Batteries. *Chemistry of Materials* **2017**, *29*, 2167–2172.

[266] Lancaster, T.; Blundell, S. J.; Pratt, F. L.; Brooks, M. L.; Manson, J. L.; Brechin, E. K.; Cadiou, C.; Low, D.; McInnes, E. J.; Winpenny, R. E. Muons as a probe of magnetism in molecule-based low dimensional magnets. *Journal of Physics: Condensed Matter* **2004**, *16*, S4563–S4582.

[267] Campbell, B. J.; Stokes, H. T.; Tanner, D. E.; Hatch, D. M. ISODISPLACE computer programs. *J. Appl. Cryst* **2006**, *39*, 607–614.

[268] Miller, S. C.; Love, W. F. *Tables of irreducible representations of space groups and co-representations of magnetic space groups*; Pruett: Boulder, CO, 1967.

[269] Pramanik, A.; Bradford, A.; Lee, S. L.; Lightfoot, P.; Armstrong, A. R. $Na_2Fe(C_2O_4)(HPO_4)$: A Promising New Oxalate-Phosphate based Mixed Polyanionic Cathode for Li/Na Ion Batteries. *Journal of Physics: Materials* **2021**, *4*, 024004.

[270] Ji, B.; Yao, W.; Zheng, Y.; Kidkhunthod, P.; Zhou, X.; Tunmee, S.; Sattayaporn, S.; Cheng, H.-M.; He, H.; Tang, Y. A fluoroxalate cathode material for potassium-ion batteries with ultra-long cyclability. *Nature Communications* **2020**, *11*, 1225.

[271] Yao, W.; Armstrong, A. R.; Zhou, X.; Sougrati, M.-T.; Kidkhunthod, P.; Tunmee, S.; Sun, C.; Sattayaporn, S.; Lightfoot, P.; Ji, B.; Jiang, C.; Wu, N.; Tang, Y.; Cheng, H.-M. An oxalate cathode for lithium ion batteries with combined cationic and polyanionic redox. *Nature Communications* **2019**, *10*, 3483.

[272] Keen, D. A.; Goodwin, A. L. The crystallography of correlated disorder. *Nature* **2015**, *521*, 303–309.

[273] Simonov, A.; Goodwin, A. L. Designing disorder into crystalline materials. *Nature Reviews Chemistry* **2020**, *4*, 657–673.

[274] Kawamura, H.; Watanabe, K.; Shimokawa, T. Quantum Spin-Liquid Behavior in the Spin-$\frac{1}{2}$ Random-Bond Heisenberg Antiferromagnet on the Kagome Lattice. *J. Phys. Soc. Japan* **2014**, *83*, 103704.

[275] Khatua, J.; Orain, J. C.; Ozarowski, A.; Sethupathi, K.; Rao, M. S. R.; Zorko, A.; Khuntia, P. Signature of a randomness-driven spin-liquid state in a frustrated magnet. **2021**, Preprint at http://arxiv.org/abs/2107.08668v1.